How Curved Creases Enhance the Stiffness and Enable Shape Morphing of Thin-Sheet Structures

by

Steven R. Woodruff

A dissertation submitted in partial fulfillment
of the requirements for the degree of
Doctor of Philosophy
(Civil Engineering)
in the University of Michigan
2022

Doctoral Committee:

Assistant Professor Evgueni T. Filipov, Chair
Associate Professor Ann E. Jeffers
Professor Jason P. McCormick
Assistant Professor Serife Tol

Steven R. Woodruff

stevenrw@umich.edu

ORCID iD: 0000-0003-0049-2108

Acknowledgments

On its surface, this dissertation represents a culmination of my research over the past five years at the University of Michigan. On closer inspection, the work described in this document rests upon a foundation built and maintained by the people in my life. From countless conversations, emails, Zoom meetings, collaborations, text messages, and phone calls, I have learned so much and am happy to present my findings here. It is necessary that I recognize the people who have had a positive impact on my life, and subsequently, my work.

First, I would like to thank my doctoral advisor and dissertation committee chair, Dr. Evgueni Filipov. From you, I have learned what it means to be a dedicated and curious researcher. As my advisor, you have shown me the power of high-quality work and the great heights a professor can reach in their early career. I hope to have even a fraction of your talent and dedication as I move forward in my own career. Additionally, you have helped me cultivate my love for learning, teaching, and policy – all skills that have led me to my next step. Early in my time at the University of Michigan, I was taught the difference between a mentor and an advisor. I am happy to say that I have found both in you. Thank you for all your support, input, and understanding.

Additionally, I want to thank the each of the other members of my dissertation committee for their contributions to my research and professional development. Dr. Ann Jeffers, thank you for your guidance over the years as my professor, my GSI mentor, a job reference, as a role model for LGBTQ+ leadership in engineering, and as an advocate for mental health in academia. From you, I know what it means to be a strong educator and leader. Dr. Jason McCormick, thank you for your contributions as a member of my preliminary exam committee, job reference, and as the leader of many service activities during my years at the University of Michigan. From you, I understand the impact and joy of community engagement in engineering. Finally, Dr. Serife Tol,

thank you for your unique perspectives on my research. From you, my dissertation is stronger and more accessible to those outside the field of civil engineering.

Furthermore, I would like to thank the friends and colleagues I have gained over the years. To the DRSL group, Maria Redoutey, Zhongyuan Wo, Yi Zhu, Yutong Xia, and Hardik Patil, thank you for your collaboration and constructive critique of my work over the years. I am also grateful for the other Ph.D. students in the CEE department for their advice and friendship. To HWL, thank you for your guidance and support; my journey here would have been nearly impossible without you. To Freddy and Jordan, thank you for inspiring me to pursue a doctoral degree and for being my friends. I wish you all the best of luck moving forward.

Next, I want to thank my family for their constant love and support. Mom, Dad, Megan, Melissa, Will, and Erik, thank you for being there for me. I also want to thank Uncle Joe, Auntie Lisa, Uncle Scott, Sienna, Auntie Rose, Lindsay, Brandan, Uncle Ronnie, Auntie Holly, Adam, Josh, and Grandma. Finally, to Nonna, Nonno, Auntie Anna, and Grandpa, I wish you could have been there to see me finish my degree, but I know that with your love and memories, I have achieved everything you had hoped for me. I am finally going to be a professor, Nonna.

Finally, I want to extend my sincerest gratitude to my partner and best friend, Dr. Ben Blankenship. Your constant love and belief in me was, and continues to be, ballast in the stormy sea of life. Your guidance and advice to me as a Ph.D. candidate was worth its weight in gold. You brought me strength, a helping hand, levity, perspective, and wisdom over our (nearly) five years together. I cannot imagine where I would be without you, Lori, Meghan, Stew, Hailey, Delaney, Lynxie, and Raven. I am excited to continue building our lives together. Thank you.

—

The research presented in this dissertation is based on work supported in part by the National Science Foundation's Graduate Research Fellowship Program (Grant No. DGE 1841052) and the Office of Naval Research (Grants No. N00014-18-1-2015 and N00014-20-5-B001). Any opinions, findings, conclusions, or recommendations expressed in this document are those of the author and do not necessarily reflect the views of these institutions.

Table of Contents

List of Figures

List of Tables

List of Appendices

Abstract

When a thin sheet is folded about curved creases, the resulting shape resists loads in some directions and deforms into compact states in other directions. These curved-crease, origami-inspired structures display a number of functional behaviors advantageous to a design, such as tunable stiffness and shape morphing. This dissertation develops an understanding of how these behaviors are related to the crease pattern and how engineers can exploit these traits in their designs through mechanics.

The dissertation introduces a method for simulating the structural properties of curved-crease origami using a simplified numerical method called the bar-and-hinge model. Based on the geometry and material of the sheet, stiffness expressions were derived for three deformation behaviors, including stretching of the sheet, bending of the sheet, and folding along the creases. The model is capable of capturing the folding behavior, and the simulated deformed shapes are sufficiently accurate when compared to experiments and to theoretical approximations. This model is used to explore the mechanical characteristics of curved-crease structures throughout the dissertation.

Next, the dissertation explores the bending stiffness of curved-crease corrugations that are made by folding thin sheets about curves and without linerboard covers (i.e., flat sheets adhered to the corrugation to give the structure a more isotropic bending stiffness behavior). Curved-creases break symmetry in the corrugation, which allows for a unique property that redistributes stiffness to resist bending deformations in multiple directions. Two formulations for predicting the bending stiffness of any planar-midsurface corrugation were developed and experimentally validated with three-point bending tests.

Then, the dissertations explores a unique behavior seen in creased sheets where localized changes in the folding (i.e., pinching of the structure) result in global bending and twisting deformations. It was found that the increase in curvature and torsion of the crease due to pinching

are proportional to the curvature of the crease before folding. Physical prototypes and numerical simulation were used to explore how geometry and the number of creases on a sheet change the global bending and twisting. These relations were used to create a framework for choosing a crease pattern that generates a desired deformation upon pinching.

Continuing the investigation on how pinches cause global deformations, an inverse-design scheme was created that solves three problems related to shape-fitting origami. The first problem aims to find a crease pattern that folds to a desired planar curve. The second problem aims to find a crease pattern and actuation scheme that maximizes the deflection at the end of the crease during pinching. The last problem aims to find a design whose end will reach a target point in three-dimensional space upon folding and pinching. A forward-process to describe the deformation of a single crease composed of several circular arc segments was developed. Using analytical equations and data from the bar-and-hinge method, the deformation values were calculated and were then used in an optimization process. These analyses are a first step towards practical shape fitting of curved-crease origami.

This dissertation sets a foundation for practical application of curved-crease origami in structural engineering by developing appropriate simulation methods and an understanding of how these crease patterns offer unique stiffness properties and shape-morphing capabilities.

Chapter 1

Introduction

In the built environment, curves are a formidable design feature. As a departure from straight lines and planar surfaces, curves are broadly defined, difficult to analyze, and complicated to construct. However, the rewards for designing with curves are significant: stunning shapes, unique functional behaviors, and optimal forms. Indeed, curves are found throughout the natural world in the form of plants bent towards light, rocks weathered smooth, and eyes bending light into retinas, among countless others. If the goal of engineering is to solve human problems, then it is imperative that we design with curves, despite their apparent complexity, to improve the built environment and enjoy the benefits of curved designs, reminiscent of nature.

Curved-crease origami are thin sheets folded about curved creases. Unlike traditional straight-crease origami, the folded shapes of curved-crease origami necessarily exhibit curvature in the form of curved surfaces between the curved edges of creases. Various examples of curved-crease origami made from paper sheets are shown in Figure 1.1. These models show the breadth of curved-crease origami designs and the aesthetically pleasing shapes they can form from flat sheets.

In recent years, much attention has been given to origami due to its ability to efficiently solve certain engineering problems. Origami principles have been used in a wide range of fields from architecture to robotics, biology to medicine. For instance, there are medical stents that can fold to a small form and unfold at vital points in the body (Kuribayashi et al., 2006; Rodrigues et al., 2017). Also, there are compactable solar arrays which take up little room in a spacecraft during launch and unfold to capture sunlight for power while in orbit (Miura, 1985; Tang et al., 2014). From a structural engineering standpoint, origami can be useful in a number of ways, including designing lightweight members that use less material, constructing structures from flat sheets that can be

Figure 1.1 – Paper models of folded curved-crease origami geometries.

easily shipped and quickly deployed, and creating stiff geometries through careful placement of material via folding.

Compared to straight-crease origami, there has been little research into the engineering benefits of curved-crease origami. The majority of research on curved-crease origami, in general, has focused on geometric analysis, specifically about finding the folded shape of sheets in response to a given curved crease (a thorough review of the literature about curved-crease origami is presented in Chapter 2). Although this is a necessary area of knowledge, geometry is not sufficient in describing the structural benefits of curved-crease origami. Therefore, I propose using analyses that build off geometry and include ideas from mechanics and physics. A mechanics-based approach will provide a holistic representation of curved-crease origami necessary for applications in structural engineering.

1.1 Defining Curved-Crease Origami

Curved-crease origami, also called "curved origami" and "curved-fold[1] origami," is defined differently across the literature. The definition I chose for my work comes from an engineering context,

[1] Although "crease" and "fold" are used interchangeably in the literature, I specifically refer to the edges where rotations occur as "creases" and the action of rotating as "folding".

where we need to consider the design, loading analysis, and construction of these systems. As such, *I define curved-crease origami as thin sheets locally folded about a crease along a curve*. This definition makes no presumptions about the folded shape or the foldability of the chosen crease pattern (the two-dimensional layout of creases that will be folded).

The engineering process of creating a curved-crease structure is shown in Figure 1.2. I start with a flat sheet with known material properties and dimensions (Figure 1.2(a)). Because sheets are easily manufactured and can be stacked and shipped, starting with a flat sheet is convenient for practical application, and therefore is a reasonable assumption. Next, I choose a crease pattern imposed on the flat sheet, including the shape of the curves and the direction of the folding (Figure 1.2(b)). I then fold the structure using actuators or external loads. The structure can be folded to some defined angle or or with some defined moment such that the sheets come to equilibrium (Figure 1.2(d)). In many materials, such as paper or polyester film, once the sheet is folded, the creases permanently deform and upon releasing the folding moments, the sheet maintains a three-dimensional folded shape; this permanent deformation could be another way of defining the amount of folding (Figure 1.2(c)). Finally, I can load the folded structure with external forces to achieve various design goals, such as carrying structural loads (Figure 1.2(e)).

Although curved-crease origami is sometimes thought of as a subcategory of all origami geometries, concepts defined for straight-crease origami in the literature often do not apply, supporting the argument that curved-crease origami is a superset of origami (and straight-crease origami are just patterns with curved creases of zero curvature). For example, *rigid foldability* is a property of some origami where the sheets can be folded without deformation other than the folding rotation (the deformations can be considered rigid-bodies linked with hinges) (O'Rourke, 2011). Rigid foldability never applies to curved-crease origami because curved-crease sheets always bend upon folding (Duncan and Duncan, 1982).

Another concept in straight-crease origami that does not strictly apply to curved-crease origami is called *flat foldability*. A flat-foldable origami has at least two different configurations which are completely flat (think of a piece of paper – one flat state; then it is folded in half – another flat

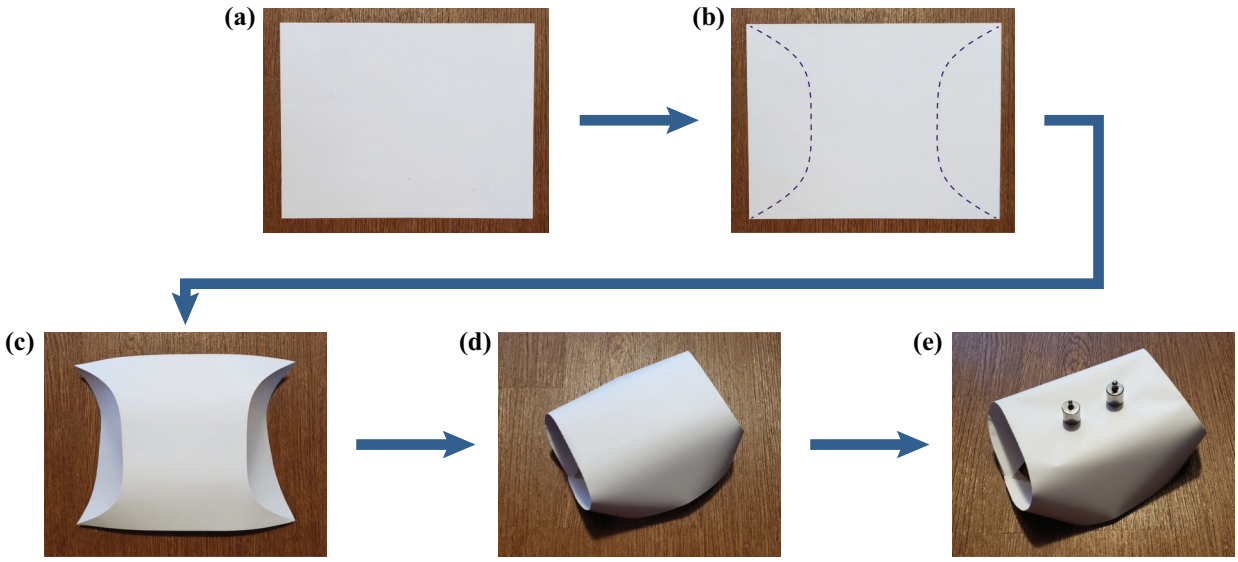

Figure 1.2 – Overview of the process of constructing a curved-crease structure. **(a)** A flat sheet is a good start for the process because it can be easily manufactured and shipped. **(b)** On the flat sheet, a crease pattern is prescribed indicating where the sheet will be folded and whether the folding rotations will occur in one direction or in another (mountain or valley crease assignment). **(c)** The next step is to fold the sheet as per the crease pattern. In many materials, there is plastic damage at the creases which permanently deforms the sheet after folding. **(d)** The folding can continue using actuators or external forces to create the desired final structure. **(e)** The final step is to load the structure for its functional use.

state). Typically, folding curved-crease origami from a flat state to another results in mechanical frustration, which leads to large curvatures or stretching in the sheet. Folding curved-crease origami to another flat state is possible, but is rarely as simple as that shown in straight-crease folding.

A third concept found in straight-crease origami analysis is called *mechanism degrees-of-freedom*. Straight-crease origami can be conceptualized as a mechanism (a system of rigid bodies that can move relative to each other about hinges and links). Distinct from structural degrees-of-freedom, a mechanism degree-of-freedom defines the number of independent motions a system can have without the input of external forces or moments. Because folding thin sheets about curved creases always results in sheet bending, curved-crease origami is never a system of independent rigid bodies. Some researchers have circumvented this problem by defining *compliant mechanism* where rotations of sheets about creases are much more flexible compared to the deformations within the sheets (Howell, 2013), and the system is seen as connected deformable bodies. However, within curved-crease origami, the deformations of the creases and sheets interact with each other during folding. This interaction suggests that the motions of curved-crease origami are cou-

pled; thus, curved-crease origami do not exhibit any mechanism degrees-of-freedom. As such, categorizing curved-crease origami by mechanism degrees-of-freedom might be moot.

A fourth and final concept in straight-crease origami analysis does apply to curved-crease origami and is called *developability*. Here origami can be flattened into a single plane. All of the geometries I explore in this dissertation start from a flat sheet and satisfy developability. However, researchers have published about origami tubes which cannot flatten to a single plane (Filipov et al., 2015; Garrett et al., 2016; Yao et al., 2020b). Additionally, folds can be imposed onto surfaces (such as spheres and hyperboloids) with non-zero Gaussian curvature (Bende et al., 2015).

As such, most of the traditional categories for straight-crease origami do not apply to curved-crease origami. Thus, I propose a different framework centered around defining the deformations of thin sheets. This brings us back to the idea that curved-crease origami is a deformation of a thin sheet by folding about curved creases.

A visual for the framework for categorizing the deformation of thin sheets is shown in Figure 1.3. I start with the flat sheet that has known material properties, crease pattern, and dimensions. This sheet can be deformed through an initial loading. The deformations from this initial loading are categorized as either *isometric* or *non-isometric*.

Isometric[2] deformations are those which preserve distances along the surface. This means that as a sheet is folded, there is no stretching or shearing in the surface. Sheets can undergo two types of isometric deformations. The first is folding where extreme rotations occur at creases. Although in a real sheet, folding rotations would cause local in-plane strains (Peraza-Hernandez et al., 2014), the deformation is highly concentrated and can be lumped into one area aligned with the crease. The second type of isometric deformation is sheet bending. Curved-crease origami always display sheet bending along with folding. Indeed, curved-crease origami have been idealized as purely isometric deformations that result in *piecewise-developable* surfaces.[3] In this conceptualization, a curved-crease origami is simply developable surfaces linked together at creases.

[2]From the Greek *isos-*, "equal" and *-metria*, "measurement."

[3]A developable surface is an isometrically deformed sheet and includes cones, cylinders, and tangent developable surfaces; this is distinct from developability described earlier in that developable surfaces are an assumed deformation without stretching and developability is a folded shape that comes from a flat sheet, even with stretching.

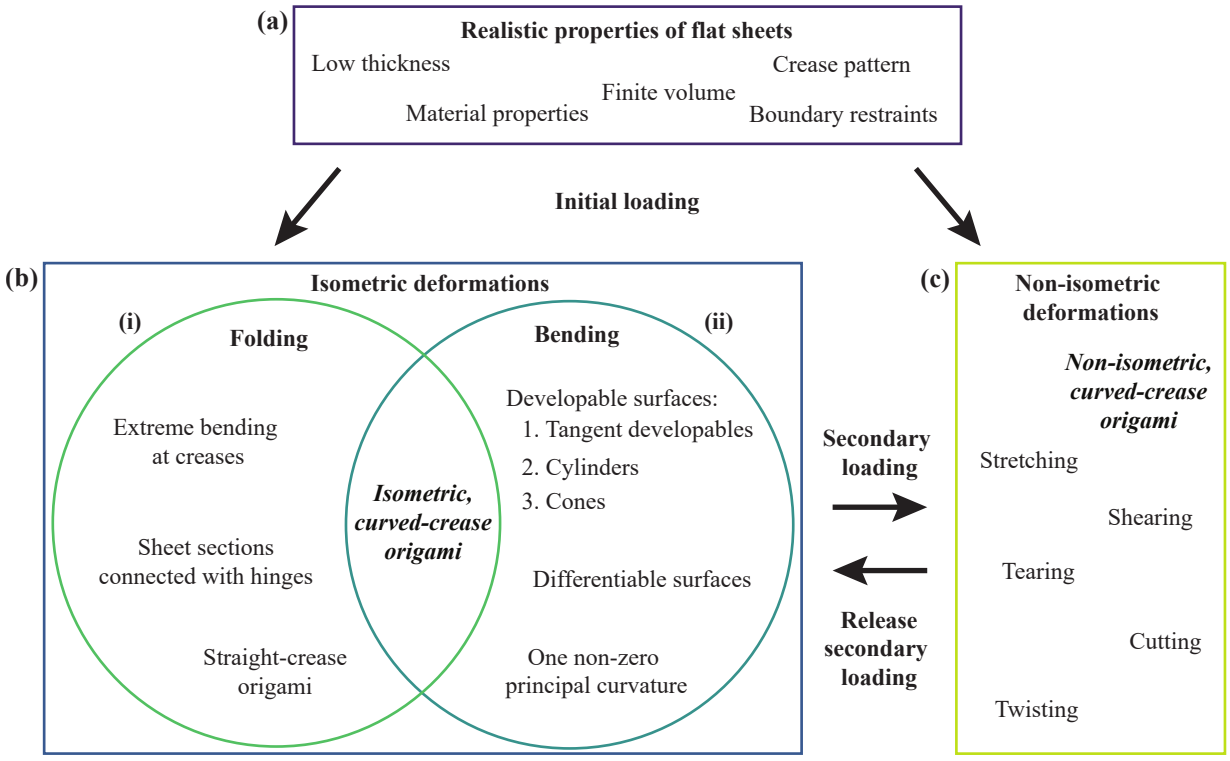

Figure 1.3 – Framework for categorizing the deformations of thin sheets. **(a)** My framework begins with flat sheets with realistic properties. The sheet might experience an initial loading method (such as folding about a crease) which results in either isometric or non-isometric deformations. **(b)** Isometric deformations preserve distances along a surface (no stretching) and include (i) folding and (ii) sheet bending, the union of which describes many curved-crease origami deformations (called isometric, curved-crease origami). **(c)** Non-isometric deformations do not preserve distances along a surface and come about by either folding certain curved-crease patterns or by loading already isometrically deformed origami (secondary loading).

Non-isometric deformations can occur in one of two ways. The first is when an isometrically deformed sheet (a folded geometry) is loaded with external forces (a process I call secondary loading). Non-isometric deformations of this type will occur in most applications of curved-crease origami structures, where the structure is loaded after folding. Another way non-isometric deformations occur is when certain crease patterns with many curved creases are folded. However, this version of non-isometric, curved-crease origami is greatly understudied. In fact, some researchers have called origami with non-isometric deformations "impossible designs," while still acknowledging their foldability, just knowing that the isometric mathematics describing the creases and sheets do not apply (Demaine et al., 2018). In these cases, the creases interact in a way that stretching or buckling occurs. Additionally, according to isometric deformation theory, the curvatures in the sheets approach infinity as curved-crease origami is folded. As a mechanical process, it is likely that as bending curvatures approach infinity, stretching or buckling would occur as a lower-energy alternative (Woodruff and Filipov, 2022).

As stated earlier, much of the research on curved-crease origami is founded upon the assumption that folding results in purely isometric deformations. Although this does not describe all curved-crease origami, isometric deformations are, indeed, a low-energy deformation. This can be explained, at least at a local level, using mechanics. Assume we have a thin sheet of thickness, t, and length, l (length is measured as the dimension perpendicular to the direction of bending and parallel to the direction of stretching). The stretching stiffness of a sheet is of order $O(t/l)$. And, the bending stiffness of a sheet is of order $O([t/l]^3)$. Since the thickness-to-length ratio is small, $t/l << 1$, the bending stiffness should be significantly smaller than the stretching stiffness, and the system will tend to deform in bending (Pini et al., 2016).

This definition of curved-crease origami is suitable for research into origami structures because the inputs are known, the crease pattern can be arbitrary, and the deformed shape is deterministic. Because this definition is based in physics, results will mirror those found in real experiments. By following an engineering process, I can determine what the structural benefits of curved-crease origami are without having to make unrealistic assumptions about the deformations.

1.2 Structural Advantages of Curved-Crease Sheets

Origami-inspired structures, of all types, possess features that are advantageous to structural designs. For instance, because origami is made from thin sheets, structures can be prefabricated (by scoring or perforating sheets), shipped, and deployed on site. Additionally, folding thin sheets displaces material away from the centroid of the geometry. This increases the structure's ability to resist bending. Origami-inspired structures are lightweight and use little material, as well.

Beyond these advantages, curved-crease origami offers unique structural benefits not found in straight-crease origami. When curved-crease origami are folded, the sheets adjacent to the curved creases will always bend. This sheet curvature offers a greater local bending stiffness (on top of global bending stiffness gains) since material is displaced from the neutral axis. An experiment inspired by Pini et al. (2016) shows this (see Figure 1.4): take a flat piece of paper and hold one end of it so that the flat side is perpendicular to the floor (like a cantilever beam); now, rotate the corners of the paper at the end you are holding so that the sheet curves slightly. You should see that in the flat state, the paper cannot support its own weight in bending. By applying the small curvature, the sheet gains enough bending stiffness to prevent collapse.[4] In curved-crease origami, this local bending stiffness gain is distributed throughout the geometry (although, in a highly anisotropic manner). Sheets between creases can support their own weight without the use of stiffeners.

Another unique benefit of curved-crease origami is that there are an infinite number of designs available, even with a single crease. This design freedom comes from the fact that there are an infinite number of paths between two points on a plane (a straight crease is the shortest path). This high degree of design freedom can make analysis challenging since managing the scope of the geometries becomes a salient task. However, this freedom can be exploited so a folded shape fits a specific desired shape. Additionally, because a curve can span all of a two-dimensional plane, there is greater freedom to place creases throughout the sheet without having to add sharp intersections

[4]Coincidentally, Wired published an article two days before the Pini et al. paper was published about surface curvatures that shows the same experiment, but with pizza instead of paper (Bhatia, 2014)

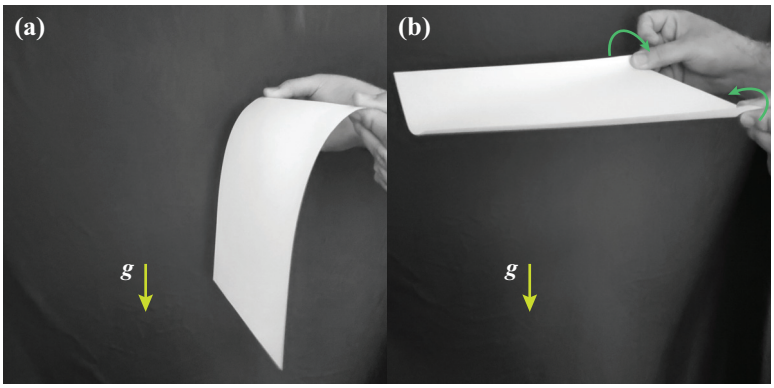

Figure 1.4 – Surface curvature imparts bending stiffness to sheets. **(a)** A cantilevered sheet will collapse under its own weight. **(b)** Slightly curving the same sheet moves material away from the neutral axis, imparting bending stiffness that resists gravity, **g**.

(that might focus a structural failure).

The stiffness response of a curved-crease structure can also be tailored by varying the crease geometry. As shown by Woodruff and Filipov (2020b), curved-crease structures can be designed for global stiffness isotropy (such as creating a plate-like structure that resists bending in all directions with less material). Conversely, curved-crease origami can be designed for high global stiffness anisotropy where there is a direction of loading that resists deformations and a direction that gives in, offering a compactable system that can be deployed to bear loads.

When a sheet is folded about curved creases, the sheets adjoining the crease will always bend. In an elastic sheet, folding will build potential energy in the form of bending strains. This potential energy can be used for rapid deployment where a structural member needs to be released quickly (for example, in crash-landing gear or to deploy solar arrays). An example of rapid deployment is shown in Figure 1.5. Additionally, the stiff response of the folded sheets can resist motions, ultimately stopping a deploying process without causing uncontrollable vibrations (an anecdotal example of this problem comes from NASA, where solar arrays made from straight-crease origami were deployed, and the panels continued to rotate and crashed into each other, damaging the panels[5]).

Beyond structural advantages, the curved sheets between creases can be used to create acoustic

[5]This story was shared with the author at the 2018 ASCE Earth and Space Conference by a NASA employee who attended the author's presentation on curved-crease structures; the contents of the presentation are published in Woodruff and Filipov (2018).

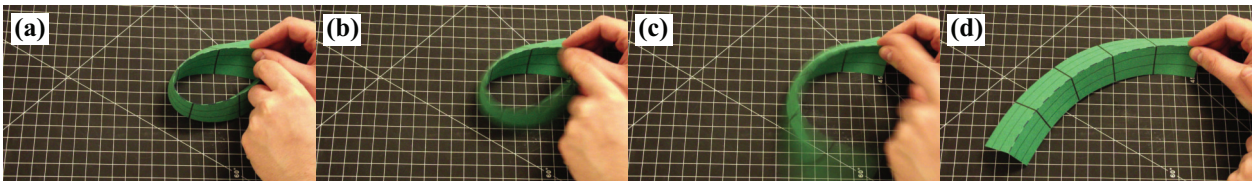

Figure 1.5 – Sheet bending stores elastic strain energy that can be used to deploy origami rapidly. **(a)** A folded, curved-crease origami sheet can be wound up and **(b-d)** quickly unfurls upon release.

or thermal focusing or diffusing surfaces. Since changes in the folding angles changes the curvatures of the surface, curved-crease origami structures could potentially be used for tailored wave control.

The structural benefits of curved-crease origami are backed by foundational ideas in structural mechanics. Because curved-crease origami have multiple curved surfaces and the deformations are coupled, these theories must be shown in actual curved-crease structures to better support these ideas.

1.3 Dissertation Goals

The goal of this dissertation is to develop a better understanding of the structural properties of curved-crease origami using a mechanics-based approach. Ultimately, the knowledge presented should help develop design and analysis methodologies so that a curved-crease, origami-inspired structure can be manufactured from a flat sheet and deployed to achieve specific goals inline with the unique behaviors of curved-crease geometries.

To that end, I explore three main areas. The first area aims to develop a holistic structural analysis process for the curved-crease origami. That is, prescribing a crease pattern and structural restraints onto a flat sheet and modeling the sheet folding to a functional, three-dimensional shape with the possibility of loading the resulting structure. Due to large degree of design freedom presented by a curved-crease crease pattern, I want a process that can capture a variety of curved-crease geometries and is rapid enough to explore the structural behavior of patterns in a parametric fashion. Furthermore, the model should give the equilibrium state of the folded sheet in response to loads and boundary conditions so that results from the simulation will approximate the behav-

iors of real sheets under identifiable loading conditions. Such a simulation tool will prove useful to identifying the unique properties of curved-crease origami starting from an easily designed, flat crease pattern.

The second area of the dissertation explores how curved creases can be designed to control the stiffness response of origami. Knowing that curved-crease folding reorients sheets in ways that enhance stiffness, I aim to determine the link between the crease pattern on a flat sheet and the folded structure's stiffness. Establishing such a link will allow engineers to exploit the unique behaviors of curved-crease origami to enhance the structure's stiffness where needed.

Finally, the third area of the dissertation explores the shape morphing of curved-crease structures due to pinching and creates sample designs that deform to match desired shapes after actuation. Since a single curved crease can take on an infinite number of shapes in a sheet, there is great potential for fitting origami to target points, surfaces, or volumes. I discover relationships between the crease pattern geometry and the deformation response of origami after actuation. What I learn is then used to develop a method for generating a crease pattern that solves three shape-fitting problems of varying complexity, a tangible demonstration of the design potential hidden in the curves and edges of these structures.

1.4 Dissertation Organization

The dissertation is organized as follows. In Chapter 2, I present a review of the literature related to curved-crease origami. The chapter includes a section on applications of curved-crease origami including those in art, architecture, and engineered technology. I then show the development of analysis methods for describing the folded shape and mechanical response of curved-crease origami. I conclude the chapter with a discussion about what areas of knowledge are missing relating to the dissertation research goals described earlier.

In Chapter 3, I explore how a low-degree-of-freedom numerical method, called the bar-and-hinge method, can be used to model folding behavior and secondary loading responses of curved-crease origami. I formulate stiffness expressions describing the stretching of sheets, bending of

sheets, and folding of creases based off parameters a user knows before analysis, such as the material properties and boundary conditions applied to the sheet. I validate these expressions using theoretical mechanics, closed-form, geometry-based methods, and experimental methods. I finish the chapter by modeling different curved-crease origami folding and secondary loading, revealing some of the inherent, globally anisotropic stiffness behaviors of the systems. I find that the bar-and-hinge model is a reliable and rapid method of folding from a flat sheet with considerable accuracy. I also use the bar-and-hinge model in subsequent chapters.

In Chapter 4, I introduce and explore a unique curved-crease corrugation structure that resists bending deformations in all directions at nearly the same stiffness (i.e., globally isotropic bending stiffness). I create a qualitative framework identifying the important geometric features of a curved-crease corrugation at multiple scales. I use this qualitative framework to create two quantitative methods for predicting the bending stiffness of corrugations in three given directions based off the second moment of area. I validate these results using three-point bending tests on polyester-film specimens. I find that certain curved-crease patterns result in a folded corrugation with isotropic bending stiffness.

In Chapter 5, I develop fundamental relationships between the crease pattern of single- and multi-crease origami and the degree of bending and twisting seen after a local actuation (i.e., a pinch). Using a local pinch to generate a large, global response will reduce the actuation complexity of a curved-crease, origami deployable in much the same way as a one-degree-of-freedom crease pattern allows for rapid deployment (e.g., Miura-ori tubes (Filipov et al., 2015)). I determine the relationship between the crease pattern geometry and the degree of bending and twisting generated from a pinch. Once a relationship between the crease pattern and the pinch-deformation response is determined, I can develop an inverse-design scheme that can generate a crease pattern capable of hitting a desired shape.

In Chapter 6, I use the information from the prior chapter to develop the inverse-design scheme. I focus on three problems that aim to find a crease pattern and actuation scheme for a single crease with discrete, variable curvature that folds and pinches to a desired shape. I develop the

forward process for determining the shape of such a structure using vector math and bar-and-hinge-generated deformation data. Then, I employ a genetic algorithm to find a crease pattern satisfies three shape-fitting problems. With this method, I am able to find a sufficient crease pattern for a wide variety of target points, shapes, and deflections. This chapter demonstrates how curved creases allow for versatile design.

In Chapter 7, I conclude the dissertation with a summary of the work presented along with discussion on future directions for work, both in the near- and long-term. Discussions on future work in the near-term are presented at the end of each chapter and are summarized in this conclusions chapter. Directions of future work in the long-term aim to address more complex challenges associated with analyzing and designing curved-crease origami structures. These areas include application of artificial intelligence for origami analysis and design, large-scale analysis and design of curved-crease origami, and combining these two areas to develop smart, adaptive structures and metamaterials from curved creases.

I provide two appendices that show work that I did not closely develop myself, but are important to explaining the ideas and methods that I developed in the bulk of the dissertation. These appendices act as a closer literature review and background information with specific applications to the curved-crease origami I use in the rest of the dissertation. For those familiar with curved-crease origami, reading these appendices might be unnecessary.

In Appendix A, I describe a method of generating a curved-crease origami geometry from a single, already-deformed crease using closed-form, geometric relationships (under the assumption that all deformations are isometric). Understanding this method, despite its significant limitations, will help explain important concepts about curved-crease origami that will be useful in subsequent chapters.

In Appendix B, I explain how curved-crease origami can be modeled using finite elements in Abaqus. I show the process of modeling a crease using connector hinges and sheets with shell elements. Additionally, I explore four different methods of actuating the structure to generate folding. With finite elements, I can find local behaviors of the structure, but at the cost of model complexity

and runtime.

Chapter 2

Literature Review: Engineering Curved-Crease Origami

Ah, the creative process is the same secret in science as it is in art.

They are all the same absolutely.

–Joseph Albers

The purpose of this chapter is to motivate the idea that a practical understanding of curved-crease origami requires applying the principles of mechanics and structural analysis on top of geometric analysis. A practical understanding of curved-crease origami would facilitate the design process for curved-crease systems starting from a flat sheet and ending with a folded geometry with desired structural properties. The ultimate goal of this research, from an engineering perspective, is solve difficult problems in structural engineering with the novel characteristics and benefits of curved-crease origami. To meet this goal, the context and achievements of prior research should be recognized in order to identify undone research that will likely result in a better practical understanding of curved-crease origami.

In this chapter, I will explore three main areas related to existing literature on curved-crease origami. First, I will look at applications of curved-crease origami in art, architecture, and engineering. Next, I will explore existing methods for analyzing the folding of flat sheets, the deformed shape of folded, curved-crease origami, and the structural analysis of curved-crease origami. In the final section, I will identify and explain undone research synthesized from the existing literature. This body of missing knowledge will be addressed in the remainder of the dissertation.

Note that this chapter is not a comprehensive review of all literature related to curved-crease origami. There are no lists of different curved-crease patterns or a complete examination of the

fields that eventually were brought together to form curved-crease origami as an academic pursuit. Rather, I examine a curated set of research, identifying seminal publications and a few historical records, that ultimately helps motivate and support the goals of this dissertation.

2.1 Applications of Curved-Crease Origami

An application of curved-crease origami is any attempt at using thin sheets with curved creases to achieve some goal (be it aesthetic or functional). Most applications to date were designed using trial-and-error methods. As often stated in academic literature, understanding of curved-crease origami is deficient. Thus, use of rigorous methods of analysis are similarly limited. Setting aside, for now, the exact methods of design used to create curved-crease art and technology, I explore the achievements of past practitioners. The existing body of applications for curved-crease origami shows the breadth of their aesthetic and functional properties, further motivating the use of curved-crease origami in structural engineering.

2.1.1 Artistic Curved-Crease Origami

An artistic application of curved-crease origami is any example of a curved-crease form constructed for mainly aesthetic purposes. The methods used to construct artistic curved-crease origami are mainly of the trial-and-error type. Quantification of the deformed shape of the folded sheets is beyond the scope of artistic applications of curved-crease origami. However, art often motivates the rigorous analysis of curved-crease origami, and shows the breadth of this type of form.

Unlike straight-crease origami, curve-crease origami is not deeply rooted in traditional Japanese art. In fact, the earliest records of curved-crease origami forms come from seventeenth-century Germany (Koschitz, 2014). For instance, there are illustrations of napkins folded about curved creases from 1699. These pieces depicted abstract forms using a repeated pattern of mountain and valley folds. Napkin folding was practiced in Europe until the eighteenth century, when the art faded out of fashion.

Recorded examples of curved-crease origami began to reappear in the early twentieth century,

coincidentally, in Germany. The Staatliches Bauhaus school, originally in Weimar, Germany, was an art and design school opened in 1919 and closed by the Nazis in 1933 (Chilvers, 2009). The school became famous for its influence in the realm of design, often referred to as the Bauhaus movement. One of the goals of the Bauhaus movement was to elevate crafts by employing them in designs, creating a bridge between aesthetics and functional applications. An instructor of architecture, Josef Albers, lead a class that explored circular, pleated annuli that buckled out of plane (Koschitz, 2014). The pleated annuli propagated through students of the school, including Alexander "Xanti" Schawinsky whose wife, Irene Schawinsky, presented a modified version of the pleated annulus (this time, with a larger center hole) at the New York Museum of Modern Art around 1944 (Demaine and Demaine, 2015). The pleated annulus form has recently been recreated and modified by other artists like Martin Demaine (Demaine et al., 2015) and Joyce Aysta (Aysta, 2019).

In the 1960s and 70s, curved-crease origami collided with computer graphics. Ron Resch, whose interests spanned from sculpture to architecture to computer science, designed a series of curved-crease origami art pieces using both physical materials and computer renderings (Resch, 1970). Around the same time, David Huffman, a computer scientist mostly known for creating "Huffman codes" used for lossless data compression, explored a large number of curved-crease forms by creating pieces made from PVC sheets folded about curved creases made using a burnishing tool (Demaine et al., 2011). Duks Koschitz's doctoral thesis focused on recording the many examples of curved-crease pieces made by Huffman (Koschitz, 2014). Huffman went on to establish the field of quantitative, curved-crease origami analysis using his expertise gained from creating curved-crease origami art.

Since the 1970s, curved-crease origami as an art form has persisted. Various example of curved-crease origami art include designs created by Hiroshi Ogawa in his 1972 book titled, *Forms of paper* (Ogawa, 1972). In fact, Huffman owned a copy of Ogawa's book which might have inspired Huffman's work into curved-crease origami (Demaine et al., 2015). Other pieces of curved-crease origami that are of interest is a series of animal masks made by Roy Iwaki in the late twentieth

century (Iwaki, 1986). Further, a curved-crease origami design by Herman van Goubergen is placed on a mirror, revealing the form of a human skull (Smeijsters, 2014). As proof of continued interest into the artistic forms of curved-crease origami, a book entirely devoted to the subject by Jun Mitani was published in 2019 (Mitani, 2019).

Artistic applications of curved-crease origami span from figurative to abstract forms. Perhaps the curved surfaces that are generated by folding sheets about curved creases are an appealing aesthetic feature that draws in artists. As I will explain, the aesthetic design of curved-crease origami has appealed to architects in their design, bringing curved-crease origami even closer to functional design purposes.

2.1.2 Architectural Curved-Crease Origami

Architectural applications of curved-crease origami straddle the line between pure aesthetics and functional uses. The purpose of many of the architectural projects I explain below is to explore the aesthetic features of curved-crease origami, but the structures themselves must be stable. The analysis guaranteeing stability of these structures is often found using trial-and-error and geometric reasoning. Rigorous structural analysis is lacking in these examples. Nonetheless, architectural designs are often a precursor for structural designs. The forms found by architects show a range of scales and fabrication methods that further inform structural design.

The first example of curved-crease origami used in architectural design is as concrete form-work. Upon observing the deformed shape of hanging chains (a process of determining compression-only structures by inverting designs created by tension-only members, called form-finding), some architects noticed that the curved shapes could be captured using curved-crease origami sheets (Bhooshan et al., 2015). Additionally, because the form-work required for casting concrete on curved surfaces is expensive and complex, the architects in this project realized they could simplify the process by creating these compression-only structures using curved-crease origami sheets as form-work. In this case, curved-crease origami was used as a means of constructing a structure, not the structure itself.

Another architectural use of curved-crease origami explores creating accent pieces for non-structural purposes. Because curved-crease origami sheets have curved surfaces, thermal or acoustic waves can be focused or dispersed by reflecting off these structures. Tachi and Epps (2011) designed and fabricated a dynamic solar shade built using curved-crease folding that can be opened or closed to adjust the level of sunlight passing through a window. Because of the curved creases, each panel extending from the main ring deploys smoothly using only one degree of freedom. Curved-crease origami has also been used for static forms, like accent pieces made by folding sheet-metal using a hydraulic robot called RoboFold (Epps and Verma, 2013). While it is possible to use these static accent pieces as acoustic diffusers, there has been no rigorous investigation into this idea.

The geometric forms of curved-crease origami have also been proposed as load-bearing members, like beams or columns. One example is a curved-crease beam made from timber (Buri et al., 2011). The authors of this paper proposed that this beam can be used to support bending loads (like in a floor), but admit that finite element analysis should be performed on it before continuing with its use.[1] Regardless, this beam is an example of a curved-crease origami structure being made from real materials at scale. Another example of a curved-crease member is a column. Raducanu et al. (2016) created a series of column prototypes using curved-crease sheets in paper and constructed a larger-scale column in steel. Again, in their project, there was little structural analysis, but their column shows curved-crease origami constructed from a common and stiff material.

A large portion of architectural, curved-crease origami projects have been presented at the International Association for Shell and Spacial Structures's symposia with the goal of creating self-supporting pavilion structures. As pavilions, curved-crease origami have been used in two ways. The first is as a global geometry itself, such as the *Arum* pavilion folded by the RoboFold robot (Grieco, 2012). The other way curved-crease origami has been used in pavilions is as a discrete locking system where small forms are fabricated and connected together. The *Undulatus* (Brancart et al., 2015) and *Z-Snap* (Filz and Kumrić, 2017) pavilions are examples of these

[1] Later research by Cui et al. (2018) explored different methods of manufacturing similar curved-crease beams out of steel and timber; their analysis explored surface imperfections, but did not include a mechanics-based analysis.

types of designs. One of the advantages of using discrete and connectable curved-crease origami sheets is that non-developable surfaces (like spheres and ellipsoids) can be approximated.

Although the architectural design created using curved-crease origami have not considered structural mechanics, the geometric forms explored in these projects shows the breadth of designs possible. Furthermore, these projects show that full-scale curved-crease structures can be built using practical and durable materials. By further exploring the structural properties of these geometries, engineers can create designs that serve the functional needs of these systems on top of the aesthetic values.

2.1.3 Engineered Curved-Crease Origami

By engineered applications, I mean to say curved-crease origami forms that were created to fit functional purposes via exploitation of their geometric, structural, and/or multiphysical properties. Curved-crease origami systems have been used in a wide variety of engineering disciplines including packaging, aerospace, structural, mechanical, and naval architecture.

The simplest example of curved-crease origami comes from packaging engineering where the french fry boxes served at McDonald's have curved bottoms (Luu, e 11). Curved-crease origami can fold into shapes with large voids for storing goods. Additionally, this space is preserved and the contents of the package are protected because curved-crease origami cannot fold to a flat state (besides the flat crease pattern) without applying significant forces to the surface. Thus, curved-crease boxes can be folded and their shape preserved with less tape or a single locking mechanism, compared to a rectangular box that requires more restraints.

Another example of an engineered application comes from aerospace engineering. Here, thin sheets are designed to fold around curved creases to compactly store the material. This is useful for technology like solar sails that need to be efficiently stored on the spacecraft during launch and reliably and smoothly deployed after launch. Lee and Close (2013) found that a crease pattern cut from an Archimedes spiral will wrap tightly around a cylinder, as opposed to a pattern made from circular arcs. It is important to note that their analysis was incomplete (without consideration for

sheet stretching or rigorous proof of their theory).

Foldcores are made from folded sheets that can be used as cores in sandwich structures. Gattas and You (2014) explored the response of curved-crease foldcores made from aluminum under low-velocity impact. They found that curved-crease geometries were much better at absorbing energy than straight-crease patterns. Further research on curved-crease foldcores has found that the curved surfaces of these structures could provide efficient ventilation or airflow along the surface (Klett et al., 2017a,b).

Other applications of curved-crease origami in engineering include deployable structures that are intended to have large displacements in response to a stimulus. One such example is a deployable footbridge constructed from planar-quadrilateral panels that approximate a curve (Nagy et al., 2015). Researchers at Brigham Young University have constructed compliant mechanisms using curved-crease origami fabricated with additive manufacturing (Nelson et al., 2016), such as the forceps. An interesting example of an engineered application of curved-crease origami is a small-scale propeller constructed from a flat sheet that is folded via self-assembly using heating (Miyashita et al., 2015).

These examples highlight the broad applications of curved-crease origami in structural and non-structural engineering fields. The analyses used to design these applications are as simple as trial-and-error methods or as complex as finite element modeling. In the next section, I will look more deeply at the existing methods for analyzing curved-crease origami that allow engineers to design for desired purposes and aesthetic features.

2.2 Analysis of Curved-Crease Origami

Analysis, in this context, means understanding the shape and behavior of curved-crease origami in the language of quantities, mathematical relationships, and deterministic processes. Analysis has many purposes spanning different fields. In some areas, people are interested in discovering the mathematical relationships behind folding thin sheets about curved creases. For others, understanding the range of shapes you can get from only bending and folding sheets (isometric deformations)

are important. Some researchers in the computer graphics field are interested in understanding how a curved-crease surface can be used to simplify rendering processes for three-dimensional surfaces. In this dissertation, I am interested in holistically understanding the applications of curved-crease origami by focusing on the geometry and mechanics of these systems. My aim is to inform future designs using the relationships explained in these areas of knowledge.

The framework I use to understand the analysis of curved-crease origami is divided into four parts, starting from the most basic understanding of the geometry to a robust understanding of the structural behavior of these systems. Specifically, I look at analyses based on: (1) closed-form geometry, (2) numerical geometry, (3) isometric (no stretching) mechanics, and (4) non-isometric mechanics. This framework was intentionally created to lead us to think of curved-crease origami as structural systems. However, this concept is not the only goal of research into curved-crease origami. In fact, there are some experts that would not even consider my concept of curved-crease origami as valid because I consider non-isometric deformations like stretching and buckling. Know that in this dissertation, I consider curved-crease origami to be any folding of thin sheets about curved creases from a flat state. I also want to understand deformations of these sheets after they are folded and loaded.

Getting to a point where engineers can design curved-crease origami structures reliably and quickly requires understanding the foundational work that allowed us to see paper folding as a means of solving engineering problems in the first place.

2.2.1 Closed-Form, Geometry-Based Analysis Methods

Closed-form, geometry-based analysis methods use mathematical relationships describing the folded surface of curved-crease origami derived from the field of differential geometry. Although these methods are the simplest in terms of conceptual complexity, they are limited by several idealizations and assumptions.

The first assumption is that all deformations of a thin sheet are isometric to the flat sheet. This means that as the sheet is folded about a curved crease, distances between points along the surface

are preserved. There are no in-plane deformations, like stretching or tearing, in these methods. Only sheet bending and crease folding are considered valid deformations. The isometric assumption, although not always correct in physical models, is a fair assumption since the stiffness of a sheet in tension is of order $O(t/l)$ with respect to the thickness-to-length ratio, t/l (where l is the length parallel to the stretching), and bending is of order $O([t/l]^3)$ (where L is the length of the sheet in the direction perpendicular to the bending rotation (Pini et al., 2016)). Thus, for thin sheet, $t/l << 1$, bending will be a lower-energy deformation and will be more likely to occur. The second assumption is that the shape of the crease after folding has occurred is known a priori. From this already deformed crease, the surface of the sheets surrounding the crease can be calculated.

Although these assumptions limit the practicality of these analysis methods, the insights gained from the analysis are important and later build upon more advanced analysis methods. For more detail on the process of using closed-form, geometry-based methods, see Appendix A.

One important feature of closed-form, geometry-based methods is that they represent the earliest known methods for analysis of curved-crease origami. As stated earlier, Huffman was the first to publish on the mathematical relationships of curved-crease origami. His 1976 paper established fundamental relationships between the surfaces surrounding curved creases and the unit sphere (Huffman, 1976).

In 1982, two mechanical engineers, Duncan and Duncan, were interested in using differential geometry to describe the surfaces of sheet-metal folded about curved-creases (Duncan and Duncan, 1982). This paper is important for a few reasons. The first reason is that the analysis was motivated by an engineering application. The second reason is that the mathematical relationships between the crease and the sheets are spelled out clearly (Huffman was less direct about stating these relationships, although there is quite a bit of overlap). The third reason is that their paper was solely devoted to curved-crease origami (Huffman had to bridge the interests of the computer graphics field to curved-crease origami via a long explanation of planar surfaces which means that his paper was less focused on curved-crease origami, in general). An example of the importance of their work to bridging the gap between engineering and differential geometry is shown when they

link sheet curvature and torsion to Mohr's circle.

Fuchs and Tabachnikov (1999) later added to Duncan and Duncan's paper with more explicit relationships between the crease and the sheet surface with mathematical proofs supporting the relationships. Fuchs and Tabachnikov also outlined five observations they made about curved-crease origami including limits on the width of sheets surrounding a curved crease. These three papers from the later twentieth century (Huffman (1976), Duncan and Duncan (1982), and Fuchs and Tabachnikov (1999)) form a core of work that is often cited in the literature. Although little work was conducted in the field of curved-crease origami during the early 2000s, these papers are the foundation to the explosion of research conducted in the 2010s to the present day.

One person greatly influenced by Huffman's work is Robert Lang, a former physicist who quit his job to start a career focused entirely on origami art and analysis (Wertheim, 2004). Lang has recently worked with researchers at Brigham Young University (most notably, former PhD student, Todd Nelson) on analysis of curved-crease origami for engineering purposes. Their work has included synthesis and proof of mathematical relationships for applications in compliant mechanisms (Lang et al., 2017).

Another one of the leading figures in the modern era of mathematical curved-crease origami analysis is Erik Demaine, a professor of computer science at MIT. Along with his former PhD student, Duks Koschitz, Demaine explored the previously undiscovered work about curved-crease origami by Huffman with added analysis (Demaine et al., 2011). An example of their work is shown when they reconstructed Huffman's lens tessellation pattern mathematically. Another interesting project by Demaine's group found that crease patterns made using conic sections (parabolas, ellipses, hyperbolas) with identical eccentricities and focii can fold isometrically (Demaine et al., 2018). Demaine's research is unique in that they have found instances of multi-crease curved-crease origami that can be modeled using closed-form, geometry-based methods, however limited.

2.2.2 Numerical, Geometry-Based Analysis Methods

Numerical, geometry-based analysis methods are those that employ the closed-form, geometry-based relationships described earlier, but use numerical techniques to discover relationships between folded shapes. Similar to the closed-form, geometry-based methods, the numerical analyses do not take into consideration sheet mechanics (material properties, equilibrium, etc.). This idealization might ignore important behaviors like finding the folded shape of least action and sheet buckling under high curvature. However, as with most idealized analyses, the numerical analysis methods are useful in a variety of situations.

A feature of the closed-form, geometry-based relationships developed in the late twentieth century is that the equations have a high degree of freedom. To use these equations, you must know the shape of the crease after folding. You must also know that degree of folding (the dihedral or fold angles). Because there are an infinite number of curves between two points in space, there are an infinite number of choices for the input parameters in an investigation. It is difficult to identify a rational range for these parameters. Given the high degree of freedom of curved-crease origami design, researchers have developed methods for rapid modeling using numerical methods that reduce the problem of having to limit a project's scope.

Tachi and Epps (2011) bridged the gap between the closed-form equations and numerical methods by explicitly modeling the same crease withe different generator orientations due to varying degrees of torsion on the crease (for more information on generators, see Appendix A). Tachi and Epps used their computer models to inform designs cut from thick, planar quadrilateral (PQ) panels that approximate curved surfaces.

One method of limiting the degrees of freedom in a design is to use numerical methods to fit curved-crease surfaces to a predefined shape. Kilian et al. (2008) used PQ meshes that connect to approximate three-dimensional surfaces with curved-creases. Their algorithm exploits the high degree of freedom of curved-crease origami geometries to fit specific instances. One example of the robustness of their method is shown when they used their algorithm to model the surface of a car with curved-creases. Similarly, Tang et al. (2016) approximated three-dimensional surfaces

with curved-creases using spline-based patches. Their method could model the Stanford bunny surface, approximated using curved-crease spline-based patches. Because splines are mathematically complex, numerical methods are a good way to representing their shape. Combining spline-based patches to approximate curved surfaces is only possible using computers (the mathematics controlling these methods is intractable).

Other methods of controlling the high degree of freedom of the geometric relationships is to observe patterns in the mathematics and to use numerical algorithms to simplify modeling of a certain class of geometries. Mitani and Igarashi (2011) discovered that surfaces folded from planar curved creases (creases with zero torsion) can be modeled by reflecting developable surfaces about the plane of the crease. The process of modeling a curved-crease origami using the closed-form, geometry-based equations (as shown in Appendix A) can be cumbersome, but with a computer, a simple mirror/reflection algorithm can model planar curved-crease origami easily.

Perhaps the most important contribution that numerical, geometry-based analysis methods offers is the ability to model curved-crease geometries with multiple creases (not just conic sections). Research advances in this area are much more recent. Watanabe and Mitani (2018) created a graphical user interface (GUI) that allows the user to design a curved crease (called the primary crease) that generates a folded surface. The program also allows users to design another crease (called the secondary crease) on a flat surface. Their algorithm then calculates the torsion and curvature of the secondary crease after folding based on its intersection with the folded surface. Their method mainly acts on the closed-form, geometric equations which means that some results give invalid surfaces where generators intersect. By varying parameters, a valid surface can eventually be modeled (see the right image on the same Figure). The act of back-calculating the secondary crease's geometry is intractable using pure math, but possible via numerical operations.

Other examples of curved-crease geometries with multiple creases analyzed using numerical methods include the circular pleated annuli originally modeled in the Bauhaus school using discretization methods (Jiang et al., 2019). Another interesting piece of research comes from Rabinovich et al. (2019) where they use discrete, orthogonal, geodesic nets (DOG nets) to model

curved-crease origami starting from a flat crease pattern. DOG nets are small patches that connect together to approximate the surface. As the surface is folded, an algorithm minimizes the amount of bending and stretching of the DOG nets. Essentially, their process is analogous to a finite elements method, but an arbitrary functional that is minimized describes the bending and stretching instead of a stiffness matrix. Their method is the first to allow for folding from a flat state without already knowing the deformed shape of the crease.

As explained by the existing body of literature, numerical methods make the closed-form, geometry-based analysis methods more practical by limiting the scope of the equations and observing patterns in the equations. Numerical methods, like optimization, use insights found in the math to inform these more robust methods. Numerical methods can also explain concepts in the math or concepts surrounding the math that the equations themselves do not reveal. Despite these benefits, numerical, geometry-based methods are limited in that they do not consider the mechanics of the sheet. I will explain, mechanics are important in certain situations for describing behaviors that other models cannot explain.

2.2.3 Isometric, Mechanics-Based Analysis Methods

By mechanics-based analysis methods, I mean to say the methods presented from this point on solve, either implicitly or explicitly, the equilibrium problem. This means that in these analyses, the compatibility relationships (geometric properties) are considered alongside the constitutive relationships (material properties). Mechanics-based analysis methods consider the physics of thin sheet to varying degrees. In the case of isometric, mechanics-based analysis methods, the physics are limited to the deformations of solid continua as either bending of thin sheets or folding of creases. There is no consideration for in-plane stretching or shearing of the sheets. Echoing the previous analysis methods, the isometric assumption does not represent all deformations of thin sheets folded about curved creases, but allows us to understand most cases. In certain situations, the isometric assumption will not be valid.

The value of isometric deformations of thin sheets in the context of mechanical deforma-

tions was recognized early, relative to the entire body of research of curved-crease origami, in an under-appreciated paper by Abramowicz and Wierzbicki (1979). In their research, Abramowicz and Wierzbicki noticed that when cylinders made from thin shells buckled, the shape they deformed into tended to be an isometric deformation of the original cylinder (that is, deformations were only folding about yielded creases and bending of the sheet). Although they did not identify their research as curved-crease origami, Abramowicz and Wierzbicki's paper was the earliest piece of research explicitly linking the internal forces of the sheet to isometric deformations.

Decades later, the importance of considering mechanics in describing the folded shape of curved-crease origami was further researched by Marcelo Dias, then a PhD student at the University of Massachusetts in Amherst. His thesis work was focused on the physics of thin sheets folded about circular creases. Using mechanics, Dias was able to explain why a full annulus creased at mid-radius always buckles out of plane upon folding (Dias et al., 2012). Explaining this behavior has never been accomplished in the context of pure geometric analysis. Other research by Dias includes exploring the folded shape of other circular creases, like helices, using mechanics (Dias and Santangelo, 2012).

Concepts in mechanics have also been useful in simplifying our understanding of the folding behavior of curved-crease origami. Seffen (2012) described the folding of curved corrugated shells by relating the mid-surface of a folded geometry to a shell structure, effectively linking folding and unfolding to in-plane strains of the shell. Extending his prior research with a new collaborator, Dias and Audoly (2014) related the folded shape of a creased annulus to the mechanics of a rod being twisted.

More complex curved-crease geometries have also been explored using mechanics. One example comes from Vergauwen et al. (2017) where they modeled a deployable, single-degree-of-freedom, solar shade (a design similar to Tachi and Epps (2011)) using isometric bent sheets. By minimizing the strain energy of the system, they found the shape of least action using different generator layouts. Lee et al. (2018) generated curved-crease origami by deforming sheets modeled using Euler's elastica and reflecting the surface about planar creases. Badger et al. (2019) used an

optimization technique to minimize the bending energy in singly creased, curved-crease origami by varying the generator angles. They found that most curved-crease origami will tend to fold into planar creases with slight torsion near the ends of the crease. Duncan and Duncan (1982) noticed that sheet-metal tended to fold into planar creases; thus, this new research shows that Duncan and Duncan were almost correct.

Calculating the deformed shape of curved-crease origami using mechanics is robust enough to model complex crease patterns with multiple creases. Furthermore, finding the equilibrium shape of curved-crease origami brings the research closer to the folding of real sheets of material (essential for engineering designs). Despite the unique insights found using isometric deformations via mechanics, complete modeling from a flat to folded state is missing. Additionally, there has been no consideration for deformations besides folding (such as loading after folding). The reason for these gaps in knowledge come from the isometric assumption. In order to model the folding of any crease pattern or deformation after folding, we need to abandon the idea that folding and bending are the only valid deformations. To do this, we need models that consider non-isometric deformations such as stretching.

2.2.4 Non-Isometric, Mechanics-Based Analysis Methods

Non-isometric, mechanics-based analysis methods complete isometric, mechanics-based methods by allowing deformations where the sheet is not isometric to a plane. By relaxing this constraint, behaviors like in-plane stretching and shearing can occur. While it is true that non-isometric deformations of sheet are more energy-intensive than isometric deformations, there are many cases in which isometric deformations will occur. The first case is for modeling the folding of flat sheets about multiple curved creases of arbitrary shape. In some instances, the creases will interact in such a way that stretching will appear. The second case is for modeling the structural behavior of curved-crease origami after folding. Up to this point in the literature review, the focus has been on finding the folded shape of curved-crease origami. Considering non-isometric deformations will allow us to explore the benefits and limitations of these geometries as structural systems.

Early work into the analysis of non-isometric deformations of curved-crease origami comes from Dias et al. (2012). Although they framed their energy minimization of the creased annulus around isometric deformations, they also modeled the same geometry using a spring system. They say that near the crease, stretching tends to occur. In order to minimize this stretching, the annulus buckles out of plane. Although a spring system is not a complete model for non-isometric deformations, it is sufficient to show the importance of stretching in the local planes of the sheet.

A significant portion of research into the non-isometric deformations of curved-crease origami has focused on finite element modeling. With shell and connector elements, the bending and folding predominantly found in curved-crease origami deformations can be modeled along with in-plane deformations. Bende et al. (2015) used finite elements to model snapping of shells folded about curved creases shown in physical models. Nelson et al. (2016) explored the feasibility of large rotations of sheets using lamina emergent arrays (LEAs). LEAs are made using strategic cuts in sheets that distribute stresses due to bending. Garrett et al. (2016) used finite elements to model the crushing of curved-crease origami crash boxes to assess their performance as energy absorbing structures. Vergauwen et al. (2017) modeled their deployable solar shade using finite elements to compare with their isometric models. Finite element models of a simple creased annulus sector by the author show how in-plane strains occur near the creases and that bending strains are not uniform over the entire sheet (Woodruff and Filipov, 2018).

As a means of modeling the structural performance of curved-crease origami, non-isometric, mechanics-based analysis methods offer the most robust capabilities. However, current methods are not without their limitations. Finite element modeling of curved-crease origami can be especially cumbersome. Given the large rotations of the crease due to folding and the sheet due to bending, finite element models must be fine-tuned in order to converge to a result. Often, a curved-crease, finite elements model will not converge to a solution, and if so, will take a long time to converge. For rapid prototyping and design, faster and more reliable solutions are necessary. Despite the robustness of these methods, there is still work that needs to be done. More information on finite-element modeling of curved-crease origami can be found in Appendix B.

2.3 Perspectives From the Literature

The history of curved-crease origami, from an academic perspective, spans numerous fields of interest and across a long span of time. From art to mathematics, computer science to engineering, curved-creased origami has found its place as an interesting, aesthetically pleasing, and useful artifact. As research continues, emphasis has been placed on rigorously and analytically describing the folded shape and structural response of thin sheets folded about curved creases. The research has developed from limited and simple methods stemming from differential geometry to robust means of modeling the deformations using non-isometric strains in solid continua.

From the body of literature reviewed earlier in this chapter, three areas of undone research appear. These areas of missing knowledge are important obstacles preventing efficient and safe design of curved-crease origami for structural purposes. In order to understand the structural behavior of curved-crease origami, including the advantages and limitations of these systems, researchers must continue research.

The first area of undone research involves modeling curved-crease origami reliably from flat crease patterns. Much of the existing literature on curved-crease origami has focused on describing the folded shape of systems using a priori knowledge about the deformed crease. In an engineering process, we would start from a flat sheet and fold to a three-dimensional shape. Thus, we need to understand how to model such a deformation without prior knowledge on what the deformed shape of the crease will be. Although Rabinovich et al. (2019) offers a method folding from a flat state, their process ignores important features of the structure, such as material properties and unstable deformations (snapping, buckling, etc.). Finite elements can also model folding from a flat to folded state, but convergence is difficult to achieve and program runtimes can exceed reasonable limits.

The second area of undone research involves describing the mechanics of sheets between multiple creases. Most of the existing research on curved-crease origami only considered singly-creased geometries or crease patterns with explicitly defined compatibility between creases. As multiple

creases are introduced, the mathematics governing the shape of sheets between creases becomes intractable, and no research has explicitly looked at the deformation of sheets between curves. Curved-crease origami structures will likely use multiple creases in their flat crease patterns. Thus, we need to understand how the sheets will deform during folding to properly predict failure and final deformed shapes.

The third area of research that remains undone involves treating curved-crease origami as structures themselves. Most of the existing research has focused on curved-crease origami as geometries. Indeed, the main focus of most of the research has been focused on finding the folded shape of curved creases. We know from anecdotal data and discursive theories that curved-crease origami might offer specific advantages to a structure. In order to use curved-crease origami as structures, we need to explore these advantages and determine the limitations of these systems.

It may have been strange to see concrete being used for beams and hollow steel sections in frames just a couple centuries ago. The body of research supporting these technologies have allowed engineers to exploit their niche advantages safely and cost-effectively, despite their limitations. I hope that with further development on curved-crease origami, the idea of thin sheets folded about curved-creases being structures will be realistic and accepted. Curved-crease origami has great potential, both aesthetically and functionally. The goal of this dissertation is to assert the latter.

Chapter 3

Simplified Bar-and-Hinge Analysis of Curved-Crease Origami

In this chapter, I address the problems often encountered when modeling curved-crease origami, either with geometric methods (see Appendix A) or with finite element analysis (see Appendix B). I present a method for simulating the structural properties of curved-crease origami through the use of a simplified numerical method called the bar-and-hinge model. I derive stiffness expressions for three deformation behaviors including stretching of the sheet, bending of the sheet, and folding along the creases. The stiffness expressions are based on system parameters that a user knows before analysis, such as the material properties of the sheet and the geometry of the flat fold pattern. I show that the model is capable of capturing folding behavior of curved-crease origami structures accurately by comparing deformed shapes to other theoretical and experimental approximations of the deformations. The model is used to study the structural behavior of a creased annulus sector and an origami fan. These studies demonstrate the versatile capability of the bar-and-hinge model for exploring the unique mechanical characteristics of curved-crease origami.

This chapter is organized as follows. I begin by introducing the problem and providing background information relevant to the chapter in Section 3.1. In Section 3.2, I give an overview on the bar-and-hinge method for modeling origami. In Section 3.3, I derive stiffness expressions from the material properties of the sheet and the geometry of the mesh for three main deformation modes: in-plane action, bending, and folding. In Section 3.4, I verify and explore these stiffness expressions using four methods: theoretical structural mechanics, differential geometry theory, experimental laser scanning, and folded shape simulations. Finally, in Section 3.5, I explore the anisotropy of two curved-crease origami structures using the bar-and-hinge method with commentary on the

strengths and limitations of the model.[1]

3.1 Introduction

As curved-crease origami are folded, both the kinematics and the mechanics of sheet bending must be considered to describe the final deformed shape (Demaine et al., 2015). Furthermore, understanding the structural capacity and anisotropic stiffness of curved-crease origami during and after folding requires exploring the mechanics of the sheets beyond bending. The mechanics of straight-crease patterns such as the Miura-ori are well understood (Yang et al., 2016; Gattas and You, 2014), but mechanics literature has not explored curved-crease origami in great detail.

Early work by Huffman (1976) sought to describe the geometric features of curved-crease origami with further development by Duncan and Duncan (1982) and Fuchs and Tabachnikov (1999). The mathematical relationship between crease geometry and the shape of the folded sheet requires knowing, a priori, unintuitive parameters such as the deformed shape of the crease and the exact fold angle along the crease length. These relationships are useful, but would not benefit a designer starting from a flat crease pattern. Additionally, existing mathematical expressions for curved-crease folding apply to origami with just one fold or a tessellation of similar folds. These expressions do not work for origami with more than one fold, in general. Another method involves modeling the curved surfaces of folded sheets with Euler's elastica and reflecting the surface about mirror planes (Lee et al., 2018). However, this method does not necessarily allow for minimal energy states like flattening near free edges.

While theoretical models like these are computationally efficient and elegant in their formulations, applications are limited. Many of the existing methods used to describe curved-crease systems rely on the assumption that folding and bending are the only deformation modes. However, there is evidence that stretching and shearing of the sheet in-plane, which are higher energy deformation states, also play an important role in the behavior of curved-crease structures (Dias et al., 2012; Woodruff and Filipov, 2022). Thus, methods that can fold curved-crease origami and model

[1] This chapter contains research published in Woodruff and Filipov (2020a)

the mechanics of origami after folding should also capture the non-negligible, in-plane behaviors.

Finite elements have been used to model curved-crease origami starting from flat or already-folded sheets (Vergauwen et al., 2017; Nagy et al., 2015; Woodruff and Filipov, 2018). These models allow for simulation of in-plane deformations and allow for a wider range of boundary conditions. However, finite elements can be cumbersome, with no guarantee that the formulations will be accurate, quick to implement, or that the model will converge, especially for systems with large curvatures or many folds.

In an effort to bridge the gap between limited theoretical methods and cumbersome finite element models, I offer a method for modeling curved-crease origami deployables that can capture the structural properties of a variety of curved-creased sheets with relative ease and accuracy. I improve an existing method for capturing the mechanics of straight-crease origami, called the bar-and-hinge model (Schenk and Guest, 2011; Filipov et al., 2017; Liu and Paulino, 2017; Gillman et al., 2018). I extend the capabilities of the model to describe the folding (initial loading) and post-folding (secondary loading) structural behavior of curved-crease origami structures. I find that the model is applicable to curved-crease systems of arbitrary crease number and complexity for various sheet dimensions, elastic material properties, and structural boundary conditions (see Figure 3.1 for examples). With this reformulation of the bar-and-hinge model, engineers can capture the folding, stiffness, elastic deformations, and nonlinear behavior of curved-crease origami systems.

3.2 Bar-and-Hinge Modeling of Origami-Inspired Structures

The bar-and-hinge model is a simplified structural mechanics-based numerical method that captures the deformations and internal forces of thin sheets folded about straight creases (Schenk and Guest, 2011; Filipov et al., 2017; Liu and Paulino, 2017; Gillman et al., 2018). bar-and-hinge models can capture the behavior of origami structures during folding as well as during loading after folding, a task that kinematic analysis cannot achieve. Relative to other mechanics models, such as finite elements, the bar-and-hinge method runs analyses quickly and is simple to implement with

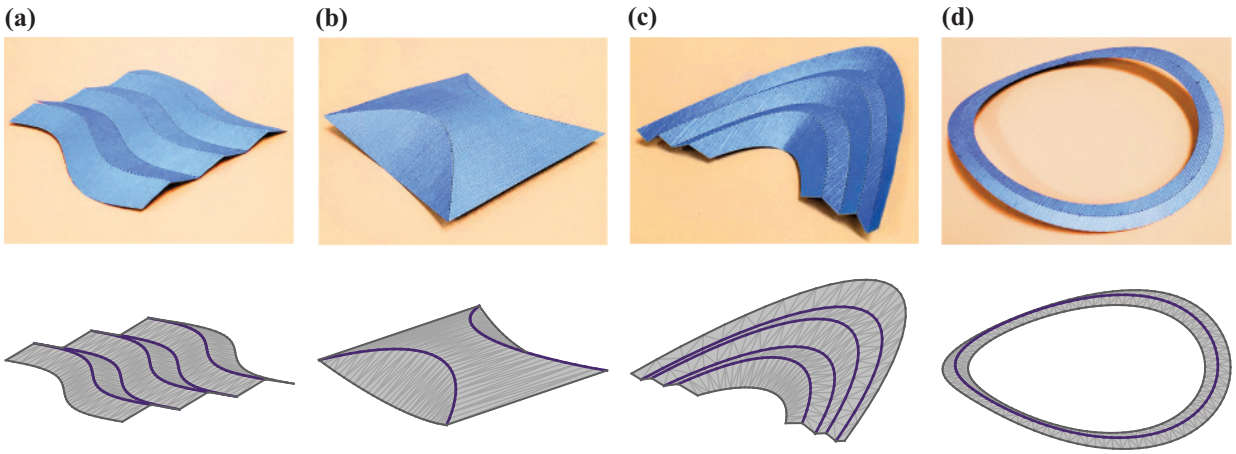

Figure 3.1 – Example geometries made using paper and using bars and hinges. The top row shows four photographs of paper, curved-crease origami constructed using a laser cutter and hand folding with the corresponding bar-and-hinge representations on the bottom row including **(a)** a sine wave tessellation, **(b)** a square with two parabolic curves, **(c)** a canopy made from parabolic curves, and **(d)** an annulus creased about mid-radius.

readily available parameters including a flat crease pattern and prescribed fold angles. The ease and simplicity of bar-and-hinge models allow engineers to quickly understand and evaluate the structural properties of origami. The rapid analysis is especially useful when exploring proof-of-concept systems, running parametric studies, or performing optimization studies. State-of-the-art computer programs, such as MERLIN (Liu and Paulino, 2017) have been made available to the community, and are able to capture geometric and material non-linearity, essential to understanding the behavior of origami structures.

However, current bar-and-hinge models are designed for straight-crease or polyhedral origami systems. Additionally, these programs usually employ arbitrary stiffness values for elements when defining the properties of the sheet. Despite these limitations, there is potential for adapting and enhancing bar-and-hinge models to approximately capture the behavior of curved-crease origami.

The simplest bar-and-hinge model uses three types of elements that capture the structural properties of the system. Figures 3.2(a-e) show how a sheet with a curved crease would be decomposed into these elements. The first element is a three-dimensional truss bar which only carries loads along its axis. These bars are connected at nodes which allow rotation, but not translation between the bars. When combined, the bars represent the in-plane stiffness of a thin sheet. The second element is a bending hinge, analogous to a spring coiled around a bar. This element serves the

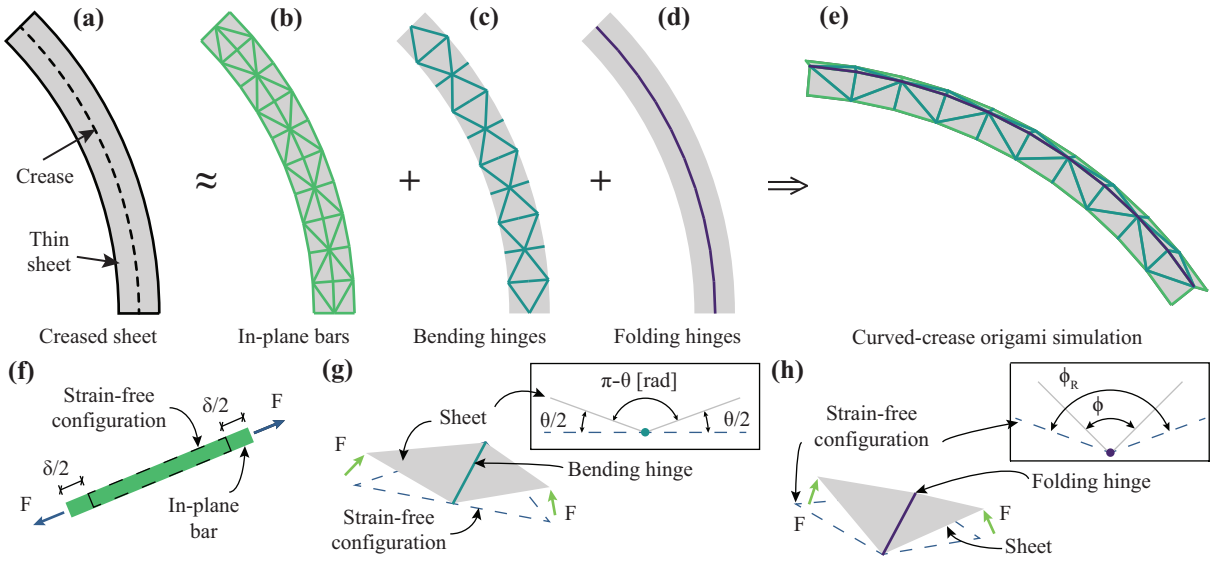

Figure 3.2 – Bar and hinge elements approximating curved-crease origami. The bar-and-hinge method works by representing **(a)** a creased, thin sheet using three elements: **(b)** bars to capture in-plane stretching and shearing, **(c)** bending hinges to capture sheet bending, and **(d)** folding hinges to capture crease folding. **(e)** The combination of all three elements simulates the deformed and folded shape of the sheet. Illustrations of element deformations due to a force, F, are shown for **(f)** bar extensions, **(g)** bending hinge rotations, and **(h)** folding hinge rotations. Inset images in **(g)** and **(h)** show a side-view with the hinge elements pointing out of the page.

model by simulating the sheet bending stiffness. The third element is a folding hinge. Similar to the bending hinge, the folding hinge simulates the rotational stiffness of the material at the crease.

The bar-and-hinge method works by calculating the total stiffness of the system using contributions from each element. The stiffness can be used to solve the equilibrium equation giving the forces and displacements of the system in response to arbitrary boundary conditions. The total strain energy in the system shows the relevant parameters of the analysis. That is,

$$U_{\text{total}} = \underbrace{\frac{1}{2}\sum_{i} k_s^i \delta_i^2}_{\text{bar energy}} + \underbrace{\frac{1}{2}\sum_{j} k_b^j \theta_j^2}_{\text{bending energy}} + \underbrace{\frac{1}{2}\sum_{p} k_f^p (\phi^p - \phi_R^p)^2}_{\text{folding energy}} . \tag{3.1}$$

Here, k_s^i is the stiffness of the i^{th} truss bar, and δ_i is the corresponding extension of the bar (see Figure 3.2(f)). The bending stiffness of the j^{th} hinge is k_b^j, and θ_j is the rotation from the flat state (see Figure 3.2(g)). Finally, k_f^p is the stiffness of the p^{th} folding hinge, ϕ^p is the dihedral angle of the folding hinge, and ϕ_R^p is the prescribed rest angle of the crease (see Figure 3.2(h)). These values are either prescribed (for example, rest angles and stiffness coefficients) or calculated by

converging to an equilibrium state (for example, bar extensions and hinge rotations).

By approximating curved creases with piece-wise linear bars, I can modify existing bar-and-hinge models for curved-crease origami. Additionally, I can relate the stiffness values of each element to the material properties and the geometry of the mesh such that the strain energy can be calculated based on the parameters explicitly defined by the designer.

3.3 Deriving Element Stiffness

In order to formulate the bar-and-hinge method for curved-crease origami without the use of arbitrary stiffness values, the stiffness of each of the three elements (in-plane bars, bending hinges, and fold hinges) should be calibrated to the mesh geometry and material properties of the sheet. In this section, I derive stiffness expressions for these elements starting from structural mechanics. I consider the three main deformation modes corresponding to the three model elements separately and verify the entire model in Section 3.4.

3.3.1 In-Plane-Bar Stiffness

The bars used in the bar-and-hinge model capture deformations in the plane of the sheet. For curved-crease origami, the main deformation modes include tension in the sheet and shearing transverse to the length of the crease. Both of these deformations should be captured by the model such that the global deformation of the curved-crease system can be approximated (for instance, due to an applied load after folding). The material properties of the sheet, the dimensions, and the discretization of the mesh are considered in deriving the stiffness of the bars.

The stiffness of each bar is described by

$$k_s = \frac{EA_{eff}}{L}, \tag{3.2}$$

where E is the elastic modulus, A_{eff} is the effective cross-sectional area of the bar, and L is the length of the bar. The effective cross-sectional area of the bar must represent the cross-sectional

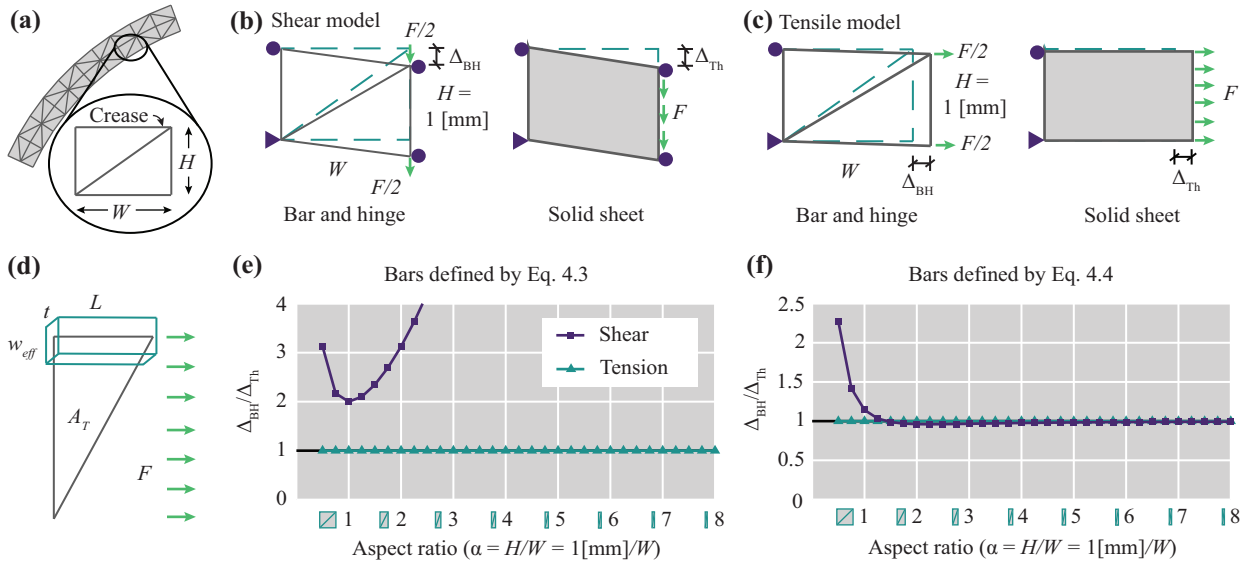

Figure 3.3 – Bar stiffness derivation. The derivation for bar stiffness, k_s, starts by looking at **(a)** a one unit truss with width, W, parallel to the crease and height, H, perpendicular to the crease. The stiffness of the unit truss bars were calibrated for: **(b)** shearing transverse to the crease and **(c)** tension parallel to the crease. The bar-and-hinge deformations, Δ_{BH}, were compared to those of a theoretical solid sheet, Δ_{Th}. **(d)** The derivation for Equation 3.3 came from spreading forces across a triangular panel into one bar. **(e)** The bar-and-hinge tensile and shear deformations versus the theoretical deformations when all bars are defined by Equation 3.3. **(f)** The deformation comparison when the bars are defined by Equation 3.4.

area of the sheet in proportion to the geometry dimensions and the discretization. In order to determine an appropriate expression for A_{eff}, I calibrate the deflection of the bar-and-hinge model of a small section of the sheet to the deflection of a similar plane stress model of the same sheet for both shear and tension (see Figures 3.3(a-c)). My goal is to set the bar-and-hinge deflection, Δ_{BH}, equal to the theoretical deflection value, Δ_{Th} (that is, the deflection ratio, $\Delta_{\text{BH}}/\Delta_{\text{Th}} = 1$).

Consider a triangular panel extracted from a sheet under uniform traction, F, as shown in Figure 3.3(d). In this case, the cross-sectional area of the bar orthogonal to the traction (that is, the cross-sectional area of the top bar) must capture the cross-sectional area of the entire triangular panel. One can calculate an effective bar width by dividing the area of the triangle, A_T, by the length of the bar. Multiplying this value by the sheet thickness gives a lumped cross-sectional area of the sheet into the bar. The stiffness of such a bar is defined as,

$$k_s = \frac{EA_Tt}{L^2}. \tag{3.3}$$

I quantify how the mesh is discretized using an aspect ratio, $\alpha = H/W$, where the panel height, H, is measured transverse to the crease and the panel width, W, is measured along the crease. In order to see how the bar-and-hinge model deflection changes with aspect ratio, I set $H = 1$ [mm] and vary W.

Figure 3.3(e) shows a comparison between the bar-and-hinge deflection with all bars defined by Equation 3.3 and the deflection of the plane stress model. For tension, this stiffness definition matches theory for all aspect ratios. However, for shear, the bar-and-hinge model is too flexible, especially at large aspect ratios.

Noticing that the diagonal bar across the panel captures the shearing of the panel, the stiffness of just that element can be increased in proportion to the aspect ratio. Closer examination of Figure 3.3(e) shows that the shear deflection ratio diverges from theory at a quadratic rate for $\alpha \geq 1$. Indeed, a quadratic regression on the data shows that the deflection ratio varies with the aspect ratio as a function of the form $\Delta_{\text{BH}}/\Delta_{\text{Th}}(\alpha) = \alpha^2/2 + 5/4$ with $R^2 = 1.000$ for $\alpha \in [1, 20]$. This domain for the aspect ratio represents a reasonable boundary for discretization size since $\alpha < 1$ will give an overly coarse approximation of the curved-crease geometry and $\alpha > 20$ might not converge to a solution. In fact, I have observed that the condition number of the model increases at a nonlinear rate for $\alpha > 12$ which indicates more difficulty for convergence. As such, to better capture the shear behavior, one can increase the stiffness of the diagonal bar quadratically with the aspect ratio to reduce the flexibility of the diagonal bar. Subsequently, the stiffness of the bars can be calculated as

$$k_s = \begin{cases} (\alpha^2/2 + 5/4)\,\dfrac{EA_T t}{L^2}, & \text{Diagonal bars} \\ \dfrac{EA_T t}{L^2}, & \text{Non-diagonal bars} \end{cases}. \tag{3.4}$$

The deflection results are shown in Figure 3.3(f), where the tensile deflection always matches the theory and the shear deflection is within 1% of theory for $\alpha > 1.5$.

Another way I could have arrived at this solution was to assume that the bars had a stiffness

defined as

$$k_s = \begin{cases} \left(a_2\alpha^2 + a_1\alpha + a_0\right)\dfrac{EA_T t}{L^2}, & \text{Diagonal bars} \\ \dfrac{EA_T t}{L^2}, & \text{Non-diagonal bars} \end{cases}. \tag{3.5}$$

The coefficients a_2, a_1, and a_0 were then found by minimizing the deviation of the bar-and-hinge deflection from the theoretical deflection. Different values of the coefficients in the range $a_2,\, a_1,\, a_0 \in [0, 10]$ were used against various aspect ratios $\alpha \in [1, 20]$. Using this metric, the optimal values of the coefficients which minimize the bar-and-hinge deflection errors are: $a_2 = 1/2$, $a_1 = 0$, and $a_0 = 5/4$. Thus, both the optimization technique and quadratic regression method arrive at the same solution. Note that this solution applies to $\alpha \in [1, 20]$ because this is a reasonable range for the mesh aspect ratio for curved-crease origami. It is possible to calibrate the shear response for low aspect ratios ($\alpha < 1$), but because such a meshing is too coarse for curved-crease geometries, this task is out of the scope of this chapter.

3.3.2 Bending-Hinge Stiffness

When folding a flat sheet about a curved crease, sheet bending is the predominant deformation mode. The stiffness of the continuous sheet must be lumped into discrete bending hinges. In order to derive an expression for the bending stiffness, I use both the geometry of the mesh and the material properties of the sheet. I modify an elegant derivation by Dudte et al. (2016) to describe the bending stiffness.

Consider a flat sheet that has been folded about a curved crease. If I mesh this sheet with bar and hinge elements, I can look at one bending hinge at the interface of two panels with areas A_1 and A_2, respectively (see Figure 3.4(a)). The bending hinge has a length L. The two panels are rotated, relative to each other, by an angle θ. The hinge elements must capture the bending of a sheet with thickness t and length s. The theoretical sheet length, s, is calculated later and is related to a representative bending region. If I assume that the region of the sheet taken from the curved surface is sufficiently narrow (that is, the mesh is fine), then I can assume that the sheet section represented by the bending hinge has constant curvature, κ.

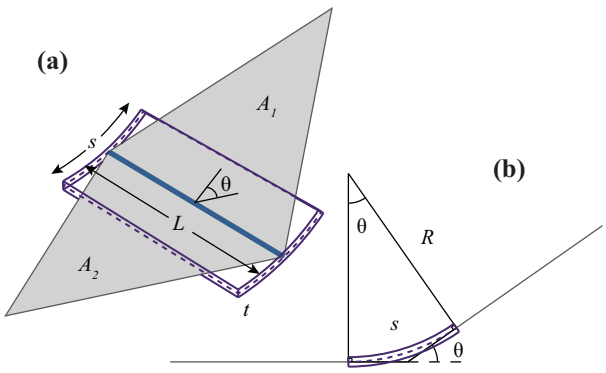

Figure 3.4 – Bending hinge derivation. The stiffness of one bending hinge connected to two triangular panels is derived by relating the strain energy in the hinge to that in an equivalent bent sheet of width, L, and length, s. **(a)** Top isometric view and **(b)** side view.

The bending energy in the sheet should then be

$$U_{\text{sheet}} = \frac{1}{2}\int_0^s EI\kappa^2 \, ds = \frac{1}{2}EI\kappa^2 s, \tag{3.6}$$

where E is the elastic modulus of the sheet and I is the second moment of area about the hinge calculated as $I = Lt^3/12$. Thus, the energy in the sheet section is

$$U_{\text{sheet}} = \frac{1}{2}\left[\frac{Et^3}{12}L\kappa^2\right] s. \tag{3.7}$$

The curvature of the sheet can be described by $\kappa = 1/R$. The length of the sheet is related to the rotation angle by $s = R\theta$. Rearranging gives $R = s/\theta$. Substituting this relationship into the curvature gives $\kappa = \theta/s$, and the strain energy in the sheet is

$$U_{\text{sheet}} = \frac{1}{2}\left[\frac{Et^3}{12}\frac{L}{s}\right]\theta^2. \tag{3.8}$$

I want to constrain the area captured by the hinges such that the total area of the entire sheet is never exceeded. This area can be expressed as $sL = (A_1 + A_2)/2$. Rearranging gives $s = (A_1 + A_2)/(2L)$. Substituting this expression into the sheet strain energy gives,

$$U_{\text{sheet}} = \frac{1}{2}\left[\frac{Et^3}{6}\frac{L^2}{A_1 + A_2}\right]\theta^2. \tag{3.9}$$

The energy in the bent sheet is set equal to the strain energy in the bending hinge,

$$U_{\text{hinge}} = \frac{1}{2} k_b \theta^2, \tag{3.10}$$

to solve for the stiffness coefficient for bending, k_b. This gives a bending stiffness of

$$k_b = \frac{Et^3}{6} \frac{L^2}{A_1 + A_2}. \tag{3.11}$$

Thus, the bending stiffness is effectively the bending modulus of a sheet from mechanics, $D = Et^3/(12[1-\nu^2])$, with $\nu = 0$, when multiplied by a non-dimensionalized parameter based on the mesh. As will be shown in Sections 3.4.1 and 3.4.2, this definition provides a converging solution for bending energy in the sheet.

3.3.3 Folding-Hinge Stiffness

Deriving the rotational stiffness of a crease based on the system properties is not yet possible. Confounding parameters such as material properties, material damage at the crease, folding history, local crease design, and geometry of the sheet around the crease could all affect the stiffness. Existing literature on the subject is mostly experimental (Lechenault et al., 2014; Beex and Peerlings, 2009; Huang et al., 2014; Mentrasti et al., 2013; Yasuda et al., 2013), and does not consider curved creases. Overall, there is no method to accurately predict the stiffness of a folding hinge directly from the material properties and mesh geometry.

A previous approach to modeling fold stiffness (Filipov et al., 2017; Lechenault et al., 2014) reduces the complexity of the crease into one equation. The model considers the bending modulus of the sheet, D, the length of the fold, L_f, and a length scale factor, L^*. The length scale factor is introduced for parameters not explicitly included in the stiffness expression. The fold stiffness is

$$k_f = \frac{L_f}{L^*} D = \frac{L_f}{L^*} \frac{Et^3}{12(1-\nu^2)} = \frac{L_f}{L^*} \frac{Et^3}{12}, \tag{3.12}$$

where E is the elastic modulus of the sheet, t is the thickness, and ν is the Poisson's ratio (for consistency with the bending derivation, I set $\nu = 0$). The proper value of L^* for curved creases is problem-specific and can only be determined numerically by looking at the difference between the prescribed folding angle and the angle the model reaches after folding (see Section 3.4.4). For straight origami creases, typical values of L^* are in the range of 25 [mm] to 100 [mm] (Filipov et al., 2017). Despite the overall incompleteness of fold stiffness modeling, I use this approach to define the stiffness, k_f, of the folding hinges.

3.4 Verifying the Element Stiffness

To verify the accuracy of the element stiffness expressions, I employ four different methods to compare deformed shapes of the bar-and-hinge model to deformed shapes of other theoretical and experimental models. The deformed shape is a result of the element stiffness expressions and acts as a proxy for verifying the stiffness directly. The methods I conduct include (1) comparing the deformed shape of a strip of material under four types of loading to structural mechanics theories, (2) comparing the deformed shape of an annulus sector folded along its center to the shape of a cone section, (3) comparing the deformed shapes of complex curved-crease origami with multiple creases to point clouds from laser scanned physical paper models, and (4) exploring the relationship between fold stiffness, rest angle, and the actual fold angle simulated by the model. These verifications serve to show the accuracy of the results as well as the limitations of the bar-and-hinge method.

3.4.1 Thin Strips Under Different Load Cases

Without considering folds, I can test to see how well the bending and the in-plane stiffness definitions capture the deformation of thin, long strips by comparing the strain energy in the bar-and-hinge model to structural mechanics solutions for the same problems. I model an isotropic, homogeneous strip using the bar-and-hinge method with linear-elastic material properties, and with various mesh sizes. In order to quantify the size of the mesh, I employ a metric called the

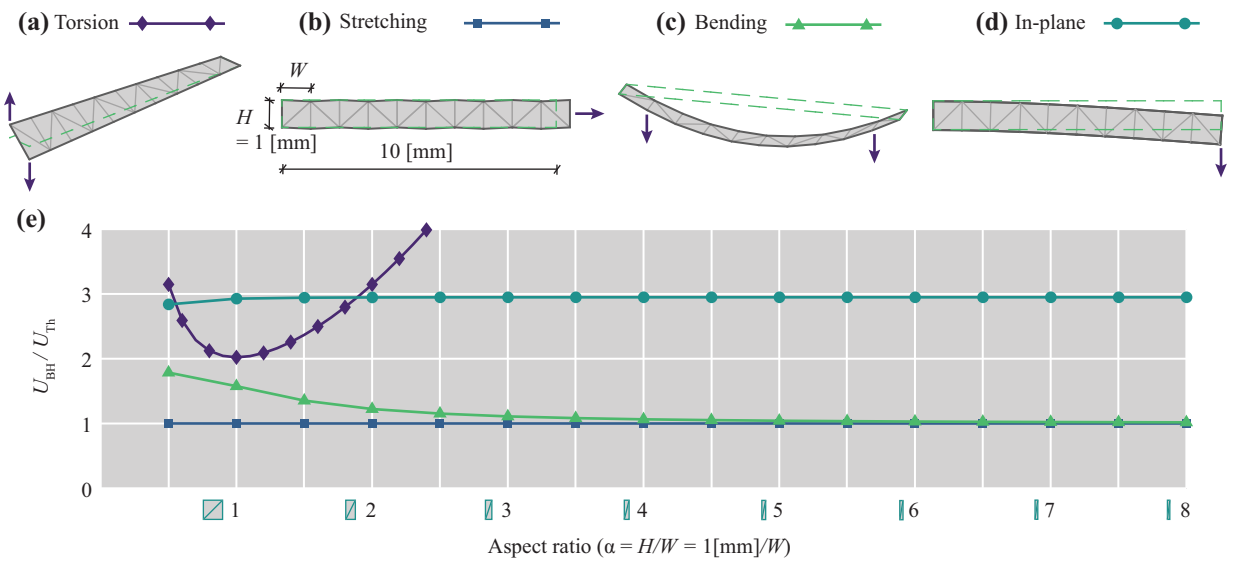

Figure 3.5 – bar-and-hinge verification using thin strips. To verify the stiffness expressions for the bar-and-hinge model, a long, thin strip was modeled and loaded in four ways: **(a)** torsion, **(b)** stretching, **(c)** bending out-of-plane, and **(d)** bending in-plane (deformations are exaggerated 1,000 times). **(e)** The strain energy in the bar-and-hinge model, U_{BH}, compared to the strain energy based on structural mechanics theory, U_{Th}, with respect to the mesh aspect ratio, α.

aspect ratio, α. Each triangular panel has an aspect ratio defined as the ratio of the side length perpendicular to the fold (H) to the side length roughly parallel to the fold (W). Because there is no fold in the strips, the aspect ratio is the ratio of the vertical side length to the horizontal side length when the strip is placed such that the long direction lies horizontally see Figure 3.5(b)). As such, a larger aspect ratio indicates a finer mesh discretization. The strip has a length of 10 [mm], a width of 1 [mm] (that is, $H = 1$ [mm]), and a thickness of 0.1 [mm]. For clarity, I use familiar SI units; however, the units are arbitrary when consistent. The strip is restrained and loaded in four different ways (see Figures 3.5(a-d)).

The first loading case represents torsion in the strip. At one end, the nodes are restrained in the x-, y-, and z-directions. At the other end of the strip, one node is pulled up and the other is pulled down by a prescribed displacement of 5×10^{-4} [mm] (see Figure 3.5(a)). The second loading case represents tension along the long axis of the strip. One end of the model is restrained in the x-, y-, and z-directions and the other end is loaded in tension along the plane of the sheet, again with a prescribed displacement of 5×10^{-4} [mm] (see Figure 3.5(b)). The third loading case represents out-of-plane bending of the strip where both ends are simply supported and the nodes

adjacent to the ends are loaded in the downward direction, similar to a four point bending test (see Figure 3.5(c)). The last loading case represents in-plane bending where one end of the strip is restrained in the x-, y-, and z-directions and the other end is loaded perpendicular to the long axis of the strip similar to a cantilevered beam (see Figure 3.5(d)).

The energy in the bar-and-hinge model, U_{BH}, is calculated by summing the strain energy in the bending hinges and bars after loading. Each of the four loading cases has a structural mechanics solution for the strain energy, which was calculated based on the geometry and material properties of the strip. I call this analytically calculated energy the theoretical energy, U_{Th}. I compared the bar-and-hinge energy to the theoretical energy for each loading case at different aspect ratios. From Figure 3.5(e), the bar-and-hinge model overestimates the energy (and stiffness) in torsion compared to the structural mechanics solution. At an aspect ratio of one ($\alpha = 1$), where the height of each triangular panel is equal to its width, the bar-and-hinge energy achieves its minimum strain energy solution, which is roughly double that of the theoretical solution. In this minimum torsion case, $\alpha = 1$ and the bending hinges align with the 45° axis. This hinge orientation most closely aligns with the deformation from real torsion and thus gives the closest approximation. For other aspect ratios, the diagonal bars in the bar-and-hinge model do not align with the real torsion deformation, and high-energy bar straining occurs. For loading cases where torsion is present, the bar-and-hinge model will overestimate the stiffness of the structure (see Section 3.5.2 for an example).

Because the unit truss model is used to derive the tensile stiffness definition in Section 3.3.1, the strip in tension matches the theoretical solution for all aspect ratios. These results are encouraging for post-fold loading modeling of the structure because loading deformations are often dominated by stretching.

For out-of-plane bending, the result depends on the aspect ratio of the bar-and-hinge model. For low aspect ratios (that is, coarser meshes), the bending hinges overestimate the stiffness of the sheet. However, as the aspect ratio increases, the strain energy approaches the theoretical solution. Aspect ratios over three ($\alpha > 3$) will give out-of-plane bending solutions within 10% of the theoretical value. Aspect ratios over four ($\alpha > 4$) will give solutions within 5%. Because bending

deformations dominate the folding behavior of curved-crease origami, one should expect better overall folding results with a finer mesh that still has a convergent solution.

Finally, for in-plane bending, the bar-and-hinge model overestimates the stiffness of the sheet by a factor of about three. This is due to the discrepancy between the theoretical stress distribution across the cross-section of the sheet and the bar-and-hinge's treatment of stress as concentrated bar forces. The factor of three can also be back-calculated from the initial bar definitions in Equation 3.4. This increased stiffness should not affect the folding of curved-crease models because shear is rarely present; however, it might become important in post-fold loading of the structure. For structures where in-plane bending is dominant, the bar areas can be reduced by three to get the bar-and-hinge model to approach theory. However, because in-plane bending is coupled with stretching, such a reduction will result in underestimating the stretching stiffness by the same factor of three.

Overall, these strip tests show the benefits and limitations of the bar-and-hinge model as formulated here. For folding of the models where low-energy bending deformations dominate, the model will capture the final shape and stiffness well. For analyzing the behavior of structures after folding, some user discretion must be applied to ensure that the results are accurate. For cases where torsional deformations of the system are expected, an aspect ratio of $\alpha \approx 1$ should be used and stiffness may still be overestimated by a factor of two. For cases with global in-plane bending deformation, the user could assume that the stiffness will be overestimated by a factor of about three.

When modeling most other curved-crease origami, the analyst should choose a moderate aspect ratio. Through experience with modeling various geometries, the recommended range for the aspect ratio is $\alpha \in [5, 12]$. In this range, the mesh is fine enough to properly approximate the curved geometry of the creases and will meet the theoretical stiffness for stretching, shearing, and out-of-plane bending. Additionally, such a range will give solutions that reliably converge (although the model will converge for $\alpha \leq 30$, depending on the geometry, boundary conditions, loading conditions, and increment size). Although it is possible to modify the bending stiffness definition

in Section 3.3.2 to converge to theory for $\alpha < 5$, such a task would not benefit analysis of most curved-crease origami and is beyond the scope of this chapter.

3.4.2 Bending a Creased Annulus Sector Into a Theoretical Cone

A small subset of curved-crease origami structures can be described as a piece-wise combination of well-defined geometric surfaces, such as cones, cylinders, and tangent developable surfaces connected at a single crease (Duncan and Duncan, 1982). The non-zero principal curvature, κ_2, of these developable surfaces can be calculated and included along with the bending modulus of a sheet, $D = Et^3/(12[1-\nu^2])$, in a theoretical strain energy expression, $U_{\text{Th}} = 1/2 \int_A D\kappa_2^2 \, dA$. Using the theoretical strain energy of the surface as a point of comparison to the bar-and-hinge model, the performance of the model can be examined.

A potential candidate for a simple, piece-wise developable structure is a circular annulus sector folded about its center (see Figure 3.6(a)). If the structure is restrained in a specific way, differential geometry can be used to show that the deformed midsurface of the folded sheet is a portion of a cone with well-defined, non-zero principle curvature.

Suppose I have a thin, elastic sheet with thickness, t, and elastic modulus, E, that is cut into the shape of a circular annulus sector with width in the radial direction, $2w$, and a sector angle of ς_0 (see Figure 3.6(a)). I prescribe a parametric, flat crease, $\mathbf{c}_0(u)$, into the sheet such that the crease is always parallel to edges of the sheet that follow the polar direction. This crease is a circular arc with radius of curvature, R_0, placed evenly between the inner and outer radial edges of the sheet (that is, the distance between the crease and the inner and outer radial edges is w).

The flat crease has curvature, κ_0, constant along its length. After folding to some dihedral angle, $\phi \in (0, \pi)$ [rad], constant along the length of the curve, the deformed crease, $\mathbf{c}(u)$, remains planar using structural restraints (in the z-direction), and has a different curvature, κ, and radius of curvature, $R = 1/\kappa$ (see Figure 3.6(b)). Fuchs and Tabachnikov (1999) proved that the curvature of the deformed crease can be calculated with $\kappa = \kappa_0 / \cos \eta_L = \kappa_0 / \sin(\phi/2)$.

The crease lies in one osculating plane (that is, the plane in which the tangent and normal

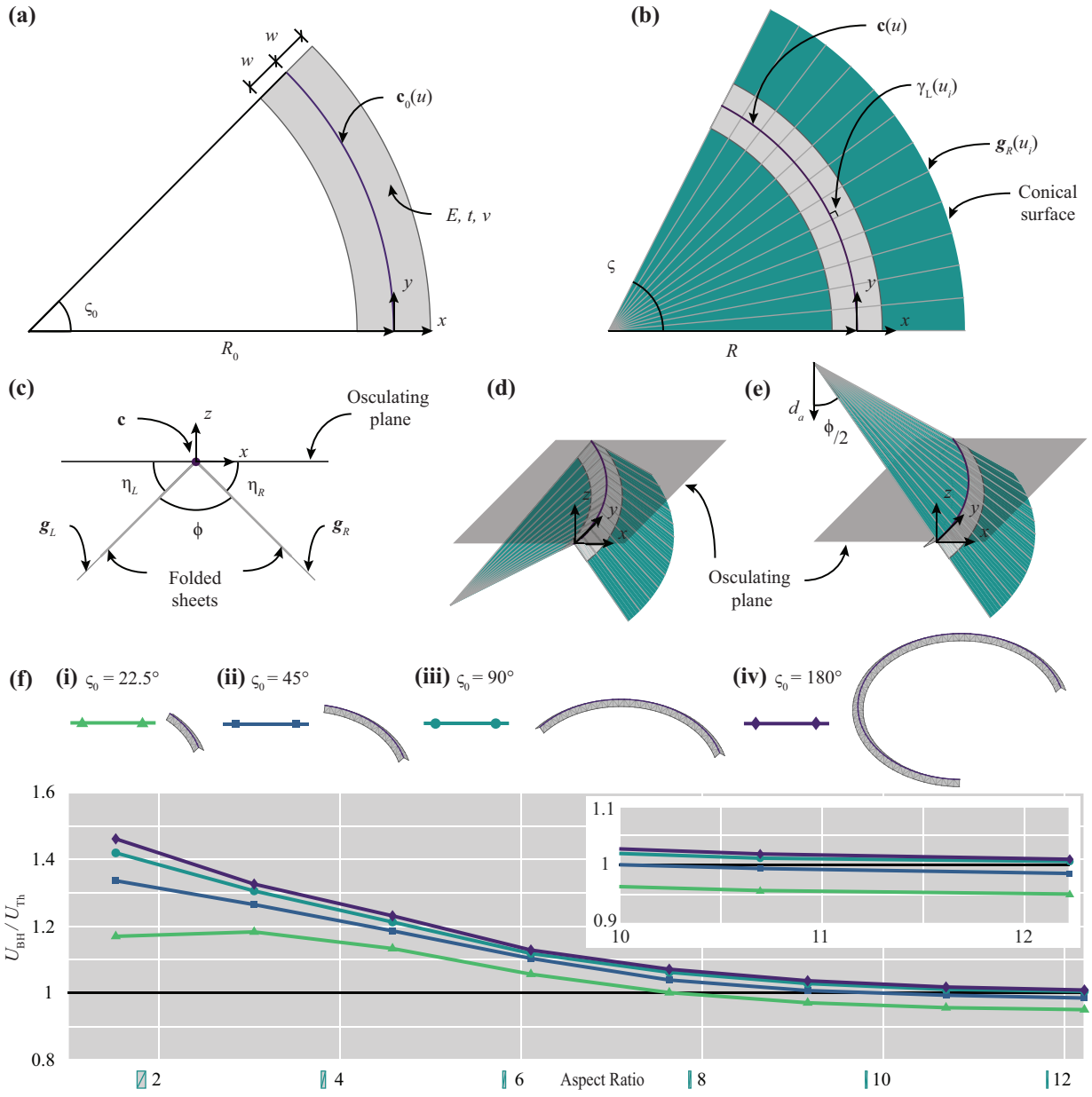

Figure 3.6 – Creased annulus geometry cone derivation. **(a)** Illustration of the parameters for a flat, circular annulus sector creased about its mid-radius. **(b)** Top-view illustration of the parameters for the same circular annulus sector that has been folded. **(c)** Illustration of the cross-section at some point, u_0, along the length of the folded curve with additional parameters. **(d)** The creased annulus sector coincides with portions of a cone. **(e)** When the upper portion of the cone is reflected about the osculating plane touching the crease, the conical shape of the origami structure becomes clearer. **(f)** A comparison of the bar-and-hinge strain energy, U_{BH}, with the strain energy of a cone, U_{Th} for **(i-iv)** four different flat sector angles, ς_0.

vectors at all points along the crease lie). The angle between the surface of the osculating plane and the midsurface of the sheet to the left of the crease is η_L and is related to the dihedral angle by $\eta_L = (\pi - \phi)/2$ (see Figure 3.6(c)). By definition, the torsion of the deformed, planar crease, τ, is zero everywhere. Additionally, because the fold angle is constant, the angle η_L does not change along the length of the crease.

The generators represent rulings on the curved, developable surfaces and coincide with the direction of zero principle curvature, $\kappa_1 = 0$. By definition, the non-zero principle curvature of the surface is orthogonal to the generators in the neighborhood of the crease. Additionally, the layout of the generators (defined by $\gamma_{_L}$) describes the geometric properties of the surface.

If all the assumptions are applied and calculations are made for the circular creased annulus sector, Equation A.12 (the equation that relates generator angles to the already-deformed crease's curvature, torsion, dihedral angle, and folding velocity) has the solution $\gamma_{_L} = \pi/2$ [rad]. Thus, the generators of this creased annulus are normal to the crease at all points. These generators coincide with the direction of curvature, κ, and meet at one point (the apex), and the folded shape is identical to a segment of a right cone (see Figures 3.6(b) and (d)). A similar process can be used to show that the generator angles to the right of the crease, $\gamma_{_R}$, are also perpendicular to the crease. As shown in Figures 3.6(d-e), the creased annulus sector coincides with a portion of a cone with the upper portion and apex reflected about the osculating plane of the crease. This observations is consistent with Mitani's method for planar, curved folding (Mitani and Igarashi, 2011).

The non-zero principal curvature of a right cone is calculated as

$$\kappa_2(u) = \frac{1}{\tan(\phi/2) d_a \sqrt{1 + \tan^2(\phi/2)}}, \tag{3.13}$$

where d_a is the distance from the apex of the cone extending down through the center (Weisstein, 2019).

I used the bar-and-hinge method to model the creased annulus sector made with different sector angles (see Figures 3.6(f)i-iv). The bending and stretching energy of these models, U_{BH}, is plotted

for different aspect ratios and normalized by the theoretical cone energy, U_{Th} (see Figure 3.6(f)). The aspect ratio is defined as the mean aspect ratio of all the triangular panels as defined earlier. For coarser meshes with low aspect ratios, the bar-and-hinge model overestimates the energy and stiffness of the sheet. As the mesh size decreases, the energy in the bar-and-hinge model approaches the theoretical solution. For models with an aspect ratio greater than seven ($\alpha > 7$), the bar-and-hinge solution is within 10% of the theoretical solution. For sufficiently high aspect ratios, the bar-and-hinge energy dips below the theoretical solution. Underestimating the theoretical cone energy is consistent with finite element solutions of the same problem carried out in (Woodruff and Filipov, 2018). The energy underestimation indicates that the bar-and-hinge model is capable of capturing some of the end effects (also called the "free edge effect" (Lee et al., 2018)) where the unsupported edges of the curved-crease annulus sector do not achieve the curvatures of a pure cone (Badger et al., 2019).

3.4.3 Laser-Scanning Verification of Complex Curved-Crease Origami

For certain curved-crease origami patterns, there is no existing theoretical description of the deformed shape. Kinematics and elasticity formulations alone cannot give the surface shape between two curved creases unless the pattern is highly constrained, for instance, using a tessellation of creases (Lee et al., 2018). Additionally, theories of developable surfaces used to verify the deformed shape of the creased annulus sector in Section 3.4.2 become complicated for surfaces that are neither conical or cylindrical, called tangent developable surfaces. Understanding the shape of this general tangent developable surface requires parameters such as generator angles that are not apparent given the flat crease pattern. A recent method by Badger et al. (2019) finds the natural shape of general developable surfaces using an energy minimization method. However, this method is limited to finding the energy minimal case when only one crease is used on the pattern.

The bar-and-hinge method implicitly accomplishes energy minimization; thus, comparison between the previous methods would be either unrealistic (e.g., requiring, a priori, assignment of generator angles) or trivial given an appropriate mesh size. Instead, I verified the deformed shapes

of complex models by comparing them with the shapes of physical paper models. The process of capturing and comparing the folded shape of a paper model is shown in Figure 3.7(a). Starting from a flat, curved-crease pattern, I fabricated the physical model from sturdy, 0.274 [mm] thick, linen paper. All models are about 10 [cm] by 10 [cm] when flat. I cut the pattern using a laser cutting machine, and I hand-folded the model such that the crease material yields and the model holds some natural rest angle. Using a NextEngine 3D Laser Scanner HD machine, I captured the deformed shape of the paper model with an accuracy of 0.127 [mm] (0.005 [in]) and at a resolution of 10,400 [points/cm^2] (67,000 [points/in^2]), which is the highest quality scan available. From the scan, a set of points with position values in three-dimensional Cartesian coordinates, called the point cloud, is saved and used in the comparison. I chose to sample every fifth point in the point cloud to expedite analysis (the largest unprocessed point cloud included about 250,000 points).

Simultaneously, I modeled the same system with the bar-and-hinge model using the paper's material properties and the geometry of the crease pattern. The prescribed fold angle was estimated from the point cloud, and various L^* values were tested to find the result giving the lowest mean error (see Section 3.4.4). To represent the shape of the surface between the creases in the bar-and-hinge folded model, I enrich the mesh by adding points along the length of each bar. I then chose three points from the point cloud and three corresponding points from the enriched mesh to align the two systems (usually, three easily identifiable locations such as corners or crease ends). After alignment, for each point in the enriched mesh, I found the closest point in the point cloud and calculated the distance between them. This distance is the Hausdorff distance of that point.

I plotted the Hausdorff distances of each point in the enriched bar-and-hinge mesh and calculated simple statistical values (mean distance, standard deviation of distances, and the median distance). The sine wave tessellation (Figure 3.7(b)) has an average Hausdorff distance of less than 2 [mm], and all other example have an average Hausdorff distance less than 1 [mm]. In the far-right images in Figures 3.7(b-e), the deformed shapes of the bar-and-hinge models agree with the physical models. The largest errors, about 8 [mm], occur at edges and are mainly caused by human errors in choosing the alignment points or are due to local deformations not captured by the bar-

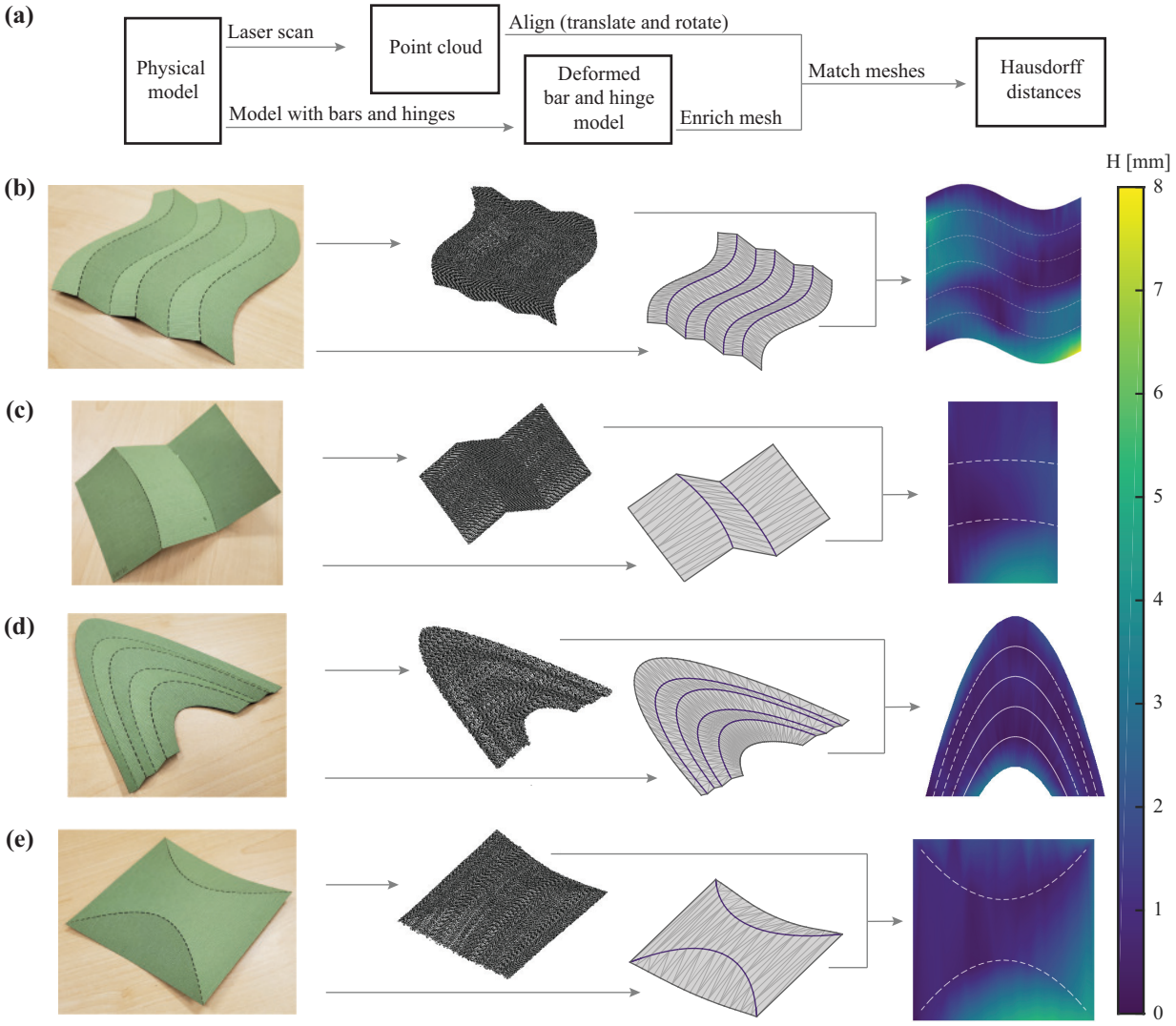

Figure 3.7 – bar-and-hinge verification using laser scanning. The accuracy of the bar-and-hinge model was assessed by comparing the simulated deformed shape to the shape of folded paper models measured using laser scanning. **(a)** The analysis process starting with a physical model leading to a plot showing the Hausdorff distances at each node on the bar-and-hinge enriched mesh. Four examples of complex curved-crease origami are shown, including **(b)** a sine wave tessellation, **(c)** a rectangular sheet with two circular arc creases of different radii, **(d)** a canopy made from repeated parabolic creases, and **(e)** a square with two parabolic creases in opposite directions.

and-hinge model. From these comparisons, the bar-and-hinge model is capable of approximating the deformed shape of complex folded curved-crease origami structures.

3.4.4 The Effect of Rest Angle and Fold Stiffness on the Geometry

As shown in Equation 3.1, the in-plane, sheet bending, and the crease folding energy all contribute to the energetic equilibrium of the structure. The crease folding energy is a function of the fold stiffness, k_f, as well as the difference between a prescribed rest angle, ϕ_R, and the actual fold angle of the crease, ϕ. The fold stiffness is inversely proportional to the length scale parameter, L^*, which is prescribed in the bar-and-hinge model. To fold the origami into a three-dimensional state, the rest angle is sequentially reduced from $\phi_R = 180°$, downward. For curved-crease origami, any folded state results in elastic bending energy stored in the sheet. This elastic energy is counteracted by elastic folding energy in the creases. Thus, in any folded state, $\phi_R \neq \phi$, the difference between the prescribed and actual fold angles depends on the prescribed length scale parameter, L^*, which factors into the fold stiffness. As discussed in Section 3.3.3, there is no straightforward method for determining the value of L^*. Instead, here I explore how this value affects the overall folded geometry.

In Figure 3.8, I explore the folded geometry of two structures: a creased annulus sector and a rectangular sheet with two curved folds of different, uniform curvature. Different values of L^* are used to define the fold stiffness, and the systems were analyzed by decreasing the rest angle of the crease. High values of L^* indicate a flexible fold, while low values indicate a stiffer fold. Previous research has shown that for origami, L^* can be assumed to be in the range of 25 [mm] to 100 [mm], while experimental results on folds have varied from 1 [mm] to 700 [mm] (Filipov et al., 2017).

I first study the behavior of the curved-crease annulus sector which was introduced in Section 3.4.2. Comparing Figures 3.8 (a) and (b), the mesh discretization does not have a significant influence on achieving the prescribed fold angle. Furthermore, the fold angle, ϕ, tends to be close to the rest angle when realistic values of L^* are used, and when $\phi_R > 90°$. As expected, when ϕ_R is reduced further, the rest angle and the actual fold angle deviate. An exception is the stiffest

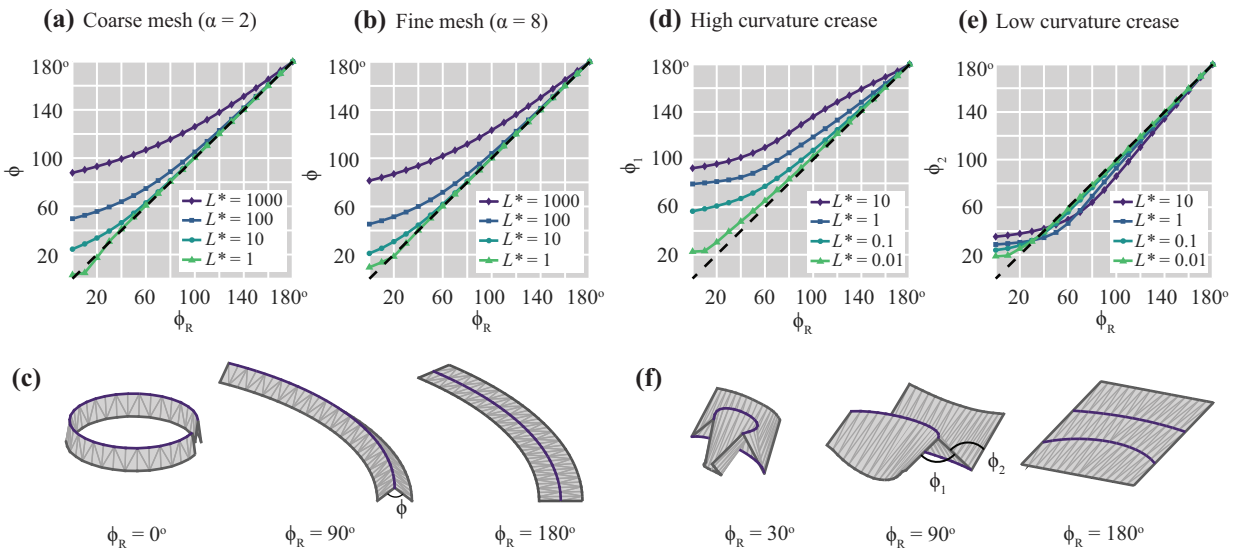

Figure 3.8 – Effects of bar-and-hinge length scale parameter on achieved fold angle. The value for folding length scale, L^*, and the prescribed fold angle, ϕ_R, both affect the folded geometry of curved-crease origami. **(a)** The actual crease angle versus the rest angle for a creased annulus sector with a coarse mesh and **(b)** a fine mesh for different values of L^*. **(c)** The deformed shapes with three prescribed angles and $L^* = 1$. **(d-e)** The actual crease angle versus the prescribed fold angle of a rectangular sheet with two curved creases with different curvatures uniform along their lengths. **(f)** Deformed shapes with $L^* = 0.01$.

folds ($L^* = 1$) which essentially restrains the annulus to take the prescribed fold angle Lang et al. (2017) predicts that as the dihedral angle approaches zero, the nonzero principal curvature of the sheet about the crease asymptotically increases towards infinity. My results further verify this observation by showing that all systems have some finite deviation from $\phi_R = 0°$. The study of the curved-crease annulus sector shows that for simple, single-crease systems, the folded state is not highly dependent on the choice of L^*, and an approximate folded state can be achieved by defining the rest angle, ϕ_R. Furthermore, the same folded geometry (angle ϕ) can be achieved with different combinations of L^* and ϕ_R.

The curved-crease origami with two folds of different, uniform curvature exhibits a more varied response when L^* is changed (see Figures 3.8(d-e)). In addition to the counteraction between crease folding energy and sheet bending energy, here the incompatibility between the crease curvatures also affects the folded state. The crease with low curvature (that is, the straighter crease with fold angle ϕ_2) tends to stay close to the prescribed rest angle regardless of L^*. On the other hand, the crease with high curvature can only approach the rest angle when the crease is much

stiffer than a realistic origami system ($L^* = 0.01$). In reality, this would correspond to using a mechanical system to restrain the crease. For realistic values of L^* (e.g., $L^* = 10$), the crease with higher curvature, ϕ_1 deviates from the prescribed fold angle which indicates that there is more counteraction between energies in the system. From these case studies, the value for L^* can have a more significant influence for more complex curved-crease origami, and choosing an appropriate value of L^* is problem-specific (for example, affected by differential curvature of folds in the pattern). A user could perform similar parametric studies by varying both ϕ_R and L^* to find the combination that gives a reasonable approximation of the folded structure. As shown in the next section, finding a reasonable approximation of the folded geometry is important before moving on to post-fold loading problems.

3.5 Modeling the Anisotropy of Curved-Crease Structures

The unique structural properties of curved-crease origami come from their folded geometry and post-folding behavior. Specifically, folded curved-crease origami will resist loads and store energy differently depending on the direction of loading. I describe this behavior as global stiffness anisotropy of the structure, or simply, anisotropy. With the inclusion of variable parameters such as the fold angle or post-loading deformed shape, the anisotropy takes on a new dimension and can be functionally tunable. For engineering applications, this anisotropy can be used to create structures which are stiff enough to support loads in one direction, but can deform and fold in a prescribed fashion when loaded in other directions. Curved-crease geometries can also reduce anisotropy in structures like corrugations by varying the direction of the creases (Woodruff and Filipov, 2020b).

The bar-and-hinge model seems to be well-suited for exploring this anisotropy because it can simulate different boundary conditions and load cases, it converges reliably, and can provide relatively accurate results when considering global structural behavior. Moreover, the model is numerically efficient which allows for parametric studies on the anisotropy and future optimization of these unique behaviors. The bar-and-hinge formulation presented in Section 3.3 limits the number of user-specified parameters (for example, L^*) which makes the system behavior directly depen-

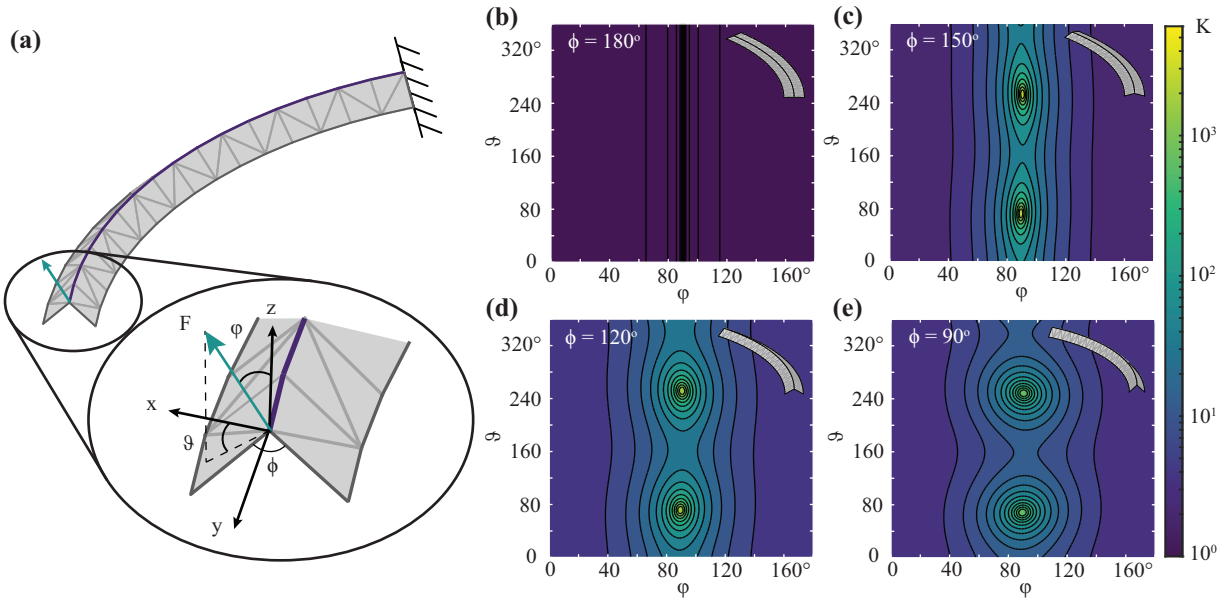

Figure 3.9 – Small-deformation response of the loaded creased annulus. **(a)** A creased annulus sector is fixed at the right end and loaded with a point load on the left. The point load is applied in different directions defined by spherical coordinates, ϑ and φ. **(b-e)** The stiffness, K, for different loading directions (that is, ϑ and φ) is shown for four different fold angles of the structure, ϕ.

dent on geometric and material properties which greatly simplifies a user's role in an optimization process. Furthermore, Figure 3.8 suggests that linear variations in L^* result in smooth variations in the structural response. I also expect that other linear variations in geometry and materials would result in smooth behavior variations, allowing for convex functions in different parametric optimizations. In this section, I use the bar-and-hinge model to study the anisotropy of two curved-crease origami structures after folding and use these studies to evaluate the capabilities and limitations of the method.

3.5.1 Multi-Directional Stiffness of a Cantilevered, Creased Annulus Sector

The creased annulus sector described in Section 3.4.2 has interesting anisotropy despite being made with only a single crease. I looked at the stiffness of this geometry when it is folded to different fold angles, restrained at one end, and loaded at the other end (see Figure 3.9(a)).

The tip of the structure is loaded in different directions denoted by the spherical coordinate system with φ as the polar angle (that is, the angle to the z-axis) and ϑ as the azimuthal angle (that

is, the angle to the x-axis). A small displacement analysis is performed. After loading, the resultant forces acting on the structure, F, is calculated in the same direction as the applied displacement, Δ, and these two quantities are used to calculate the stiffness, $K = F/\Delta$. Figures 3.8(b-e) show the results of this analysis for four folded states of the creased annulus sector, represented by the fold angle, $\phi \in \{180^\circ, 150^\circ, 120^\circ, 90^\circ\}$.

In all folded states, the stiffest loading directions are in the plane of the creases where $\varphi = 90^\circ$. When the sheet is flat ($\phi = 180^\circ$), there is high stiffness for any in-plane loading (that is, the x-y plane where $\varphi = 90^\circ$). As the structure starts to fold out-of-plane, it also gains stiffness in other azimuthal (φ) directions. Two distinct points with high stiffness emerge at $\vartheta \approx 80^\circ$ and 260° when $\varphi = 90^\circ$. These points correspond to directions of loading that are nearly parallel to the crease at the tip (that is, the y-axis as shown in Figure 3.9(a)). These directions and regions change slightly as the system is folded. The regions with higher non-orthogonal and out-of-plane stiffness increase in domain size with more folding (that is, the eccentricity of the ellipses of high stiffness lowers and becomes more circular with increased folding).

3.5.2 Large Deformation Response of a Cantilevered, Creased Annulus Sector

I continue the analysis above by loading the creased annulus sector in the upward direction and exploring the large deformation response. Figure 3.10(a) shows the deformed shapes of a physical model of the creased annulus sector made from paper. From these pictures, the global deformation includes torsional bending of the thin sheet. In Section 3.4.1, I found that the proposed formulation for the model overestimates torsional stiffness in thin strips of material. This overestimation varied with the mesh size, and a minimal error occurred when the aspect ratio of the panels is one.

For a structure such as this creased annulus sector, the effects of stretching, shearing, bending, and torsion all play a part in this large, upward deformation. Assigning a mesh with an aspect ratio of one will give poor results in bending and shearing (that is, will overestimate the stiffness), but an aspect ratio of eight will give poor results in torsion. I first explored the deformed shape of these two mesh discretizations by subjecting the creased annulus sector to a displacement-controlled

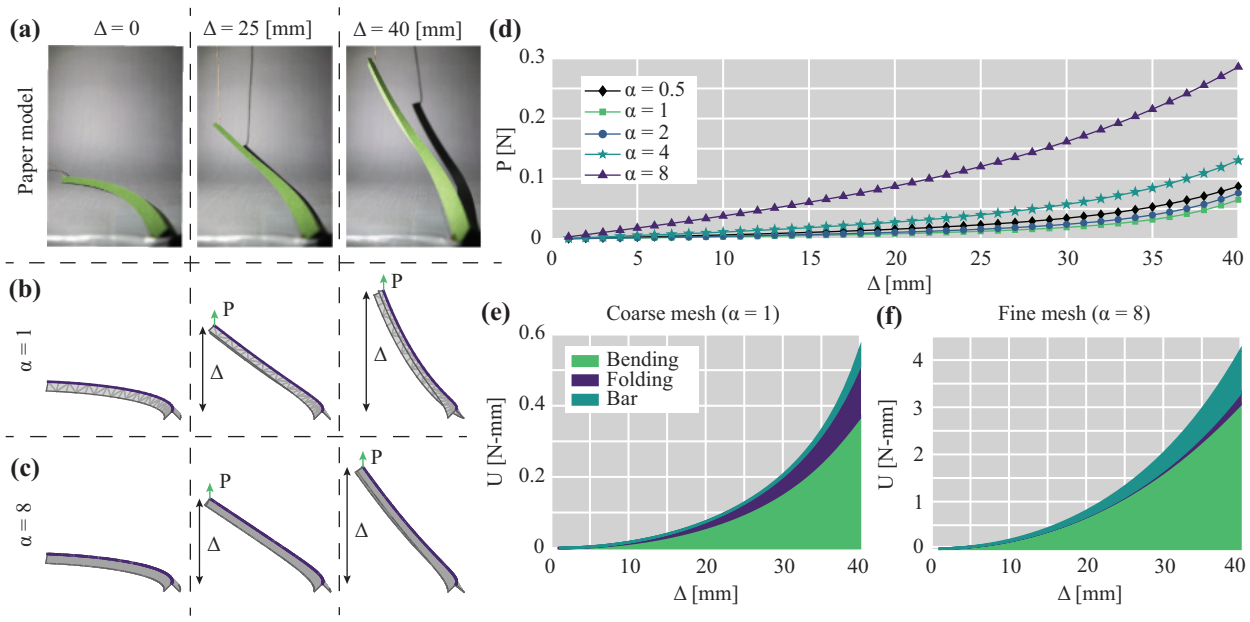

Figure 3.10 – Large-deformation response of the loaded creased annulus. When the creased annulus sector is subjected to an upward displacement, the large displacement response includes torsional deformations. **(a)** A physical model made from paper. bar-and-hinge simulations with **(b)** a coarser mesh ($\alpha = 1$) capture the torsional displaced shape better than **(c)** a finer mesh ($\alpha = 8$). **(d)** The load-deformation plot of five models with different mesh discretizations. The energy distribution of **(e)** the coarse mesh has lower bending and bar energy than **(f)** the finer mesh under the same displacement.

simulation. Figure 3.10(b) shows that the coarser mesh ($\alpha = 1$) can capture more twisting about the fold than the finer mesh ($\alpha = 8$) shown in Figure 3.10(c). Furthermore, Figure 3.10(d) shows that the finer mesh ($\alpha = 8$) has a significantly stiffer load-deformation response. Moreover, the coarse mesh ($\alpha = 1$) gives the lowest stiffness and force response. From my preliminary analysis with this model, the lowest stiffness solution would also be the most accurate when compared to the real-world behavior. Figures 3.10(e) and (f) show the strain energy of different elements for the coarse ($\alpha = 1$) and fine ($\alpha = 8$) meshes, respectively. Both cases have a high proportion of bar stretching energy which is expected for this type of non-conforming vertical displacement. The coarser mesh has a substantially lower total energy, and both the sheet bending and crease folding contribute to the total system energy. These element deformations are essential for capturing the global torsion of the structure. The finer mesh has about the same magnitude of crease folding energy; however, it overestimates the bending and stretching energy in global torsion.

For problems with large twisting, the bar-and-hinge model can give a reasonable approximation

of the true deformed shape. However, the forces and stiffness in the load-deformation response will likely be overestimated. A user of this model who is analyzing a structure and load case with high torsion should consider using different aspect ratios to identify which case gives the lowest forces and energy. This case will likely have a low aspect ratio and would provide the approximation closest to reality.

3.5.3 Anisotropy of a Pinched Fan

One curved-crease origami structure with novel potential for engineering use is a folded fan made with pleated creases that is pinched after folding (see Figures 3.11(a-d)). This model has a low rotational stiffness about the pinched point and large stiffness in the direction of the creases. Such a system could be used to create rotational hinges with variable and programmable stiffness with potential applications in robotics, architecture, and beyond.

Here, I quantify the difference between rotational and axial stiffness for this structure by performing a deformation-controlled analysis using the bar-and-hinge model. The axial stiffness, K_a, is computed from a point load applied into the middle crease line, P_a, while the rotational stiffness, K_r, is obtained from a point load, P_r, that is orthogonal to the same crease. The fan is supported through its center in the x- and z- directions with an additional y-restraint at the lowest node on the support line (see Figure 3.11(a)). The analysis was performed over two separate regimes. The first regime involved folding the flat pattern into the three-dimensional fan shape with fold angles of $90°$. The next regime involved pinching the folded fan in the center to create the rotating hinge. During the pinching process, I encountered a case where sequential folds in the pattern buckle together similar to other origami pleats in the literature (Filipov and Redoutey, 2018). Each of the analysis regimes was divided into 100 displacement increments, and the axial and rotational stiffness were calculated at each increment (Figure 3.11(e)).

For all increments, the axial stiffness is greater than the rotational stiffness. Figure 3.11(f) shows the ratio of the rotational stiffness to the axial stiffness. As the model is pinched, this ratio decreases indicating a larger difference between the rotational and axial stiffness. At the final incre-

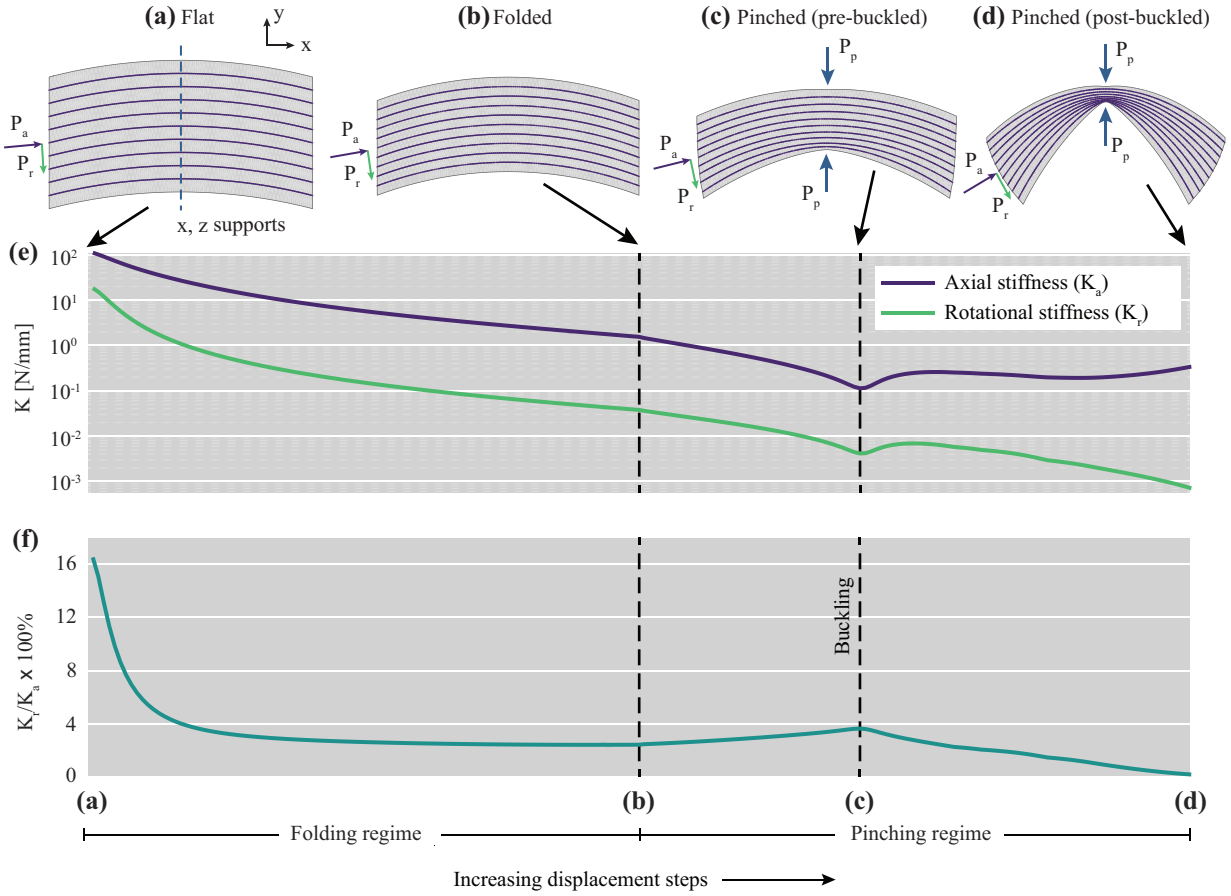

Figure 3.11 – Radial and axial stiffness of a pleated fan being folded. The deformation and stiffness of a curved-crease origami fan was modeled with the bar-and-hinge method. The structure was folded in the first regime **(a-b)** and is subsequently pinched in the second regime **(c-d)**. **(e)** The rotational and axial stiffness of the structure changes during the two regimes. **(f)** The ratio of rotational to axial stiffness drops as the structure is pinched indicating the formation of a hinge.

ment, the rotational stiffness is about 0.2% that of the axial stiffness which indicates the formation of a rotational hinge in the structure. If the pinching on the structure is released, then system will recover to a state with higher rotational stiffness. This type of stiffness anisotropy in curved-crease origami could be exploited for creating joints and structures with tunable characteristics.

3.6 Conclusions

In this chapter, I have introduced a bar-and-hinge method for simulating the structural behavior of curved-crease origami during and after folding. This method is rapid and can model a variety of curved-crease origami structures with different boundary conditions. There are three element types, in-plane bars, bending hinges, and folding hinges, which together can capture the global deformation of the structure. I derived the stiffness values of each element based on the system geometry, the mesh discretization, and material properties.

The stiffness expressions were verified and explored using different theoretical and empirical models of simple and complex curved-crease origami structures. The first verification method compared the deformation response of long strips of material modeled using the bar-and-hinge method to theoretical solutions from structural mechanics. The stiffness expressions were also verified using differential geometry solutions and by comparing the deformed shape of paper models to bar-and-hinge models through laser scanning. The influence of choosing a rest angle and a fold stiffness were also explored in relation to the final folded shape.

The method can be used to explore the complex, post-fold stiffness anisotropy of various curved-crease origami structures. I first showed a cantilevered creased annulus sector that has regions of high stiffness which correspond to loading parallel to the fold lines. The out-of-plane stiffness of this structure increases as it becomes more folded. When the cantilevered annulus sector is loaded upward, it experiences a complex, torsional deformation. I also explored a curved-creased fan for its stiffness parallel and perpendicular to the fold lines. This structure shows a tunable anisotropy where a rotational hinge can be tuned and created by pinching the center of the fan.

My exploration of this new formulation of the bar-and-hinge model shows that it is well suited

for capturing the folding sequence of curved-crease origami. Because the folding primarily engages sheet bending, the deformed shape and stiffness can be captured well with moderately fine mesh discretization sizes ($\alpha \in [5, 12]$). Stretching and shearing stiffness is captured well by the model; however, the stiffness of in-plane bending is overestimated by a factor of three, regardless of the mesh. This stiffness overestimation can be reduced by cutting the bar stiffness by a third (though, a three-fold loss of stretching stiffness would also occur). The bar-and-hinge model can approximate global torsional deformations, but typically overestimates stiffness for this behavior. Coarser meshes tend to perform better when high levels of torsion occur. These preliminary studies show how curved-crease origami structures can be used to create novel mechanical behaviors such as anisotropic stiffness and tunable stiffness properties. I have made this program available to the public (Woodruff and Filipov, 2020a) so that other researchers may benefit from the speed and information that the model provides.

Chapter 4

Enhancing the Bending Stiffness of Corrugations With Curved Creases

Corrugations offer a convenient way to make thin, lightweight sheets into stiff structures. However, traditional, v-shaped corrugations made from straight creases result in highly anisotropic stiffness which leads to undesirable flexibility in some directions of loading. In this chapter, I explore the bending stiffness of curved-crease corrugations with a planar midsurface – developable corrugations made by folding thin sheets about curves and without linerboard covers on the top or bottom. The curved-crease corrugations break symmetry in the pattern and can redistribute stiffness to resist bending deformations in multiple directions.

To study these systems, I formulate a framework for predicting the bending stiffness of any planar-midsurface corrugation from its multiple geometric features at different scales. I use the framework to create two predictive methods that provide valuable insight to the global stiffness of corrugations without a detailed analysis. Results from these methods match well with experimental, three-point bending tests of five corrugation geometries made from polyester film. I found that corrugations with elliptical or parabolic curved-creases that intersect with one edge of the pattern are best at redistributing stiffness in multiple directions. While a straight-crease pattern has a stiffness of about 4 [N/mm] in one direction and about 0 [N/mm] in the other, a parabolic crease pattern has a stiffness of about 2.5 [N/mm] in both directions. These curved-crease corrugations can enable the self-assembly and fabrication of practical, stiff structures from simple, developable sheets. This chapter demonstrates the tunable properties of curved-crease origami, allowing for strong and material efficient structures.

The format of the chapter is as follows. Section 4.1 gives background information and motivation for the problem. In Section 4.2, I describe a framework for qualitatively connecting geometric

characteristics of a corrugation to its bending stiffness about any direction in the xy-plane. In Section 4.3, I present the geometries of five origami corrugation patterns used in subsequent analyses and experiments. In Section 4.4, I use two methods to quantitatively predict the bending stiffness of the folded, three-dimensional corrugation geometries estimated using a bar-and-hinge analytical simulation. In Section 4.5, I present three-point bending tests of physical corrugations made from polyester film and compare the results to the predictions made in Section 4.4. Conclusions and discussion of future work are presented in Section 4.6.[1]

4.1 Introduction

Corrugations are an essential geometric feature in a wide range of load-resisting applications. By deforming a flexible, thin sheet into a pattern of ridges and grooves using wrinkles or creases, the structure gains significant resistance to bending. Using the same amount of material as a plate, a simple corrugation can see an increase in stiffness of about three orders of magnitude (Gilewski et al., 2014). Applications span many fields including: (1) civil engineering where corrugated roofs and floor slabs limit the dead weight of the structure while maintaining strength, stability, and serviceability, (2) packaging engineering with corrugated cardboard, (3) aerospace engineering where corrugated sandwich panels are used for lightweight wings, (4) mechanical engineering with examples like corrugated hoses and gaskets, and (5) ship decks designed by naval architects (Dayyani et al., 2015).

Corrugations are an example of lightweight, and therefore, efficient structures, but they are not without limitations. In their simplest form, corrugated structures are made by folding a flat, developable sheet along straight creases, which results in highly anisotropic bending stiffness behavior. Figure 4.1(a) shows an example of such a traditional, v-shaped corrugation made with straight creases. This geometry can resist bending about one direction (Figure 4.1(b)), but collapses when loaded about another direction (Figure 4.1(c)). Prior research has addressed this limitation of corrugated structures in a number of ways. For instance, a traditional means of resisting compliant

[1] This chapter contains research published in Woodruff and Filipov (2020b)

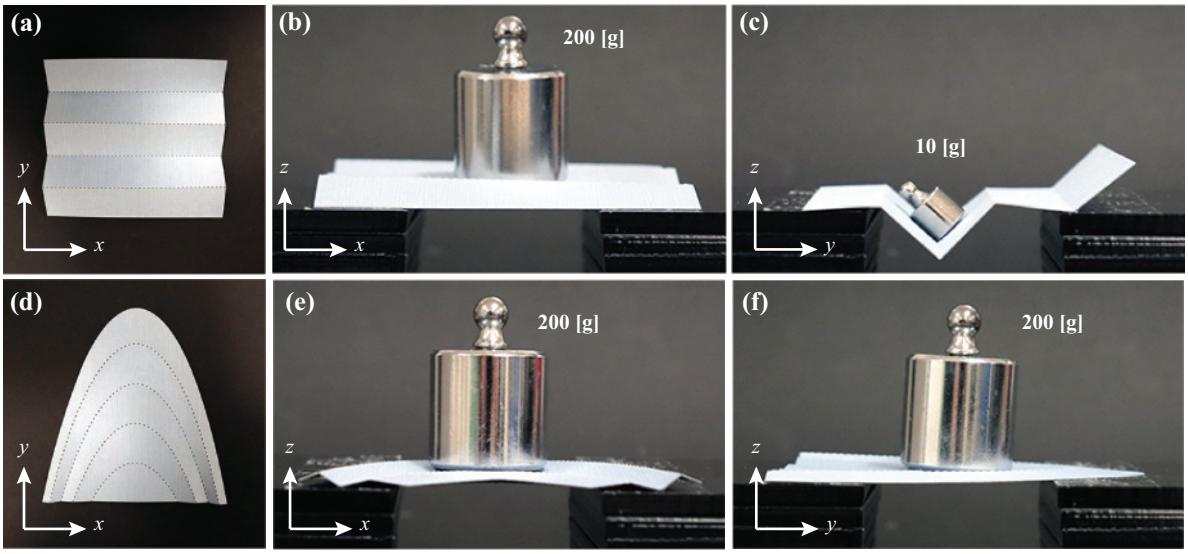

Figure 4.1 – [Bending stiffness anisotropy: straight-crease versus curved-crease. Not all corrugated systems are the same. **(a)** A v-shaped, straight-crease corrugation **(b)** can support 200 [g] in bending about the y-direction, but **(c)** collapses when carrying 10 [g] in bending about the x-direction. **(d)** A parabolic, curved-crease corrugation supports 200 [g] in bending about both the **(e)** y-direction and **(f)** the x-direction.

unfolding in roof structures is by supporting the edges with beams and columns at each valley crease (Ketchum, 1955). Other means of restricting unfolding involve embedding a corrugation into a material matrix, like steel into concrete (Fraser et al., 2018) or copper in tin (Bouaziz, 2013). Similarly, corrugations can be restrained using partial embedding on one side, similar to composite, concrete-metal decking (Gholamhoseini et al., 2018).

Arguably, the most popular method to overcome the anisotropy and to improve the corrugation bending behavior is to sandwich it and connect it with two linerboards (for instance, corrugated cardboard (Zhang et al., 2014) or sandwich corrugations (Seong et al., 2010)). Others have seen functionality in the stiffness anisotropy of corrugations and used them to design morphing structures (Norman et al., 2008, 2009; Thill et al., 2010). Origami principles have also inspired new corrugation designs with tunable stiffness characteristics. Another benefit of origami is rapid fabrication from flat sheets through self-assembly (Gracias et al., 2002). Furthermore, origami tube (Filipov et al., 2015) and arch (Gattas et al., 2017) systems have been shown to increase stiffness while reducing global anisotropy.

The above solutions to stiffness anisotropy are limited, however. Additional supports com-

plicate the design and might be unavailable for certain applications. Composite-embedded structures add additional weight to the corrugation that may be disadvantageous to a design. Sandwich corrugations complicate the design and manufacturing of the structure with additional adhesion between layers. Many straight-crease origami designs require locking mechanisms or complex, non-developable manufacturing. Although some origami-inspired corrugations may exhibit improved global "isotropy" (for example, miura-ori or egg box patterns), this improved isotropy comes at a great loss of global stiffness. For example, the strong direction of a traditional, v-shaped corrugation made with straight creases is over seventy-five times stiffer than the Miura-ori pattern (Gilewski et al., 2014). It would be ideal if engineers could construct corrugations with stiffness isotropy, that are made from a simple, flat, developable sheet, and do not require added support or adhesion.

In this work, I introduce an origami-inspired, *curved-crease corrugation* that achieves this unique stiffnesss isotropy. The system is made from a thin, developable sheet, but instead of straight creases, curves are used to fold parabolic or elliptical corrugations into three-dimensional shapes that have a planar midsurface. Figure 4.1(d) shows an example of these curved-crease corrugations made from paper. This structure is stiff enough to resist significant loads in both directions (Figure 4.1(e-f)).

Early work on the structural properties of curved-crease corrugations explored their performance under impact (Gattas and You, 2015). Other research has suggested that curved-crease corrugations possess non-structural advantages such as improved performance for gas or fluid transport (Klett et al., 2017a,b). Existing research has not identified the unique stiffness isotropy possible with curved-crease sheets. Additionally, there is currently no framework or method to predict or estimate the bending stiffness of such corrugations.

4.2 Stiffness Contributions at Multiple Scales

When considering a corrugated system for structural function, engineers often want the system to support external loads while minimizing the overall displacement. Consider a thin, isotropic,

homogeneous rectangular plate lying in the xy-plane with applied loads that cause a small deflection, w, in the z-direction and internal bending moments per unit width, M_x, M_y, and M_{xy}. The moment-curvature relationships for this plate are

$$M_x = D\left(\frac{\partial^2 w}{\partial x^2} + \nu\frac{\partial^2 w}{\partial y^2}\right); \tag{4.1}$$

$$M_y = D\left(\frac{\partial^2 w}{\partial y^2} + \nu\frac{\partial^2 w}{\partial x^2}\right); \tag{4.2}$$

$$M_{xy} = -D(1-\nu)\frac{\partial^2 w}{\partial x \partial y}, \tag{4.3}$$

where $D = Eh^3/[12(1-\nu^2)]$, E is the elastic modulus of the plate material, h is the thickness of the plate, and ν is the Poisson's ratio (Timoshenko and Woinowsky-Krieger, 1959). Assuming, for simplicity, that $\nu = 0$ and that a line load is applied that causes bending about the y-direction (without loss of generality), the moment-curvature relationships reduce to that of a beam with a bending moment about the y-direction, M, that varies along its length in the x-direction, but is constant across its width, b. That is,

$$M = EI\frac{d^2 w}{dx^2}, \tag{4.4}$$

where $I = bh^3/12$ is the second moment of area about the y-direction. Through double integration over the length of the plate and application of boundary conditions, the deflection can be calculated from Equation 4.4.

When corrugations are folded into geometries with a flat midsurface and applied loads are unidirectional, the corrugation's deflection should behave similarly to that of a plate. Keeping the boundary and loading conditions the same between different corrugation geometries and maintaining the same homogeneous material properties of the sheet, the second moment of area should be the only structural property that changes with the corrugation geometry. Given the complex geometry of a folded corrugation, the exact second moment of area will be heterogeneous and will depend on the location in the corrugation's xy-plane. Through careful consideration of the corru-

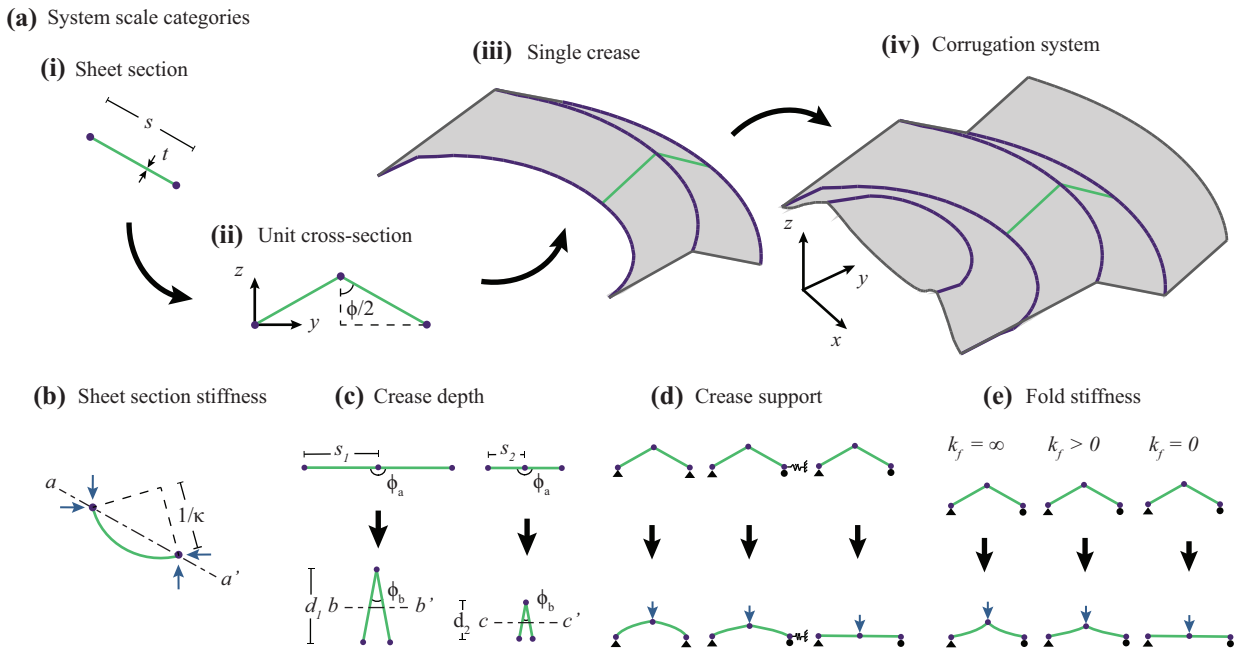

Figure 4.2 – Qualitative framework for predicting bending stiffness of a corrugation. **(a)** The stiffness of a corrugation depends on its geometric properties at multiple scales combined into the full system. **(b)** Sheet section stiffness for bending about its original plane (a-a') is the most local property giving stiffness to a system. **(c)** Crease depth adds bending stiffness about directions in the xy-plane by distributing material away from the neutral axes (b-b' and c-c'). **(d)** The supports at the edges of a unit cross-section affect the stiffness as well as the crease's ability to resist flattening and large deformations. **(e)** Similarly, fold stiffness gives the unit cross-section stiffness to resist flattening and determines whether the sheet or the crease will deform more.

gation's folded geometry, the second moment of area can be represented as one averaged value, and subsequently, simplify the deflection analysis.

In this section, I examine planar-midsurface corrugation systems created by folding about arbitrarily oriented creases and identify how variations in the geometry affect the bending stiffness of the structure. I organize the observations as a framework that considers the geometry at multiple scales, including the basic sheet section, unit cross-section, a single crease, and the entire corrugated system (Figure 4.2(a)). The qualitative geometric framework is then used to formulate two methods for predicting the averaged second moment of area value, and thus, the stiffness of an arbitrary curved-crease geometry.

4.2.1 Sheet Section

Breaking down the geometric characteristics of a creased corrugation, the smallest relevant property is the stiffness of the sheet section spanning between creases (Figure 4.2(a)(i)). Bending the sheet section over its length, s, can first be characterized by its second moment of area

$$I_{\text{sheet}} = \frac{\omega t^3}{12(1-\nu^2)}, \tag{4.5}$$

where ω is the width of sheet under consideration (into the page), t is the thickness of the sheet, and ν is Poisson's ratio of the material. Here, I assume that the width of the sheet, ω, is much greater than s, which makes the bidirectional Poisson's effect important for considering sheet bending. This second moment of area for the sheet is a function of thickness cubed. Considering that the sheet thickness is small, this relation shows that bending between creases is overly flexible, and thereby unwanted in the overall corrugation. Another important geometric quality of the section stiffness is the spacing between creases, s. Similar to the importance of length to a beam in bending, the crease spacing affects the ability of the sheet to resist local bending. A larger crease spacing will give a longer, unsupported span that will bend more easily than a smaller crease spacing.

4.2.2 Unit Cross-Section

The next scale I consider is the unit cross-section defined at each point along the length of the crease (see Figure 4.2(a)(ii)). Here, I consider bending to occur orthogonal to the cross-section (about b-b' and c-c' in Figure 4.2(c)); therefore, the folded unit cross-section redistributes material away from the neutral axis. The unit cross-section has two important qualities that contribute to how it redistributes material, and thereby, how much it increases the global bending stiffness of the corrugation. The first quality is the depth of the unit cross-section and the second is how well it maintains its folded shape.

The depth of the unit cross-section is the distance between the top crease and the lower creases. The bending stiffness of a cross-section (in this case, about the cross-section's centroid in an xy-

direction) increases as material is moved away from the neutral axis. The deeper the cross-section, the greater its second moment of area and the greater its bending stiffness will be. The second moment of area of half of the unit cross-section (one rectangular sheet) is

$$I_{\text{rect}} = \frac{st}{12}\left(s^2\cos^2\frac{\phi}{2} + t^2\sin^2\frac{\phi}{2}\right), \tag{4.6}$$

where ϕ is the fold angle (see Figure 4.2(a)(ii)). If additional sheets are to be taken into account, a new neutral axis can be computed, and the total second moment of area can be found using the parallel axis theorem.

Because $s >> t$, the bending stiffness of the unit cross-section is mostly dependent on two important parameters, s and ϕ. Increasing s will increase the depth of the unit and result in a larger bending stiffness (Figure 4.2(c)). Additionally, the more a unit cross-section is folded ($\phi \to 0$), the greater its depth (within the domain $0 < \phi \leq \pi$ [rad]). However, from a practical perspective, it is not useful to have overly folded creases because the surface area covered by the corrugation would go to zero. In a general sense, the unit cross-section bending stiffness is going to be much greater than the section bending stiffness because the way in which the sheet is loaded. For bending about the unit cross-section, the upper portions of the corrugation will carry compression while the lower portions will carry tension, or vice versa. In this scenario, bending of the actual sheet is avoided and the structure is much stiffer.

It is important for a unit cross-section to maintain its folded shape during loading, because if it flattens, its depth will be reduced, and the overall stiffness of the corrugation will decrease. The boundary conditions surrounding the unit cross section, the local crease stiffness, and the sheet section stiffness will all affect the ability of the system to maintain its shape. The boundary conditions or supports surrounding the unit-cross-section are dependent on the adjacent creases in the corrugation and will likely fall between a case with two fully pinned ends and a case with a pin and a roller support (Figure 4.2(d)). In curved-crease corrugations, the different geometry of separate creases will lead to stiffer boundary conditions for each individual crease. Next, a high crease stiffness, k_f,

will also maintain the folded shape better, regardless of the boundary conditions. Creases in corrugations often have lower stiffness than the base sheet because of intentional damage during the fabrication (for instance, perforation). In some cases however, plastic deformation and strain hardening of the creased material can lead to a stiffer crease than the base material. Finally, the sheet section bending behavior as discussed in Section 4.2.1 will also have an effect in the unfolding of the corrugation during loading (see cases with high fold stiffness in Figure 4.2(e)) (Lechenault et al., 2014).

4.2.3 Single Crease

The next geometric scale I consider is the single crease shown in Figure 4.2(a)(iii). The single crease connects two continuous sheets together, and forms a full, three-dimensional, beam-like structure. The first geometric quality to consider for a single crease is the unsupported length or distance that it spans. The longer this distance, the more flexible the full system would be. Furthermore, I assume that creases will continuously span through the entire, or at least through most of the corrugation. Although it may be possible to interweave multiple creases that together form a span, one should expect that the transfer locations that connect creases will result in weak points susceptible to bending.

The next important geometric characteristic is the directionality of the crease. Straight creases, such as those in the Figure 4.1(a) will have a high second moment of area in one direction, but will not be able to provide stiffness in orthogonal directions. In contrast, a curved crease will reorient the unit cross-section over its length, and can thereby provide additional stiffness to the structure in multiple directions. The curved-crease approach can accomplish this cross-section reorientation with only one crease and does not require the introduction of additional creases, or any external stiffeners. Indeed, a straight-crease geometry like a hornbeam leaf (sometimes modeled as a row of Miura-ori units (Mahadevan and Rica, 2005)) has greater directionality than a traditional, v-shaped corrugation, but gains flexibility from the additional creases. Moreover, bending stiffness would still concentrate around the few directions perpendicular to the crease. Note, however, that

the curved creases also introduce a fundamental problem to the overall beam-like crease structure because the system becomes asymmetric. If the crease is loaded in the center and supported at the ends, then this asymmetry will result in combined bending and torsional deformations, which would make the structure substantially more flexible than a straight crease design. In the next subsection, I discuss how the full corrugation design can reduce these unintended torsional deformations.

4.2.4 Corrugation System

The corrugation brings together the geometric properties from multiple scales into one interdependent structural system. It should span a distance and be stiff regardless of how it is oriented. I consider a corrugation made from a single, developable sheet where no external components or constraints are used to stiffen the structure. The geometry of the crease pattern can directly give insight to some of the stiffness characteristics. Creases that are placed close together would result in a smaller depth and smaller second moment of area. However, creases that are spaced far apart may leave large regions of the sheet unrestrained, which could result in unwanted and flexible deformations of the sheet section (Figure 4.2(b)). Greater folding of the corrugation typically leads to a deeper section and a higher second moment of area; however, the amount of folding also needs to consider the desired geometry (for instance, final surface area). The ability of the corrugation to maintain its folded state (and thereby, stiffness) during loading will depend on the crease stiffness, the sheet section stiffness, and the intrinsic boundary conditions that restrain each crease. I have observed that curved-crease corrugations with different crease geometries provide better restraint to prevent unfolding and flattening. Curved creases are important for reorienting the cross-section to provide multi-directional stiffness for the corrugation. The curved creases should have a large enough change in directionality such that the depth of the cross-section covers multiple axes (for instance, a change of more than $120°$). When placing multiple creases together, it is beneficial to use creases with different geometries such that they can counteract torsional deformations of each individual crease. The curved creases can vary in both curvature and general shape.

4.3 Corrugation Geometries

In order to compare and analyze the effects of curved creases on the bending stiffness of a planar-midsurface corrugation, I chose five different crease patterns to explore. Each corrugation starts with the following assumptions for its flat crease pattern: (1) the origin of the coordinate system lies at the lowest vertical point in the pattern and at the middle horizontal point, (2) the pattern is symmetric about the y-axis (this helps ensure the folded shape has a planar midsurface), (3) the longest part of the pattern in the x-direction lies on $y = 0$ and has length W, (4) the longest part of the pattern in the y-direction lies on $x = 0$ and has length H, (5) the pattern has n_f creases and $n_s (= n_f + 1)$ sheets between creases or between a crease and an edge, and (6) the curves are defined by one-to-one functions in the x-domain. These assumptions do not include all possible corrugation patterns, but limits the scope of the analysis.

Each of the five models I chose displays different geometric features that theoretically change the bending stiffness of the corrugation and allows for insights about how key qualitative parameters laid out in Section 4.2 affect the bending stiffness of the corrugation. Key qualitative parameters include the diversity of a crease's tangent directions and the depth of the cross-section throughout the structure. By folding physical models and running numerical simulations of folding (the bar-and-hinge method), I know that each model folds with little to no stretching deformation, does not intersect itself in the tested range of folding, and does not display buckling out-of-plane or other unstable behavior.

Each crease pattern starts with a zeroth curve that is just a line segment defined as $y_0 = 0$ on $-W/2 \leq x \leq W/2$. The curves y_1 through y_{n_s} are defined based on the specific geometry being used. Starting with the base constraining assumptions, the following crease patterns and resulting corrugations are constructed. Additionally, for each of the five geometries, $W = 100$ [mm], $H = 100$ [mm], $n_s = 5$, and $i \in \{1, 2, 3, 4, 5\}$

Straight-Crease Corrugation The straight-crease corrugation serves as the baseline geometry for a traditional corrugation design with a v-shaped cross-section, which I then use to compare

Table 4.1 – Geometric parameter values for example straight-crease pattern (see Figure 4.3(a)).

$y_i = a_i, \quad -r_i \leq x_i \leq r_i$		
i	a_i [mm]	r_i [mm]
1	20.0	50.0
2	40.0	50.0
3	60.0	50.0
4	80.0	50.0
5	100	50.0

the different curved-creased designs. The geometry has only one input beyond the constraining assumptions: a_i. The function defining the i^{th} curve of the crease pattern is,

$$y_i = a_i, \tag{4.7}$$

where,

$$a_i = \frac{H}{n_s} i. \tag{4.8}$$

The functions are defined in the domain $-W/2 \leq x \leq W/2$. An example crease pattern used in the analyses and experimentation is shown in Figure 4.3(a) with corresponding parameter values in Table 4.1.

Parabolic-Point Corrugation The parabolic-point corrugation is constructed using parabolic curves that share roots. Because the curves meet at a point, the creases are easy to restrain (for instance, using a pinned connection at the root). However, because the curves meet at a point, the spacing between the creases decreases near the root, which reduces the corrugation depth. The parabolic geometry has two inputs beyond the constraining assumptions: b_i and c_i. The function defining the i^{th} curve is,

$$y_i = b_i x_i^2 + c_i, \tag{4.9}$$

where,

$$c_i = \frac{H}{n_s} i; \qquad b_i = -\frac{4c_i}{W^2} = -\frac{4H}{W^2 n_s} i. \tag{4.10}$$

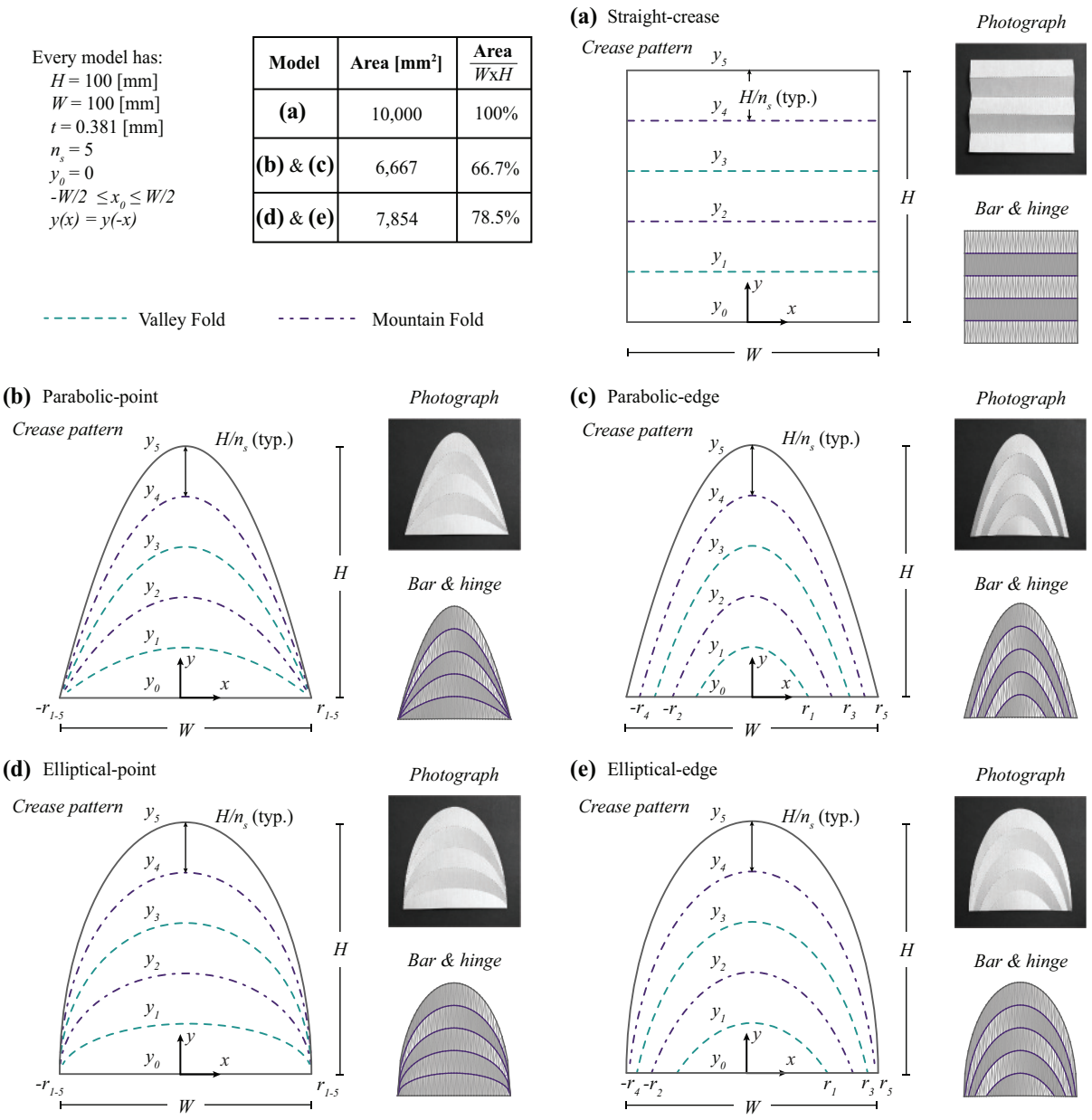

Figure 4.3 – Corrugation fold patterns and geometry. Five corrugations with flat crease patterns, folded paper specimens, and folded bar-and-hinge simulations. The geometries used in subsequent analysis are: **(a)** The straight-crease geometry, **(b)** the parabolic-point geometry, **(c)** the parabolic-edge geometry, **(d)** the elliptical-point geometry, and **(e)** the elliptical-edge geometry.

Table 4.2 – Geometric parameter values for example parabolic-point pattern (see Figure 4.3(b)).

$y_i = b_i x^2 + c_i, \quad -r_i \leq x_i \leq r_i$			
i	b_i [mm^{-1}]	c_i [mm]	r_i [mm]
1	-0.008	20.0	50.0
2	-0.016	40.0	50.0
3	-0.024	60.0	50.0
4	-0.032	80.0	50.0
5	-0.040	100	50.0

Table 4.3 – Geometric parameter values for example parabolic-edge pattern (see Figure 4.3(c)).

$y_i = b_i x^2 + c_i, \quad -r_i \leq x_i \leq r_i$			
i	b_i [mm^{-1}]	c_i [mm]	r_i [mm]
1	-0.040	20.0	22.4
2	-0.040	40.0	31.6
3	-0.040	60.0	38.7
4	-0.040	80.0	44.7
5	-0.040	100	50.0

The functions are defined in the domain $-r_i \leq x_i \leq r_i$, where $r_i = \sqrt{-c_i/b_i} = W/2$. An example crease pattern is shown in Figure 4.3(b) with corresponding values in Table 4.2.

Parabolic-Edge Corrugation The parabolic-edge corrugation is constructed by shifting the y_{n_s} curve of the parabolic-point corrugation down an equal spacing, H/n_s. In this pattern, the creases do not terminate at the same point, which makes the pattern more prone to unfolding. However, the depth of the corrugation is more consistent across the pattern. Similar to the parabolic-point, this geometry has two inputs beyond the constraining assumptions: b_i and c_i. The function defining the i^{th} curve is,

$$y_i = b_i x_i^2 + c_i, \tag{4.11}$$

where,

$$b_i = -\frac{4H}{W^2}; \qquad c_i = \frac{H}{n_s} i. \tag{4.12}$$

Each curve is defined in the domain $-r_i \leq x \leq r_i$, where $r_i = \sqrt{-c_i/b_i} = \sqrt{W^2 i/(4n_s)}$. An example crease pattern is shown in Figure 4.3(c) with corresponding values in Table 4.3

Table 4.4 – Geometric parameter values for example elliptical-point pattern (see Figure 4.3(d)).

$y_i = e_i\sqrt{1-(x_i/d_i)^2} + f_i, \quad -r_i \leq x_i \leq r_i$				
i	d_i [mm]	e_i [mm]	f_i [mm]	r_i [mm]
1	50.0	20.0	0.00	50.0
2	50.0	40.0	0.00	50.0
3	50.0	60.0	0.00	50.0
4	50.0	80.0	0.00	50.0
5	50.0	100	0.00	50.0

Elliptical-Point Corrugation The elliptical-point corrugation is constructed using positive y-value, elliptical curves that share roots and have semi-axes aligning with the x- and y-axes. The elliptical shape has a larger area underneath the curve than the parabola, giving a larger surface area for the corrugation. Furthermore, the elliptical shape is beneficial in that the roots give vertical folds (aligned with the y-axis) which gives greater resistance to bending about the x-direction near the bottom edge. However, the elliptical shape has low curvature near $x = 0$ which could reduce the corrugation's ability to resist bending about the x-direction in other parts of the corrugation. Similar to the parabolic-point, the elliptical-point corrugation will resist unfolding at the roots with fewer restraints, but will have less depth near the roots. The geometry has three inputs beyond the constraining assumptions: d_i, e_i, and f_i. The function defining the i^{th} curve is,

$$y_i = e_i\sqrt{1-\left(\frac{x_i}{d_i}\right)^2} + f_i, \tag{4.13}$$

where,

$$d_i = \frac{W}{2}; \quad e_i = \frac{H}{n_s}i; \quad f_i = 0. \tag{4.14}$$

Each curve is defined in the domain $-r_i \leq x_i \leq r_i$, where $r_i = d_i\sqrt{1-(-f_i/e_i)^2} = W/2$. An example crease pattern is shown in Figure 4.3(d) with corresponding values in Table 4.4.

Elliptical-Edge Corrugation The elliptical-edge corrugation takes the y_{n_s} curve of the elliptical-point corrugation and shifts it down a spacing, H/n_s. Like the parabolic-edge corrugation, depth is better preserved with this pattern, but the system becomes more prone to unfolding. Again,

Table 4.5 – Geometric parameter values for example elliptical-edge pattern (see Figure 4.3(e)).

$y_i = e_i\sqrt{1-(x_i/d_i)^2} + f_i, \quad -r_i \leq x_i \leq r_i$

i	d_i [mm]	e_i [mm]	f_i [mm]	r_i [mm]
1	50.0	100	−80.0	30.0
2	50.0	100	−60.0	40.0
3	50.0	100	−40.0	45.8
4	50.0	100	−20.0	49.0
5	50.0	100	0.00	50.0

the geometry has three inputs beyond the constraining assumptions: d_i, e_i, and f_i. The function defining the i^{th} curve is,

$$y_i = e_i\sqrt{1-\left(\frac{x_i}{d_i}\right)^2} + f_i, \tag{4.15}$$

where,

$$d_i = \frac{W}{2}; \quad e_i = H; \quad f_i = H\left(\frac{i}{n_s} - 1\right). \tag{4.16}$$

Each curve is defined in the domain $-r_i \leq x_i \leq r_i$, where $r_i = d_i\sqrt{1-(-f_i/e_i)^2}$ $= W/2\sqrt{2i/n_s - (i/n_s)^2}$. An example crease pattern is shown in Figure 4.3(e) with corresponding values in Table 4.5.

These five crease patterns are used in the following sections. I later predict the bending stiffness of these corrugations and verify the prediction with experimental, three-point load tests.

4.4 Predicting Bending Stiffness From the Folded Shape

Given a flat crease pattern, one could estimate the bending stiffness of the folded corrugation using the framework presented in Section 4.2. For a geometry like the straight-crease model, the depth of the structure, the sheet section stiffness, and the effects of boundary restraints are easy to predict, and thus, the stiffness can be inferred. For more complicated geometries, like the curved-creased corrugations, there is greater variation in the spacing between the curves and the fold angles that minimize strain energy in the sheets. This makes the process of surmising the folded bending stiffness from the flat crease pattern prohibitively challenging.

In order to simplify the process of predicting the bending stiffness of a folded corrugation, I offer two methods that employ a bar-and-hinge simulation to find the folded shape of a flat crease pattern and calculate quantitative metrics for bending stiffness. In both methods, the quantitative metric is analogous to the average second moment of area of the cross-sections of the corrugation. In beam bending, the second moment of area is used to describe the variation of area in a cross-section about its centroid, which is associated with resistance to strains in an elastic beam. Since a folded corrugation does not have the same cross-section across its length, the average second moment of area only gives an approximate way of predicting the bending stiffness of the system. Additionally, the methods I present only look at the geometry of the folded shape which ignores the effects of fold restraint. Despite these limitations, I found that these methods for predicting the bending stiffness offer key insights into the performance of the structure without having to run physical tests or high-fidelity finite element models.

For each of the five crease patterns, I ran bar-and-hinge simulations to find the folded shape (see Chapter 3 for details on this method). The bar-and-hinge method is suitable for folding corrugations because the majority of the deformation energy comes from bending. With a sufficiently fine mesh size, I was able to find the folded shape quickly and accurately. The material properties are defined to be those of the polyester film used to make physical specimens for the experimental study in Section 4.5. Each model was folded such that the depth of the corrugation, calculated as the difference between the highest point of the mountain creases and the lowest point of the valley creases in the z-direction, was identical. These three-dimensional folded shapes are then analyzed using the two methods for quantifying the stiffness of the corrugation.

4.4.1 Top-Down Method

The first procedure that I propose for predicting the bending stiffness of a folded corrugation is called the top-down method. In this procedure, I investigate the entire corrugation as a whole, and evaluate the cross-section at different points along the span of the corrugation. Starting with the three-dimensional folded shape of the corrugation, I pick a direction, d, in the xy-plane, which

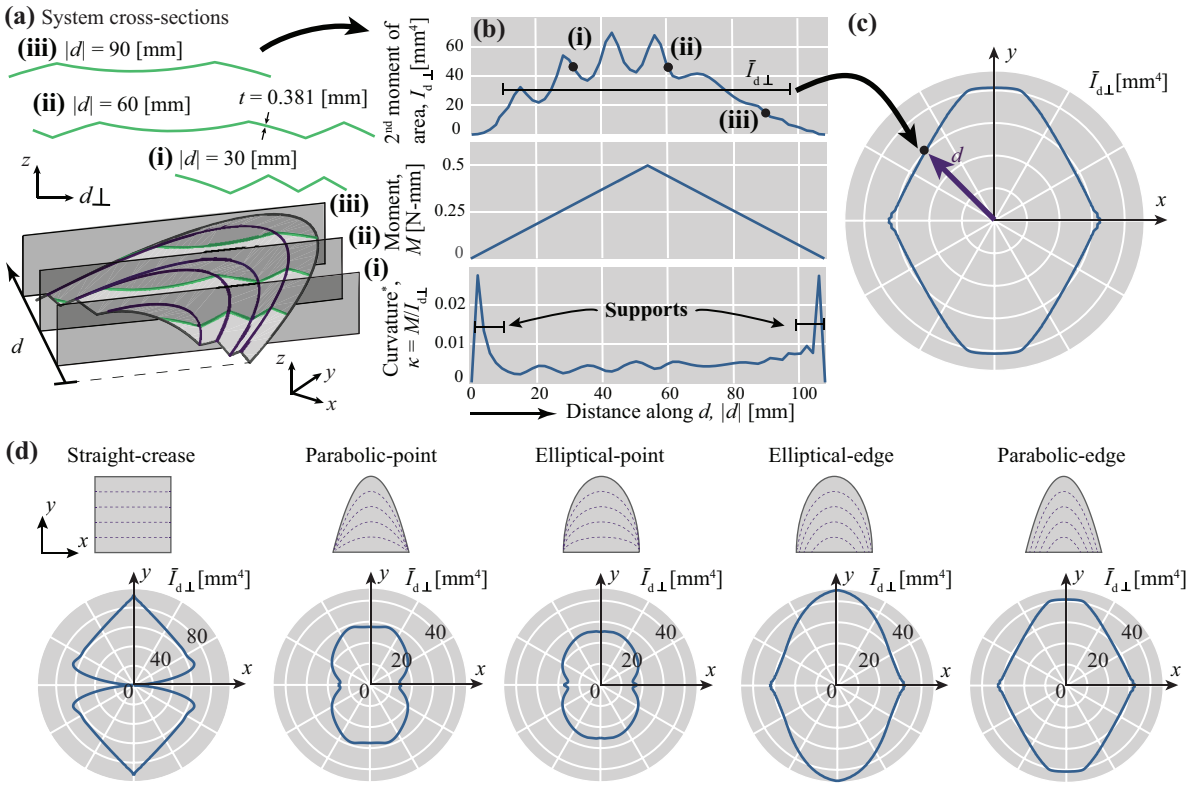

Figure 4.4 – Top-down method for predicting corrugation bending stiffness. **(a)** The cross-section geometries perpendicular to the direction d are obtained for multiple points (for example, (i), (ii), and (iii)) over the span of the folded corrugation. **(b)** The cross-sections are then used to compute the second moment of area $I_{d\perp}$ along the distance of d. If an applied moment from a three-point bending is considered over the entire span, then most of the normalized curvature (*with no elastic modulus) would occur at the ends of the corrugation; thus, I assume the ends are supported. **(c)** The second moment of area is averaged over the central 80% of the span for all directions in the xy-plane and is presented as a radial plot. **(d)** $\bar{I}_{d\perp}$ for all directions in the xy-plane for the five corrugation models.

I will consider as the span direction (Figure 4.4(a)). The cross-section of the corrugation in the perpendicular direction ($d\ \perp$) is then used to compute the second moment of area, $I_{d\perp}$, with a sheet thickness used in the later experimental tests, $t = 0.381$ [mm] (Figure 4.4(b)). The cross-section is divided into segments, the neutral axis is found, and Equation 4.6, together with the parallel axis theorem, are used to find $I_{d\perp}$.

Figure 4.4(b) shows how the second moment of area in the d-direction of the parabolic-edge corrugation varies along the length of the span. Peaks in $I_{d\perp}$ correspond to portions of the corrugation with large and deep cross-sections, while low points correspond to smaller and shallower cross-sections. At the ends of the span, the cross-section size and resulting $I_{d\perp}$ approach zero. This distribution of bending rigidity along the span is similar to conventional tapered beam designs that have a smaller depth where the bending moments are lower. Under three-point bending, the normalized curvature $k = M/I_{d\perp}$ (without an elastic modulus) tends to be low until the ends of the span where $I_{d\perp}$ approaches zero. For a practical application, one can assume that those ends of the corrugations will be supported vertically, and will not experience any moments.

The average of the second moments of area is taken for the central 80% of the span to provide a single quantitative value, $\bar{I}_{d\perp}$, for the corrugation in the given direction, d. This averaged value for second moment of area can then be presented for all directions in the xy-plane as a polar plot where distance from the centroid represents a higher magnitude (Figure 4.4(c)). Polar plots for all five models are shown in Figure 4.4(d). As expected, this procedure shows that the straight-crease pattern has a high rigidity for bending about the y-axis, but a low bending rigidity for bending about the x-axis. About the x-axis, the second moment of area is $\bar{I}_{d\perp} = Wt^3/12 = 0.461$ [mm^4], which implies just bending of the thin sheet. The curved-crease corrugations have higher second moments of area regardless of the direction, and there is never a case where the cross-section is entirely flat in the xy-plane.

4.4.2 Bottom-Up Method

The second procedure for predicting the bending stiffness of a folded corrugation is called the bottom-up method. This procedure involves analyzing the corrugation at discrete points along the length of the mountain creases, calculating a second moment of area for that local area, and averaging the set of values across the entire corrugation.

The bottom-up procedure relies on the discretization of the corrugation such that each mountain crease bar (folding element within the bar-and-hinge model) represents the size of the sheet locally. Figure 4.5(a) shows a representation of the parabolic-edge corrugation. With this crease pattern, there are two mountain creases (shown as a dark line within the corrugation). Figure 4.5(b) shows the corrugation divided into discrete bars extending between points (for example, between p_i and p_{i+1}). Each bar coincides with a vector, $\mathbf{T}_i$, that is roughly tangent to the folded crease at that point. The portion of this vector lying in the xy-plane is inclined an angle, θ_i, from the x-axis. I treat this portion of the tangent vector as the normal vector to a plane in which the z-axis lies. This plane, defined by the coordinates z and $z \times \mathbf{T}_i$ (where "$\times$" is the cross product), defines the surface on which the two-dimensional unit cross-section shown in Figure 4.2(c) lies.

The next step in the bottom-up procedure involves finding the intersection between that plane and the two adjacent valley fold bars. The vectors $\mathbf{S}_i^L$ and $\mathbf{S}_i^R$ originate at the point p_i and extend to those intersection points. The unit cross-section shown in Figure 4.5(c) represents the local cross-section of that crease. Using Equation 4.6, one can calculate the second moment of area of each sheet section, I_i^L or I_i^R, of the local cross-section where $s = s_i^L = |\mathbf{S}_i^L|$ or $s = s_i^R = |\mathbf{S}_i^R|$ and t is the prescribed thickness of the sheet (0.381 [mm]). The dihedral angle, $\phi = \phi_i^L$ or $\phi = \phi_i^R$, is calculated for each sheet section. I sum the second moment of area for each sheet section to get the local second moment of area, I_i^{loc}. Because the length of each local mountain crease bar might vary, I weigh the local second moment of area by the length of the bar, $L_i^f = |\mathbf{T}_i|$, divided by the length of all the mountain crease bars, $\sum_{j=1}^{n_{mf}} L_j^f$, where n_{mf} is the number of mountain fold bars in the bar-and-hinge model. The local second moment of area for the $i^{\mathbf{th}}$ mountain crease bar is

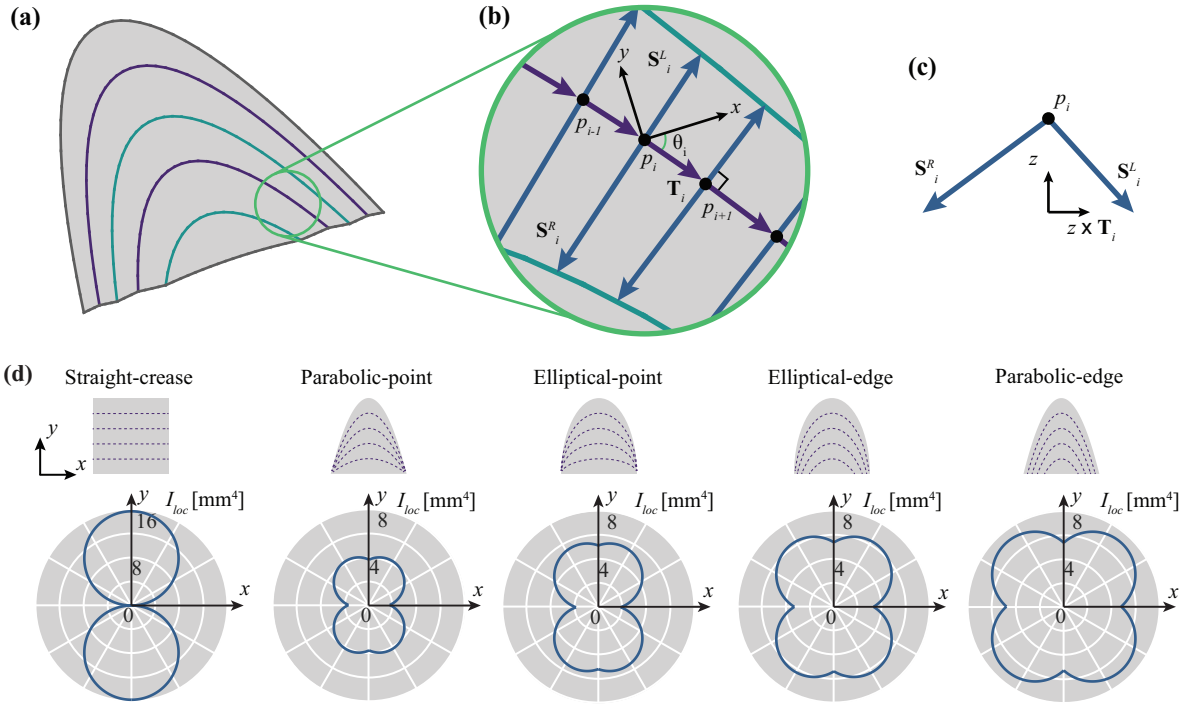

Figure 4.5 – Bottom-up method for predicting corrugation bending stiffness. The process for calculating local second moment of area starts by looking at **(a)** the mountain creases of a folded corrugation. **(b)** For each division of the crease (bars), I find the tangent to the crease, $\mathbf{T}_i$, at the mid-point, p_i, and **(c)** calculate a vector in the tangent plane to the adjacent valley creases, $\mathbf{S}_i^L$ and $\mathbf{S}_i^R$. The resulting vectors are used to generate inclined rectangle cross-sections, and I calculated the local second moment of area of each rectangle. I normalized and averaged these values, I_{loc}, for each model and calculated the projection of each unit cross-section second moment of area onto the x- and y-axes using θ_i. **(d)** I_{loc} is presented for each model folded to the same corrugation depth about all directions in the xy-plane.

computed as

$$I_i^{loc} = \frac{L_i^f}{\sum_{j=1}^{n_{mf}} L_j^f} \left(I_i^R + I_i^L \right). \tag{4.17}$$

This expression represents the ability of the local unit cross-section to resist bending about the $z \times \mathbf{T}_i$ direction. In order to predict the corrugation's ability to resist bending about another direction, one can find the projection of the local second moment of area onto that direction. I calculate the local second moment of area projected onto the x- and y-directions and sum them to find a single value for the corrugation using

$$I_x^{loc} = \sum_{i=1}^{n_{mf}} |I_i^{loc} \sin\theta_i|; \tag{4.18}$$

$$I_y^{loc} = \sum_{i=1}^{n_{mf}} |I_i^{loc} \cos\theta_i|. \tag{4.19}$$

One can then project these values onto any direction, $\mathbf{d} = [\cos\alpha \ \sin\alpha]$, in the xy-plane angled, $\alpha \in [0, \pi/2]$ [rad] from the x-axis using

$$I_{\mathbf{d}}^{loc} = \begin{bmatrix} I_x^{loc} & I_y^{loc} \end{bmatrix} \cdot \mathbf{d} = I_x^{loc} \cos\alpha + I_y^{loc} \sin\alpha. \tag{4.20}$$

I assume that bending about $\mathbf{d}$ is equivalent to bending about $-\mathbf{d}$ and exploit the symmetry of the given models about the y-axis in this formulation.

The local second moment of area is calculated at each point along the length of the mountain creases. Portions of the model are excluded from this summation to account for restrained portions of the structure. I calculated the local second moment of area for each of the five specimen models with boundary conditions similar to those in the physical tests described in Section 4.5. These values are shown in Figure 4.5(d). Notice that the results are similar to those found in the top-down method shown in Figure 4.4(d). Because of the weighing factor and different approach to the methods, the values are different, but the relative magnitudes are similar. Next, I compared these prediction results to the results of experimental tests on physical corrugation specimens.

4.5 Three-Point Bending Tests of Corrugations

In this section, I describe and assess experimental load-deformation tests on corrugations made from polyester film sheets using the crease patterns described in Section 4.3. The experimental tests were designed to assess the stiffness of the corrugations in bending about the x-, xy- (the direction angled $45°$ from the x-axis), and y-axes. I conducted these tests to address two main points. The first purpose was to demonstrate that curved-crease corrugations reduce the difference in stiffness between the weakest bending direction and the strongest, effectively allowing the corrugation to behave more like an isotropic plate than a highly orthotropic structure. The second purpose was to demonstrate that the qualitative framework presented in Section 4.2 used to create the quantitative predictions for stiffness found in Section 4.4 is suitable for predicting the stiffness of the corrugations. The experiments aimed to reduce the complexity of the framework by making all specimens with the same material properties, thickness, corrugation depth, and similar boundary conditions.

4.5.1 Experimental Setup and Procedure

Each of the five corrugation specimens were designed and fabricated using the flat crease patterns described in Section 4.3. The pattern was drafted in a computer-aided design software, and then cut into Graphix Dura-Lar polyester film sheets using a laser cutting machine. I chose this material because of its predictable material properties, its ability to undergo large deformations without permanent damage, and for its ability to hold folded shapes mostly due to plastic damage in the creases after folding. The sheets were 0.381 [mm] (0.015 [in]) thick, and each corrugation was folded by hand such that the final depth, defined as the distance between the highest point along the mountain creases and the lowest point along the valley creases, was approximately 6 [mm] deep. Each of the five crease patterns was cut and folded three times, giving three samples for each corrugation.

The corrugations were loaded using a Mark-10 test stand (ESM1500FG) and force gauge (M5-

50) (see Figure 4.6). The load cell had a resolution of 0.05 [N], which is less than 1% of the maximum load carried by the specimens. Displacement of the specimen was measured by the machine, and the magnitudes were verified using camera recordings. The forces for these tests are low, and deformation within the equipment is negligible compared to the specimen. The folded corrugations were placed on top of two aluminum supports which gave an unsupported span of 50 [mm]. Double-sided tape applied to the top of the aluminum supports held the corrugations in place and limited unfolding early in the loading process. The corrugations were aligned on the aluminum supports using guides that pointed to the center of the specimen. The corrugations were placed in one of three directions: x, xy, or y, which correspond to orientations of the load bar relative to the corrugation coordinate system. The load bar was 10 [mm] wide and made out of an acrylic sheet. The load bar was designed to allow for rotations with minimal friction at the connection to the load transfer box (an acrylic box that connects to the force gauge). The rotations allowed the bar to come into contact with multiple mountain creases on the corrugation without generating a notable axial force at the load cell. At the load transfer box, loosely attached clamps were used to prevent the bar from sliding along the dowel between the two supports.

A displacement-control test was conducted at a rate of 3.0 [mm/min]. Collection of the load data started when a trigger load of 0.10 [N] was measured to ensure that the load bar made full contact with the mountain creases. The load-displacement data was recorded at a sampling rate of three points per second for the duration of the test.

The displacement was carried out for 10 [mm] after the trigger load was measured. During the displacement-control test, I observed four stages of behavior. These stages demarcate the start and end points of where the data was analyzed to calculate the stiffness of the structure (see Figure 4.7). The first stage involves partial contact between the load bar and the mountain creases of the corrugation, and thus, the stiffness is low. Once the load bar has rotated to the point where full contact is made with multiple mountain creases, the stiffness rises. This stage is used to calculate the bending stiffness of the corrugation, k. As loading continues, the bar might come into contact with other parts of the corrugation (Figure 4.7(b)). This ends the stiffness extraction stage

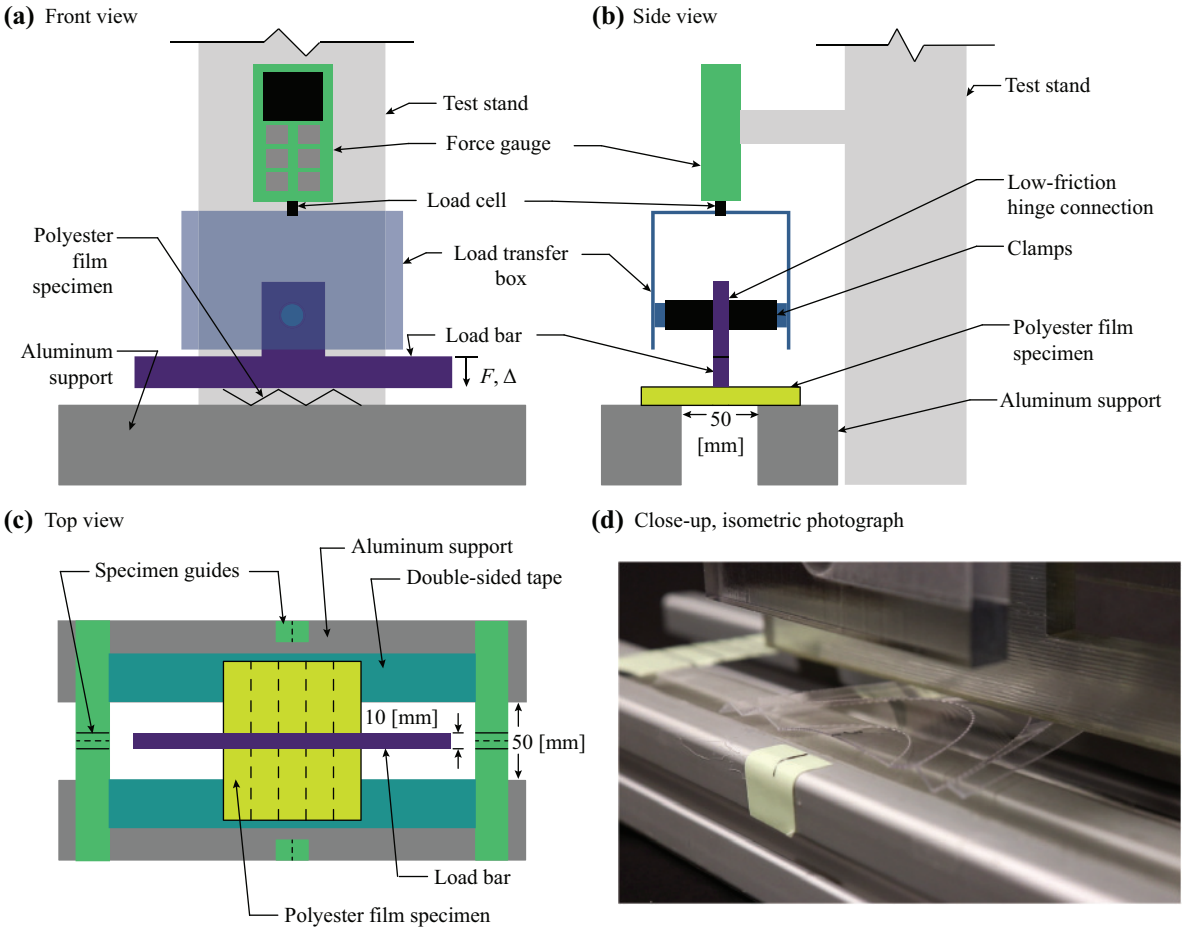

Figure 4.6 – Experimental setup for three-point bending tests of the corrugations. **(a)** Front view illustration detailing flow of forces between support, through polyester film specimen, to the force gauge and test stand. **(b)** Side view illustration showing load bar to load transfer box connection. **(c)** Top view illustration showing load bar on top of specimen resting on aluminum supports with double-sided tape. **(d)** Close-up, isometric photograph showing a specimen beneath the load bar.

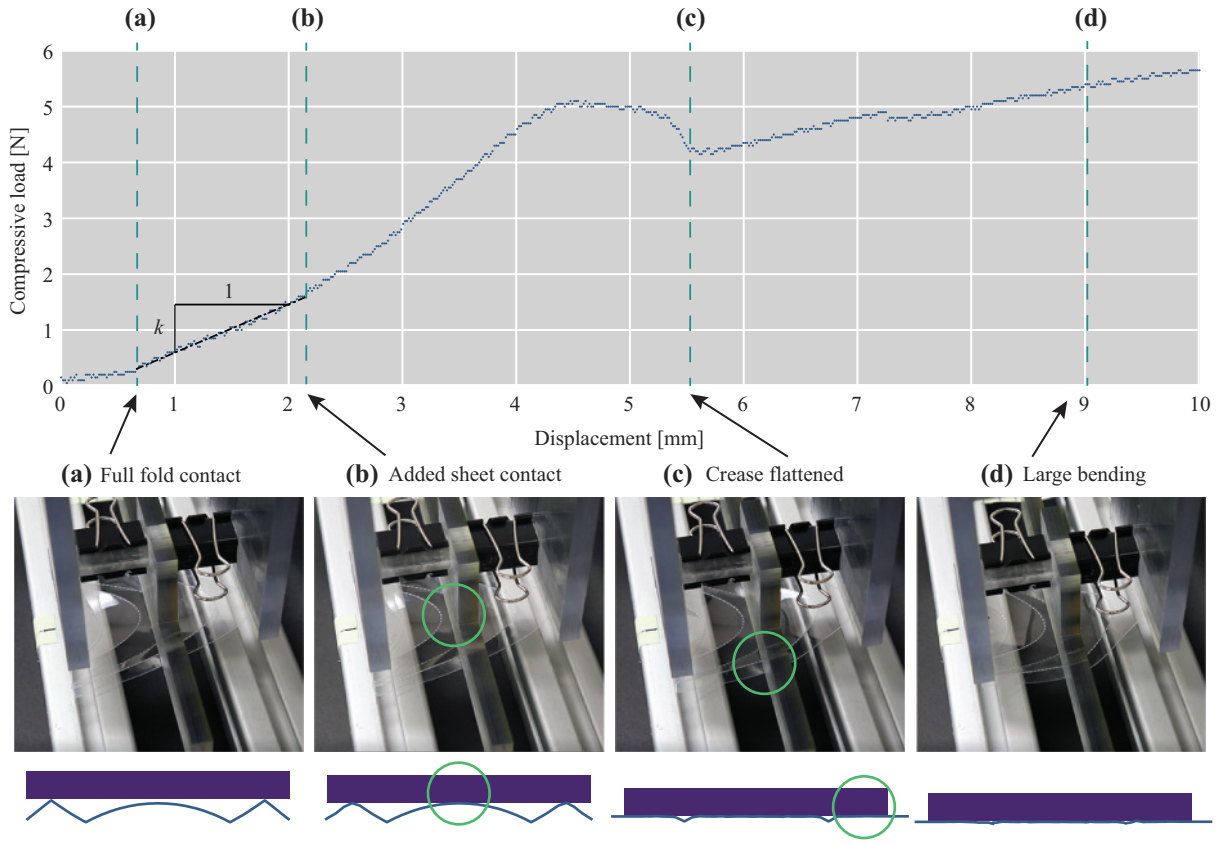

Figure 4.7 – Corrugation bending stiffness extraction. The process of extracting the corrugation stiffness, k, from the raw load-displacement data starts with moving the load bar downward for a total distance of 10 [mm]. Initially, the load bar only has partial contact with the mountain creases. **(a)** Once the load bar has full contact with the mountain creases, regression analysis gives the slope of the data (that is, the stiffness). **(b)** As the specimen continues to deform, additional parts of the sheet come into contact with the load bar. **(c)** Stiffness becomes negative once the first crease flattens and **(d)** loading continues with large bending deformations.

and starts a period of increased stiffness due to greater participation of the material in resisting loads. This stage continues until one of the mountain creases flattens, resulting in a loss of stiffness (Figure 4.7(c)). The last stage involves large bending deformations with low stiffness due to the corrugation progressively becoming flatter (Figure 4.7(d)).

In the second stage, the load-deformation data is more-or-less homoscedastic (that is, the data surround a linear trend line with small variance). Using linear regression, the slope of the trend line can be calculated which represents the stiffness of the corrugation in the downward direction. Because the ratio of the depth of the corrugation to the unsupported span is about 12%, one can assume that the corrugation is slender and that the deformation in this stage is mostly due to bending about the direction parallel to the load bar. The stiffness extraction process was repeated

for each of the three samples of the five corrugations in the x-, y-, and xy-directions, resulting in a total of 45 tests and analyses. The R^2 value of each analysis was always greater than 0.95 with most analyses exceeding 0.98, which suggests that the data closely fit with the linear model. I found the average of the slopes of the trend lines (that is, the average of the stiffness values) from the three samples in one load direction for each corrugation, which I call the stiffness of the structure, k. Load-displacement results from the experimental tests that were used to find the stiffness values are shown in Figure 4.8.

4.5.2 Experimental Results and Discussion

The five corrugation geometries in Figures 4.4, 4.5, 4.8, and 4.9 are ordered based on the ratio of the stiffness in bending about the x-direction, k_x, to the stiffness in bending about the y-direction, k_y, for the average values from the experimental data. This ratio, k_x/k_y, is one way of describing the corrugation's ability to resist bending in multiple directions. The closer the ratio is to 1, the more isotropically the corrugation behaves. As predicted, the experimental results show that the ratio for the straight-crease specimen is the lowest, $k_x/k_y = 3.74\%$. For the parabolic-point specimen, the ratio is, $k_x/k_y = 56.1\%$. For the elliptical-point specimen, $k_x/k_y = 58.0\%$. For the elliptical-edge specimen, $k_x/k_y = 70.5\%$. The parabolic-edge specimen had the largest ratio, $k_x/k_y = 93.4\%$.

Figure 4.8 shows the load-displacement results for each model in each of the three loading directions, where a single direction trend (for example, x) is obtained from averaging the slope of the three sample experiment regressions. The trend lines show the isotropy visually where with the straight-crease model (Figure 4.8(a)), the average stiffness trends are separated, but with the parabolic-edge model (Figure 4.8(e)), the lines coincide. The representation in Figure 4.9(c) offers greater insight into the results as it shows the magnitude of the stiffness relative to the other specimens. Notice that although the parabolic-edge specimen shares similar stiffness in bending about the x-, xy-, and y-directions, the magnitude of the stiffness is less than the maximum magnitude of the straight-crease model. Thus, I say that curved creases "redistribute" stiffness to emphasize the trade-off made when the corrugation's directionality is no longer uniform. In cases where the

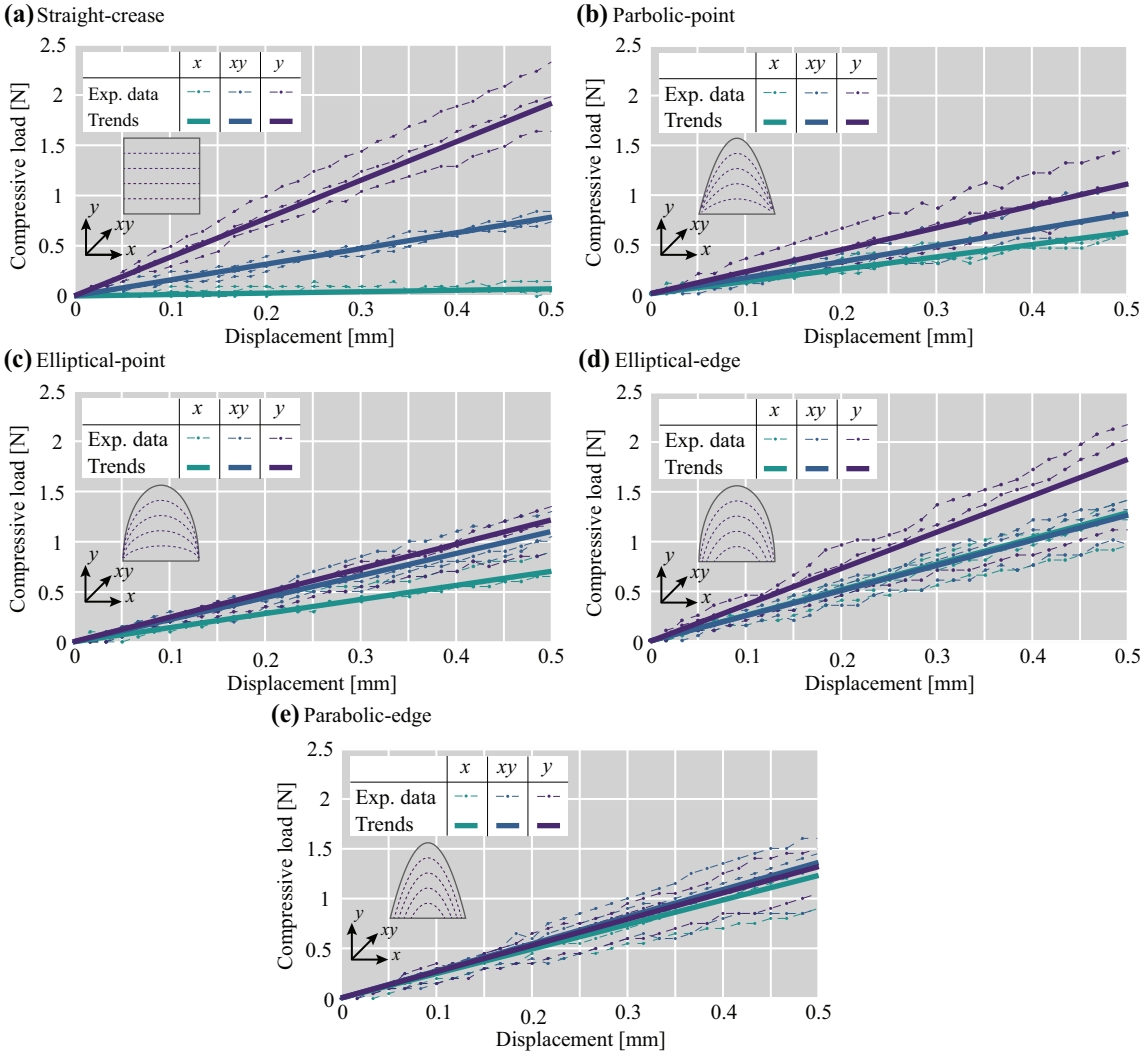

Figure 4.8 – Load-deformation response of five corrugations from experimental testing. Regression analysis on each test is used to calculate the slope (i.e., the stiffness), and the average slope is presented as the trend line. **(a)** The straight-crease model displays the greatest difference between direction stiffness. **(b)** The difference significantly narrows with the parabolic-point model and continues with the **(c)** elliptical-point model and **(d)** elliptical-edge model. **(e)** The load-deformation response of the parabolic-edge model shows the most consistent stiffness in all directions (as predicted).

corrugation must have a similar bending stiffness in all directions without adding additional members or stiffeners to the structure, curved creases may offer a solution, at the cost of reducing the maximum bending stiffness.

Between the four curved-crease corrugation specimens, the results differ. Namely, the specimens whose flat crease patterns come to a point at the corner give lower stiffness values than the crease patterns that meet at the edge. The point models behave similarly to the straight-crease model in that stiffness in bending about the x-direction is lowest, followed by bending about the xy-direction, with bending about the y-direction being the stiffest. This pattern between direction stiffness is not maintained for the edge specimens.

4.5.3 Comparison With Theoretical Predictions

Next, I compare the bending stiffness predictions made in Section 4.4 to the experimental results. The values of the top-down procedure (Section 4.4.1) take an average of the second moment of area, $\bar{I}_{d\perp}$, over the length of the system while the bottom-up procedure (Section 4.4.2) averages the local second moments of area, I_{loc}. Thus, these approximate predictions do not directly correspond to the experimental, load-deformation stiffness, k, which is computed as a representative value for the bending rigidity of the structure. Like with a tapered beam, this bending stiffness of the corrugations does not directly relate to the average second moment of area of the cross-sections. With this in mind, one can compare the predicted bending stiffness to the experimental results by looking at the magnitudes of the measured values (either $\bar{I}_{d\perp}$, I_{loc}, or k) relative to the other bending directions or the other geometries (see Figure 4.9).

In general, the predictions made by both the bottom-up and top-down procedures predicted the general stiffness relationships well. For the parabolic-point and elliptical-point models, the magnitude of $\bar{I}_{d\perp}$ (Figure 4.9(a)) relative to the three bending directions matches the relative magnitude of the average stiffness found in experimental testing (Figure 4.9(c)). The relative pattern is also found from the magnitude of I_{loc} (Figure 4.9(b)). For the elliptical-edge model, the top-down procedure gave a more accurate prediction of the experimental results when looking at the relative

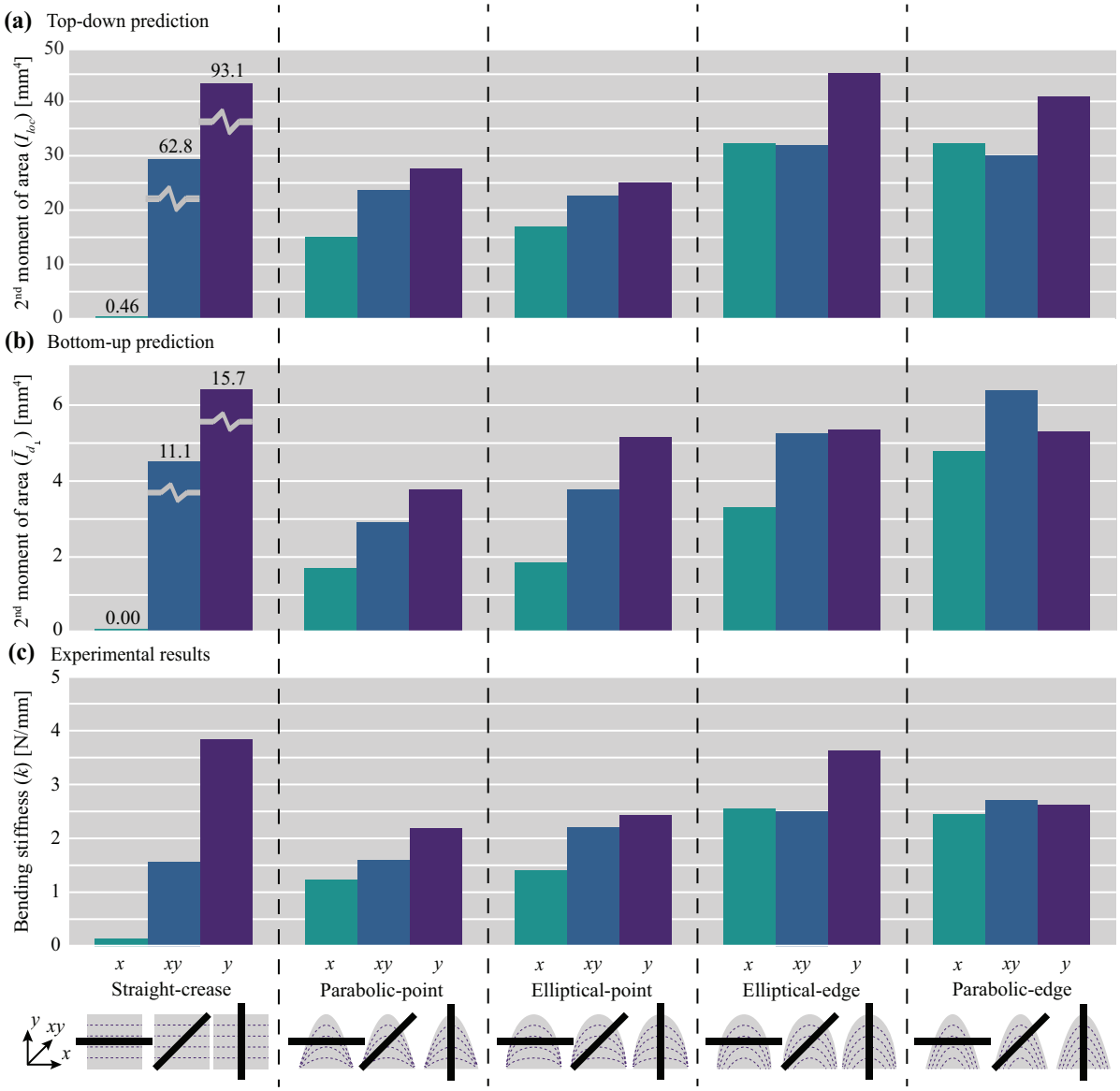

Figure 4.9 – Corrugation bending stiffness results. A comparison between the theoretical bending stiffness predictions and the experimental results in the x-, xy-, and y-directions for each of the five models. The prediction methods, **(a)** top-down and **(b)** bottom-up, use different averages for the second moments of area about directions in the xy-plane as a proxy for bending stiffness. The shapes of the bars in **(c)** the experimental results corresponds to the shapes of the bars in the prediction results, suggesting that second moment of area is proportional to the bending stiffness, with errors stemming from the limitations of each prediction method.

magnitudes of $\bar{I}_{d\perp}$ in all three directions. The bottom-up procedure overestimated the corrugation's ability to resist bending about the xy-direction. For the parabolic-edge model, the bottom-up procedure for calculating I_{loc} gave a better prediction of the relative bending stiffness than the top-down procedure did. However, the bottom-up procedure did overestimate the bending stiffness about the xy-direction.

For both the bottom-up and top-down procedures for predicting bending stiffness of the straight-crease corrugation, the stiffness in the xy- and y-directions was overestimated compared to the values measured in experimental testing. This overestimation is likely due to the inability of the prediction procedures to incorporate unfolding of the corrugation upon loading. The predictions rest on the assumption that the corrugation will not unfold when loading starts. However, as observed during loading, the models do unfold as the load bar makes contact with the mountain nodes. With curved-crease corrugations, this effect is less pronounced due to greater crease restriction from other creases surrounding the single crease section, and thus those predictions appear to be better. This discrepancy illustrates the importance of considering all aspects of the qualitative framework, including the properties that cannot be captured from the folded geometry alone (that is, fold restriction and geometric characteristics that reduce unfolding).

Additionally, either method for predicting the bending stiffness of a corrugation from the folded geometry presupposes that the predominant deformation is bending. Although bending plays an essential role in the deformation, torsion within the folded corrugation also contributes to deformations. Both $\bar{I}_{d\perp}$ and I_{loc} fail to capture the ability of the crease to deform in torsion about the crease direction. This issue, along with the inability to approximate the unfolding behavior, results in these second moment of area estimates to consistently overestimate the actual stiffness of the structure by factors of three to four. For clarity, I do not present these quantitative comparisons here.

Despite these limitations, the methods for predicting bending behavior of a corrugation, either including the full qualitative framework or just the geometric elements, offers a simpler solution than either experimental testing or finite element modeling. The benefits of the top-down and

bottom-up procedures start with the benefits of using a simple bar-and-hinge model to estimate the folded shape. The bar-and-hinge model can fold corrugations quicker than with a finite element model and is more likely to converge to the desired fold shape. Although the predictions for bending stiffness do not offer an exact mapping to the experimental performance, they offer key insights into the behavior of the corrugation relative to other crease patterns with a simple values (such as I_{loc}). In cases where a pattern must be chosen to accomplish some goal (for instance, having a similar bending stiffness in all directions in the xy-plane), designs can be compared quickly as prototypes. The final design can be modeled with greater fidelity in a finite elements program to better account for torsional and fold restriction effects.

4.6 Conclusions

In this chapter, I introduced and explored corrugations with curved creases which are unique because they have a high bending stiffness in multiple directions. I then presented a theoretical framework and two predictive methods that use the geometry of a corrugation to qualitatively estimate its stiffness characteristics. Experimental data verified the multi-directional bending stiffness of corrugations, and confirmed the validity of the predictive methods.

I offered a theoretical, qualitative framework for relating the bending stiffness of a corrugation to its geometric properties at four scales: (1) sheet sections, (2) unit cross-sections, (3) single creased sheets, and (4) the corrugation system. The framework suggests that the depth of creases, the ability of the system to resist flattening, the curvature and orientation of curved creases, and the different variety of crease geometries in a corrugation are all important characteristics influencing the stiffness. This framework allows a designer to make a rough estimate of the bending stiffness and identify issues with a corrugation by looking at the folded geometry.

I also offered two methods to predict the bending stiffness of a corrugation by analyzing the geometry that is simulated by a bar-and-hinge model. Both methods make an approximation of the second moment of area within the corrugation geometry. The top-down method approaches the problem globally by looking at the entire cross-section at different points along the span of

the corrugation. The bottom-up method looks locally at the orientation of crease segments and evaluates their contribution for different directions of bending.

I analyzed five example corrugations, where one was a straight-crease pattern and four had different curved-crease designs. The two predictive methods gave similar results to each other, and identified differences between the corrugation designs. I then validated the theoretical framework and predictive model using experimental three-point bending tests on polyester film specimens of the example corrugation. I found that the theoretical frameworks effectively estimated the relative magnitude of the bending stiffness for each model in the x-, xy-, and y-directions. There were small deviations attributed to the fact that the quantitative framework cannot capture certain features of the corrugation, such as fold stiffness and boundary restraints on the structure. Each method showed that traditional, v-shaped corrugations made with straight creases have stiffness anisotropy, while the curved-crease corrugations are stiff in multiple directions. Additionally, patterns where curved creases intersected one edge gave higher bending stiffness than patterns where creases coincide at the corners.

This work is a starting point for future research on the conception, analysis, or design of curved-crease corrugations with novel mechanical properties. The proposed framework can predict corrugation stiffness, but could be further improved to include the influence of boundary conditions and flattening of the creases during loading. The multi-directional stiffness of the curved-crease corrugations can be reasonably explained by the diverse directionality of creases; however, it would be worthwhile for future work to explain exactly how these corrugations resist bending and torsional deformations. Insight to the stress distribution and load paths within the corrugation can give a more elegant explanation to the local mechanics responsible for the unique multi-directional stiffness. Additionally, further investigation into the influence of the Poisson's effect within the corrugation would improve the accuracy of these findings for a more thorough mechanical treatment of curved-crease corrugations.

The corrugation geometries that I have presented in this work were developed through trial and error, and were refined based on my geometric framework in Section 4.2. However, many varia-

tions are possible with curved-crease geometries, and it would be helpful to systematically explore these through parametric studies (for example, number of creases, curvatures, spacings, etc.). These studies could be further extended to perform optimization of the stiffness, anisotropy, or shape of the pattern. Additionally, understanding the predominant stiffness of nonplanar-midsurface corrugations could begin by using the insights found in my investigation of planar-midsurface corrugations with the addition of predicting the torsional and shear stiffness. Finally, future work is needed to explore practical applications of the curved-crease corrugations in both conventional applications such as stiff decking or in emerging applications such as morphing or multi-functional structures. This chapter sets an important starting point for analyzing general corrugations, including curved-crease corrugations, by offering qualitative and quantitative methods for analyzing the structures relative to other designs. I hope that further research into the topic will expand the scope of our knowledge and allow for a complete understanding of the bending behavior, including a theoretically or empirically verified mapping between the average second moments of area and the bending stiffness.

My methods for describing the bending stiffness of corrugations offers a way for engineers to design for isotropy of bending stiffness by visually analyzing the folded pattern and running quick folding simulations using a simple bar-and-hinge model. This process does not require complex finite element simulations, which from my experience, can be difficult to carry out for curved-crease folding patterns. These new methods have the possibility of connecting the form of curved-crease origami to its function in a variety of applications that require continuous, lightweight sheets as structural members.

Chapter 5

Pinching of Curved Creases for Bending and Twisting Shape Morphing

In this chapter, I introduce a unique behavior seen in creased sheets where localized changes in the folding (i.e., a pinch) result in global bending and twisting deformations. Using isometric deformation theory, I identify the connections between pinching, crease curvature, and crease torsion that begin to explain the shape-morphing behavior. Given the limitations of isometric deformations, the bar-and-hinge model is used to model folding and pinching (see Chapter 3), where the sheet is allowed to stretch. With this tool, I found that the increase in crease curvature and torsion due to pinching are proportional to the curvature of the crease before folding and that curved creases facilitate the bending and twisting.

Additionally, I explored the bending and twisting of sheets with more than one crease. I found that sheets with an even number of creases generate more intense twisting than those with an odd number of creases and experience twisting even when the creases are straight. The number of creases had little effect on the pinch-induced bending of the origami. The stiffness of the sheets had little effect on the amount of bending and twisting, but greater spacing between the creases resulted in more bending with little effect on the twisting.

Based on these results, I created a framework to design crease patterns to have desirable bending and twisting that can be coupled or not, and demonstrated this programmability with simulations and by pinching physical prototypes. My findings enable shape morphing of creased sheets with a low-complexity input and a versatile output. These curved-crease sheets are capable of significant shape-morphing that include bending and twisting using a single pinch. This deformation is fully reversible, can be prescribed using intuitive crease pattern design, and results in a decoupled, bimodal response with tunable deformation magnitude and sign.

In this chapter, I start by motivating the problem and providing background information on shape-morphing thin sheets (Section 5.1). Then, I introduce the geometric features of curved-crease sheets and isometric theory that form a basis for thinking about how pinching causes deformations (Section 5.2). With key limitations to isometric theory, I supplement our understanding with a mechanics-based numerical model that allows stretching, and with geometries specifically chosen to help explain the bending and twisting of these structures (Section 5.3). In Section 5.4, I investigate the effect that pinching has on the curvature and torsion of a crease that results in global bending and twisting of the structure. I also explore the parameters of origami with more than one crease and how those features affect global twisting and bending. I conclude with a framework for generating tunable bending and twisting, show example crease patterns with desirable behaviors, and present conceptual applications for these shape-morphing systems (Section 5.5). [1]

5.1 Introduction

Shape-morphing is the ability to change orientation or geometry in order to alter the intrinsic properties of the system for some functional advantage. Morphing from one configuration to another is achieved using kinematic rotations and translations, mechanical deformations, or a combination of the three. Shape morphing is a foundational property of emerging smart and adaptable structures that use sensors to detect the environment then adapt to that state using actuation. Shape-morphing systems can be found in nature (Wang et al., 2018; Rivera-Tarazona et al., 2020) and in a variety of engineering fields, including biomedical engineering (Holmes et al., 2011; Kirillova and Ionov, 2019; Agarwal et al., 2021), aerospace engineering (Concilio and Ameduri, 2020; Gu et al., 2020), resilient and sustainable infrastructure (Fiorito et al., 2016; Ding and Kareem, 2020; Asfaw and Ozbulut, 2021), metamaterials (Sakovsky and Ermanni, 2020; Wenz et al., 2021), and soft robotics (Hu et al., 2018; Liu et al., 2021; Kim et al., 2021; Shah et al., 2021).

Implementation of shape-morphing systems in technology faces significant challenges. For instance, shape-morphing often requires expensive materials (e.g., shape-memory alloys or shape-

[1] This chapter contains research published in Woodruff and Filipov (2022)

memory polymers) and distributed actuation. Thus, using few and simple actuators is preferred to reduce cost and simplify fabrication (Anumodh et al., 2021). Furthermore, when multiple actuators or distributed actuation are used, controlling the shape of the system becomes increasingly complex. And many existing shape-morphing materials and structures can deform in only one way, limiting the range of shapes the system can attain. Additionally, the parameters determining the final deformed shape can be highly coupled and lead to difficult design frameworks.

Concepts from origami (i.e., folding of thin sheets) and kirigami (i.e., cutting of thin sheets) have inspired novel shape-morphing systems. The advantages of these approaches include simple manufacturing (design and fabrication can start from a flat state), scale independence, and achievable large deformations without permanent damage. Examples of shape-morphing origami and kirigami include adaptable grippers for robotics (Yang et al., 2021), dynamic façades, locomotive robots inspired by pelican eels (Kim et al., 2019), and resilient drones inspired by dragonfly wings (Mintchev et al., 2018). However, many origami- and kirigami-inspired systems are limited by the disadvantages experienced by existing shape-morphing systems explained above (such as requiring multiple actuators), and these structures are also sensitive to imperfections (Liu et al., 2020).

Beyond the traditional straight-crease origami, curved-crease origami allows folding of thin sheets about arbitrary curves (Demaine et al., 2015). With curved-crease origami, the sheets between creases always bend upon folding, combining kinematics with deformation mechanics (Dias and Santangelo, 2012). Designs with curved creases have allowed for unique, tunable stiffness properties (Zhai et al., 2020; Woodruff and Filipov, 2020b) and bistable behaviors (Bende et al., 2015), showing potential for shape morphing using these systems. In this chapter, I explore the effect of pinching on curved-crease sheets, where intense folding is applied to a small portion of the crease using a local actuation. Figure 5.1 shows a creased, circular annulus sector that is folded from polyester sheets (brand name Dura-Lar). When a single pinch is applied at the middle of the structure, it experiences large bending deformation in-plane (i.e., in the xy-plane). Furthermore, one may see that the same pinch results in visibly large twisting deformations and a large

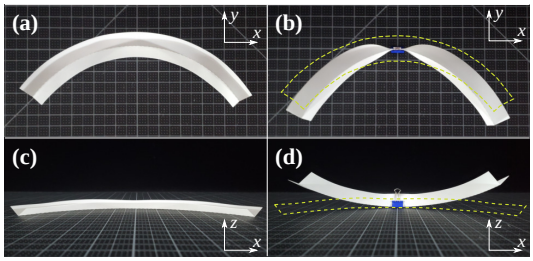

Figure 5.1 – The effects of pinching on a curved-crease polyester sheet. **(a)** A creased annulus sector is folded and has some curvature. **(b)** When pinched at the middle, the structure bends with greater curvature (the unpinched reference shape is shown with dashed lines). **(c)** When unpinched, this creased sheet lies flat on the surface and exhibits no twisting. **(d)** When pinched, the ends of the structure lift, demonstrating a global twisting.

displacement out-of-plane (in the z-direction).

5.2 Theory

5.2.1 Geometry of Curved-Crease Sheets

In order to understand the relationship between the crease pattern and the effects of pinching, I start by identifying the relevant features of the geometry. An origami structure can be thought of as a set of creases connected by sheets in three dimensions. The crease can be reduced to a parametric space curve in Cartesian coordinates, $\mathbf{c} = \{x(u)\ y(u)\ z(u)\}$, where u is the parameter indicating position along the curve (see Figure 5.2). In this chapter, I consider only curves that are at least three-times continuously differentiable, and I do not consider creases that intersect within the sheet.

The crease, represented as a space curve, will have two important properties that describe its shape. The first is the *curvature* of the crease, κ. Curvature measures the degree to which the crease bends away from its tangent, locally, and can be calculated as,

$$\kappa = \frac{|\mathbf{c}' \times \mathbf{c}''|}{|\mathbf{c}'|^3}, \tag{5.1}$$

where ($'$) and ($''$) indicate first and second differentiation with respect to, u, respectively, and ($|\ |$) is the l^2 norm of the vector inside the lines (Kreyszig, 1991).

The second property of the crease I am interested in is its *torsion*, τ. Torsion measures the

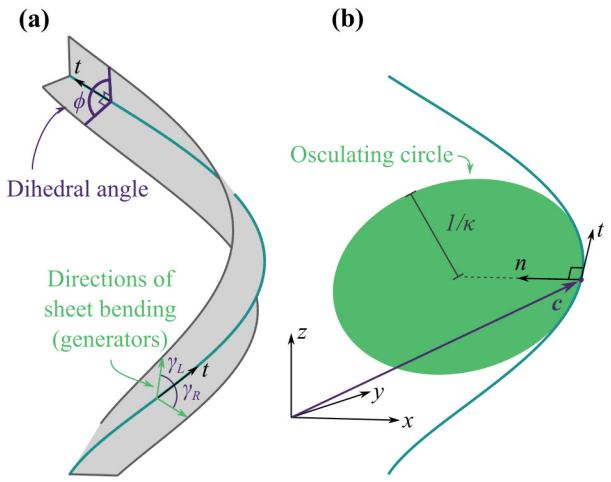

Figure 5.2 – Origami can be represented with surfaces connected to a space curve. **(a)** The deformed shape of creased sheets can be described using the dihedral angle, ϕ, and the generator angles showing the orientation of local sheet bending, γ_L and γ_R. **(b)** With the crease as a space curve, $\mathbf{c}$, one can determine the curvature of the crease as the reciprocal of the radius of the osculating circle and the torsion as the rate at which the osculating plane, $\mathbf{tn}$-plane (or the normal vector, $\mathbf{n}$), twists about the tangent, $\mathbf{t}$ (defined at each point along the crease).

degree to which the crease turns away from its osculating plane (see $\mathbf{tn}$-plane in Figure 5.2(b)), locally, and can be calculated as,

$$\tau = \frac{(\mathbf{c}' \times \mathbf{c}'') \cdot \mathbf{c}'''}{|\mathbf{c}' \times \mathbf{c}''|^2}. \tag{5.2}$$

Here, $(\times)$ indicates the cross product, $(\cdot)$ is the dot product of the vectors, and $(''')$ indicates the third derivative with respect to u (Kreyszig, 1991).

The curvature and torsion describe the local shape of the crease and give insight to the global shape of the structure. I will use these equations to calculate the curvature and torsion of the creases before and after pinching. Because I will use a discrete numerical model (Section 5.3.1), I estimated the derivatives using a finite-difference calculation that provides a reasonably high-accuracy estimation (errors are of order $O(\Delta u^4)$).

Another important geometric feature of origami structures is the *dihedral angle* of the crease, ϕ. The dihedral angle describes the angle between the sheets extending perpendicular from the crease tangent (see Figure 5.2(a)), defined at each point along the crease. To prevent the sheets from intersecting upon folding, the dihedral angle is limited to the domain, $0 \leq \phi \leq 2\pi$ [rad].

Figure 5.3(a) shows examples of the dihedral angle in this domain and Figure 5.2(a) shows the dihedral angle on a folded sheet. In this paper, all creases with $\phi \in [0, \pi)$ [rad] are mountain creases (indicated with a lighter, blue color) and creases with $\phi \in (\pi, 2\pi]$ [rad] are valley creases (indicated with a darker, purple color). Notice that when $\phi = \pi$ [rad], the sheet is flat.

The first derivative of the dihedral angle with respect to the crease parameter, u, is called the *fold rate*, ϕ'. When the crease is pinched, $\phi' \neq 0$. I use the fold rate to quantify the pinch, and this quantity will be useful in predicting the torsion generated in a crease after pinching.

5.2.2 Isometric Theory of Curved-Crease Origami

The properties given in Section 5.2.1 describe the geometry of the crease at a specific state or configuration. In order to map between different configurations of the crease geometry or deformation states, one can assume that deformations of the origami exist only as bending of the sheets and crease. This is called the *isometric deformation* assumption. Under this assumption, there is no stretching in the sheet or the crease. This is a reasonable assumption given that the in-plane stiffness of the sheet is of order $O\left(t/l\right)$, the bending stiffness of the sheet is of order $O([t/l]^3)$, and that $t/l << 1$, where t is the thickness of the sheet and l is the characteristic length (Pini et al., 2016). In summary, bending usually requires less energy than stretching, so the system will tend to bend and follow isometric deformations.

From the isometric deformation assumption, one can derive several relationships between the geometry of the crease before folding and after pinching. These equations help us predict the behavior of origami after pinching and set a theoretical basis for why curved-crease origami twist and bend when pinched.

The first relationship I consider describes how the curvature of a crease changes as it is folded. This curvature-folding relation is,

$$\kappa = \frac{\kappa_0}{\sin(\phi/2)}, \tag{5.3}$$

where, κ is the curvature of the crease after folding (see Figure 5.2(b)) and κ_0 is the curvature before folding (when $\phi = \pi$ [rad]) (Duncan and Duncan, 1982; Fuchs and Tabachnikov, 1999;

Lang et al., 2017). This equation is plotted as a solid line in Figure 5.3(a) for a crease with $\kappa_0 = 0.005$ [mm^{-1}]. This relationship shows that as the crease is folded from a flat state, the curvature of the crease will increase as long as $\kappa_0 > 0$ (according to isometric deformation theory).

The second relationship I consider describes the torsion of the crease as it is folded. This relationship can be described with,

$$\tau = \frac{1}{2}\kappa_0 \cot\frac{\phi}{2}\left(\cot\gamma_L + \cot\gamma_R\right), \tag{5.4}$$

where, γ_L and γ_R are the generator angles on the left and right sides of the crease, respectively (see Figure 5.2(a)) (Lang et al., 2017). The generator angles describe the orientation of bending in the sheets adjacent to the crease and are defined as the angle between the crease tangent, $\mathtt{t}$, and the flat ruling on the surface (i.e., a line segment extending from the crease across the sheet, which exists for all developable surfaces with non-zero mean curvature). The generator angles are limited to the open interval, $(0, \pi)$ [rad]. The direction of bending in the sheet will align with the direction of the generator. Note that when $\gamma_L + \gamma_R = \pi$ [rad], torsion vanishes.

The third relationship is similar to the last, but describes the fold rate of the crease as it is folded. This relationship is,

$$\phi' = -s\kappa_0 \cot\frac{\phi}{2}\left(\cot\gamma_L - \cot\gamma_R\right), \tag{5.5}$$

where $s = |\mathbf{c}'|$ is the speed of the curve (Lang et al., 2017). Again, the fold rate depends on the bending of the sheets adjacent to the crease. Note that when $\gamma_L = \gamma_R$, the fold rate vanishes.

Combining Equations 5.4 and 5.5, a relationship between the crease torsion and the fold rate appears. Namely,

$$\tau = -\phi'\left(\frac{\cot\gamma_L + \cot\gamma_R}{2s\left[\cot\gamma_L - \cot\gamma_R\right]}\right). \tag{5.6}$$

Notice that torsion can only occur when the fold rate is nonzero. A pinched crease will have a nonzero fold rate; thus, non-zero torsion can occur in pinched structures.

It is difficult to predict what the generator angles will be after folding because the local bending of the sheets depends on the adjacent creases, the forces applied to the sheets, and the restraints on the structure. Because Equation 5.6 depends on the generator angles, one cannot be certain that pinching will generate torsion or to what degree. Currently, there is no explicit relationship linking the generator angles to the boundary conditions and crease pattern. However, one can implicitly determine the deformed shape of the origami sheets using an energy minimization scheme (Badger et al., 2019). Alternatively, a mechanics-based analysis can be used to determine the deformed shape of the origami, as I describe in Section 5.3.1. Using this method, one can better understand exactly how torsion is related to the curvature of the creases, the dihedral angle, and the fold rate.

For now, I know that crease torsion can only exist when: (1) the flat crease is curved ($\kappa_0 \neq 0$), (2) the crease is folded away from a flat state ($\phi \neq \pi$ [rad]), and (3) the crease is allowed to diverge from its originally flat plane (there can be no boundary conditions preventing twisting). Curvature will always exist for an initially curved crease.

5.2.3 Limitations of Isometric Theory

From Equation 5.3, isometric deformation theory tells us that as a curved crease approaches complete folding ($\phi \to 0$ or $\phi \to 2\pi$ [rad]), the curvature of that crease will approach infinity. Intuitively, this seems incorrect. Indeed, when a paper prototype of a curved-crease origami is folded completely, the sheets appears to flatten out, rather than curve infinitely. This flattening suggests that the isometric deformation assumption fails to describe the deformed shape of real origami structures, where stretching is possible, at least for some domain of dihedral angles. And pinching does result in near-complete folding of a crease. Thus, to examine how pinching affects the shape of origami structures, the limitations of the isometric deformation assumption must be considered and a more versatile means of determining the deformations of curved-crease origami must be implemented.

An alternative to isometric theory is to perform a mechanics-based analysis on an origami structure. I use a numerical model to simulate the folding and pinching of origami, which is described

in Section 5.3.1. This numerical model calculates the equilibrium state of the origami structure in response to forces and/or moments that generate folding. The model includes bending, folding, and stretching deformations, allowing for possible in-plane deformations ignored in isometric theory. The numerical model uses elastic elements with a nonlinear geometric response. I use this numerical model to explore the performance of the isometric deformations assumption under different degrees of folding.

Figure 5.3(a) shows the normalized curvature, κ/κ_0, of a crease with $\kappa_0 = 0.005$ [mm^{-1}] after folding with the corresponding dihedral angle, ϕ. The origami used in Figure 5.3 is a circular annulus sector that is creased along its mid-radius to a dihedral angle, ϕ, which is held constant along the crease length (see Figure 5.3(d)(i)). Notice that the curvature ratio aligns with the isometric theory for moderately folded dihedral angles ($\pi/3 \leq \phi \leq 5\pi/3$ [rad]). However, for more complete folds, the numerical model starts to diverge from the isometric theory.

Figure 5.3(b) shows the normalized curvature, but for dihedral angles close to complete folding ($0 \leq \phi \leq \pi/10$ [rad]). Notice that as the dihedral angle approaches zero, the curvature of the numerical model is significantly less than what isometric theory predicts. After $\pi/50$ [rad], the curvature of the model starts to decrease, and the crease flattens when completely folded (see Figure 5.3(d)). I changed the stretching stiffness in the mechanics-based model by a factor of c_s to see how the crease curvatures changed, and saw that the stiffer models ($c_s = 1.5$) would curve more than the models with less stiffness ($c_s = 0.5$), but all mechanics-based models eventually flattened to zero curvature.

When determining the shape of origami after folding using a mechanics-based model and allowing the sheets to stretch, approaching complete folding of curved-crease origami results in flattening, rather than infinite curvature. Because the origami flattens as it is completely folded, and the normalized curvature is related to the stretching stiffness of the model, this indicates that stretching is important for the sheets in highly folded configurations. Indeed, Figure 5.3(c) shows that as the dihedral angle approaches zero, the bending strain energy decreases and stretching strain energy increases. Effectively, stretching and flattening the sheet becomes more energetically effi-

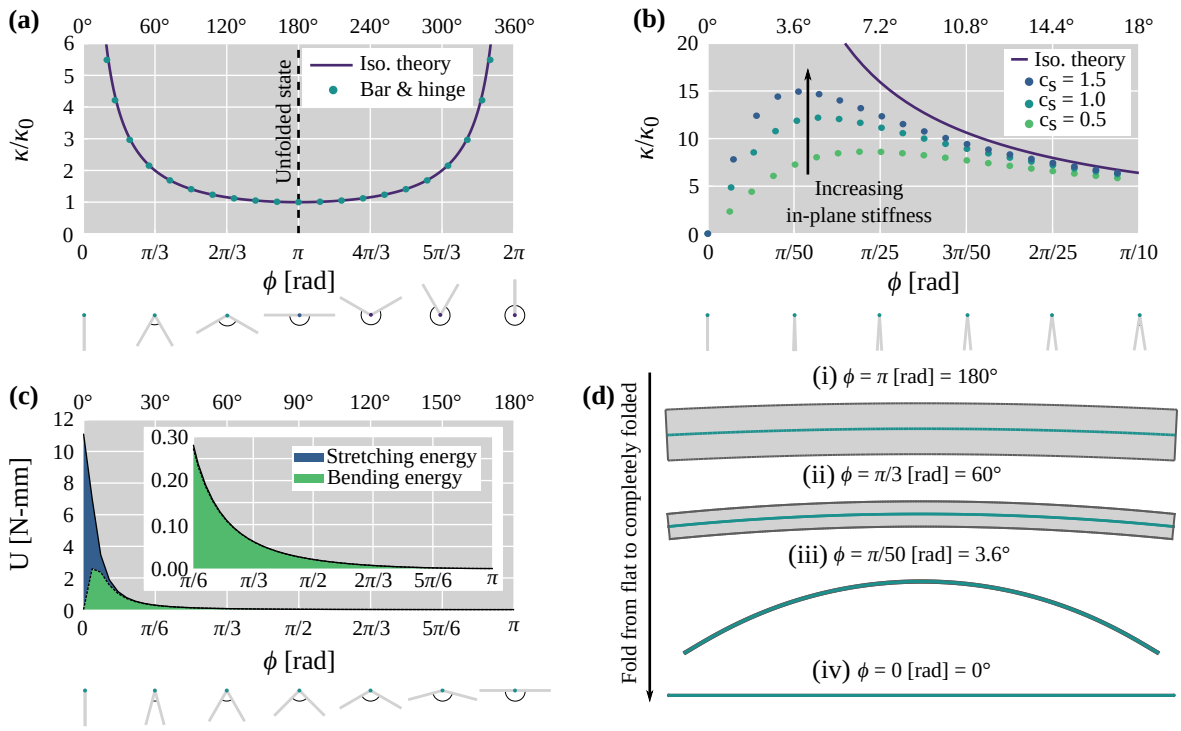

Figure 5.3 – Isometric deformation of thin sheets is a valid assumption for a limited range of folding, but is insufficient for pinching folds. **(a)** The curvature of a curved-crease annulus before, $\kappa_0 = 0.005$ [mm^{-1}], and after, κ, folding is the same for the isometric theory and a bar-and-hinge model in a large domain of dihedral angles (the images below the x-axis show the cross-section of the origami and the corresponding dihedral angle of the annulus sector at some point along its length, with the tangent vector pointing into the page). **(b)** For dihedral angles approaching complete folding, the curvature peaks and falls to zero with the numerical model, rather than approaching infinity. The stiffness of the sheet in stretching (multiplied by a factor, c_s) impacts the change in curvature, suggesting that in-plane deformations dominate at extreme dihedral angles. **(c)** The strain energy in the bar-and-hinge model shows that the stretching energy dominates for extreme dihedral angles, defying the assumption that deformations are predominantly in bending. **(d)** The folded shape of origami shows crease curvature increases as it is folded, peaks, then flattens to avoid infinite curvature once the dihedral angle is zero.

cient than it is to bend the sheet to an infinite curvature. This result holds for the other folding extreme as $\phi \to 2\pi$ [rad]. Using a finite-element model with identical material properties and dihedral angles, I found that in-plane deformations also occur in the sheet and are located near the crease, supporting my claim that isometric theory fails to capture the deformation of origami made from elastic sheets at extreme dihedral angles, where stretching occurs.

From these results, isometric deformations are a reasonable assumption for moderately folded origami ($\pi/3 \leq \phi \leq 5\pi/3$ [rad]), but one should expect stretching deformations to occur for dihedral angles outside of this domain; specifically, at a region near where a crease is pinched. One can use the isometric relationships to gain insight on how real origami structures work, especially for folding, but a more versatile method is required to explore the effects pinching on a structure.

5.3 Materials and Methods

5.3.1 Bar-and-Hinge Modeling of Creased Sheets

In order to supplement the isometric theory for exploring how pinching affects the deformed shape of creased sheets, I used a numerical model to simulate the folding and pinching of thin sheets. This method, called *the bar-and-hinge model* (Schenk and Guest, 2011; Liu and Paulino, 2017; Filipov et al., 2017), represents sheet deformations using three elements. The first is a three-dimensional truss element called a bar, which combined with other bars captures the in-plane deformations of the sheet (i.e., stretching and shearing). The second element is a hinge, or a rotational spring, that captures bending deformations of the sheet by lumping the bending into discrete rotations. The third element is also a hinge, but captures crease rotations due to folding.

The combination of these three elements allows us to model the deformation of origami structures under folding and post-fold loading (e.g., a pinch). Each element is assigned a stiffness value, which has been calibrated to the physical stiffness of thin sheets based on the mesh size, thickness of the sheet, and the sheet material properties (Woodruff and Filipov, 2020a). The bar-and-hinge model arrives at a solution using a Newton-Raphson solver, accommodating geometric non-linearity (Wriggers, 2008). The bar-and-hinge model can capture the deformation of curved-

crease origami with a reasonably high accuracy. Indeed, comparing the deformed shape of several hand-folded paper sheets to simulated bar-and-hinge models gave an average Hausdorff distance error of 0.4% the maximum length of the models (Woodruff and Filipov, 2020a). And, because the bar-and-hinge model uses fewer elements than a finite elements model, convergence occurs in less time (in the geometries depicted in this paper, usually less than ten seconds) and with a greater rate of successful convergence.

I use the bar-and-hinge model to capture the deformed shape of the folded and pinched sheets described below. The data I collect from the models are used to calculate the torsion and curvature of the creases and the global twisting and bending of the structure.

5.3.2 Model Geometries and Parameters

All of the curved-crease sheets studied in this work shared certain geometric features and parameters. First, all of the creases and edges were uniformly spaced, meaning the distance between each crease and between the creases and the edges were some set distance, w. Using uniform crease spacing eliminates twisting due to folding, a source of twisting distinct from the pinch-induced twisting investigated here, because uniformly spaced creases fold to a mostly torsion-free configuration (small amounts of torsion will occur near the ends of the creases, but this torsion is minor (Badger et al., 2019)). Next, all models were restrained so that the sheets were free to fold without generating noticeable twisting and could be freely pinched while maintaining global stability. All restraints lie on the line extending from the pinch force in the flat plane (at the mid-point along each crease). Finally, every model was designed from a flat crease pattern, ensuring developability so the origami could be easily fabricated.

The first set of model simulations explored the curvature and torsion that occurs from pinching on a single-crease sheet structure. For these analyses, the crease pattern is a circular annulus sector creased at mid-radius (see Figure 5.4). Each of the creases had a constant length, $L = 100$ [mm], were folded to $\phi_R = \pi/2$ [rad] ($90°$), were spaced $w = 5$ [mm] from the edges, and the stiffness factor of the creases was $L^* = 2$ [mm] (Filipov et al., 2017). The sheets had constant thickness,

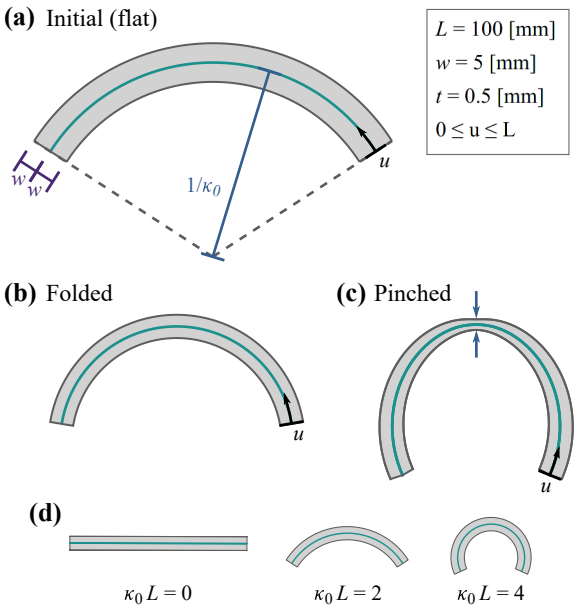

Figure 5.4 – Single-crease, annulus sectors share common geometric properties. **(a)** The structure starts as a flat crease pattern with a constant initial curvature, κ_0. **(b)** As the structure is folded, the curvature increases. **(c)** After folding, the sheet is then pinched at the mid-length and the curvature and torsion are calculated. **(d)** Annulus sectors with different initial curvatures.

$t = 0.5$ [mm] and elastic modulus, $E = 4000$ [N-mm]. The creases were pinched to the dihedral angles shown in Figure 5.5(a), with a minimum dihedral angle, ϕ_p, of $\pi/14$ [rad] ($12.86°$). This minimum dihedral angle was chosen to ensure model convergence and to avoid local instabilities, such as sheet wrinkling, which are sometimes seen in models with high initial crease curvature. The curvature of the creases before folding, κ_0, varied from zero to 0.05 [mm^{-1}] (see example unfolded shapes in Figure 5.4(d)).

For the second set of analyses, I used models with multiple creases to see the effects of other factors that become important with more than one crease (i.e., number of creases, sheet stiffness, and crease spacing). For these simulations, the geometry was again a creased annulus sector where the crease with the lowest curvature was a mountain crease, had a length, $L = 100$ [mm], and all references to crease curvature are the curvature of that crease. The creases alternate between mountain and valley folds where the mountain creases were folded to $\phi_m = \pi/2$ [rad] ($90°$), and the valley creases were folded to $\phi_v = 3\pi/2$ [rad] ($270°$). The creases were pinched so that the dihedral angles were $\pi/18$ [rad] ($10°$) away from being completely folded. The stiffness factor

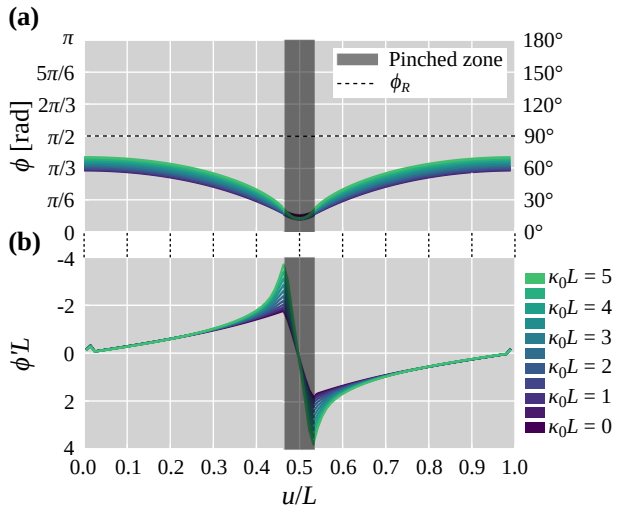

Figure 5.5 – Pinching varies the dihedral angle, ϕ, and fold rate, ϕ', of the creased sheet for various initial curvatures, κ_0. **(a)** The dihedral angle of a pinched mountain crease decreases near the pinch into the domain where isometric theory fails. **(b)** The fold rate for a pinched crease is non-zero, especially near the pinch.

of the creases was $L^* = 2$ [mm]. The thickness of the sheets was, $t = 0.5$ [mm], except for the analyses varying sheet stiffness. The spacing between the creases and the edges was $w = 5$ [mm], except for the simulations varying crease spacing, and the number of creases was three, except for the analyses varying this value. Each of the analyses were run with three different initial crease curvatures ($\kappa_0 = 0,\ 0.005,\ 0.01$ [mm^{-1}]).

5.4 Results

5.4.1 Local Effects of Pinching

Curvature and torsion describe the manner in which a curve is moving through space, relative to nearby points on the curve. The curvature tells us how the curve is bending and torsion tells us how the curve is twisting, both on a local scale. Curvature and torsion do not directly explain the total amount of bending and twisting. But, in general, greater curvature and greater torsion will lead to more bending and twisting, respectively. As an analogy, curvature and torsion are to bending and twisting as strains are to deformations. Understanding the local curvature and torsion generated from pinching will help link the crease pattern parameters to global deformations.

Figure 5.6(a) shows the curvature along the length (i.e., the curvature profile) of an annulus

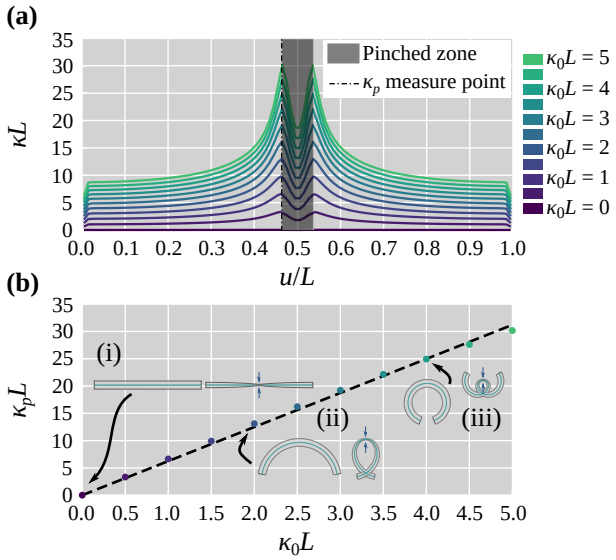

Figure 5.6 – **(a)** Pinching single-crease sheets causes changes in the curvature of the crease along its length, u. For all geometries where the initial curvature, κ_0, is not zero, the resulting curvature, κ, will increase near the pinch point and taper off towards the ends. **(b)** The peak curvature upon pinching, κ_p, is proportional to the initial curvature of the crease pattern (inset images (i-iii) show the folded [left] and pinched [right] shapes, displaying the increase in curvature).

sector creased at mid-radius and pinched at mid-length. The curvature profile was found for crease patterns with varying initial curvatures. Notice that for all crease patterns with non-zero initial curvature, the curvature of the crease increases drastically just outside the pinch location, then tapers down towards the curvature expected from the folded, non-pinched shape. Within the pinched zone (i.e., the portion of the crease length where pinching forces were applied), the curvature is significantly reduced. This reduction occurs because the high degree of folding does not allow isometric deformations. The pinching causes local flattening and a reduction in curvature (as shown in Figure 5.3). Notice that pinching generates a local, highly curved portion of the structure that acts as a hinge and generates global bending. Note that towards the ends of the crease ($u/L \approx 0$ and $u/L \approx 1$), there are errors in the curvature calculation that stem from the finite difference approximations of the derivatives. These errors do not affect the results away from the ends.

For each initial curvature, the peak value, κ_p, was measured, with the location of this peak near the edge of the pinched zone (indicated in Figure 5.6(a) with a dotted line). This peak curvature was plotted against the initial curvature in Figure 5.6(b). Notice that the peak curvature is proportional

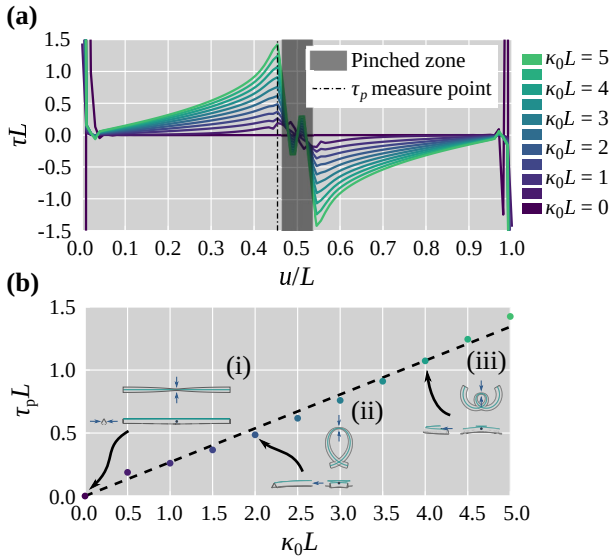

Figure 5.7 – Pinching single-crease sheets with non-zero initial curvature causes a large increase in the torsion, τ, of the crease. **(a)** Upon pinching, the crease torsion increases near the pinch then tapers off. **(b)** The peak torsion, τ_p, is proportional to the initial curvature, κ_0, of the crease pattern (inset images (i-iii) show the top, front, and side views of various origami models, showing twisting deflections).

to the initial curvature of the crease, indicating that greater local curvature from a pinch can be gained with higher initial curvatures.

Figure 5.7(a) shows the torsion along the length (i.e., the torsion profile) of the same circular creased annuli. Notice that pinching results in large crease torsion for creases with nonzero initial curvature. The torsion in the crease peaks near the pinch, then tapers down to zero moving away from the pinch. Notice that the shape of the torsion profile is similar to that of the fold-rate profile shown in Figure 5.5(b) (the vertical axes on this plot are reversed to accommodate the negative relation between torsion and fold rate given in Equation 5.6). This similarity between the fold-rate profile and the torsion profile suggest that the rate of change of the dihedral angle could be useful for prescribing a desired torsion profile. Additionally, the magnitude of torsion appears to increase with the initial curvature of the crease, suggesting that the shape of the torsion profile can also be scaled by altering the initial curvature of the pinched creases. Again, the torsion values near the ends of the crease are erroneous due to approximation errors and should not be considered an accurate reflection of the crease torsion.

Figure 5.7(b) shows how the peak torsion, τ_p, varies with the initial curvature of the crease.

The peak torsion was measured along the dotted, black line in Figure 5.7(a), just outside the pinch where the torsion profiles peak. Notice that the peak torsion is proportional to the initial curvature of the crease. This confirms that the amount of twisting in the structure can be prescribed by varying the initial curvature of the crease.

In these analyses, the creases were all folded to mountain folds, but the curvature and torsion of valley folds will be the same (because curvature and torsion are intrinsic properties of the curve and do not vary with the coordinate system). The global bending and twisting do depend on the mountain/valley crease assignment, but are related to each other. Notice, from the inset deformed shapes in Figure 5.6(b), that pinching the sheets increases the curvature of the crease, resulting in bending towards the center of curvature. Bending towards the center of curvature will occur for both mountain and valley creases. For twisting, as shown in Figure 5.7(b), the torsion of the crease causes the structures to twist downward due to the pinch (for the case where the mountain crease lies on top of the sheets). For a valley crease, the origami would twist upward. Formally, pinching a curved crease will result in the sheet to move opposite the direction of the binormal vector, or the vector describing the positive normal to the osculating plane (see the $\mathbf{tn}$-plane in Figure 5.2(b)). In more relatable terms, the origami will twist away from the direction the crease is pointing, where in this case, mountain creases point upward and valley creases point downward.

5.4.2 Deformations of Pinched Sheets With Multiple Creases

When sheets are folded with more than one crease, the deformations of the creases become coupled, and properties of the sheet become important to the global behavior (Demaine et al., 2014; Watanabe and Mitani, 2018). These parameters of interest include the number of creases in the crease pattern, the stiffness of the sheet determined from its thickness and elastic modulus, and the spacing between the creases. I varied the aforementioned parameters and found the deformed shape of pinched origami with multiple creases and measured the effect on global bending and twisting of the structures.

To measure bending and twisting of multi-crease origami, I start by finding the mid-plane that

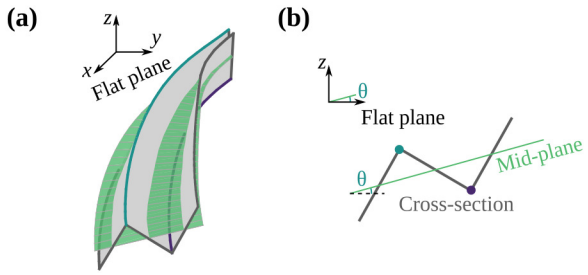

Figure 5.8 – Unlike torsion, the global twisting of a multi-crease system depends on the coordinate system. **(a)** At each point along the length of the crease, a mid-plane is calculated, splitting the origami into an upper and lower portion. **(b)** The mid-plane with respect to the cross-section. The twist angle, θ, is calculated from the xy-plane, and the twist angle at the ends are used to measure global twisting.

cuts the cross-section through the middle (see Figure 5.8). The mid-plane is calculated at each point along the length of the origami by forming a line between the point that lies between the edge and the first crease and the point between the last crease and the adjacent edge. These lines are connected to form a surface representing the mid-plane. The bending angle for the multi-crease origami is the angle between the lines extending from the center of the mid-length of the mid-plane (the location of the pinch) to the center of the mid-plane at the ends of the structure. To measure the bending behavior due to pinching, the bending angle was calculated after folding the origami, β_f, and after pinching, β, and the difference between the two was calculated (see Figure 5.11(c)). The change in twisting angle, $\theta_f - \theta$, was measured as the angle between the mid-plane at the right end of the structures and the flat plane (xy-plane, where the unfolded origami lies) for the folded (θ_f) and pinched (θ) configurations.

Figure 5.9(a) shows the change in bending angle from pinching the origami with different number of creases for three different initial curvatures. The reported initial curvature is for the topmost crease, which has the lowest curvature of all creases in the sheet. Notice that the number of creases is not strongly related to the amount of bending. Because all the creases share a center of curvature, all creases bend towards that direction without disruption from adjacent creases.

Figure 5.9(b) shows that the number of creases has a large effect on the twisting of the structure. The first trend is the difference between origami with an even number of creases and those with an odd number of creases. Origami with an odd number of creases will exhibit a smaller, positive

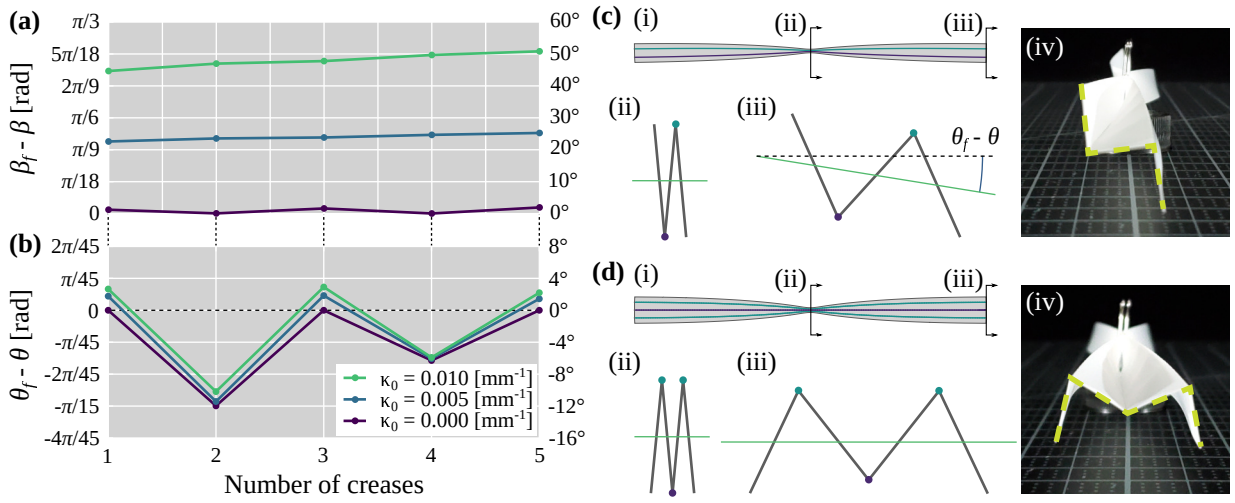

Figure 5.9 – Effect of crease number on bending and twisting. **(a)** The change in bending angle due to pinching, $\beta_f - \beta$, does not vary substantially with the number of creases for all initial crease curvatures, κ_0. **(b)** The change in twist angle, $\theta_f - \theta$, is greatly affected by the number creases. **(c)**(i) An origami structure with two creases and $\kappa_0 = 0$ is folded and pinched. (ii) The cross-section at the mid-length has no twisting, but (iii) the cross-section at the end is twisted. (iv) A photograph of the same model made with Dura-Lar shows the same behavior (dashed lines added for emphasis). **(d)** For an origami structure with three creases, there is no twisting.

twisting angle, while origami with an even number of creases will twist in the negative direction significantly more. The different twisting for even and odd creases holds for the origami with zero initial curvature, but, the torsion for odd-numbered creases is always zero. Figures 5.9(c-d) show cross-sections of the two- and three-crease geometries at the pinch and at the right end of the structure, along with photographs of prototypes with the same crease patterns. All physical prototypes presented in this paper are made from polyester sheets supplied by Dura-Lar and have a thickness of 0.127 [mm]. For both the two- and three-crease models, the outermost sheets barely rotate away from the pinch. Because for the two-crease model, the sheets are parallel, pinching causes the mid-sheet to rotate away from the pinch, causing the global twisting. For the three-crease model, the outermost sheets are mirrored, and the center sheets do not rotate away from the pinch. The different twisting behavior for an even versus odd number of creases holds for origami with a greater number of creases and for those with non-zero curvature as well.

Another trend when varying the number of creases requires separating the even- and odd-crease origami and looking at each individually. Looking at the twist angles separately, notice that as more creases are added, the magnitude of twisting decreases, suggesting that origami with a high number

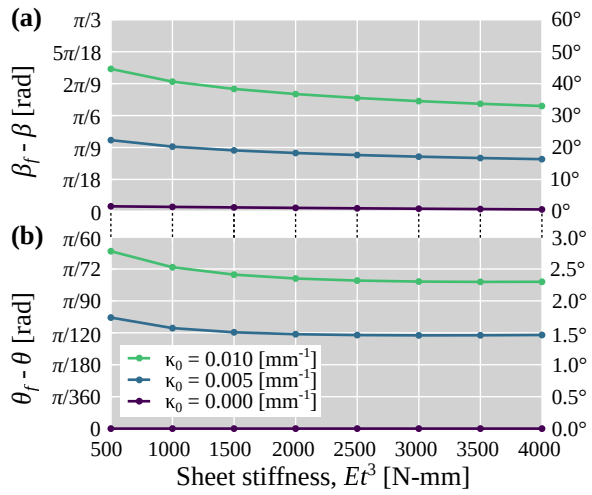

Figure 5.10 – Effect of sheet stiffness on bending and twisting. **(a)** The change in bending angle, $\beta_f - \beta$, and **(b)** the change in twisting angle, $\theta_f - \theta$, due to pinching are slightly greater for more flexible sheets.

of creases (e.g., seven) will show little twisting, especially if there are an odd number of creases.

Figure 5.10(a) shows the change in bending angle for a three-crease model when the stiffness of the sheet is varied. Observe that the sheet stiffness has a small effect on the amount of bending in the origami. The effect is most pronounced for sheets with low stiffness ($Et^3 < 2000$ [N-mm]) and higher curvature. However, the overall effect is small with only an increase of 9.80% for halving the stiffness from 1000 [N-mm] to 500 [N-mm] (for $\kappa_0 = 0.01$ [mm^{-1}]). A similar trend can be seen with twisting in Figure 5.10(b) with only an increase of 9.93% in twisting angle change when reducing stiffness from 1000 [N-mm] to 500 [N-mm] (for $\kappa_0 = 0.01$ [mm^{-1}]).

The flexibility of the sheet will determine its compliance to the crease shapes (i.e., a more flexible sheet will reconfigure to comply with the curvature and torsion of a crease than a stiffer sheet). However, the influence of stiffness is small, and the bending and twisting are affected more by the shape of the origami (e.g., κ_0).

The last multi-crease parameter I explored was crease spacing. Figure 5.11(a) shows the change in bending angle versus the distance between the creases. Notice, here, that bending is proportional to crease spacing. The greater creases are spaced, the more bending one should see. For twisting, greater crease spacing results in more twisting, but the effect is non-linear and is less than with bending (see Figure 5.11(b)).

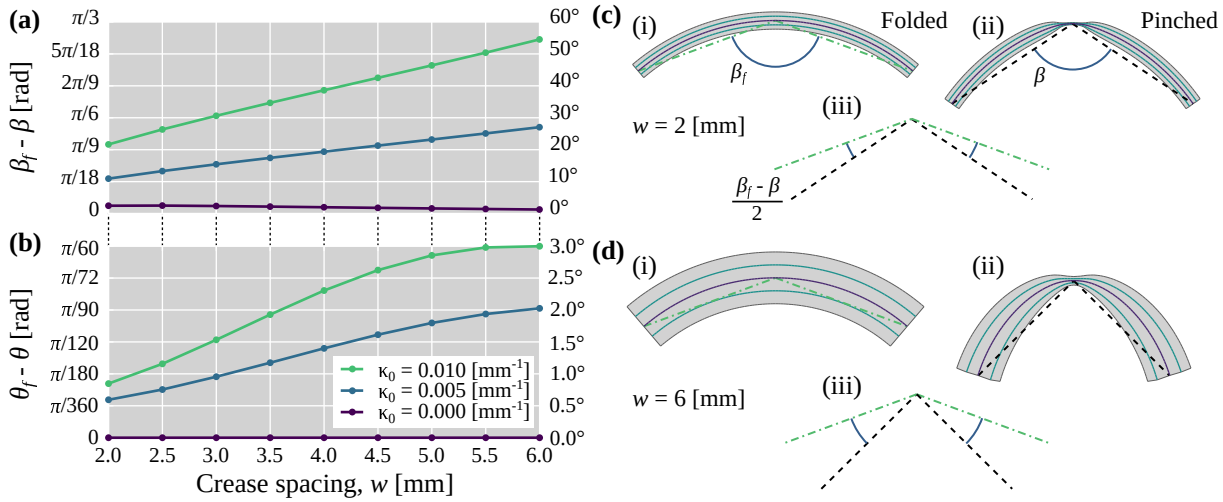

Figure 5.11 – Effect of crease spacing on bending and twisting. **(a)** The change in bending angle due to pinching, $\beta_f - \beta$, is proportional to the crease spacing with substantial effect for all non-zero initial curvatures, κ_0. **(b)** Larger crease spacing also increases twisting, but has a non-linear effect. **(c)** A three-crease model with $w = 2$ [mm] is (i) folded and (ii) pinched, with the change in bend angle shown separately in (iii). **(d)** For a three-crease model with $w = 6$ [mm], the bend angle change is more substantial.

It is important to note that as the crease spacing increases, stretching (due to the extreme folding described in Section 5.2.3) increases at the edges away from the creases. This stretching can result in local instabilities of the sheet (e.g, wrinkling), seen in both the bar-and-hinge model and in physical, polyester prototypes. As such, there is a practical limit to the crease spacing that depends on the material properties of the sheet.

5.5 Discussion

From the single and multi-crease analyses, a more complete understanding emerges about how the crease pattern and sheet properties cause bending and twisting of uniformly spaced origami when pinched. This understanding establishes a framework for prescribing pinch-induced deformations to origami to meet the needs of an adaptable system. I will then use this framework to create example crease patterns that display various combinations of deformations.

5.5.1 Generating and Tuning Global Bending

When origami is pinched, the curvature of the creases (for crease with non-zero initial curvature) increases near the pinch. This increase in curvature generates a hinge that rotates the ends of the structure, causing the origami to bend globally. The greater the initial curvature of the crease, the more it will bend upon pinching. When a curved-crease origami is pinched, the bending is towards the center of curvature. Because the center of curvature is the same for mountain and valley creases, pinching either type of crease will result in the same bending deformation, even with multiple creases. The number of creases in a multi-crease pattern does not influence the magnitude of bending, and a more flexible sheet will bend slightly more than a stiffer sheet, but stiffness has a minimal effect on bending. Finally, multi-crease systems with a greater crease spacing will generate greater bending (until local instabilities occur for large crease spacing).

5.5.2 Generating and Tuning Global Twisting

When curved creases are pinched, large torsion deformations appear near the pinch. The torsion peaks near the pinch, then tapers off towards zero away from the actuation. This torsion, along with other factors, result in global twisting in the structure. For origami with an odd number of creases, greater crease curvature will generate greater twisting. Origami with an even number of creases will generate large amounts of twisting, but this larger twisting is caused predominantly by the sheet arrangement, not the crease curvature. Mountain and valley creases will generate torsion of an opposite sign, so a single mountain crease that is pinched will deflect in one direction (the direction opposite the that of the crease's binormal vector), and a valley crease of the same shape will deflect in the other (where the binormal vector is flipped). Like bending, more flexible sheets twist slightly more than a stiffer sheet. Again, the sheet stiffness has a minimal effect. Wider crease spacing will also generate greater twisting, due to the lever arm that the sheets make between the creases.

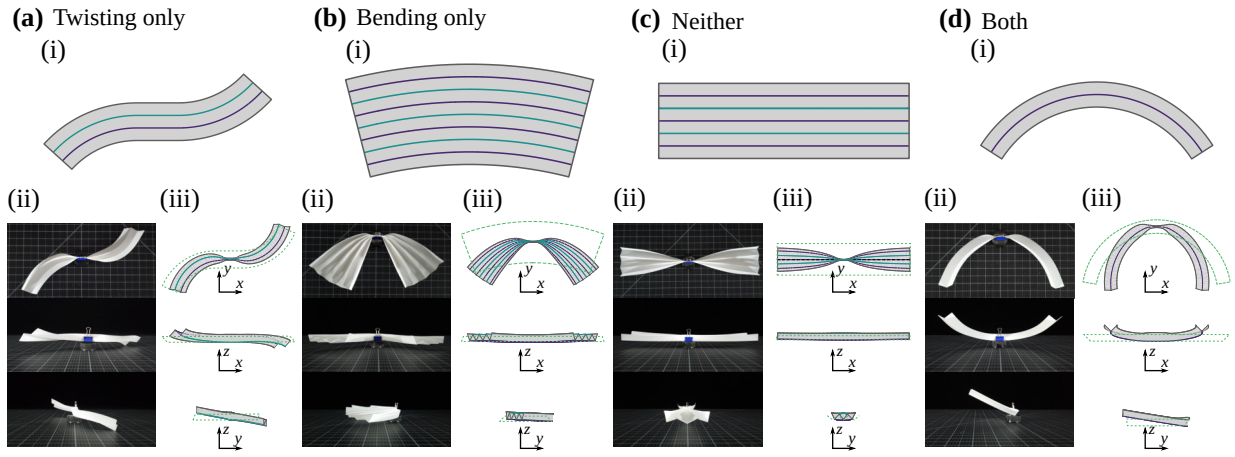

Figure 5.12 – The framework described in Section 5.5 is used to design four crease patterns with desired pinch-driven twisting and bending deformations. **(a-d)**(i) The initial crease patterns. (ii) The pinched shape of physical models made from polyester sheets are similar to (iii) the deformed shapes found using the bar-and-hinge method and validate the framework (dotted lines show the folded and unpinched configuration).

5.5.3 Crease Patterns for Isolated or Combined Bending and Twisting

With this framework, one can create crease patterns that display desired bending and twisting behaviors. Figure 5.12(a)(i) shows a crease pattern that, when pinched, experiences large twisting, but minimal bending deformations. The crease pattern has zero curvature near the center (where the pinch occurs) and has non-zero curvature near the ends. This crease pattern also uses two creases, which will generate large twisting along the curved ends of the origami. Figures 5.12(a)(ii-iii) show the effect of folding and pinching on this geometry, where there is no global bending, but large twisting at the ends.

The second geometry I created displays only bending deformations when pinched. Figure 5.12(b)(i) shows a crease pattern that has non-zero initial curvature everywhere, but has a large and odd number of creases (seven). Figures 5.12(b)(ii-iii) show that pinching the structure results in significant bending with minimal twisting deformation.

Figure 5.12(c) shows the third geometry that displays neither bending nor twisting when pinched. The crease pattern has zero initial curvature and an odd number of creases (five). Pinching this structure gives a neutral local deformation in the middle, with no global deformations (see Figures 5.12(c)(ii-iii)).

The fourth and final geometry displays both bending and twisting due to pinching. Figure 5.12 (d)(i) shows a single-crease, annulus sector crease pattern with a non-zero curvature. Pinching this structure generates significant bending and twisting deformations, as shown in Figures 5.12(d)(ii-iii).

These four geometries show only a small subset of possible crease patterns that will display isolated and combined bending and twisting behaviors. By varying the initial crease curvatures, number of creases, and crease spacing, the magnitude of these deformations can also be controlled, as needed.

Pinched shape-morphing origami have the potential to advance technology in a variety of fields, with applications requiring targeted changes in the shape of the mechanism with little actuation complexity. Pinching can occur at any point along the length of a crease and with multiple pinches for applications in soft robotics, such as a gripper (see Figure 5.13(a)). Additionally, a dynamic façade (Abdelmohsen et al., 2019; Ricci et al., 2021) composed of curved-crease panels can twist away from a building and bend to allow light in, as needed (see Figure 5.13(b)). Another potential application of shape-morphing origami is adaptable, architected materials that require simple actuation, but high complexity shape changes. Finally, my findings could support development of exoskeletons that can morph to the shape and functional needs of the wearer in real-time and generate a hinge with a locked, high-stiffness state and an unlocked, low-stiffness state using pinching (see Figure 5.13(c)). The adaptive stiffness for this type of pinched mechanism was demonstrated in my previous work (Woodruff and Filipov, 2020a).

5.6 Conclusions

When creased sheets are pinched, the deformed shapes can bend and twist in desirable ways to achieve a new, geometric state. Using pinching for shape morphing of creased sheets overcomes many of the obstacles facing existing adaptable materials and structures. For instance, the inputs to the system are a single-degree-of-freedom actuation that results in variable intensity bending and twisting that can be coupled or isolated and is fully reversible. By limiting the number and

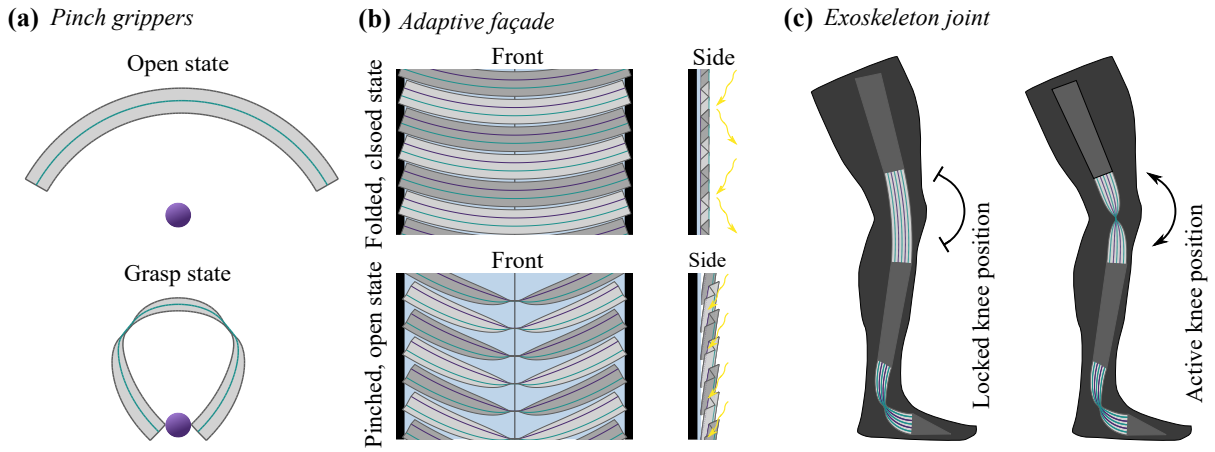

Figure 5.13 – Conceptual applications of pinch-actuated origami. **(a)** Pinches can be applied to curved-crease origami to generate intense bending along the length of the crease to achieve grasping-type motions. **(b)** An origami façade can be adapted to optimize the heat and light entering a building depending on internal and external conditions. Both bending and twisting motions can be achieved with a simple pinch. **(c)** A curved-crease sheet with an odd number of creases (limited twisting upon pinching) could allow for an exoskeleton-type system that locks or allows bending, as needed.

distribution of actuation points, the shape-morphing system becomes less complex and less expensive, requiring fewer actuation elements made from costly materials (e.g., shape-morphing alloys/polymers or piezoelectric actuators). The control system for shape-morphing origami is relatively straightforward, with the crease design and pinch location determining the magnitude and sign of global bending and twisting.

Isometric deformation theory predicts the increase in curvature and torsion caused by pinching, but it limited to moderate dihedral angles ($\pi/3 \leq \phi \leq 5\pi/3$ [rad]) and requires understanding how sheet bending is linked to the boundary conditions of the structure. My results using a mechanics-based numerical models confirm that origami with creases of higher initial curvature will generate greater curvature and torsion in the area surrounding the pinch. However, the increase in curvature exists only outside the pinched zone, and the sheet will flatten at the pinch (a result that isometric theory does not explain). These local behaviors affect the global deformation of the structure. When a sheet is folded about more than one crease, the number of creases does not influence the amount of bending seen in origami, but significantly affects the magnitude and sign of twisting. Origami with an even number of creases will result in large, negative twisting, and origami with an odd number of creases will result in smaller, positive twisting (for sheets with non-zero initial

curvature). Looking at the even- and odd-crease patterns separately, the fewer creases there are, the greater the twisting. Spacing between creases is also important in prescribing the amount of bending and twisting generated from pinching. When the spacing increases, so does the magnitude of bending and twisting. Sheet stiffness had a small effect on the amount of bending and twisting generated from pinching, where more flexible sheets experience larger deformations.

In this chapter, I have identified the potential of shape-morphing by pinching origami, and future research would enhance the capabilities of these programmable systems. For example, origami that is folded about non-uniformly spaced creases can generate twisting without any pinching. Understanding the impact that non-uniformly spaced creases has in conjunction with pinching could result in more varied shape morphing. Additionally, future research could explore the behavior due to pinching origami at different and multiple points along the length of the crease. With greater investigation of the range of motion of pinched origami, future research could develop an inverse design scheme where origami can morph into target shapes using careful crease pattern design and placement of local actuation(s). Finally, curved-crease sheets have been shown to have unique and programmable stiffness characteristics, so exploring stiffness tuning in conjunction with pinched shape morphing could open up new potential capabilities.

Chapter 6

An Inverse-Design Scheme for Point-Fitting, Curved-Crease Sheets With Pinches

In Chapter 5, I show that pinching curved-crease origami generates global bending and twisting deformations. The amount of crease torsion and curvature near the pinch in a single, constant-curvature crease was proportional to the curvature of the crease before folding. With this in mind, one can vary the curvature of a crease pattern to generate a wide variety of bending and twisting behaviors in an origami structure.

With the link between crease-pattern geometry and bending/twisting established, the question that follows is, how can one generate a crease pattern for a desired amount of global deformation? A desired amount of deformation can include fitting an origami structure to any number of points in space, eventually fitting the geometry to a given surface or space curve. Solving this problem serves to take my analysis from Chapter 5 to a design arena. The results from this current chapter exemplify the design applications of curved-crease origami using a simple inverse-design scheme. Using only pinches and a single curved crease, I am able to design a structure that fits a wide variety of points in space.

The chapter is organized as follows. I start by providing background information about shape-fitting using origami and motivating the need for shape-fitting using curved-crease sheets (Section 6.1). In Section 6.2, I introduce the origami geometry, later used in the inverse-design process, and formulate the forward process for calculating the shape of the crease before and after pinching using a vector representation of the structure, supplemented with data from closed-form, geometric equations and bar-and-hinge deformation data. I then describe three inverse-design problems, explore the complexity of these problems, and present an optimization method for finding a crease pattern that satisfies the problems using a genetic algorithm in Section 6.3. I examine the perfor-

mance of the inverse-design algorithm in Section 6.4 with discussion on the patterns found in the solutions and limitations of the inverse-design scheme. I conclude with a summary of the work and discussion for future work in shape-fitting curved-crease origami in Section 6.5.

6.1 Introduction

Shape fitting of origami is the process of finding a crease pattern that upon actuating will create a shape that approximates some given form or deflects by some desired amount. Shape-fitting can be as simple as creating a structure that reaches a finite set of points up to a complex problem of creating a structure that matches a given surface or three-dimensional lattice. In origami engineering, shape-fitting allows a designer to create a folded structure that has required geometric properties from a flat sheet, essentially defining the crease pattern and folding process that maps the flat sheet (which is simple to fabricate and ship) to the functional state.

The earliest example of shape-fitting paper sheets to three-dimensional forms using a systematic approach comes from Lang (1996) with his TreeMaker algorithm that gives a crease pattern for complex origami designs (e.g., an origami deer). Later, Tachi (2010) developed an algorithm to create crease patterns to fit complex polyhedral surfaces, such as the Stanford bunny. More recent work has explored shape fitting origami to surfaces using topology optimization (Fuchi and Diaz, 2013; Fuchi et al., 2015). Since then, researchers have developed methods for shape fitting origami to surfaces with non-zero Gaussian curvature using repeated Miura-Ori (Dudte et al., 2016) and Eggbox cells (Nassar et al., 2017), as well as fitting rigid-foldable origami units to space curves, curved surfaces, and metamaterials (Walker and Stankovic, 2022).

While there has been much success approximating curved-surfaces and paths using straight-crease patterns, there has been very little research into using curved creases to accomplish similar tasks. Existing examples of using curved-crease origami to fit complex shapes include wrapping paper about axisymmetric conical and cylindrical shapes using tucks (Mitani, 2011) and using curved-crease couplets to approximate non-zero Gaussian curvature surfaces, such as vases and baseball caps (Leong, 2011). Despite these efforts to fit surfaces with curved-crease origami, the

scope of the target shapes is limited and the methods are focused on generating artistic forms, rather than accomplishing engineering-related tasks.

It is likely that curved-crease origami could also fit these complex shapes given the design freedom offered by curved-crease origami. Furthermore, the curved edges and surfaces that occur when folding about curved creases could be useful in better fitting a general surface using fewer creases, and thus, fewer points of failure. Additionally, with local actuations, curved-crease origami could generate shapes that reach a desired target and return to a neutral position, for applications in soft robotics and emergency structures.

In this chapter, I aim to develop a method of designing a crease pattern and actuation scheme that achieves three shape-fitting goals: (1) approximating a planar curve, (2) maximizing tip deflections from folding to pinching, and (3) reaching a target point in three-dimensional space. The design will be generated automatically using an inverse-design scheme that takes in the target curve/point and initial conditions for the crease (i.e., the starting point and orientation of the starting tangent). Such an inverse-design scheme could be used to exploit the design freedom that curved creases offer to generate a versatile array of solutions that meet various engineering needs.

6.2 Formulating the Forward Process

In order to determine a crease pattern and actuation scheme (CP/AS) that will fit some given shape, I need to start by developing a method for calculating the shape of the crease as a function of the crease pattern parameters and pinch status. The goal for this forward-process is to generate a function that takes in the CP/AS parameters and returns the Cartesian coordinates of points on the crease quickly so that the inverse-design algorithm can perform the calculation several thousands times with as little computational cost as possible, while preserving the accuracy of the result. I start by defining the scope of the origami geometry used in subsequent analyses.

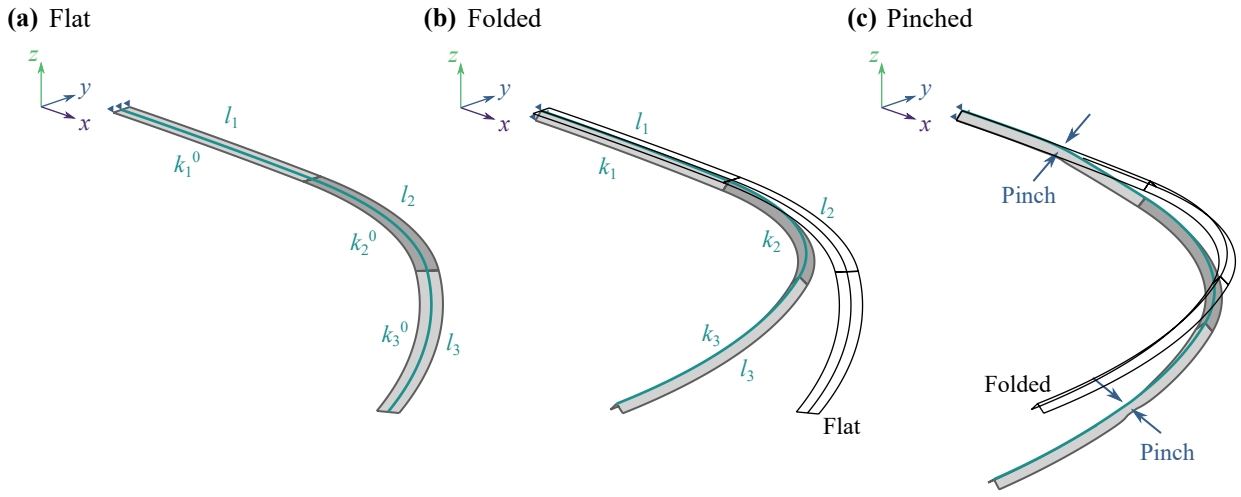

Figure 6.1 – The model geometry for all subsequent analyses. **(a)** The origami strip is created with discrete circular arc segments creases, each with a specified initial curvature, k_i^0, and length, l_i. **(b)** Folding that strip can change the curvature of the crease, k_i (flat geometry for reference). **(c)** Applying pinches to the crease at the mid-point of some segments leads to bending and twisting of the origami, altering the final shape (folded geometry for reference).

6.2.1 Model geometry

Given the wide variety of CP/AS available in curved-crease origami design, it would be useful to limit the geometries used in the model. I start with a simple, yet non-trivial origami geometry that will satisfy many shape-fitting problems.

The curved-crease geometry I use to solve the shape-fitting problems includes a single crease composed of n discrete circular arc segments (see Figure 6.1(a)). The start of the first crease segment is oriented in a specific way to simulate restraints that the structure would be anchored to, which makes the problem non-trivial. Using these arc segments allows me to vary the curvature of the crease along its length, effectively enabling a versatile range of bending and twisting deformations that could shape the crease to how I want it.

Each circular arc segment has some initial curvature before folding, k_i^0, crease length, l_i, and pinch status, $f_i = \{\text{false}, \text{true}\} = \{0, 1\}$. All crease segments are folded to a dihedral angle, $\phi_R = \pi$ [rad] $= 90°$. If $f_i = 1$, then the crease segment will also be pinched at mid-crease to a dihedral angle, $\phi_p = \pi/14$ [rad] $= 12.9°$, and will smoothly unfold back to ϕ_R from mid-crease to the ends (i.e., all crease segments will have a dihedral angle of ϕ_R at its ends).

The first crease starts at, $\mathbf{P}_0$, a position vector describing its location in Cartesian space. For all analyses in this chapter, the start of the crease lies at the origin, $\mathbf{P}_0 = \mathbf{0}$. The crease is also oriented such that its tangent at the start aligns with the x-axis of the coordinate basis rotated about the matrix $\mathbf{R}_0$. If the initial rotation matrix is the identity matrix, $\mathbf{R}_0 = \mathbf{I}$, then the crease tangent will be parallel to the global x-axis. Such is the case for all analyses in this chapter.

The crease segments are arranged such that the creases at the end of the preceding segment and the start of the following segment share a tangent and location in space. Additionally, the crease segments must be oriented such that the sheets alongside the creases share an edge, effectively forming a smooth surface between segments.

6.2.2 Vector Representation of Curved-Crease Origami

The point at the end of a crease segment, $\mathbf{P}_j$, composed of n discrete circular arc segments can be found using a sum of vectors (see Figure 6.2(c)). Namely,

$$\mathbf{P}_j = \mathbf{P}_0 + \sum_{i=1}^{j} \mathbf{T}_i, \quad j = 1, 2, \ldots, n \tag{6.1}$$

where $\mathbf{T}_i$ is the translation vector from the start to the end of the i^{th} segment's crease in the global coordinate system. The global translation vector is calculated using the segment's CP/AS parameters, as well as the parameters of the segments preceding the segment (since the orientation of the i^{th} segment depends on how the preceding segments are oriented).

One can determine what the global translation vector components will be by first analyzing the deformed shape of segments individually, then rotating and translating them into place in the global coordinate system containing the entire structure (see Figure 6.2(b)). To do so, I have devised a local coordinate system where a segment of any curvature, length, and pinch status is uniformly oriented and positioned (see Figure 6.2(a)). The start of each crease segment in the local coordinate system lies on the origin and has a tangent aligned with the local x-axis. With this uniform coordinate system to perform analyses, one can determine what the translation from start to end of the crease will be locally for each crease segment using a local translation vector, $\mathbf{t}_i$ (note that corre-

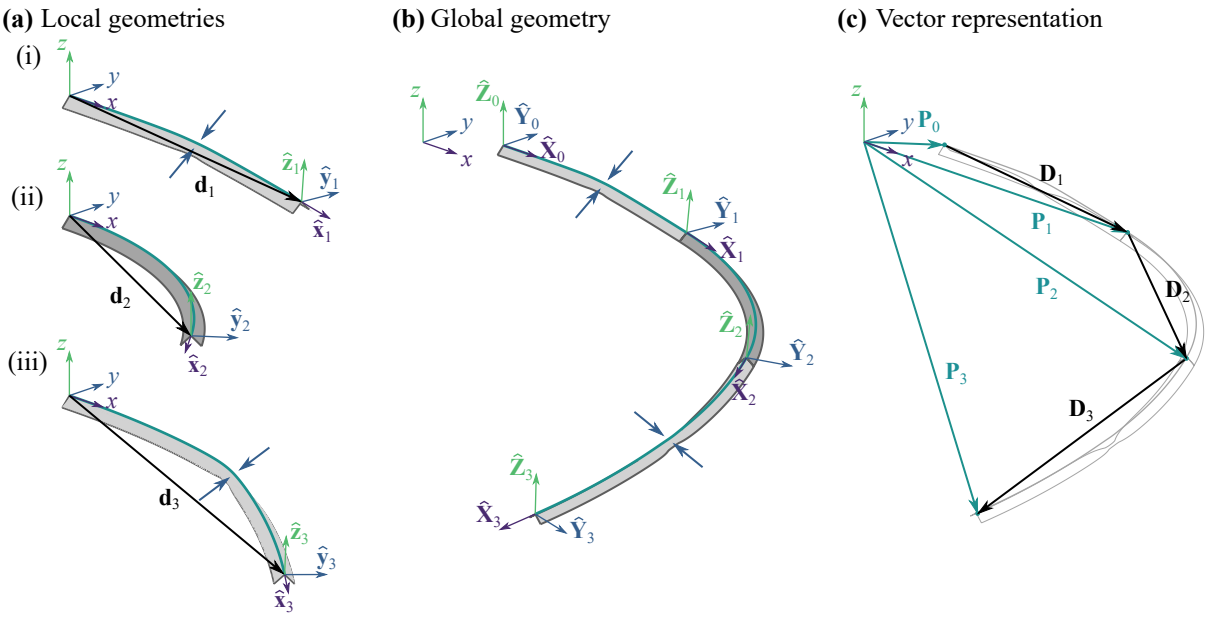

Figure 6.2 – Vector representation of the origami strip in local and global coordinates. **(a)** I first analyze individual crease segments in the local space, where the creases start at the origin and their initial tangent aligns with the x-axis. **(b)** Taking the local translation vector and end orientations, I then rotate and translate the local geometries to piece together the global structure. **(c)** Using only the global deformation vectors and the global rotation matrices, I can determine the location at the end of each crease segment.

sponding vectors in the global and local coordinate spaces are indicated with capital and lowercase letters, respectively).

One can calculate the global translation vector by rotating the local translation vector such that the crease segments are aligned and smoothly connected. That is,

$$\mathbf{T}_i = \mathbf{R}_{i-1}\mathbf{t}_i, \tag{6.2}$$

where $\mathbf{R}_{i-1}$ is the global rotation matrix describing the intrinsic rotation between the orientation of the structure's cross-section at the start of the crease to the end of the $(i-1)^{\text{th}}$ segment.

The global rotation matrix is calculated as a series of local rotations. The local rotations, calculated in the local coordinate system, determine the rotational transformation between the crease segment cross-section at the start of the crease to the end. I represent the orientation at the end of

the crease segment in local coordinates with a set of basis vectors,

$$\mathbf{r}_i = \left\{ \hat{\mathbf{x}}_i, \quad \hat{\mathbf{y}}_i, \quad \hat{\mathbf{z}}_i \right\}, \tag{6.3}$$

where $\mathbf{r}_i$ is the local rotation matrix and $\hat{\mathbf{x}}_i$, $\hat{\mathbf{y}}_i$, and $\hat{\mathbf{z}}_i$ are the basis vectors at the end of the crease (see Figure 6.2(a)). Once the local rotation matrices are calculated for each of the structure's segments, I can calculate the value of the global rotation matrices with,

$$\mathbf{R}_i = \mathbf{R}_{i-1}\mathbf{r}_i, \tag{6.4}$$

Note that $\mathbf{R}_0$ is a given value that determines how the crease is oriented at the start of the crease (at $\mathbf{P}_0$). In this chapter, I choose to set the initial rotation matrix as the identity matrix ($\mathbf{R}_0 = \mathbf{I}$) in all cases, but any initial rotation can be chosen. It is also useful to note that the order of multiplication has a significant effect on the value of the global rotation matrix. Here, the prior global rotation matrix, $\mathbf{R}_{i-1}$, is right-multiplied by the local rotation matrix, $\mathbf{r}_i$, since the current global rotation matrix is an intrinsic rotation that occurs about the global basis vectors at the end of each crease, $\hat{\mathbf{X}}_{i-1}$, $\hat{\mathbf{Y}}_{i-1}$, and $\hat{\mathbf{Z}}_{i-1}$ (see Figure 6.2(b)).

By calculating values for the local translation vector and rotation matrix for each of the n segments in a structure, one can determine the position at the end of the crease. However, doing so requires saving twelve values per crease segment (three translation components and nine rotation components). I can reduce the number of values per crease segment required to model the transformations, which will be useful when employing surrogate data later on.

Reducing the required number of values describing the rotation can happen by representing the local rotation matrices with three rotation angles. Here, I employ Tait-Bryan angles, u_i, v_i, and w_i, that describe the angle the geometry is rotated through about the local x-, y-, and z-axes, respectively (Slabaugh, 1999). Tait-Bryan angles are similar to Euler angles, but the rotations are extrinsic, meaning the rotations occur about the fixed coordinate space axes, x, y, and z (see

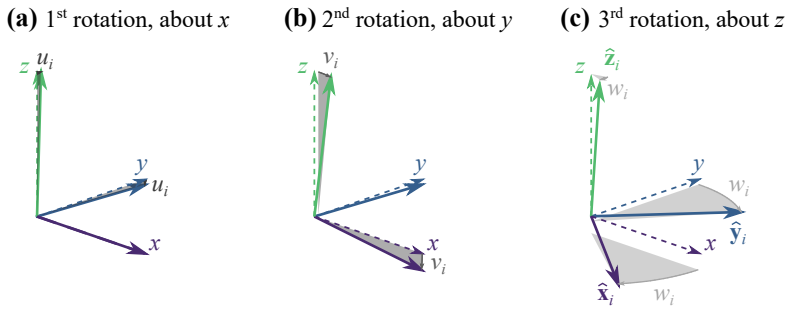

Figure 6.3 – The orientation at the end of a crease can be represented using three angles. These Tait-Bryan angles describe the amount an object (here, a set of basis vectors) rotates in three sequential steps. (a) In the first step, the object is rotated about the x-axis by the angle, u_i. **(b)** Next, the object is rotated about the y-axis by the angle, v_i. **(c)** Finally, the object is rotated about the x-axis by the angle, w_i. These angles can be used to calculate the rotation matrix mapping the original x-, y-, and z-axes on to the $\hat{\mathbf{x}}_i$-, $\hat{\mathbf{y}}_i$-, and $\hat{\mathbf{z}}_i$-vectors.

Figure 6.3). One can calculate the local rotation matrices from the Tait-Bryan rotation angles with,

$$\mathbf{r}_i = \mathbf{r}_i^z \mathbf{r}_i^y \mathbf{r}_i^x = \begin{bmatrix} \cos w_i & -\sin w_i & 0 \\ \sin w_i & \cos w_i & 0 \\ 0 & 0 & 1 \end{bmatrix} \begin{bmatrix} \cos v_i & 0 & \sin v_i \\ 0 & 1 & 0 \\ -\sin v_i & 0 & \cos v_i \end{bmatrix} \begin{bmatrix} 1 & 0 & 0 \\ 0 & \cos u_i & -\sin u_i \\ 0 & \sin u_i & \cos u_i \end{bmatrix}, \tag{6.5}$$

where $\mathbf{r}_i^z$, $\mathbf{r}_i^y$, and $\mathbf{r}_i^x$ are the rotation matrices for extrinsic, active rotations about the local z-, y-, and x-axes, respectively, for the i^{th} segment. Note that order of rotations occurs first about the x-axis, then the y-axis, and finally about the z-axis. However, the order of multiplication is reversed (left-multiplied), since the rotation is extrinsic.

The next step in the forward analysis is to generate the six translation and rotation values for a crease segment given the curvature, length, and pinch status of each segment. Figure 6.4 shows a single crease in both the unpinched and pinched forms. Plotting the location at the end of the crease during the pinching process shows that the path is highly nonlinear. I chose to limit the pinch status to a binary, pinched or unpinched, to avoid having to collect data modeling varying degrees of pinching. Since the pinch status is binary, I must assess the deformed shape of pinched and unpinched segments separately, starting with the simpler case of an unpinched segment.

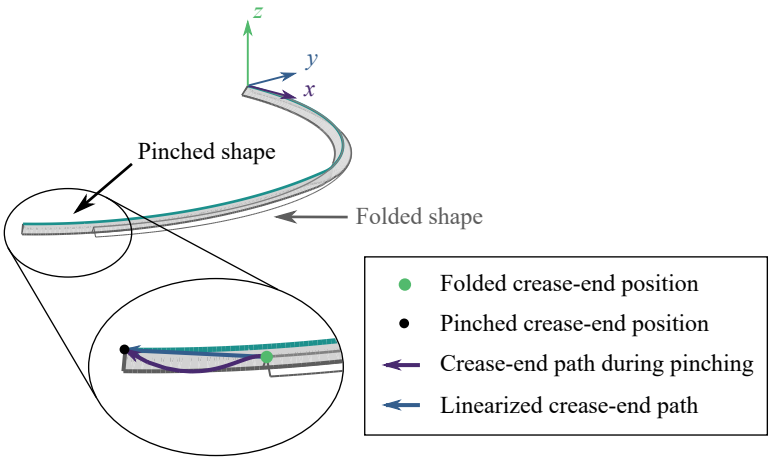

Figure 6.4 – The end of a crease follows a nonlinear path during pinching. Without additional deformation data from the bar-and-hinge model, determining the position of the end of the crease for varying pinch angles, ϕ_p, with a linear approximation would be overly erroneous. Thus, the pinch status is binary, rather than continuous.

6.2.3 Local Analysis of Unpinched Origami

When a creased annulus sector is folded to a uniform dihedral angle and the crease is held planar, the crease retains its circular shape. However, the magnitude of the curvature of the crease increases as the dihedral angle moves away from π [rad] (unfolded). The curvature, with respect to the dihedral angle, can be calculated with,

$$k_i = \frac{k_i^0}{\sin(\phi/2)}, \tag{6.6}$$

where k_i is the signed curvature of the crease after folding, k_i^0 is the signed curvature of the crease before folding, and ϕ is the dihedral angle of the crease (see Figure 6.1(a-b)).

In equilibrium, a uniformly folded, circular creased annulus sector will exhibit small torsion at the ends of the crease. However, this torsion leads to small deflections from the initial plane of the crease (a distance of about 0.6% the length of the crease (Badger et al., 2019)). For simplicity, I assume that if the crease is uniformly folded (i.e., unpinched), then the crease will remain planar. Furthermore, I can restrain the origami in such a way that the crease always lies in the original plane (in this case, the local xy-plane). With these assumptions, the crease geometry is simplified to a circular sector. Subsequently, the translation components and rotation angles in the local coordinate

system can be calculated using the curvature and length of the crease.

For instance, the local translation vector, $\mathbf{t}_i$, can be calculated with,

$$\mathbf{t}_i = \begin{cases} \left\{ \frac{1}{|k_i|} \sin\left(|k_i| l_i\right), \quad \frac{1}{k_i}\left[1 - \cos(|k_i| l_i)\right], \quad 0 \right\}^{\mathrm{T}}, & k_i \neq 0 \\ \left\{ l_i, \quad 0, \quad 0 \right\}^{\mathrm{T}}, & k_i = 0 \end{cases} . \tag{6.7}$$

Additionally, the rotation angles can be found with,

$$u_i = 0; \qquad v_i = 0; \qquad w_i = k_i l_i. \tag{6.8}$$

Note that the rotation about the z-axis, w_i, is identical to the signed sector angle of the circular arc. With these rotation angle, one can calculate the local rotation matrix, $\mathbf{r}_i$, using Equation 6.5. Equations 6.7 and 6.8 have been evaluated for a range of crease curvatures and lengths, as shown in Figures 6.5 and 6.6, respectively.

Uniform folding allows the crease to reach various points in the original, xy-plane (see Figure 6.15 for examples). However, one must include pinching the origami to reach points off this plane.

6.2.4 Local Analysis of Pinched Origami

When determining the deformed shape of pinched origami in equilibrium, one cannot assume that the shape of the crease will be circular. The pinching induces a local bending and global twisting in the crease segment, which is not easily described with common shapes, such as a circle. To determine the transformation data required for our forward process, I need to use a method that goes beyond simple geometric analysis. Here, I use the bar-and-hinge model, a mechanics-based simulation tool described in detail in Chapter 5, to calculate the shape of the crease segment after folding and pinching.

Given the speed and reliability of the bar-and-hinge model, I can determine the deformed shape of over four thousand crease segments, of various curvatures and lengths, within a couple hours. I

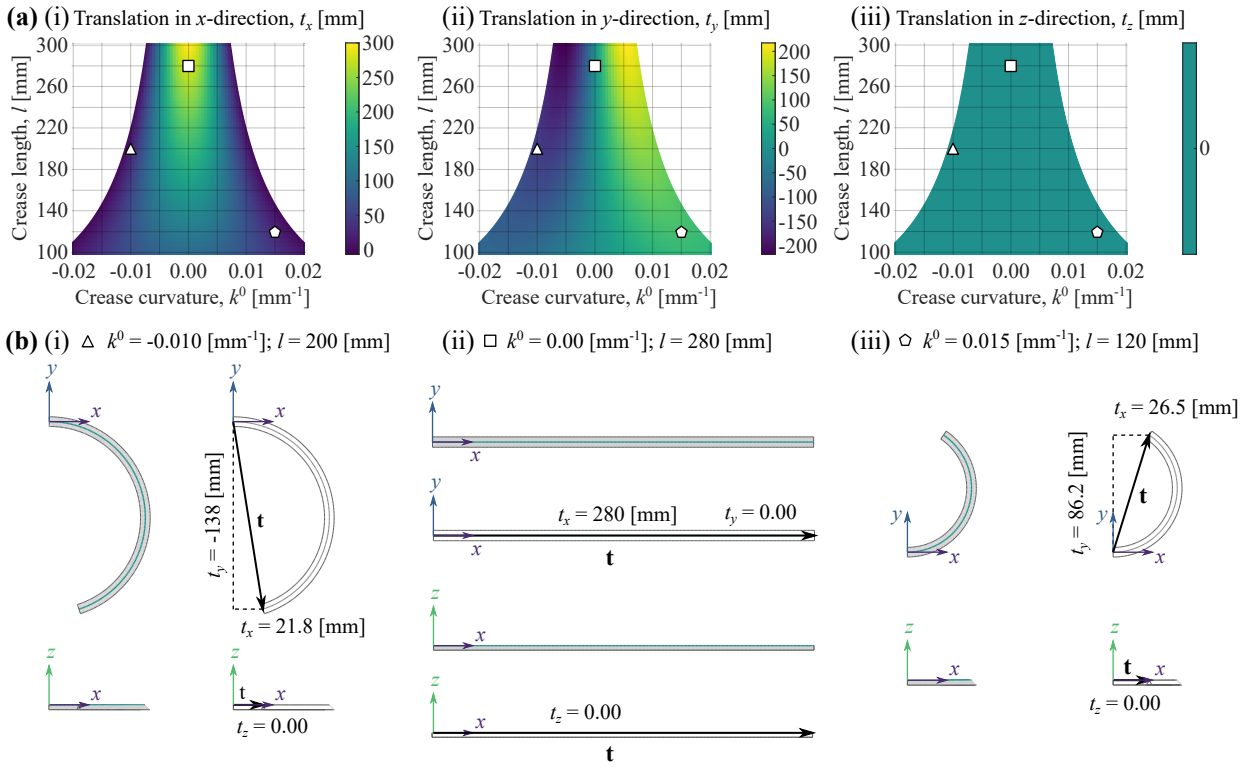

Figure 6.5 – Translation data for unpinched crease segments. **(a)** The translation components, (i) t_x, (ii) t_y, and (iii) t_z, describe the location of the connection surface for various initial crease curvatures and lengths after folding to $\phi_R = \pi/2$ [rad] (calculated from Equation 6.7). **(b)** Example deformed shapes of crease segments after folding with the three translation components shown.

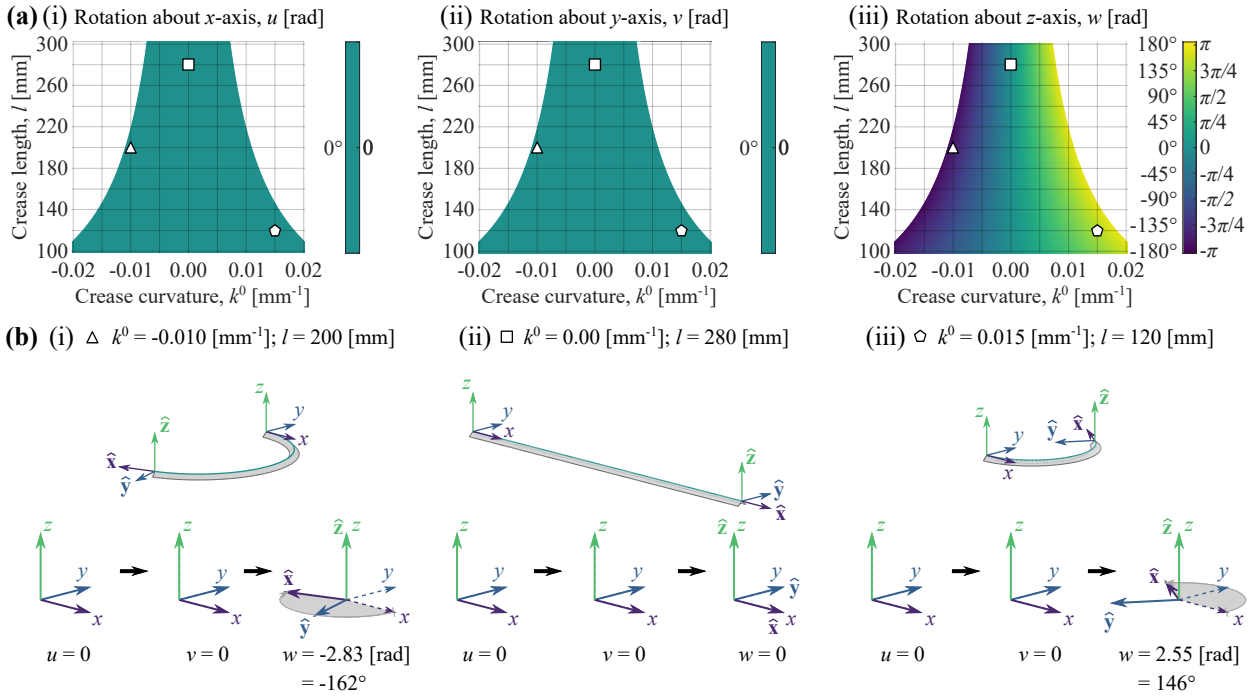

Figure 6.6 – Rotation data for unpinched crease segments. **(a)** The rotation angles, (i) u, (ii) v, and (iii) w, describe the orientation of the connection surface for various initial crease curvatures and lengths after folding to $\phi_R = \pi/2$ [rad] (calculated from Equation 6.8). **(b)** Example deformed shapes of crease segments after folding with the three rotation steps.

can extract the translation vector and rotation matrix data from the deformed shape nodes and use the values in my forward process.

First, I need to define the model parameters. For the material properties, I chose values similar to the polyester sheets used in Chapter 5. That is, the modulus of elasticity, $E = 4000$ [MPa], sheet thickness, $t = 0.1$ [mm], length scale, $L^* = 0.5$ [mm], width of sheets beside the crease, $w = 5$ [mm], and aspect ratio, $\alpha = 5$. It is important that the aspect ratio is kept constant between all crease segments to ensure a uniform deformation response (since the element stiffness is sensitive to the aspect ratio). To do so, each geometry is discretized with an identical mesh size (the distance between each node on the crease is about 1 [mm]). Therefore, longer crease segments will have more elements than shorter geometries.

Second, I need to determine the domain of the lengths that I will test and the resolution of the dataset. I start by determining a lower bound for the crease lengths. One constraint on this forward process is that the dihedral angle at the ends of each crease segment must always be the

same to ensure that the segments will fit together smoothly. I chose to fold the crease segments to $\phi_R = \pi/2$ [rad] $= 90°$, since this is a realistic angle that can be created with paper and polyester sheet prototypes with ease. Thus, the dihedral angle at the ends of any pinched crease segment should be $\pi/2$ [rad]. I found that if the crease length is less than 100 [mm], the dihedral angle at the ends of the segments might not be $\pi/2$ [rad]. Therefore, the lower bound for the crease length is 100 [mm]. I chose the upper bound for the crease length to be 300 [mm] to give a sufficiently large domain, but without adding an overwhelming amount of values to the dataset. I tested every crease length at an increment of 4 [mm] (i.e., $l_i \in \{100, 104, 108, \ \ldots, \ 296, 300\}$ [mm]) so that the mesh at the ends of the crease would be identical and to preserve the aspect ratio, $\alpha = 5$. This gives fifty-one crease lengths to test.

Finally, I need to determine the domain of the initial crease curvatures. To do so, one must consider self-intersection of the crease segment upon pinching. For certain crease curvatures and lengths, pinching might result in such large bending deformations that the ends of the crease intersect. Since the forward process does not account for collisions, such self-intersection is not permissible. I observed that when the sector angle is small enough, $\theta = |k|l = |k^0|l/\sin(\phi/2) \leq \pi$ [rad], self-intersection upon pinching does not occur. With this in mind, I can set the lower bound to a value that will fall within this constraint, considering that the lower bound for the crease lengths is 100 [mm] and the resolution is 4 [mm]. As such, I chose a lower bound of -0.02 [mm^{-1}] for the initial crease curvature. Since the constraint is symmetrical about the initial crease curvature, I chose an upper bound of 0.02 [mm^{-1}]. I tested every initial crease curvature at an increment of 5×10^{-4} [mm^{-1}], a step size that gives a meaningful difference in the deformed shape. This gives eighty-one initial crease curvatures to test.

Overall, there are, at most, 4,131 unique crease segments to fold and pinch in the bar-and-hinge model. However, many of these geometries violate the self-intersection condition and were excluded from the analysis. For the geometries that fall within the constraints, the bar-and-hinge model determined the deformed shape, which was saved for later processing. The next step was to distill the deformed shape data to the six transformation values I needed, so that I could generate a

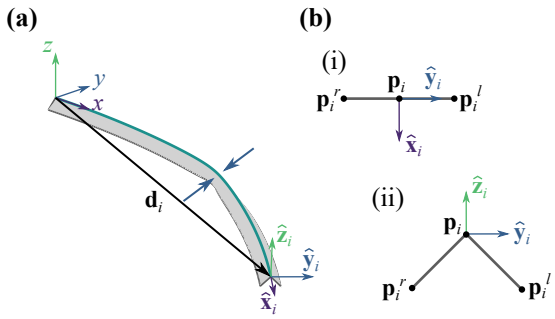

Figure 6.7 – The end of a pinched crease segment defined using three nodes. **(a)** First, the structure is folded and pinched in the local coordinate system using the bar-and-hinge method. **(b)** Next, the three nodes at the end of the structure are extracted to calculate the basis vectors used to calculate the Tait-Bryan angles for this geometry.

grid of data from which forward-process values could be interpolated.

Since every crease tested in the bar-and-hinge model was positioned and oriented identically (with the crease starting at the origin and aligned with the local x-axis), the only values I need from the bar-and-hinge deformed shape data are the positions of the three nodes at the end of the crease and sheets. Figure 6.7 shows an example geometry and the required three nodes: the position at the end of the crease, $\mathbf{p}_i$, the position at the end of the left sheet, $\mathbf{p}_i^l$, and the position at the end of the right sheet, $\mathbf{p}_i^r$.

The local translation vector for each model was found using,

$$\mathbf{t}_i = \left\{ t_x, \quad t_y, \quad t_z \right\}^{\mathrm{T}} = \mathbf{p}_i. \tag{6.9}$$

To determine the rotation angle values, I need to start by defining the plane at the end of the crease segment that must align with the other ends of the segments. I define this plane with a set of basis vectors using the three bar-and-hinge node positions. The first basis vector, $\hat{\mathbf{x}}_i$ is the normal vector to the end plane and is found with,

$$\hat{\mathbf{x}}_i = \left\{ \hat{x}_i^x, \quad \hat{x}_i^y, \quad \hat{x}_i^z \right\}^{\mathrm{T}} = \frac{(\mathbf{p}_i^r - \mathbf{p}_i) \times (\mathbf{p}_i^l - \mathbf{p}_i)}{|(\mathbf{p}_i^r - \mathbf{p}_i) \times (\mathbf{p}_i^l - \mathbf{p}_i)|}. \tag{6.10}$$

The next basis vector defines how the bottom of the sheets are oriented. I define the $\hat{\mathbf{y}}_i$ vector

as the vector aligning with the line segment between the bottom edges of the sheet using,

$$\hat{\mathbf{y}}_i = \left\{ \hat{y}_i^x, \quad \hat{y}_i^y, \quad \hat{y}_i^z \right\}^{\mathrm{T}} = \frac{\mathbf{p}_i^l - \mathbf{p}_i^r}{|\mathbf{p}_i^l - \mathbf{p}_i^r|}. \tag{6.11}$$

Finally, the last basis vector, $\hat{\mathbf{z}}_i$, must satisfy orthogonality. That is,

$$\hat{\mathbf{z}}_i = \left\{ \hat{z}_i^x, \quad \hat{z}_i^y, \quad \hat{z}_i^z \right\}^{\mathrm{T}} = \hat{\mathbf{x}}_i \times \hat{\mathbf{y}}_i. \tag{6.12}$$

Note that the $\hat{\mathbf{x}}_i$ vector is equivalent to the tangent vector at the end of the crease, and the $\hat{\mathbf{z}}_i$ vector is the unsigned binormal vector.

From these three basis vectors, one can define the rotation matrix that rotates the starting plane of the crease segment to the ending plane (i.e., the connection surface). That is,

$$\mathbf{r}_i = \left\{ \hat{\mathbf{x}}_i, \quad \hat{\mathbf{y}}_i, \quad \hat{\mathbf{z}}_i \right\} = \begin{bmatrix} \hat{x}_i^x & \hat{y}_i^x & \hat{z}_i^x \\ \hat{x}_i^y & \hat{y}_i^y & \hat{z}_i^y \\ \hat{x}_i^z & \hat{y}_i^z & \hat{z}_i^z \end{bmatrix}. \tag{6.13}$$

Again, saving all nine values in the rotation matrix would be cumbersome and unnecessary. Therefore, I calculated the Tait-Bryan rotation angles from the rotation matrix using,

$$v_i = -\arcsin(\hat{x}_i^z), \tag{6.14}$$

$$u_i = \begin{cases} \operatorname{atan2}(-\hat{y}_i^x, -\hat{z}_i^x), & \hat{x}_i^z = 1 \\ \operatorname{atan2}(\hat{y}_i^x, \hat{z}_i^x), & \hat{x}_i^z = -1 \\ \operatorname{atan2}\left(\dfrac{\hat{y}_i^z}{\cos v_i}, \dfrac{\hat{z}_i^z}{\cos v_i} \right), & \text{otherwise} \end{cases}, \tag{6.15}$$

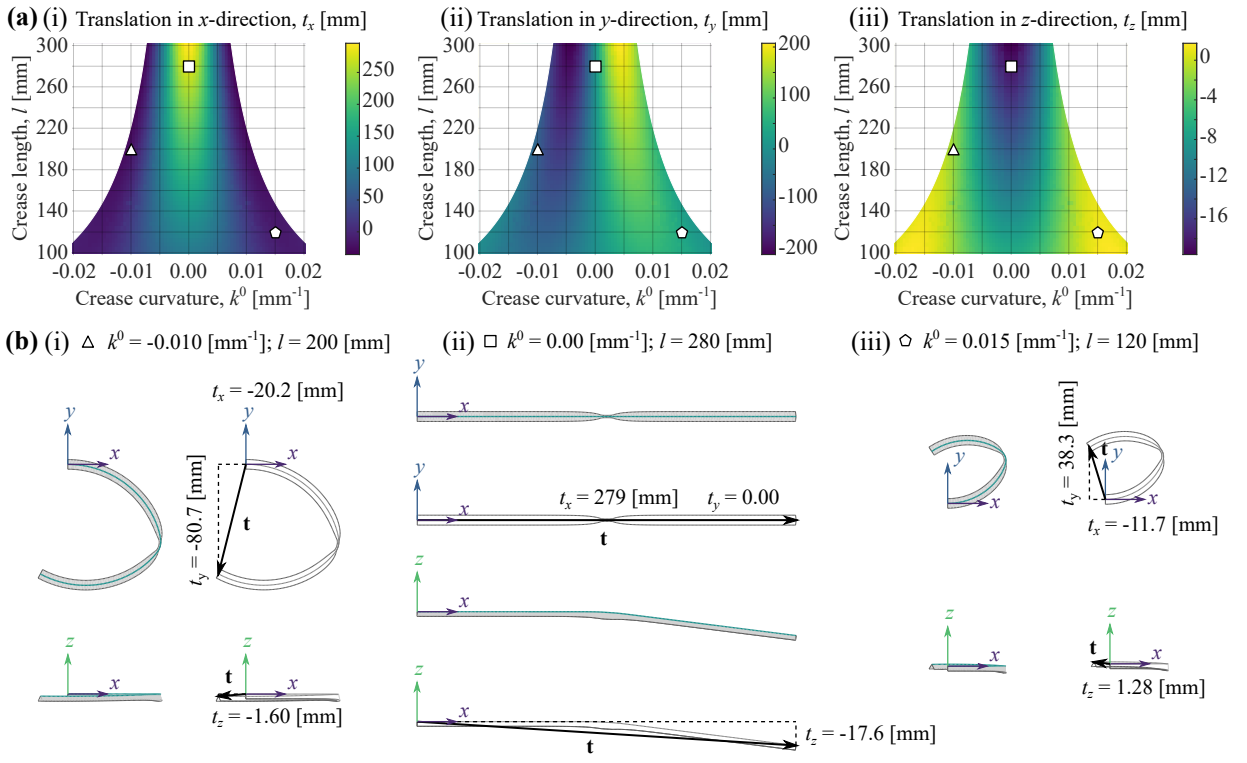

Figure 6.8 – Translation data for pinched crease segments. **(a)** The translation components, (i) t_x, (ii) t_y, and (iii) t_z, describe the location of the connection surface for various initial crease curvatures and lengths after folding to $\phi_R = \pi/2$ [rad] and pinching at mid-length to $\phi_p = \pi/14$ [rad] (calculated from Equation 6.9 using bar-and-hinge data). **(b)** Example deformed shapes of crease segments after folding and pinching with the three translation components shown.

and

$$w_i = \begin{cases} 0, & \hat{x}_i^z = \pm 1 \\ \operatorname{atan2}\left(\dfrac{\hat{x}_i^y}{\cos v_i}, \dfrac{\hat{x}_i^x}{\cos v_i}\right), & \text{otherwise} \end{cases} . \tag{6.16}$$

Note the condition for when $\hat{x}_i^z = \pm 1$. This value represents a crease that is pointing exactly up or down (parallel to the local z-axis). In this instance, the rotation loses a degree of freedom and the value of the w_i angle becomes arbitrary, a phenomenon called Gimbal lock (Slabaugh, 1999). It is unlikely that a crease segment will fold to such an extreme inclination, but consideration for Gimbal lock is included for completion.

After running the bar-and-hinge simulations and calculating the six transformation values, I saved the data for the forward-process algorithm to interpolate from later on. These data are plotted in Figures 6.8 and 6.9.

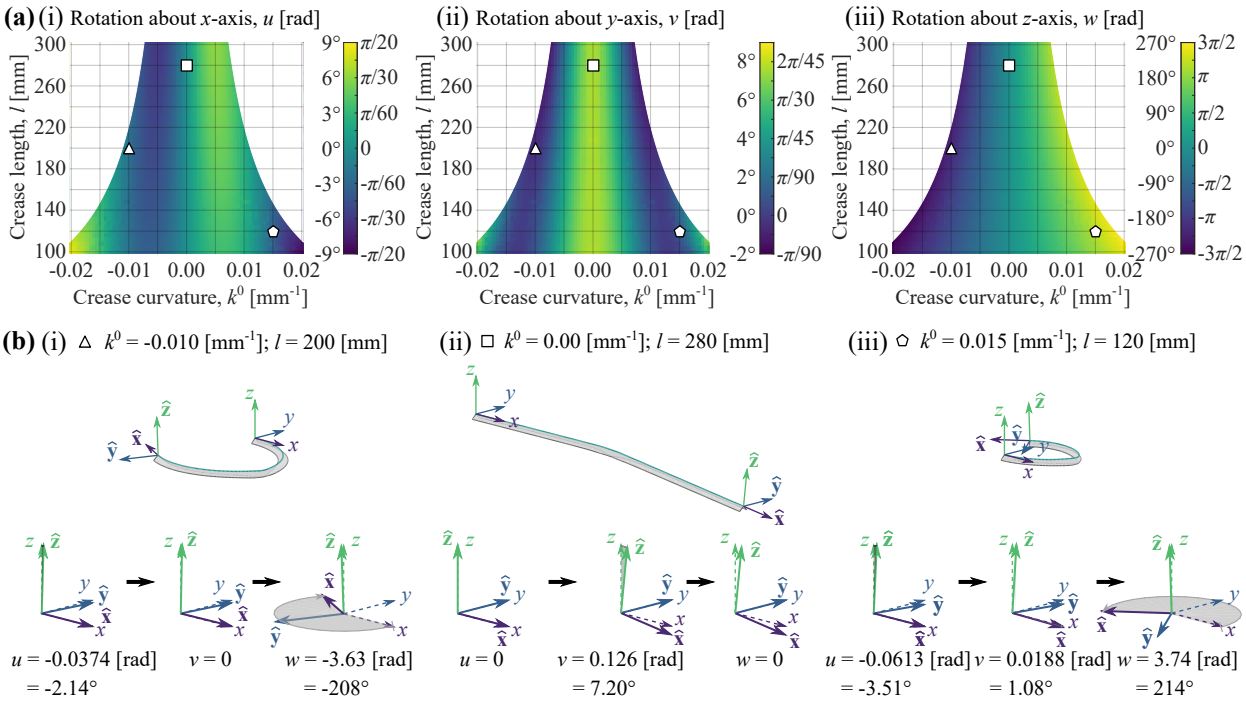

Figure 6.9 – Rotation data for pinched crease segments. **(a)** The rotation angles, (i) u, (ii) v, and (iii) w, describe the orientation of the connection surface for various initial crease curvatures and lengths after folding to $\phi_R = \pi/2$ [rad] and pinching at mid-length to $\phi_p = \pi/14$ [rad] (calculated from Equations 6.15, 6.14, and 6.16 using bar-and-hinge data). **(b)** Example deformed shapes of crease segments after folding and pinching with the three rotation steps.

With Equations 6.7 and 6.8 and the bar-and-hinge data shown in Figures 6.8 and 6.9, I can determine the local translation vector and rotation matrix for any crease segment with $k_i \in [-0.02, 0.02]$ [mm^{-1}], $l_i \in [100, 300]$ [mm], and $f_i \in \{0, 1\}$. I can use these values to find the location at the end of the crease segments using the relationships given in Section 6.2.2. Therefore, the forward process is defined.

6.3 Implementing the Inverse Design

With the forward process defined, one can find the location at the end of the crease segments with a wide variety of curvatures and pinch statuses. The solution space is made up of at least three dimensions (k_1, l_1, and f_1), with many more depending on the number of crease segments in the pattern, n. This solution space allows me to solve many inverse-design problems. I chose three different problems to exhibit the versatility of the forward process.

6.3.1 Problem Descriptions

6.3.1.1 Problem A - Fitting an Unpinched Origami to Planar Curves

For the first inverse-design problem, I consider only unpinched crease segments, limiting the target deformed crease to the original, xy-plane. Subsequently, the geometry of a crease composed of only unpinched crease segments can be calculated analytically, without the need for bar-and-hinge deformation data. Because the deformations are calculated analytically, the domains for the initial crease curvatures and crease lengths are not limited to those tested with the bar-and-hinge data. Here, the initial crease curvatures are unbounded and the crease length has a lower bound of zero. To avoid the crease from folding over itself, the sector angle after folding, $|k_i|l_i = |k_i^0|l_i/\sin(\phi/2)$, has an upper bound of 2π [rad].

Given the wide domain for the solution space and the lack of a binary input (i.e., the pinch status), one can solve complex shape-fitting problems with ease. As such, the inverse-design problem I chose involves determining a crease pattern that, upon folding, approximates the shape of a planar curve. The target curve, $\mathbf{c}_{\text{tar}}$, can be any planar curve. Here, I decided to fit the crease to segments of a parabolic curve, $\mathbf{c}_{\text{tar}}^{\text{par}}$, a logarithmic spiral, $\mathbf{c}_{\text{tar}}^{\log}$, and a single cosine wave, $\mathbf{c}_{\text{tar}}^{\cos}$. These curves are defined parametrically as,

$$\mathbf{c}_{\text{tar}}^{\text{par}} = \left\{ t,\ \frac{2t^{3/2}}{30},\ 0 \right\}^T \text{ [mm]}, \quad 0 \leq t \leq 211.6, \tag{6.17}$$

$$\mathbf{c}_{\text{tar}}^{\log} = \left\{ -e^t \cos t + 1,\ e^t \sin t,\ 0 \right\}^T \text{ [mm]}, \quad 0 \leq t \leq 5.362, \tag{6.18}$$

and

$$\mathbf{c}_{\text{tar}}^{\cos} = \left\{ t,\ 20\cos\left(\frac{t}{45.63}\right) - 20,\ 0 \right\}^T \text{ [mm]}, \quad 0 \leq t \leq 286.7. \tag{6.19}$$

Note that the arc length of each curve is 300 [mm], and the curve starts at the origin (for parameter, $t = 0$). Each curve is plotted in Figure 6.15, for reference.

To fit the folded shape of the origami to the target curves, there must be a minimal error between

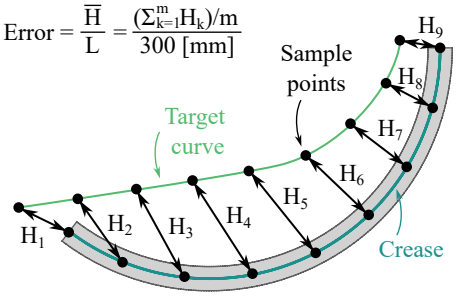

Figure 6.10 – Quantifying error between a crease pattern and a target curve. The mean distance between two sets of equally spaced points, normalized by the total length of the target crease, defines the error that the optimization aims to minimize.

the crease and the curve. The objective function is defined as the error, quantified as the mean distance between two sets of equally spaced sample points, $\bar{H}$, normalized by the total length of the target crease ($L = 300$ [mm]). See Figure 6.10 for an example.

For each target curve, I ran an optimization that searched through different initial crease curvatures and crease lengths to find a crease pattern that minimized the error. I repeated this process for different numbers of crease segments, looking to see if adding more crease segments would reduce the errors and give a better approximation of the target curve.

In summary, for the problem of fitting an unpinched origami to a planar curve, I set the optimization problem as:

$$\begin{aligned} &\text{minimize} \quad \frac{\bar{H}}{L}, \quad \text{such that :} \\ &\qquad (1) \quad l_i \geq 0; \\ &\qquad (2) \quad \frac{k_i^0 l_i}{\sin(\phi/2)} \leq 2\pi \text{ [rad]}, \quad \text{for} \quad \phi_R = \pi/2 \text{ [rad]}, \\ &\text{for} \quad i = 1, 2, \ldots, n. \end{aligned} \tag{6.20}$$

6.3.1.2 Problem B - Maximizing Tip Deflections After Pinching

The next inverse-design problem aimed to determine a crease pattern and actuation scheme that would maximize the deflection of the end of the origami from the folded state to the pinched state for a crease with n crease segments. This problem shows the extent to which a crease can deflect,

maximizing the path between the folded (neutral) and pinched (active) states.

The objective function for this problem quantifies distance between the location at end of the origami after folding, $\mathbf{P}_n^{\text{folded}}$, and after pinching, $\mathbf{P}_n^{\text{pinched}}$. Because I am maximizing the tip displacement, the objective function calculates the negative of the distance between these two points, and the optimization algorithm minimizes this value. Intuitively, more crease segments, n, should result in larger tip displacements. Thus, the minimization was performed for various crease segment numbers for comparison.

Because this problem allows the creases to be pinched, the bar-and-hinge surrogate data had to be used. This limited the domain of the search space to the crease lengths and initial crease curvatures tested in the bar-and-hinge analyses. Using interpolation, input values between the simulated crease segments could be approximated. The addition of pinching also adds an integer design variable, resulting in a non-smooth objective function.

In Problem A, unless the target curve intersects itself, or nearly does so, the optimal crease pattern should not exhibit self-intersection. However, for this problem, it is likely that a crease pattern will intersect itself. Self-intersection includes the ends of a single crease segment colliding upon pinching and other crease segments colliding due to large rotations from pinching. If the crease intersects itself before folding and pinching, the sheet would be impossible to cut from a single sheet, which would complicate construction of these structures. Additionally, self-intersection after folding and pinching would result in the sheets colliding, which would cause secondary displacements that the forward process does not account for.

Therefore, this problem is constrained in two ways to avoid collisions. The first constraint is explained in Section 6.2.4, where the sector angle of a single crease segment has an upper bound of π [rad]. To avoid crease intersections between two different segments, I created an algorithm that detects if a CP/AS results in an intersection, and determines if the CP/AS is acceptable or not. The intersection algorithm works by finding the global translation vectors, $\mathbf{T}_i$, and projecting them on to the xy-plane. The algorithm then converts the vectors into line segments and determines if the segments intersect on that plane. This algorithm is conservative in that there could be a CP/AS

whose translation vectors intersect, but the sheets themselves do not (e.g., if the crease deflects downward enough to avoid collision, such as with a helix). If one were to consider this case, they would need to know the shape of the deformed crease after pinching, which would require much more data, slowing down the algorithm.

In summary, for maximizing the tip displacement after pinching, the optimization problem is defined as:

$$\begin{aligned}
&\text{minimize} \quad -\left|\mathbf{P}_n^{\text{pinched}}(k_i^0, l_i, f_i) - \mathbf{P}_n^{\text{folded}}(k_i^0, l_i, f_i)\right|, \quad \text{such that :} \\
&\quad (1) \quad -0.02 \leq k_i^0 \leq 0.02 \ [\text{mm}^{-1}]; \\
&\quad (2) \quad 100 \leq l_i \leq 300 \ [\text{mm}]; \\
&\quad (3) \quad \frac{k_i^0 l_i}{\sin(\phi/2)} \leq \pi \ [\text{rad}], \quad \text{for} \quad \phi_R = \pi/2 \ [\text{rad}]; \\
&\quad (4) \quad \text{intersection}(k_i^0, l_i, f_i) = \text{false}, \\
&\text{for} \quad i = 1, 2, \ldots, n.
\end{aligned} \tag{6.21}$$

6.3.1.3 Problem C - Reaching a Target Point in Three Dimensions

The final inverse-design problem aimed to determine a CP/AS that upon actuation, results in the end of the origami reaching a given target point in three-dimensional space, $\mathbf{P}_{\text{tar}} \in \mathbb{R}^3$. Since the target point can be out of the original xy-plane, pinching is required to reach the full target space. Thus, the surrogate bar-and-hinge data must also be used.

The objective function for this problem is simply the distance between the end of the origami after actuation and the specified target point. Again, self-intersection is possible, so both the sector angle constraint and intersection algorithm constraint are applied.

In summary, the optimization problem for reaching a target point is defined as:

$$
\begin{aligned}
&\text{minimize} \quad |\mathbf{P}_n(k_i^0, l_i, f_i) - \mathbf{P}_{\text{tar}}|, \quad \text{such that :} \\
&\qquad (1) \quad -0.02 \leq k_i^0 \leq 0.02 \ [\text{mm}^{-1}]; \\
&\qquad (2) \quad 100 \leq l_i \leq 300 \ [\text{mm}]; \\
&\qquad (3) \quad \frac{k_i^0 l_i}{\sin(\phi/2)} \leq \pi \ [\text{rad}], \quad \text{for} \quad \phi_R = \pi/2 \ [\text{rad}]; \\
&\qquad (4) \quad \text{intersection}(k_i^0, l_i, f_i) = \text{false}, \\
&\text{for} \quad i = 1, 2, \ldots, n.
\end{aligned}
\tag{6.22}
$$

6.3.2 Problem Range and Non-Convexity

With such a broad solution space for all three inverse-design problems, finding the optimal solution can be challenging. Consider the solution space for *Problem B - Maximizing Tip Deflections After Pinching*. Figure 6.11(a-c) shows the tip displacement values for a single-segment crease for all admissible crease patterns. These plots were calculated by taking the difference between the local translation values in Figures 6.8 (pinched crease segments) and 6.5 (unpinched crease segments). The maximum displacements from a single pinched crease lie along a contour, rather than in an obvious minimum. When multiple creases are added, and the pinch status can be varied, the objective function becomes even more complex.

Figure 6.12 shows the variety of points in space that a single crease pattern can reach by varying the location of pinches. The versatility of this forward process gives a large solution space from which one will need to find a crease pattern and actuation scheme (CP/AS) that reaches a given target point.

Additionally, the objective function for point-fitting (Problem C) is, overall, non-convex. When simplifying the problem to just one crease segment with a pinch, as shown in Figure 6.13, notice that there are multiple minima for many of the target points (here, I define the objective functions as the distance between the end of the crease, $\mathbf{P}_1$ and the target point). When the target point

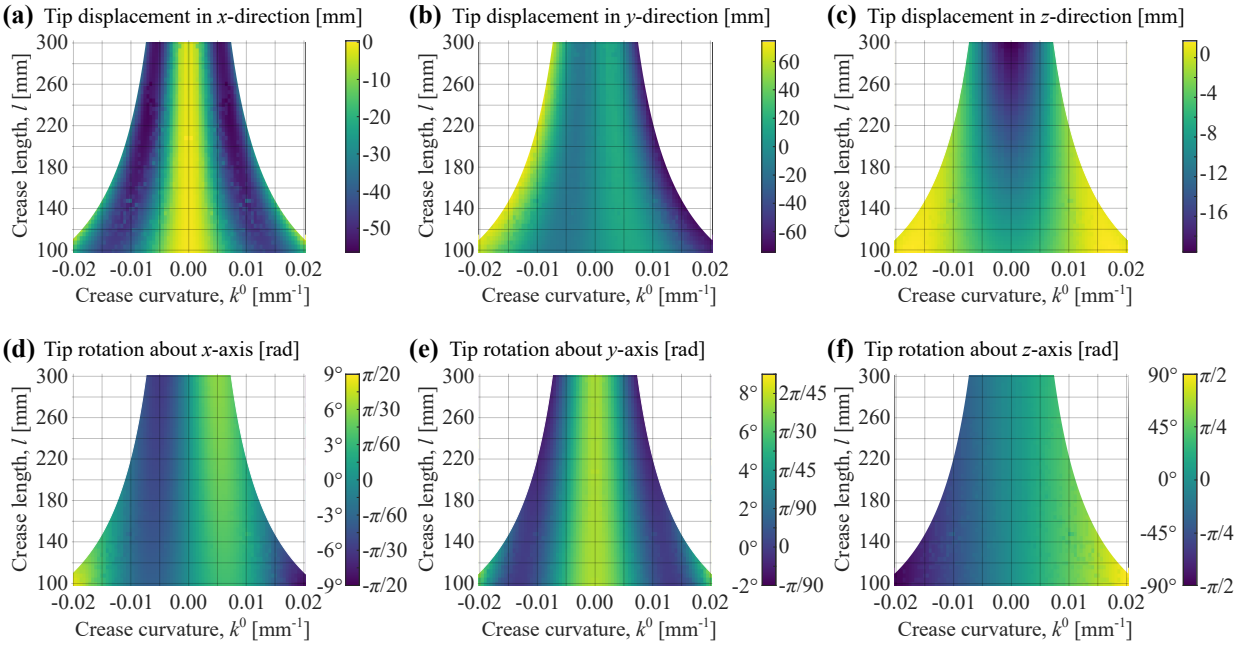

Figure 6.11 – Tip deflection and rotation data due to pinching. After a single origami crease is folded, pinching deforms the shape of the structure, leading to deflections at the tip **(a)** in the x-direction, **(b)** in the y-direction, and **(c)** in the z-direction, along with rotations of the tip **(d)** about the x-direction, **(e)** about the y-direction, and **(f)** about the z-direction

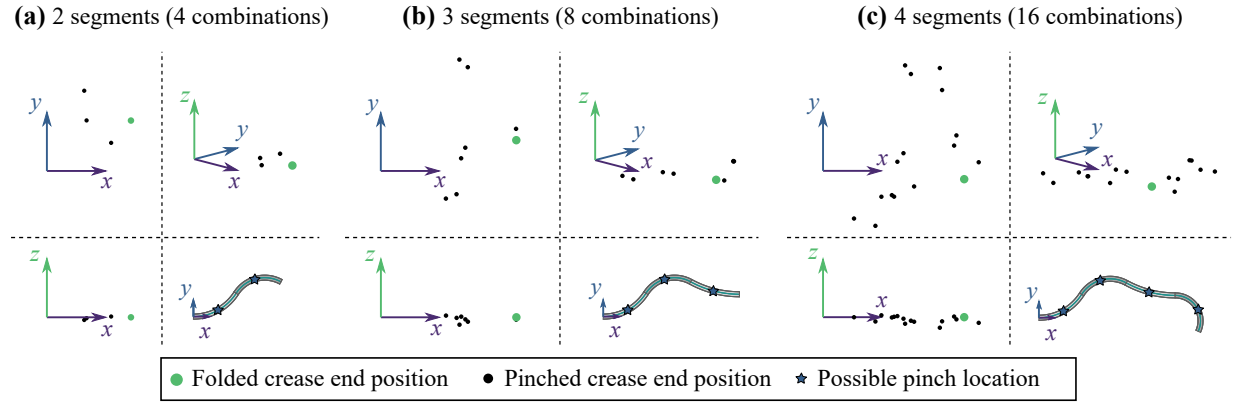

Figure 6.12 – All crease-end locations possible with various pinching combinations. A single crease pattern can reach a wide range of points in space by varying the combination of pinches on the structure, as shown for **(a)** two, **(b)** three, and **(c)** four crease segments (crease pattern and possible pinch locations shown).

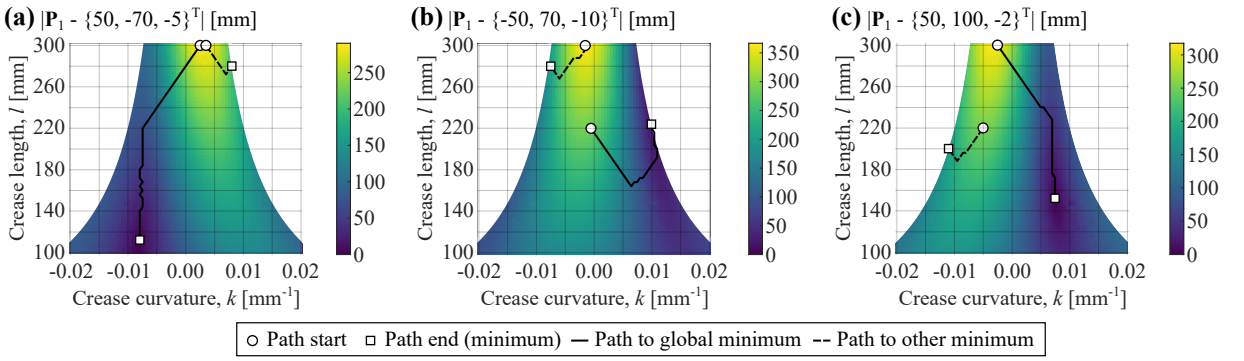

Figure 6.13 – The objective function of this problem is not usually convex. These plots show the distance between the end of a crease composed of one pinched segment, $\mathbf{P}_1$, and three different target points. The paths show a discrete descent along the objective surface towards a minimum. The paths in solid lines converge towards the global minimum, while the dashed lines do not. Multiple minima in the objective means the problem is not convex, complicating the optimization.

lies in the xy-plane, and the segment is not pinched, the function surface might be convex, but this restriction on the target points is far less interesting, since the problem is reduced to finding a circular arc that reaches the target. Including more crease segments and the option of pinching each segment or not makes the problem much more valuable to someone trying to determine a crease pattern the reaches a target in a wide variety of points in three-dimensional space, including the xy-plane.

The nature and size of the solution space poses a problem in my attempt to find the CP/AS that reaches a given target point. Since the objective function is non-convex, one cannot rely on traditional convex optimizers and nonlinear solvers for all target points. As such, I will need to use a more versatile optimizer to achieve my goal.

6.3.3 Finding Optimal Solutions with a Genetic Algorithm

The objective functions for these problem are all non-linear, often non-convex, and non-smooth for Problems B and C (since the pinch status gives an integer parameter). As such, I will need to use an optimization method capable of searching such a space. The method I chose to use to solve these problems is a guided, random-search method called a genetic algorithm (GA). Unlike traditional, gradient-based optimization methods, GA does not calculate partial derivatives of the objective function (or fitness function, a term commonly used in GA). This allows one to find minima for

problems with integer or binary inputs. Furthermore, GA is well suited to find the global minimum of a fitness function, and is robust against non-convex problems (Sivanandam and Deepa, 2008; Arora, 2015).

Given the complexity of the fitness functions I am interested in searching, GA is a reasonable option that will find a CP/AS that minimizes each problem. The major limitation of GA is that running the optimization typically takes longer than gradient-based methods. However, because the forward process uses closed-form equations and surrogate data collected from the bar-and-hinge method, the computational cost will be much less than if the deformed shape of the origami had to be analyzed using a mechanics-based method in real-time. Additionally, GA is considered a "black-box" process, so the action of finding the global minimum is more complicated than calculating a gradient. However, the CP/AS found using the GA can be tested with the forward process to ensure the objective has been met and meets the problem constraints. Moreover, GA has been used to solve complex problems in the geometric design and mechanics of metamaterials and thin-sheet structures with great success (Jha and Dayyani, 2021; Pokkalla et al., 2021; Cimolai et al., 2022).

GA is analogous to biological evolution, where "survival of the fittest" generates sufficient solutions to problems. Unlike evolution, I determine how fitness is measured. The fitness functions used in each problem are the objective functions described in Equations 6.20, 6.21, and 6.22.

For these problems, the GA works by generating a population of CP/AS with random input values. Then, the population is evaluated for, and sorted by, fitness using the fitness measure. The fittest portion of the population will crossover traits (analogous to sexual reproduction and the exchange of chromosomes between parents) and generate a new generation of CP/AS children with traits from the fittest parents. In these problems, the traits of the individuals are the initial crease curvature, crease length, and pinch status (for Problems B and C) of the CP/AS, encoded into binary strings that exchange bits during crossover. Some children CP/AS will undergo random mutations in their input parameters, allowing the algorithm to explore other parts of the fitness function if the population is converging towards a local minimum that is not the global minimum.

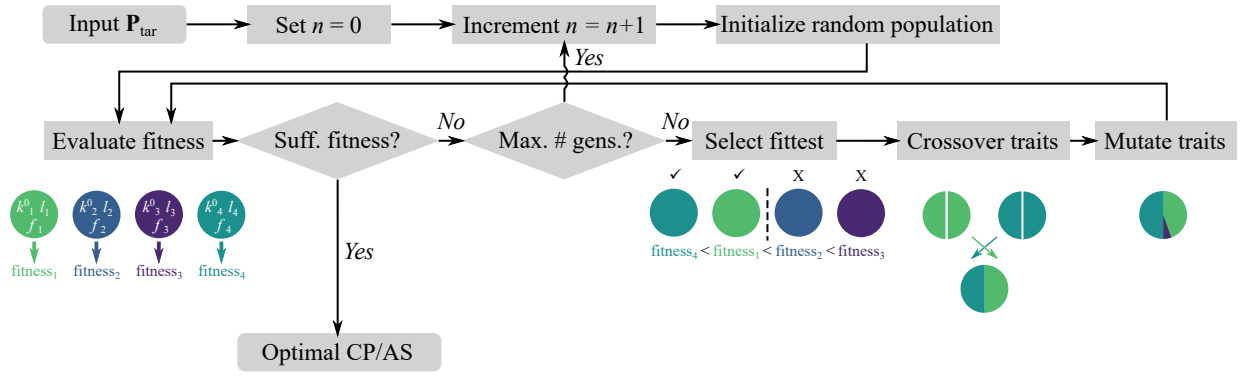

Figure 6.14 – Inverse-design scheme for Problem C with genetic algorithm. The user begins by inputting a target point for the crease to reach at its end. Then, the algorithm loops through an increasing number of crease segments, using the genetic algorithm (GA) to find a crease pattern and actuation scheme (CP/AS) that gives a sufficient fitness ($|\mathbf{P}_n - \mathbf{P}_{\text{tar}}| \leq 1$ [mm]). This algorithm excels at finding solutions in a non-linear, non-convex, and non-smooth fitness function, such as the one given in this problem.

The process of generating a new population and evaluating the fitness of each individual continues until either a CP/AS gives a sufficient solution, the change in fitness is negligible, or if the number of generations (loops) exceeds a set value. For Problem A, the algorithm stops when the average error is less than 1 [mm]. For Problem B, there is no sufficient solution limit, and the algorithm stops when the change in fitness is negligible. For Problem C, the algorithm stops when the distance between the target point and crease end are within 1 [mm].

For Problems A and B, I looked for the optimal solution for various crease segment numbers, looking to see how the number of creases impacts the shape-fitting. For Problem C, I looked for a CP/AS that reached the target point, regardless of the number of creases. Although there is no explicit consideration for the length of the crease in the fitness functions, implicitly I limited the crease length by setting the number of crease segments, n, to one, attempting to find a solution with the GA, and adding segments until a solution was found. Figure 6.14 shows a flowchart explaining the algorithm for Problem C.

I used the `ga()` function in MATLAB to implement the optimization algorithm and find minimal solutions to the three inverse-design problems. The options I used in the analysis follow the recommended parameters for each type of problem (e.g., problems with linear constraints, integer variables, etc.) for the MATLAB function (MathWorks, 2022). In cases where an optimal solution

that satisfied the minimum fitness was not found, parameters such as the function tolerance and maximum number of generations were altered until an appropriate solution was found.

6.4 Results and Discussion

6.4.1 Problem A - Fitting an Unpinched Origami to Planar Curves

For each of the three target curves, $\mathbf{c}_{\text{tar}}^{\text{par}}$, $\mathbf{c}_{\text{tar}}^{\log}$, and $\mathbf{c}_{\text{tar}}^{\cos}$, the GA was used to minimize the error between the target and the folded crease geometry. The optimization was performed for $n = 1, 2, \ldots, 6$. Figure 6.15 shows the results of the optimization process.

For all three target curves, the error between a single folded crease segment and the target curve is always large compared to two or more crease segments. This is because a single crease segment has a constant curvature, which does not approximate the actual curvature of the target curves over their arc lengths very well. Figure 6.16 shows these curvature profiles for each target curve. Notice that the curvature of the logarithmic spiral has a large slope along its length. Having constant curvature segments (flat curvature profiles) approximating this highly inclined curvature profile would be erroneous, even with many segments.

Compare that to the curvature profile of the cosine wave. Notice that the slope of the curvature profile is not as large as the logarithmic spiral's curvature profile. As such, constant curvature arcs can better approximate the shape of the cosine wave. As more crease segments are added to the crease pattern, the errors tend to reduce. However, having only two crease segments gives a significantly better approximation than just one crease segment, with diminishing improvements as crease segments are added. The largest discrepancies between the target curve and the optimal folded crease tend to occur where the slope of the curvature profile is large (i.e., where the curvature is changing quickly along the length of the curve).

The GA along with my forward process was able to approximate the shape of planar curves well and returns crease patterns that fold to the desired shape.

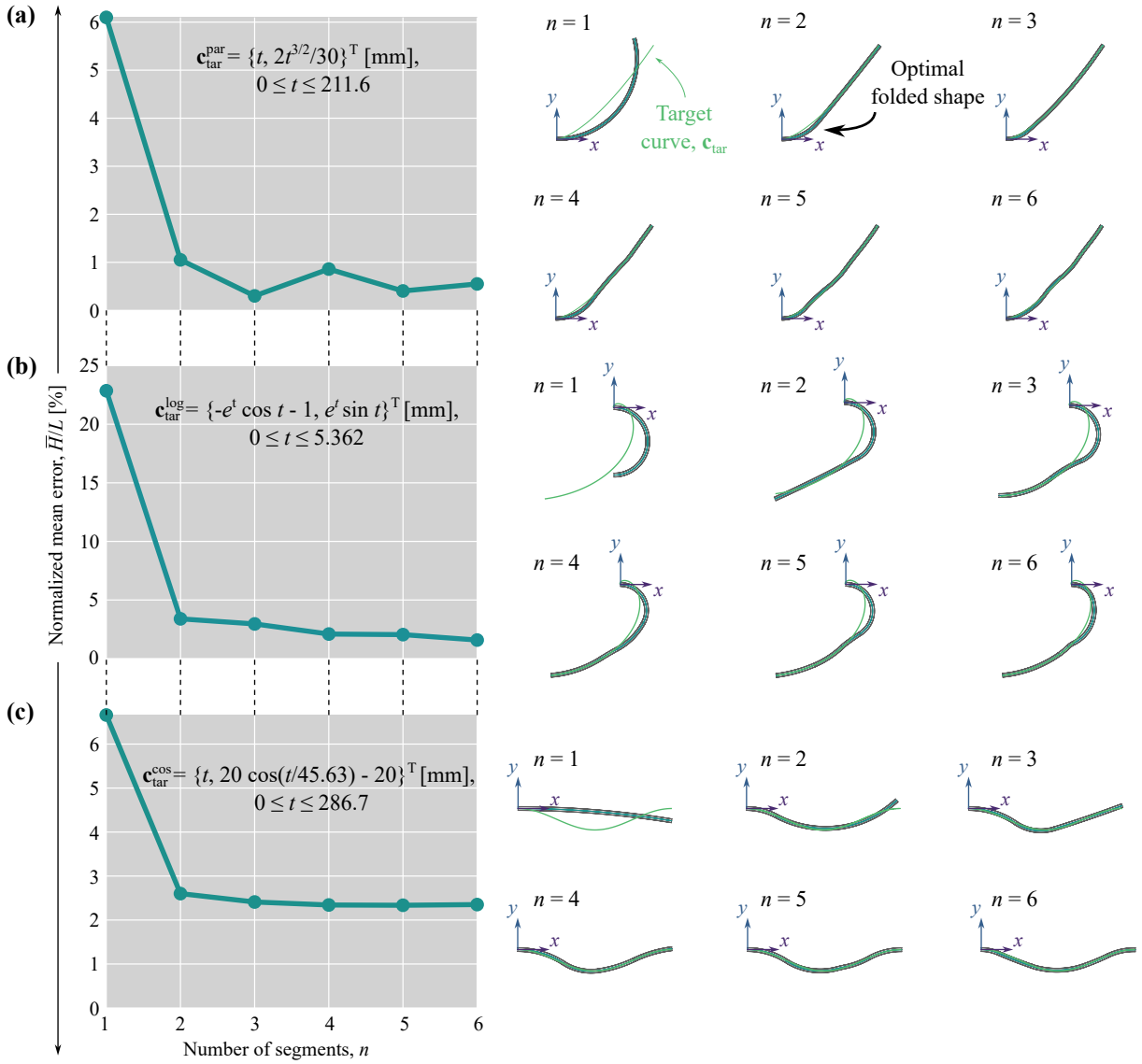

Figure 6.15 – Shape fitting unpinched creases to planar curves. A target curve segment, $\mathbf{c}_{\text{tar}}$ was defined for **(a)** a parabolic curve, **(b)** a logarithmic spiral, and **(c)** a single cosine wave, each with an arc length of 300 [mm] and a starting point on the origin. The genetic algorithm was used to find the initial crease curvatures and lengths that fit the target curve with minimal error. The plots show the average error between the folded crease and the target curve normalized by the arc length, $\bar{H}/L$. The shapes on the right show the folded origami against the target curves for various crease segment numbers.

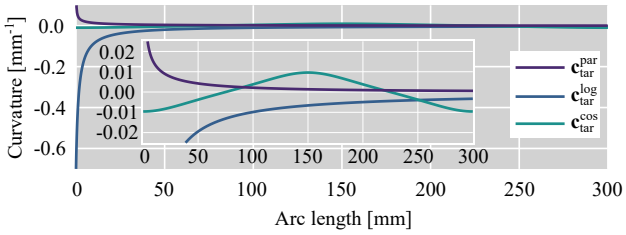

Figure 6.16 – Curvature of the target curves. Since the circular arc crease segments have constant curvature, the curves with lower variation in the curvature along the arc length will result in better shape fitting. Inset plot shows the same values, but with a zoomed-in vertical axis to better distinguish between the curvature values further from the start of the curve.

6.4.2 Problem B - Maximizing the Tip Deflection After Pinching

Moving from a two-dimensional target shape to three dimensions, I used the genetic algorithm and vector representation of the origami crease to determine the CP/AS that would maximize the tip deflection from the folded to the pinched state for $n = 1, 2, 3,$ and 4 crease segments. Figure 6.17 shows the results of this analysis.

As predicted by the tip deflection plots in Figure 6.11, the CP/AS with maximal displacement for a single crease segment is pinched, has a moderate curvature, and longer, but not the longest, length. To maximize the deflection, the CP/AS must balance the amount of bending and twisting that occur from a pinch. If the crease has too large of a curvature and length, the end of the crease tends to rotate back up towards the original xy-plane, limiting the deflection in the z-direction. As expected, the single crease segment gives the smallest displacement magnitude compared to CP/AS with more crease segments.

One pattern that appeared in the analysis was that the first crease segment was always moderately curved and long, and always pinched. Additionally, the subsequent crease segments were nearly, but not exactly, straight and very long. These low-curvature segments were sometimes pinched and sometimes unpinched, depending on the sign of the curvature and whether pinching would bend the crease further from the folded tip. This suggests that most of the deflection is caused by the bending and twisting of the first crease segment, and the other segments simply extend the tip further from the origin. Figure 6.17(c) confirms this result, showing that as more crease segments are added, the tip displacement magnitude increases nearly linearly.

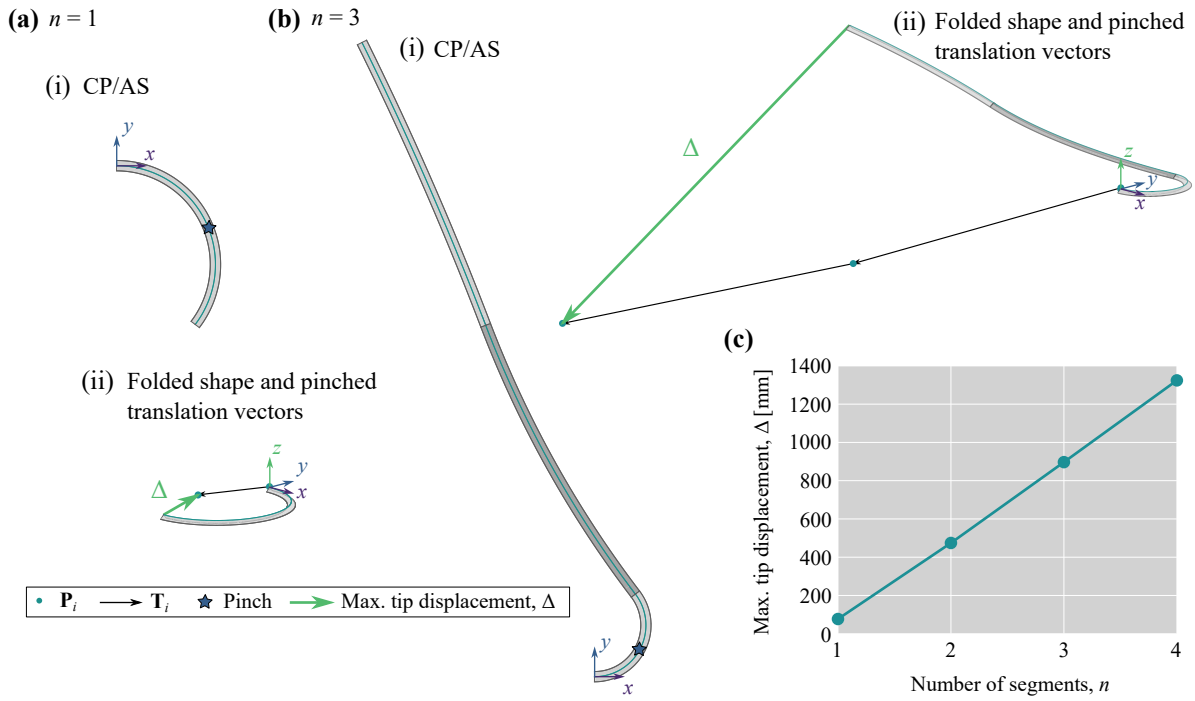

Figure 6.17 – The maximum tip displacement for n segments. Once the origami structure is folded, the tip displacement is measured as the distance between the end of the structure before and after pinching. The maximum tip displacement for n crease segments was found: **(a)** for $n = 1$, the (i) CP/AS and (ii) folded shape and translation vectors are shown. Similarly for **(b)** $n = 3$. **(c)** Maximum tip displacements are plotted versus the number of segments.

Although the forward process is not capable of modeling the nonlinear path that the end of the crease takes during pinching, this optimization shows the extent to which a crease can deflect upon actuation, setting an upper bound for use in applications of this origami structure.

6.4.3 Problem C - Reaching a Target Point in Three Dimensions

For the final inverse-design problem, the aim was to exhibit the wide range of positions that the end of a crease can hit in three dimensions. I implemented the inverse-design scheme for 605 target points spread evenly around the starting point of the crease, $\mathbf{P}_0 = \mathbf{0}$, with the tangent at the start of the crease aligned with the global x-axis ($\mathbf{R}_0 = \mathbf{I}$). For all 605 input target points, a CP/AS was found that satisfies the constraints. The target points fall within the sets: $P^x_{\text{tar}} \in \{-100, -80, \ldots, 80, 100\}$ [mm], $P^y_{\text{tar}} \in \{-100, -80, \ldots, 80, 100\}$ [mm], and $P^z_{\text{tar}} \in \{-10, -5, 0, 5, 10\}$ [mm] (where $\mathbf{P}_{\text{tar}} = \{P^x_{\text{tar}}, P^y_{\text{tar}}, P^z_{\text{tar}}\}^T$). For each target point, the inverse design algorithm found a number of segments, n, initial crease curvatures, k^0_i, crease lengths, l_i,

and pinch statuses, f_i (for $i = 1, 2, \ldots, n$). After each CP/AS was found, I confirmed that the design met the constraints set in the problem and gave a crease end within 1 [mm] of the target point. Additionally, I recorded the total length of the crease, $L = \sum_{i=1}^{n} l_i$. Figure 6.18(a) shows color plots where the center of each cell represents the location of the target point and the color of the cell represents the total crease length. Each plot shows a different P^z_{tar} value, representing planes parallel to the xy-plane.

One pattern that is important to notice is that the plots are symmetrical about the P^x_{tar}-axis. For all the CP/AS found, the initial crease tangent aligns with this axis of symmetry, so a pattern with some sign for all initial crease curvatures will generate crease end locations opposite in the P^y_{tar} space for a CP/AS with the opposite signs (i.e., $P^y_{\text{tar}}(-\mathbf{k}^0) = -P^y_{\text{tar}}(\mathbf{k}^0)$). Recognizing this symmetry is useful for reducing the target points needed to put into the inverse design scheme in the future.

Next, consider the plot representing the plane $P^z_{\text{tar}} = 0$. Since this is the plane that the crease lies in before pinching, it makes sense that solutions here will not contain pinched crease segments. Additionally, some of the shortest total crease lengths are also found on this plane, noticeably in the positive P^x_{tar}-quadrants. Recall that the shortest crease length allowed in the problem is 100 [mm], so a curved contour of relatively short solutions (the darkest purple color) appears, starting from $\mathbf{P}_{\text{tar}} = \{100, 0, 0\}^T$ and sweeping around in a nearly circular pattern. These solutions represent CP/AS with a single crease segment. The negative P^x_{tar}-quadrants give longer total crease lengths since I imposed the constraint on sector angles, forcing the optimizer to find a solution with at least two crease segments. Figure 6.18(ii) shows the global translation vectors and CP/AS for a solution on this plane.

Additionally, the other plots representing planes offset from the xy-plane show important patterns. Here, pinching must occur for the end of the crease to reach a place off the original plane. The pinching might occur throughout the crease pattern (as with the example solution shown in Figure 6.18(i)) or only at the first crease (as with the example shown in Figure 6.18(iii)). In the plot for $P^z_{\text{tar}} = -5$ [mm], there is (to a lesser extent) a contour of shorter total crease lengths along

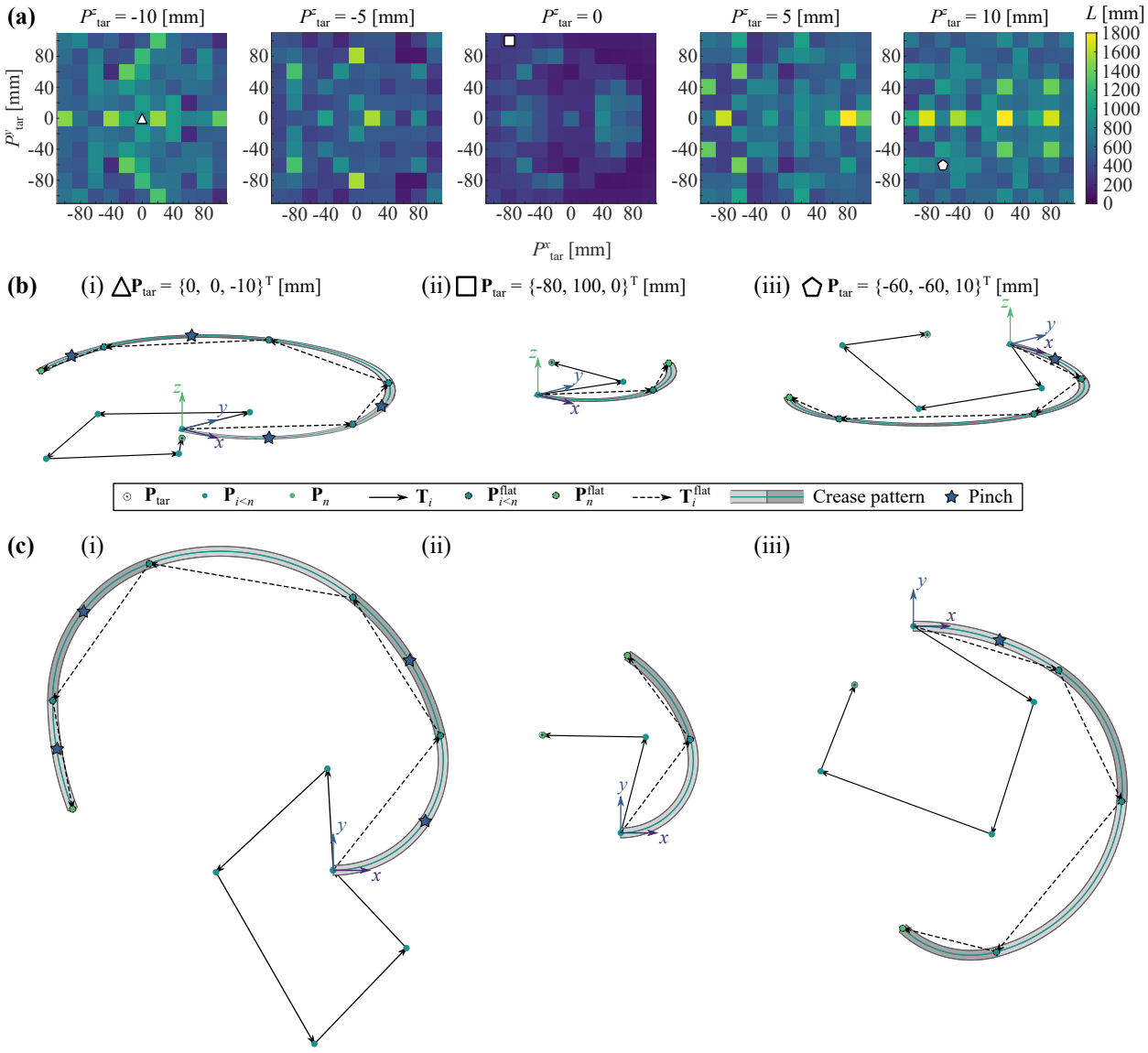

Figure 6.18 – Finding a crease pattern that reaches a target point in $\mathbb{R}^3$ results. A crease pattern and actuation scheme was found using the optimization method for target points at discrete locations near the starting position of the crease ($\mathbf{P}_0$). **(a)** The center of each cell represents the location of the target point, $\mathbf{P}_{\text{tar}} = \{P^x_{\text{tar}}, P^y_{\text{tar}}, P^z_{\text{tar}}\}$, with the color/shade indicating the total length of the crease, L. **(b)** The translation vectors of the solutions indicated in the plots, represented by the white polygon markers: (i) a triangle ($\mathbf{P}_{\text{tar}} = \{0, 0, -10\}$ [mm]), (ii) a square ($\mathbf{P}_{\text{tar}} = \{-80, 100, 0\}$ [mm]), and (iii) a pentagon ($\mathbf{P}_{\text{tar}} = \{-60, -60, 10\}$ [mm]), showing the crease ends reaching the target points. **(c)** The corresponding crease pattern and actuation scheme for the three example solutions.

a nearly circular path in the positive P_{tar}^{x}-quadrants. These CP/AS solutions also contain only one crease segment, but this time, the segment is pinched. Notice that the contour does not exist in the $P_{\text{tar}}^{z} = 5$ [mm] plane. This is because pinching a single crease causes downward deflections for most shorter creases. However, a single crease can twist far enough to deflect into the positive P_{tar}^{z}-planes, as seen in the negative P_{tar}^{x}-quadrants of the same plot. Finally, some of the longest creases are found on the P_{tar}^{x}-axis. This is because to reach a point off the xy-plane, a crease must contain a pinched segment with non-zero curvature (a pinched straight-crease origami will not generate significant twisting and P_{tar}^{z}-deflections). However, pinching a single crease with non-zero initial crease curvature will also generate bending and deflections from the P_{tar}^{x}-axis. Thus, to find a point on the P_{tar}^{x}-axis, the crease must revolve around the origin of the crease, resulting in a high total crease length.

Besides these patterns, the results for the total crease length appear mostly random. This is because our fitness function did not explicitly consider crease length. Although the algorithm looped through different numbers of crease segments starting from one, I ended the genetic algorithm (GA) after only 100 generations. This time-saving analysis parameter might have ended the analysis for a smaller number of creases prematurely, and the algorithm simply moved on to a CP/AS with more segments. If one were interested in designing CP/AS using a little material as possible, they should reformulate the optimization problem to include crease length in the calculation directly, either in the fitness function itself or with a multi-objective analysis. However, my analyses have shown that constraining the problem with considerations for crease length results in much longer GA run times and less reliability in finding a sufficient CP/AS.

One interesting behavior of pinched curved-crease origami is that the amount of twisting and bending increases smoothly with the amount of pinching applied (as measured by decreases in the dihedral angle, ϕ_p). This means that even more solutions can be found using many different pinch intensities. However, implementing this degree of freedom would likely make the solution space even more difficult to search and would require additional bar-and-hinge data for the GA to interpolate from. If a designer were interested in determining the path that the end of a crease follows

during pinching, such a result could be found using our inverse design scheme, but supplemented with this additional data.

Finally, these solutions represent target points only near the origin of the crease. The value of looking in this location is that given the constraints of the problem (I do not want the crease to self-intersect), these solutions are more difficult to find than solutions for target points farther from the crease origin and near the xy-plane. One could refine the self-intersection algorithm to determine if a crease is looping underneath or above itself, without intersection, to allow the inverse design scheme to find solutions at more extreme P^z_{tar} values while potentially limiting the total crease length.

6.5 Conclusions

In this chapter, I took my understanding of the deformation response of pinched, curved-crease origami and applied it to three inverse-design problems that find CP/AS composed of discrete circular arc segments that, (1) approximate a planar curve, (2) maximize the deflection of th end of the crease during pinching, and (3) give an end that reaches a given target point in three-dimensional space. I formulated a vector representation of a crease composed of both pinched and unpinched crease segments with some initial curvature and length. The unpinched crease segments could be analyzed with closed-form equations derived from geometry. The pinched segments were analyzed using deformation data generated from a bar-and-hinge model of the origami structures. With these data and equations, I implemented my inverse-design algorithm that includes a genetic algorithm to find an optimal CP/AS solution for each of the three minimization problems.

Although these problems include many degrees of freedom, the algorithm was able to find a CP/AS for that satisfied the objective and constraints. Given the complexity of these problems, the inverse-design scheme allows a designer to find a crease pattern and actuation scheme that reaches a desired shape or deflection with high reliability. This practical solution shows the wide variety of shapes that a single curved crease can take (even when limiting the shape to discrete circular crease segments). While other research has used repeated cells of origami to find some

target shape (see Fuchi and Diaz (2013); Dudte et al. (2016)), this research confirms that one can use a single crease, with fewer folding connections with high failure risk, to meet geometric design requirements. The work from this chapter is the first to explore shape-fitting of curved-crease origami, showing the potential that curved creases have for engineering design.

I could continue this path of research by refining the inverse-design scheme to fit an origami structure to many points in three-dimensional space or by including multiple creases to potentially decouple twisting and bending deformations for more versatile solutions. Further work can formulate an inverse-design scheme that includes consideration for limiting material in the design or meeting other needs, such as plotting deformation paths as a crease is pinched. Applications for pinch-actuated origami structures range from soft robotics to intelligent infrastructure systems that require a known actuated geometry and would benefit from the lightweight, easy-to-fabricate, and strong properties of curved-crease origami.

Chapter 7

Conclusions and Future Work

The goal of this dissertation was to explore the mechanics of curved-crease origami and identify beneficial properties for structural design, including stiffness control and shape morphing. To explore the behaviors of curved-crease origami I pursued three interrelated research aims. The first aim sought to develop a rapid simulation tool for the folding and post-fold loading of origami to generate structural data for a wide variety of geometries, such as the deformed shape and reaction forces. The second aim sought to explore how curved creases can be used to tune the stiffness of structures through reorientation of material, while maintaining the constructability of the structure. The final aim sought to explore how the shape of origami could be controlled using simple actuations, displaying the design freedom that curved-crease origami offers to engineers. The information found in this dissertation forms a starting point for applications of curved-crease origami by providing evidence for the benefits of these structures, developing an understanding of the underlying mechanics, and generating methods that advance research and might allow engineers to implement these designs in the future.

7.1 Dissertation Contributions and Broader Impacts

In this dissertation, I introduced curved-crease origami, giving an engineering-centered definition and by discussing the benefits that these structures might offer based on what little research has been generated prior. I distinguished curved-crease origami from traditional straight-crease origami, showing that many of the common categories and assumptions made about straight-crease origami do not apply to curved-crease geometries. I moved beyond mathematical definitions of

curved-crease origami by considering post-fold loading that might result in non-isometric deformations of the sheet. Ultimately, I framed the analysis of curved-crease origami as a problem of folding flat sheets to some functional state. This definition revealed unsolved problems with curved-crease structures, which led to the goals of the dissertation.

In Chapter 2, I reviewed existing applications of curved-crease origami in the fields of art, architecture, and engineering, showing that engineers have already exploited (to a limited degree) the benefits of simple curved-crease designs. I also reviewed existing methods for analyzing the deformed shape and structural properties of curved-crease origami. These methods include: (1) closed-form, geometry-based analysis, (2) numerical, geometry-based analysis, (3) isometric, mechanics-based methods, and (4) non-isometric, mechanics-based methods. From this literature review, the limitations of existing designs and analysis methods were revealed and the overall lack of research about curved-crease origami was noted, which motivated the work in subsequent chapters.

In Chapter 3, I developed a simplified, mechanics-based method for modeling the folding and post-fold loading of origami called the bar-and-hinge method. This tool modeled origami using three elements: (1) truss bars to capture in-plane sheet deformations (shearing and stretching), (2) bending hinges to capture sheet bending, and (3) folding hinges that capture crease rotations. I derived the stiffness of these elements based on the material properties of the sheet and the crease-pattern geometry using different models and calibration techniques. I verified the stiffness of these elements against theoretical solutions to problems in mechanics, isometric theory of deformations, and laser-scanned paper prototypes. Once the model was verified, I applied it to explore the complex structural behaviors of curved-crease sheets, such as calculating the stiffness of a cantilevered creased annulus sector in three-dimensions, profiling the large-deformation response of the same cantilevered structure, and showing how the stiffness of a pinched fan is highly anisotropic and changes during actuation. This chapter established the most common method for analyzing a wide variety of curved-crease origami in the rest of the dissertation, given its speed and reliability, effectively addressing the first aim of the dissertation. Furthermore, the bar-and-hinge

model is a new method for analysis that has been made public to researchers interested in performing rapid parameter-sweep studies on many curved-crease origami geometries (Woodruff and Filipov, 2020a). While the bar-and-hinge model is a reduced-order model, it provides a wealth of information including, the folded shape in equilibrium, stiffness characteristics, large deformation analysis, and local actuation. The model is easy to use and has the potential to open up the field of curved-crease origami.

In Chapter 4, I showed how curved creases can reorient material in a thin-sheet corrugation to generate an isotropic bending stiffness response. I created a qualitative framework that describes the corrugations and how different features of the geometry contribute to the global bending stiffness. I then created two quantitative analysis methods that predict the relative stiffness of any corrugation. I applied my framework and methods to five corrugation designs, one straight-crease corrugation and four curved-crease structures. I found that curved creases reorient depth in the structure's cross-section, which for certain geometries leads to an isotropic bending response. With curved creases, these corrugations can now behave more similarly to a plate, which can be rotated, supported on different edges, and will resist transverse loading, regardless of load orientation. I confirmed these findings with experimental, three-point bending tests of polyester-film specimens and found strong agreement. This chapter addressed the second aim of the dissertation, exploring a mechanism for how curved-creases can be used to tune the stiffness of thin-sheet structures. The structures generated in this chapter represent the first examples of linerboard-free corrugations that can support loads with an isotropic bending behavior. Moreover, the methods developed in this chapter can be used for other corrugations to predict, analyze, and ultimately design the performance of other curved-crease origami corrugations.

In Chapter 5, I introduced a unique behavior of origami whereby pinching a folded crease, one can generate global bending and/or twisting deformations. I explained this response, partially, using isometric deformation theory. Given the limitations of isometric deformations, I performed numerical simulations of pinched origami using the bar-and-hinge method. I found that for a single crease, pinching generates increased crease curvature and torsion near the pinch, proportional to the

initial crease curvature before folding. I continued my investigation by seeing how multiple creases responded to pinching. I found that the number of creases had a strong effect on the amount of twisting displayed by the structure. I also found that the spacing between creases had a strong effect on the amount of bending and twisting that the structure displays after pinching. I demonstrated my findings by generating four crease patterns that displayed decoupled bending and twisting, depending on the initial crease curvature and number of creases used in the pattern. This chapter addressed the third aim of the dissertation, showing how a simple actuation and specific crease design could be used to generate versatile behaviors.

In Chapter 6, I continued to address the third aim of the dissertation by taking what was learned in the previous chapter and applying it to an inverse-design scheme. I described three shape-fitting problems that give a crease pattern and actuation scheme that will generate some desired shape or deflection. I developed the forward process that calculates the location at the end of the crease using vector math and bar-and-hinge data. I then applied the forward method to a genetic algorithm to form the inverse-design process. By the end of this chapter, I was able to determine a crease pattern design that would approximate given shapes and deflections with high reliability. This chapter demonstrates how curved-crease origami offers versatile designs that can meet the needs of engineers. This chapter also forms a starting point for future curved-crease origami optimization in areas such as shape-fitting, the design of metamaterial behavior, and tuning of the structural behaviors of curved-crease origami.

7.2 Directions of Future Work

From this dissertation, there are many directions for future work that build off the analyses and methods shown in the prior chapters. Additional work in the area of curved-crease origami structures will help facilitate practical design and implementation of this technology, helping engineers exploit the benefits that these systems offer. The following text suggests what directions are most meaningful to pursue in order to achieve this goal.

7.2.1 Continuing Work From the Dissertation

The work presented in Chapters 3-6, while complete, offer directions of future work that could be pursued in the near term. For instance, with the bar-and-hinge method, I was able to simulate the global behavior of a wide variety of curved-crease origami structures with high convergence and speed, compared to finite elements. However, the bar-and-hinge method cannot analyze the local behaviors of structures, such as stress concentrations, fractures, or wrinkling. If an engineer is interested in the local behavior of a curved-crease structure and requires a method that will converge reliably and quickly, there are no such existing solutions. It would be worthwhile to implement a method that balances speed and result resolution. One such method that could address these constraints is isogeometric analysis.

Isogeometric analysis is similar to finite element analysis (Cottrell et al., 2009). However, instead of modeling the geometry using a mesh of polygonal elements, the mesh is generated using non-uniform rational B-spline (NURBS) patches. NURBS meshes are able to capture the shape of a curved edge perfectly (with finite elements, the curve can only be approximated). Because of the smoothness of an isogeometric model, it is likely that convergence for a curved-crease origami structure would be simpler to achieve. Additionally, the number of NURBS patches used to model the sheet could be much smaller than the number of elements used in a finite elements analysis (again, since many elements are needed to approximate a curve, and a NURBS surface can generate a curved edge with only a few patches). Having fewer patches would decrease the number of degrees-of-freedom of the model, increasing the speed of the analysis (but still balanced with accuracy). Implementing isogeometric analysis for curved-crease origami would require developing a method for modeling the hinges and connecting the NURBS surfaces to each other.

Another direction of research comes from Chapter 4. There, I found that curved creases can be used to tune the bending stiffness of a corrugation. Future research could explore how a given bending stiffness can be programmed to generate a crease pattern. The algorithm presented in Chapter 6 could be a starting point for implementing such an inverse-design process. Generating a crease pattern that gives a desired bending stiffness in a corrugation would be useful in applications

such as origami floor systems, where the stiffness must be more isotropic to support distributed loads.

Finally, there is much room for future work regarding shape-fitting curved-crease origami with pinches. The results from Chapters 5-6 show how a simple problem can be solved with curved creases, pinches, and an inverse design. The methods there could be continued with optimization problems that include reducing the length of the crease to improve material efficiency. Additionally, a pinched origami crease pattern and actuation scheme could be designed for a structure hitting many points in three-dimensional space or having some desired stiffness. Such future work could push curved-crease origami closer to practical design.

7.2.2 Implement Artificial Intelligence for Origami-Inspired Structures

Artificial intelligence (AI) has been gaining traction in the engineering mechanics community in recent years. Methods in this area excel at creating mappings between complex system inputs and a mechanical behavior. These methods process large amounts of data generated from mechanics-based simulations, which enable rapid analysis of structures (Jung et al., 2020; Nie et al., 2020; Shin and Kim, 2020; Yao et al., 2020a; Vurtur Badarinath et al., 2021). AI has been applied to assessing the mechanics of metamaterials (Wu et al., 2020; Jiao and Alavi, 2021) and origami, to a limited degree (Yasuda et al., 2020). Given the complex variety of design parameters seen in origami structures, AI could be the key to rapidly analyzing thin-sheet structures.

Furthermore, methods in AI would be useful in helping characterize the multi-physical behaviors of thin-sheet structures and metamaterials. For instance, machine learning using neural networks or decision tree methods could be used to generate mappings between the many input parameters of an origami design (e.g., curvature, degree of folding, crease length) to the structural/multi-physical behavior one is interested in (e.g., stiffness, acoustic wave propagation, thermal control).

The algorithms would be trained using rapid parameter sweep tests (i.e., using the bar-and-hinge method) and verified with traditional computational methods (e.g., finite elements) and experimental data. The design of origami has many degrees of freedom and understanding the rela-

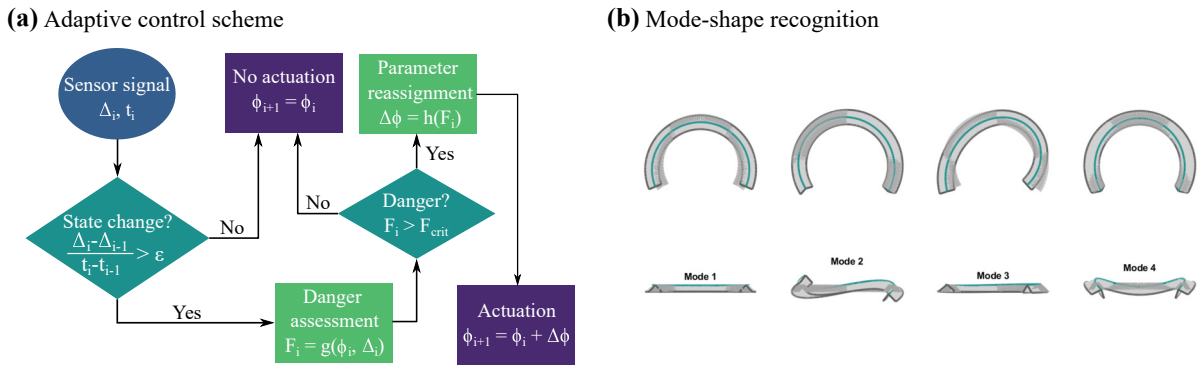

Figure 7.1 – Artificial intelligence used in the analysis of origami structures. **(a)** Methods in artificial intelligence could allow rapid analysis of origami systems for use in adaptive systems and smart cities. **(b)** Artificial intelligence could also help engineers with analyses that usually require human interpretation, such as mode-shape recognition. These tools would be trained with data from mechanics-based models or through human training.

tionship between these inputs and the behavior requires complex mappings and pattern recognition. AI would generate the mappings, while avoiding explicit development of traditional relationships (e.g., constitutive relationships, multi-stability, governing equations, boundary considerations).

These deep-learning algorithms would create the relationships that will be necessary for the application of origami and thin sheets in smart metamaterials and structures, facilitating the mapping between system inputs and responses in a rapid manner (see Figure 7.1(a)). Additionally, AI could facilitate analysis of origami structures that normally requires human interpretation, such as mode-shape recognition (see Figure 7.1(b)) (Miller and Ziemiański, 2020). Such a project would engage in a truly multidisciplinary realm that combines traditional structural engineering science and computational methods with data science, increasing the analytical abilities of engineers and enabling complex infrastructural systems.

7.2.3 Enable Large-Scale Construction and Testing of Curved-Crease Origami

Using origami to solve civil engineering problems requires performing analyses and creating designs at a large scale. Currently, the bulk of research on large-scale origami has focused on straight-crease designs, such as considerations for panel collision in thick sheets (Tachi, 2011; Lang et al., 2018), solar arrays (Tang et al., 2014; Zirbel et al., 2014, 2015), inflatable structures (Schenk et al., 2014; Melancon et al., 2021), and origami shelters (Martínez-Martín and Thrall, 2014).

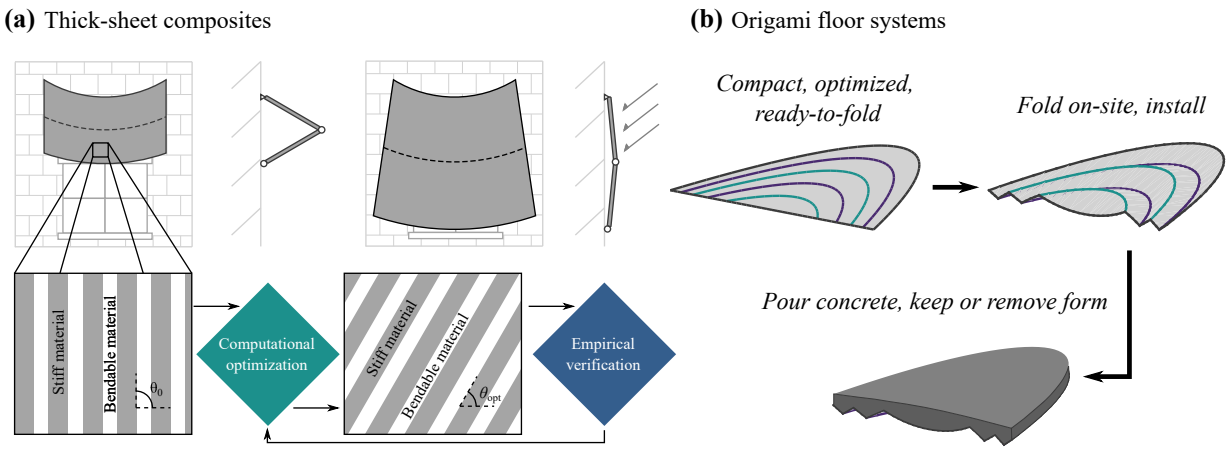

Figure 7.2 – Concepts for large-scale, curved-crease structures. **(a)** Implementing curved-crease origami in civil infrastructure (such as a deployable shade) will require scaling up the thickness of sheets. The challenges of scaling up could be overcome using bendable composites that combine stiff and bendable materials to allow for folding of curved-crease structures. **(b)** The bending stiffness isotropy gained from using curved creases (see Chapter 4) could be used to create origami floor systems that distribute concrete in an optimal pattern, and the origami itself could be used as a composite reinforcement or as reusable formwork that can be assembled on site.

Almost all research surrounding the mechanics and design of curved-crease origami has focused on structures at the centimeter scale. It will be important to discover the challenges that scaling up curved-crease origami will create as research moves closer to civil infrastructure, meter-scale design. Some of the obstacles preventing scaling up include designing sufficiently strong and compliant materials as well as characterizing imperfection sensitivities and mitigating real-world behaviors such as local fractures, buckling, and material yielding. It will important to explore the design of architected materials made from traditional constituents (e.g., steel, timber, fiber composites). Through computational simulations and parametric-sweep testing, researchers could identify the effects that material orientation and strategic cuts (Nelson et al., 2016) have on the strength and flexibility of thin sheets and create design frameworks that allow for resilient, thin-sheet structures (see Figure 7.2(a)). Additionally, researchers could employ large-scale testing of origami-inspired structures to discover real-world behaviors of thin-sheet systems, such as an origami composite floor system (see Figure 7.2(b)). The information could inform computational models and uncover failure mechanisms that must be avoided in large-scale applications.

Origami-inspired structures offer material-efficient and adaptable technology capable of re-

sponding to extreme loading events, while limiting the weight and carbon-footprint of the infrastructure. As the benefits of origami are uncovered, it is important that engineers understand the real-world behaviors of these structures to avoid failures and complexities due to scaling up. Combining computational modeling with large-scale testing will help engineers design useful origami-inspired structures that display novel behaviors and are safe to use.

7.2.4 Develop Smart, Adaptive Structures With Curved Creases

The final direction for research I consider combines the prior two areas. With rapid analysis using AI and design considerations for large-scale origami, it would be worthwhile to develop curved-crease, smart structures. For instance, metamaterials made of repeated shell structures that can be actuated to achieve desired stiffness and multi-physical (e.g., acoustic, thermal) behaviors (see Figure 7.3(a)). Using 3D printing, manufacturing these metamaterials for experimental testing and prototype creation will be feasible. Alongside the geometric design of the unit structures, researchers must develop methods for actuation (e.g., hydraulics, thermal expansion) that allow changes in the multi-physical behavior of the metamaterial that can be automatically implemented in a smart system. To characterize the response of the metamaterial, researchers could deploy a deep-learning framework, trained with numerical and experimental data. Metamaterials reorient matter to achieve optimal multi-physical behaviors while reducing the weight of the metamaterial without significant loss of strength. Shells structures are particularly stiff, and their behavior can be manipulated by actuation.

Beyond metamaterials, large-scale curved-crease structures could be designed and manufactured, such as an adaptive façade that allows variable amounts of light, wind, or rain through its surface, actuated with pinches (see Figure 7.3(b)). With the large variety of structural benefits that curved-crease origami offers, implementing these geometries into adaptive systems across engineering fields will be worthwhile.

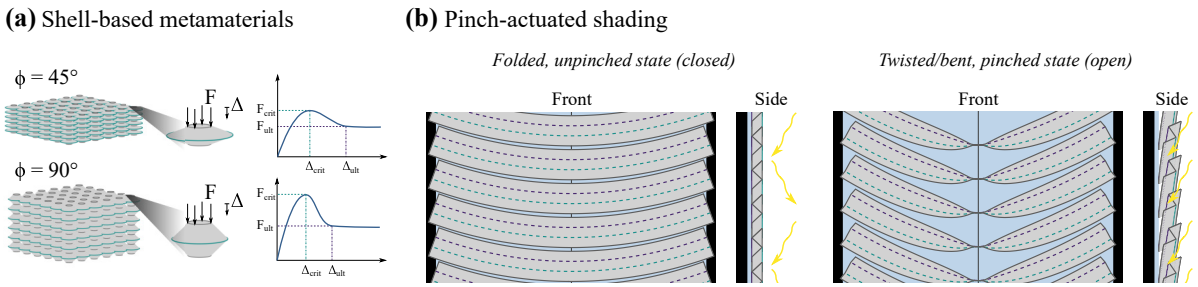

Figure 7.3 – Smart structures using curved-crease sheets. Combining rapid analysis using AI and large-scale design of curved-crease origami, researchers could develop smart, adaptive structures the exploit the benefits of curved-crease origami including the strength of curved shell surfaces and pinch-actuation. For example, **(a)** a metamaterial made from repeated shell structures could actuate and change mechanical properties or **(b)** a pinch-actuated façade or shading could be developed that allows light, wind, rain into a structure as needed.

Appendix A

Isometric Deformation Analysis of Curved-Crease Origami

The purpose of this appendix is to describe the process of calculating the deformed geometry of a thin sheet folded about a curved crease using only geometric relationships found in the field of mathematics and to assess the limitations of such a process. This analysis process takes two inputs: (1) the geometry of the crease after folding (called the *already-deformed crease*) in the form of a parametric space curve and (2) the degree of folding along the length of the crease. Despite the fact that from an engineering prospective, it is more practical to describe the deformed shape of a sheet starting from a flat crease pattern than by starting with a prescribed, already-deformed crease, the mathematics behind the analysis process will prove useful when explaining concepts throughout this dissertation.

The geometric analysis process draws from a long history of mathematics, especially from the fields of differential geometry and developable surfaces. Information from these fields can be found in many introductory textbooks, such as Kreyszig (1991). Research efforts in the late twentieth century by Huffman (1976), Duncan and Duncan (1982), and Fuchs and Tabachnikov (1999) were the first to employ geometric analysis to assess the folded shapes of curved-crease origami. Later publications refined and applied the mathematics with accommodations for creases with arbitrary curve speed (Lang et al., 2017) and insights into compatibility of creases made from conic sections (Demaine et al., 2018). This appendix introduces a process of generating a folded sheet geometry from an already-deformed crease explicitly and algorithmically so that the process may be used by others.

Figure A.1 shows a flowchart describing each of the main steps in the geometric analysis process. Details on how to complete these steps are described later on in the appendix. The process

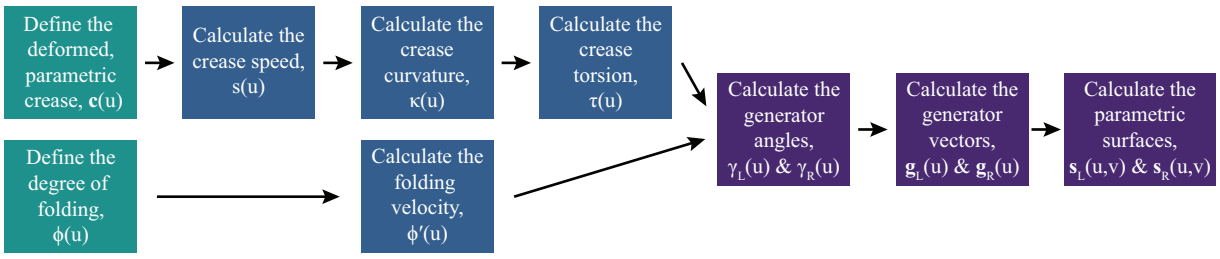

Figure A.1 – Analysis process for generating curved-crease surfaces from an already-deformed crease. To generate a three-dimensional surface representing a sheet folded about a curved crease, the geometry of the crease after folding, $\mathbf{c}(u)$ (the already-deformed crease), must be defined as a parametric function along with the degree of folding (the dihedral angle, $\phi(u)$), defined as a scalar quantity of the same parameter. Intermediate calculations on the crease and dihedral angle lead to key values that define the curved surface (the generator angles) and, ultimately, define the folded sheet geometry.

starts by defining the already-deformed crease and the degree of folding. Intermediate calculations are performed on these two inputs which are then combined to describe the geometry of the folded sheet.

Before I proceed, it would be helpful to describe the mathematical conventions I will use in the appendix. First, all symbols in **bold** represent vector-valued quantities. Symbols followed by parameters, such as $\phi(u)$ or $\mathbf{s}_{_L}(u,v)$, represent the entire domain of those functions, and I mean to describe the entire crease or surface. When those same symbols do not show a parameter, such as ϕ or $\mathbf{s}_{_L}$, I am discussing those quantities described at some point along the crease or on the surface.

A.1 Process Inputs: The Already-Deformed Crease and the Degree of Folding

The two inputs into the geometric analysis process are the already-deformed crease and the degree of folding. Looking at the thin sheet folded about a curved crease in Figure A.2, notice that the geometry can be broken down into three main shapes. The first shape is the already-deformed crease which can be defined using a three-dimensional space curve. Points on the curve are defined by a vector-valued position function,

$$\mathbf{c}(u) = \Big\{ x(u), \quad y(u), \quad z(u) \Big\}^{T}, \tag{A.1}$$

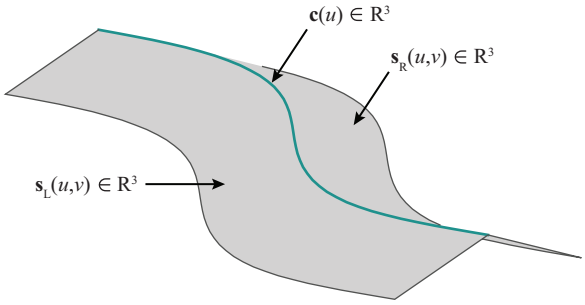

Figure A.2 – Defining a curved-crease surface using an already-deformed crease. A curved-crease surface can be defined using a space curve, $\mathbf{c}(u) \in R^3$, to model the deformed crease geometry and two surfaces, one on the left of the crease's tangent direction, $\mathbf{s}_L(u,v) \in R^3$, and one on the right, $\mathbf{s}_R(u,v) \in R^3$.

where u is a scalar parameter and $x(u)$, $y(u)$, and $z(u)$ are vector components in a Cartesian coordinate system. Although it is not necessary to use a parametric equation to describe the space curve, this method is versatile enough to capture the geometry of commonly used creases, including creases that cannot be described using one-to-one functions (like a complete circle). Additionally, other coordinate systems can be used, such as a cylindrical or spherical coordinate system, but such considerations are outside of the scope of this appendix.

The other two parts of the folded sheet in Figure A.2(a) are the surfaces on the left and right of the crease, $\mathbf{s}_L(u,v)$ and $\mathbf{s}_R(u,v)$, relative to the crease tangents along the curve. Each surface is defined as a vector-valued position function of two parameters, u and v. The parameter u is the same as that describing the crease. The parameter v describes the distance from the curved crease along a generator. Computing expressions for the sheet surfaces requires first describing the degree of folding that relates the position of the sheets relative to each other.

Two ways of defining the degree of folding of a crease include assigning a dihedral angle, $\phi(u) \in [0,\ 2\pi]$ [rad], or assigning a fold angle, $\tilde{\phi}(u) \in [-\pi,\ \pi]$ [rad], each along the length of the crease (see Figure A.3). The fold angle, $\tilde{\phi}(u)$, measures the smallest angle between the initial flat surface of the sheet to the folded surface and is convenient for simulating folding from the flat configuration, but is difficult to see in a folded geometry. The dihedral angle, $\phi(u)$, measures the smallest angle between two sheets about a crease and is easy to measure and observe, but is less commonly used.

Because the dihedral angle is easier to identify on a folded sheet, I will use this as the metric

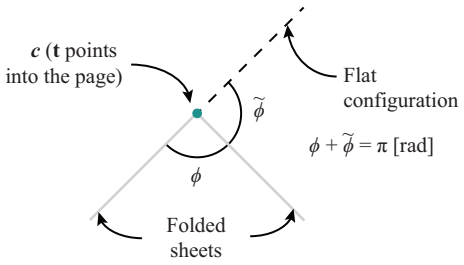

Figure A.3 – Defining the degree of folding at each point along a crease. Two ways of defining the degree of folding of a crease include assigning a dihedral angle, ϕ, or assigning a fold angle, $\tilde{\phi}$. The fold angle, $\tilde{\phi}$, is convenient for simulating folding from the flat configuration, but is difficult to see in a folded geometry. The dihedral angle, ϕ, is easy to measure and observe, but is less commonly used.

for the degree of folding. If one wanted to use the fold angle instead, the dihedral angle and fold angle are related by,

$$\phi(u) + \tilde{\phi}(u) = \pi \text{ [rad]} \qquad \Rightarrow \qquad \phi'(u) = -\tilde{\phi}'(u), \tag{A.2}$$

where $(')$ means differentiation with respect to u.

A.2 Intermediate Calculations on the Crease and Dihedral Angle

In order to describe the folded shape of sheets on either side of the already-deformed crease, further analysis must be completed on the input parameters, $\mathbf{c}(u)$ and $\phi(u)$, separately.

The first intermediate calculation is used to determine the folding velocity, or fold rate. This signed quantity describes the rate at which the sheets are folded or unfolded about the crease. This folding velocity, $\phi'(u)$, is simply the first derivative of the dihedral angle with respect to the parameter.

The next set of calculations aim to assess the rate of change of the crease along its length. Specifically, I am interested in calculating the speed, curvature, and torsion of the crease described by the space curve. These three values, defined at every point along the crease, are independent of the dihedral angle, but are essential to describing the shape of the folded sheets.

The speed of the crease, $s(u)$, is defined as the magnitude of the velocity of the curve defining

the already-deformed crease. That is,

$$s(u) = |\mathbf{c}'(u)|\,. \tag{A.3}$$

The value of the speed of the crease depends on the parameterization used to define the geometry and must be considered for subsequent calculations. Although calculations for curvature and torsion are simpler when the crease is defined using an arc-length parameterization (that is, $s(u) = 1$), many common curves cannot be defined this way (for instance, a parabola has no explicit arc-length parameterization).

Before I describe the process of calculating the curvature and torsion of the crease, it would be helpful to describe a way of visualizing these quantities. One way is to use the Frenet-Serret frame. A frame is a way of breaking down a crease into simple components at the local level (that is, at each point along the crease) using three orthogonal unit vectors. The Frenet-Serret frame uses the crease tangent, $\mathbf{t}$, the crease normal, $\mathbf{n}$, and the crease binormal, $\mathbf{b}$, vectors as its basis. These vectors are calculated using the following expressions:

$$\begin{aligned} \mathbf{t}(u) &= \frac{\mathbf{c}'(u)}{s(u)}; \\ \mathbf{n}(u) &= \frac{\mathbf{t}'(u)}{|\mathbf{t}'(u)|}; \\ \mathbf{b}(u) &= \mathbf{t}(u) \times \mathbf{n}(u), \end{aligned} \tag{A.4}$$

where $(\times)$ is the cross product. An example Frenet-Serret frame at one point along an already-deformed curved crease is shown in Figure A.4(a).

The Frenet-Serret frame is related to the crease curvature, κ, and torsion, τ, by

$$\begin{Bmatrix} \mathbf{t}' \\ \mathbf{n}' \\ \mathbf{b}' \end{Bmatrix} = s \begin{bmatrix} 0 & \kappa & 0 \\ -\kappa & 0 & \tau \\ 0 & -\tau & 0 \end{bmatrix} \begin{Bmatrix} \mathbf{t} \\ \mathbf{n} \\ \mathbf{b} \end{Bmatrix} \tag{A.5}$$

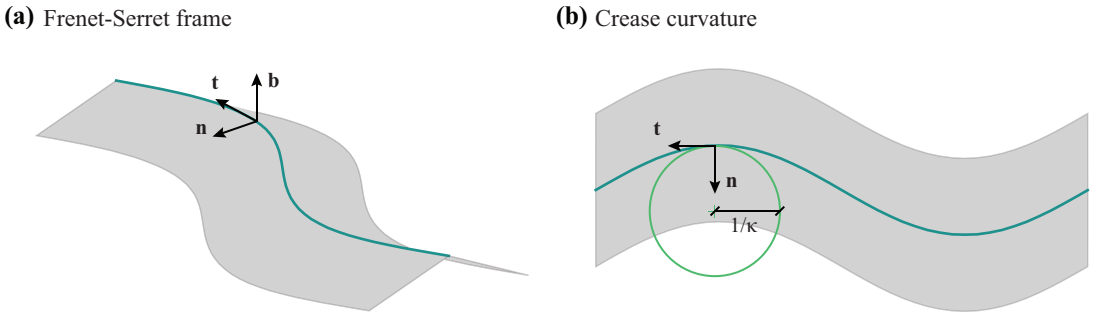

Figure A.4 – Visualizing crease curvature and torsion with the Frenet-Serret frame. **(a)** The Frenet-Serret frame is a set of three orthogonal unit vectors defined at each point along the crease. The unit vectors include the crease tangent, $\mathbf{t}$, the crease normal, $\mathbf{n}$, and the crease binormal, $\mathbf{b}$. **(b)** The crease curvature lies in the binormal plane and represents the inverse of the radius of the osculating circle at some point along the crease.

From this system of equations, notice that the crease curvature is proportional to the rate of rotation of the crease tangent vector about the binormal vector. That is, the greater the curvature, the quicker and more tightly the curve turns along its length. The crease curvature can be easily visualized using the osculating circle (a circle that lies in the binormal plane and is tangent to the crease) whereby the inverse of circle's radius is the value of the curvature (see Figure A.4(b)). Additionally, notice that the crease torsion is proportional to the rate of rotation of the binormal vector about the tangent vector. That is, the greater the torsion, the quicker the curve rotates about the direction is is pointing.

The crease curvature can be calculated directly from the space curve by

$$\kappa(u) = \frac{|\mathbf{c}'(u) \times \mathbf{c}''(u)|}{s^3(u)}. \tag{A.6}$$

The crease torsion can also be calculated directly from the space curve by

$$\tau(u) = \frac{(\mathbf{c}'(u) \times \mathbf{c}''(u)) \cdot \mathbf{c}'''(u)}{|\mathbf{c}'(u) \times \mathbf{c}''(u)|^2}, \tag{A.7}$$

where $(\cdot)$ is the dot product.

A.3 Defining the Sheet Surfaces From the Crease and Dihedral Angle

Calculating expressions for the left and right surfaces describing the deformed shape of curved-crease sheets depends on the quantities already calculated up to this point. In summary,

$$\begin{aligned} \mathbf{s}_{_L}(u,v) &= \mathbf{f}(\mathbf{c},\, \phi,\, s,\, \kappa,\, \tau,\, \phi';\, u,\, v); \\ \mathbf{s}_{_R}(u,v) &= \mathbf{g}(\mathbf{c},\, \phi,\, s,\, \kappa,\, \tau,\, \phi';\, u,\, v), \end{aligned} \tag{A.8}$$

where $\mathbf{f}$ and $\mathbf{g}$ are vector-valued position functions of the crease and folding angle properties with parameters u and v. Determining the exact expression for these functions is the final step of the geometric analysis process and requires a few steps to complete. It would be useful to start by explaining the framework used to describe the surface.

As stated earlier, this geometric analysis process originates from analyses of developable surfaces. A developable surface is a surface that is isometric to a plane. That is, as the structure is folded from a flat state, the sheet surrounding the crease deforms only by bending. Distances between points along the surface are the same, regardless of the dihedral angle, and there are no in-plane deformations like stretching or tearing.

Any smooth surface has, at any point, two orthogonal directions of principal curvature. Much like with the principal stresses of a two-dimensional stress-state, these directions of principal curvature represent the minimum and maximum values of curvature for a curve inscribed in the surface, κ_1 and κ_2, respectively. In fact, the directions of principal curvature can be found using a Mohr's circle (Duncan and Duncan, 1982), but such an analysis is unnecessary for this geometric process.

For a developable surface that does not experience stretching, $\kappa_1 = 0$, at all points. Therefore, at any point, there is a line across the surface that has zero curvature and lies flat along a plane. Indeed, this flat line extends through the surface and intersects with the crease. If one can calculate the direction of this line extending from every point along the crease, a ruled surface that represents

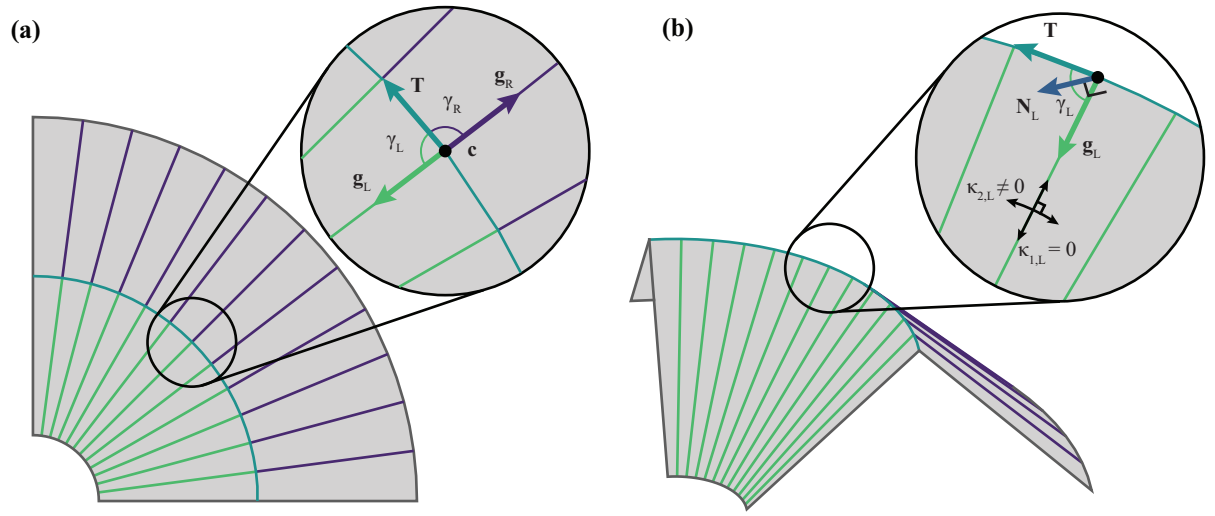

Figure A.5 – Defining sheet curvature using generators. **(a)** At each point along a crease, the tangent vector, $\mathbf{T}$, can be calculated, and the surface on either side of the crease can be defined using vectors called generators, $\mathbf{g}_L$ and $\mathbf{g}_R$. The orientation of the generators mapped onto the flattened geometry can be described using generator angles, γ_L and γ_R, measuring the rotation from the tangent vector to the generator in the flat plane. **(b)** The generators point in the direction of zero principal curvature, $\kappa_{1,L} = \kappa_{1,R} = 0$. Perpendicular to the generators are the directions of non-zero principal curvature, $\kappa_{2,L} \neq 0$ and $\kappa_{2,R} \neq 0$. The surface normals on either side of the crease, $\mathbf{N}_L$ and $\mathbf{N}_R$, represent the axes of rotation between the tangent and the generators after folding.

the deformed shape of the folded sheets can be generated. Such a surface can be defined by

$$\begin{aligned} \mathbf{s}_{_L}(u,v) &= \mathbf{c}(u) + v\mathbf{g}_{_L}(u); \\ \mathbf{s}_{_R}(u,v) &= \mathbf{c}(u) + v\mathbf{g}_{_R}(u), \quad v \geq 0. \end{aligned} \tag{A.9}$$

These expressions define the left and right surfaces of the folded sheets by starting a ruling line at some point along the crease and extending it a distance v off in a direction defined by unit vectors, $\mathbf{g}_{_L}(u)$ and $\mathbf{g}_{_R}(u)$, called generators (see Figure A.5).

The generators can be calculated using the intermediate values found earlier. The generators will have unit magnitude and will lie on the surface they represent. Thus, one needs to determine what the orientation of the surface is near some point along the crease and the direction the generator points relative to the crease. To start this process, I need to define a new frame for the sheet surfaces.

Similar to the Frenet-Serret frame, the Darboux frame describes the changes a space curve

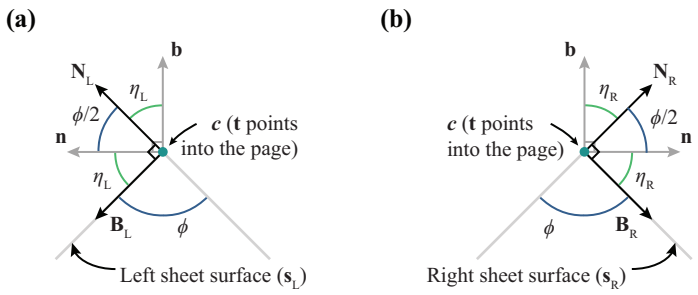

Figure A.6 – Defining the sheet surface using the Darboux frame. **(a)** The left sheet surface at some point along a crease, $\mathbf{s}_L$, can be found by rotating the Frenet-Serret frame about the tangent vector by η_L, giving the normal vector to the sheet surface, $\mathbf{N}_L$. **(b)** Since $\eta_R = -\eta_L$, the right sheet and generator projection can be found by rotating the Frenet-Serret frame in the opposite direction.

makes along its length. The Frenet-Serret and Darboux frames are related by

$$\begin{Bmatrix} \mathbf{T} \\ \mathbf{B} \\ \mathbf{N} \end{Bmatrix} = \begin{bmatrix} 1 & 0 & 0 \\ 0 & \cos\eta & \sin\eta \\ 0 & -\sin\eta & \cos\eta \end{bmatrix} \begin{Bmatrix} \mathbf{t} \\ \mathbf{n} \\ \mathbf{b} \end{Bmatrix}, \tag{A.10}$$

where $\mathbf{T}$ is the tangent vector (identical to the Frenet-Serret frame tangent vector, $\mathbf{t}$), $\mathbf{B}$ is the tangent normal vector (which does not have a physical meaning in this process), $\mathbf{N}$ is the surface normal vector describing the plane of the sheet, and η is an angle sometimes called the Darboux angle (Lang et al., 2017). The Darboux frame is essentially the Frenet-Serret frame rotated about the tangent vector by the Darboux angle. Unlike with the Frenet-Serret frame, the Darboux frame is defined differently for the left and right surfaces (that is $\mathbf{N}_L \neq \mathbf{N}_R$). Indeed, the left and right surfaces can be related using the Darboux angle, where $\eta_L = -\eta_R$ (see Figure A.6).

Upon further inspection of Figure A.6, observe that $\eta_R = (\pi - \phi)/2$ [rad] and $\eta_L = -(\pi - \phi)/2$ [rad]. Thus, the surface normals on the left and right side can be calculated by

$$\begin{aligned} \mathbf{N}_L(u) &= -\left[\cos\left(\frac{\phi(u)}{2}\right)\mathbf{n}(u) + \sin\left(\frac{\phi(u)}{2}\right)\mathbf{b}(u)\right]; \\ \mathbf{N}_R(u) &= -\cos\left(\frac{\phi(u)}{2}\right)\mathbf{n}(u) + \sin\left(\frac{\phi(u)}{2}\right)\mathbf{b}(u). \end{aligned} \tag{A.11}$$

Since the orientation of the sheet surfaces on either side of the crease are now known, the next

step is to find the orientation of the generators within that surface. One way to define the orientation of the generators is to find the angle between the generator and the tangent vector, $\mathbf{T}$, within the sheet surface. This angle, called the generator angle, must be calculated for both the left, $\gamma_{_L}$, and right $\gamma_{_R}$, sides.

Expressions originally found by Fuchs and Tabachnikov (1999) and improved upon by Lang et al. (2017) can be used to calculate the generator angles. These equations are,

$$\begin{aligned}\gamma_{_L}(u) &= \text{arccot}\left[\frac{\tau(u) - \phi'(u)/(2s(u))}{\kappa(u)\cos(\phi/2)}\right];\\ \gamma_{_R}(u) &= \text{arccot}\left[\frac{\tau(u) + \phi'(u)/(2s(u))}{\kappa(u)\cos(\phi/2)}\right].\end{aligned} \tag{A.12}$$

The final step in the analysis process is to calculate the generator vectors using the surface normals and generator angles. As stated earlier, the generator vectors can be found by rotating the tangent vectors about the surface normal by the generator angle value. Such a rotation can be calculated using Rodrigues's rotation formula (Rodrigues, 1840). Plugging in the values from above, I have,

$$\begin{aligned}\mathbf{g}_{_L}(u) &= \mathbf{T}(u)\cos\gamma_{_L}(u) + [\mathbf{N}_{_L}(u)\times\mathbf{T}(u)]\sin\gamma_{_L}(u) + \mathbf{N}_{_L}(u)\,[\mathbf{N}_{_L}(u)\cdot\mathbf{T}(u)]\,[1-\cos\gamma_{_L}(u)];\\ \mathbf{g}_{_R}(u) &= \mathbf{T}(u)\cos\gamma_{_R}(u) - [\mathbf{N}_{_R}(u)\times\mathbf{T}(u)]\sin\gamma_{_R}(u) + \mathbf{N}_{_R}(u)\,[\mathbf{N}_{_R}(u)\cdot\mathbf{T}(u)]\,[1-\cos\gamma_{_R}(u)].\end{aligned} \tag{A.13}$$

One can plug the values found in Equation A.13 and the crease definition from Equation A.1 into the parametric expression for the left and right sheet surfaces in Equation A.9. The folded sheet surfaces can be found by calculating the position of points on the surface as a function of the parameters, u and v.

A.4 General Patterns Found in the Math

Within the equations used to define the folded surface of curved-crease origami sheets, there are patterns that appear that will be useful for analyses in this dissertation. The first observation is that

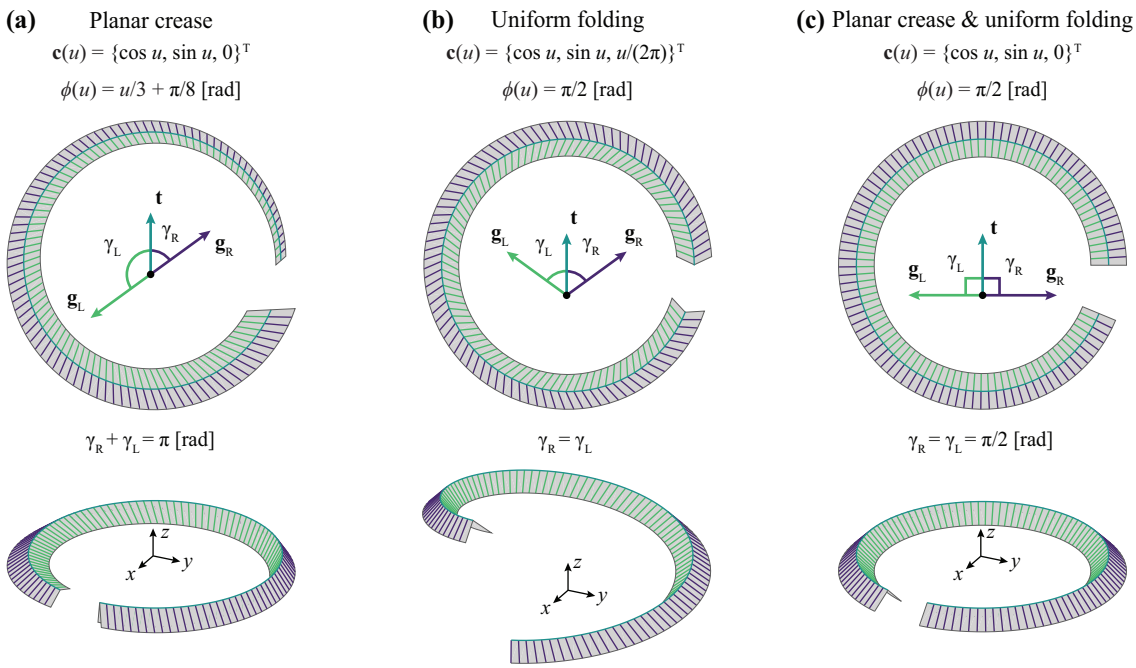

Figure A.7 – Examples of curved-crease surfaces generated from an already-deformed crease. Top row shows the top view of the folded sheets and bottom row shows an isometric view. Each crease projects down into a circular arc with the same sector angle ($0 \leq u \leq 15\pi/8$ [rad]) and width ($0 \leq v \leq 0.2$). **(a)** This surface has a planar crease which unfolds along its length. Such a planar crease lies in one plane and will always result in generators whose angles sum to π [rad]. **(b)** This surface has a non-planar crease (a helix) with a constant dihedral angle. Such a uniformly folded crease will have identical generator angles at all points along the crease. **(c)** This surface has a planar crease with a constant dihedral angle. Such a crease will give generators inclined $\pi/2$ [rad] from the tangent vector.

a planar crease (a crease that lies in one plane with $\tau(u) = 0$) will have generator angles that sum to π [rad] (see Figure A.7(a)). As observed by Badger et al. (2019) and first postulated by Duncan and Duncan (1982), real curved-crease origami sheets will tend to form planar creases (except near the ends of the crease), since this minimizes bending energy. Thus, planar creases will be commonly found in engineering applications of curved-crease origami.

The second observation from the math is that a uniformly folded crease (that is, $\phi'(u) = 0$) will give $\gamma_L(u) = \gamma_R(u)$. A simple curved-crease origami structure might be folded using actuators that deform the sheet into a uniform fold (see Figure A.7(b)). The third observation is that a planar crease with uniform folding will only exist when generators are perpendicular to the crease tangent (see Figure A.7(c)).

A.5 Limitation to the Geometry-Based Analysis Process

The mathematics describing the deformed shape of thin sheets folded about curved creases is closed-form; thus, computing the deformation can be done quickly using a symbolic or numerical computer program (such as MATLAB or Mathematica), if not by hand calculations. Even without considering physics, the mathematical relationships between creases and curves reveal important properties of isometrically deformed curved-crease origami.

Despite the simplicity of this process, there are a few limitations that restrict what inputs and outputs can be found. For instance, there is no mapping between the flat and folded states. Because the folded sheets come from the already-deformed crease, one cannot know (in most cases) what the geometry of the flat crease is. The shape of the already-deformed crease does not come from boundary conditions or material properties (the geometry is simply made up). In a manufacturing process, curved-crease structures would likely start from a flat state, so mapping between the flat and folded states is essential.

The next limitation of the geometry-based process is that the surface is modeled based off one crease. For a crease pattern with more than one crease, this method cannot fully describe the folded shape. Although a primary crease can be well-defined and the other crease geometries can be back calculated, there is no guarantee that the surface will be valid (see Watanabe and Mitani (2018)). To calculate the deformed surface of a folded multi-crease, curved-crease pattern, the minimal energy state must be found, which is outside the capabilities of this geometric process.

Another limitation of this method is that there is no consideration for panel thickness. Since sheets are modeled using zero-thickness surfaces, real sheets with finite thickness might touch near creases or wrinkle under large enough rotations. The mathematics might give a folded surface that would fail if made from real materials.

Finally, the geometry-based method cannot describe post-folding deformations. If one wants to explore engineering uses for curved-crease origami, they must go beyond modeling just folding and see how the structure responds to loads and boundary conditions after it is folded. Such de-

formations might include stretching and tearing of the sheet that are prohibited in the geometric process. Additionally, certain nonlinear deformations like buckling, snapping, and crumpling of the sheet cannot be modeled using mathematics alone.

A.6 Conclusions

If the shape of a single curved crease is known after folding and the degree of folding is known, then the surface of the sheets can be approximated well without having to use more complicated methods. A series of closed-form expressions describe this limited case of curved-crease origami structures. The mathematics behind the process of generating the curved-crease surface contains useful concepts such as generators and degrees of folding which will appear in mechanical analyses throughout the dissertation.

However, the geometry-based analytical method presented here is limited to well-define deformations of singly creased structures with zero thickness. In order to apply curved-crease origami to engineered structures, a more robust treatment is required. Such a treatment would need to consider the mechanics of thin sheets (see Chapter 3).

Appendix B

Finite-Element Analysis of Curved-Crease Origami

Finite-element (FE) analysis is often used for modeling the deformation and structural properties of thin-sheet structures. The versatility of the method makes FE a valuable tool for engineers and origami researchers. In this appendix, I explore finite element modeling of a curved-crease structure, explore some of the local effects one can capture using the method, and discuss limitations to FE for curved-crease origami. The purpose of this appendix is to show that although FE is useful in some cases, it is limited in its usefulness to modeling curved-crease origami, motivating the use of the bar-and-hinge method described in Chapter 3.[1]

The appendix is organized as follows: Section B.2 discusses the fundamental geometric and stiffness characteristics associated with curved folding of thin sheets. Section B.3 presents the definitions for the analytical model. The model is used in Section B.4 to study different methods for folding a simple thin sheet, and its internal energy is compared with a theoretical model based on conical curvatures. Section B.5 presents preliminary extensions of the computational model. Final conclusions and recommendations for future research are discussed in Section B.6.

B.1 Introduction

Folding thin sheets about curved creases results in sheet bending. Unlike with rigid-foldable, straight-crease origami, kinematics alone cannot describe a curved-crease structure without making sweeping assumptions about the shape. To determine the structural properties of a curved-crease origami, one needs a method of modeling the elastic bending of thin sheets.

[1] This appendix contains results published in Woodruff and Filipov (2018)

One common method for modeling curved-crease origami is finite element (FE) analysis. These models have been used to analyze the folding of curved-crease sheets. For instance, in Vergauwen et al. (2017), the FE approach is compared with isometric deformation modeling approaches (see Appendix A) and physical models. The approach presented in this work uses a commercially available FE package to model curved-crease structures. Different methods for actuating and folding the system are defined and explored in detail. The analytical model is also verified with theoretical energy definitions of a developable surface folded to conform to a conical shape. The interplay between in-plane and out-of-plane localized effects are also explored.

B.2 Properties of Curved-Creased Sheets

A key attribute of origami-inspired structures using thin sheets is that, locally, the in-plane stiffness of the sheet is high relative to the out-of-plane bending stiffness. Folding a sheet about a curved crease forces the surface to bend along with the curvature of the crease. Because of this differential stiffness in thin sheets, a folded structure undergoes large bending deformations with negligible in-plane effects in the surface of the sheet. Assuming that the stretching and shearing deformations are negligible, the sheet can be idealized as a set of piece-wise developable surfaces connected at the creases.

Theoretically a developable surface is restricted to isometric deformations, where the surface cannot stretch. A developable surface must also have zero Gaussian curvature at all points (Duncan and Duncan, 1982; Huffman, 1976). Gaussian curvature is the product of the two principal curvatures on the surface. In order to satisfy zero Gaussian curvature, there must be rulings, called directors or generators, along the surface of the sheet which lie flat in the surface (i.e., the tangent planes along the length of each director are identical). Non-zero principal bending of the sheet must lie perpendicular to the director within the surface (see Figure B.1).

One method of approximating the shape of a curved-crease structure after folding is by using a piece-wise developable surface composed of simple developable surfaces like cones and cylinders. These surfaces have known curvatures which can be used to calculate the bending energy and

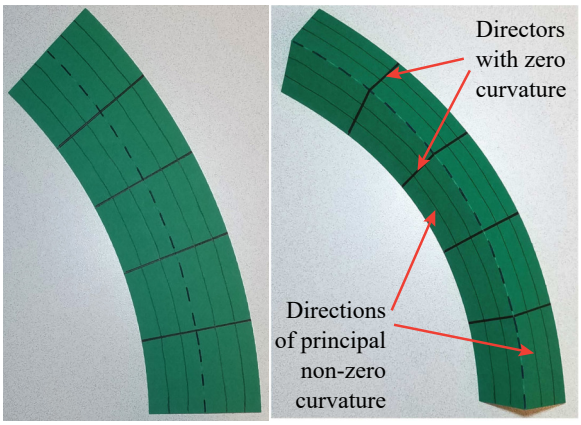

Figure B.1 – A flat (left) and folded (right) piece of paper with a single curved crease.

approximate the deformation of a curved-crease structure. For general developable surfaces, the mean curvature is half of the non-zero principal curvature in the surface. The bending energy for a developable surface subjected to a single direction of bending can be calculated in a simplified form as

$$U_b = \frac{1}{2} \int_A D_b k_1^2 \, dA, \tag{B.1}$$

where D_b is the bending stiffness (rigidity) of the sheet, k_1 is the non-zero principal curvature, and A is the area of the developable surface. The bending stiffness of an isotropic, homogeneous sheet is

$$D_b = \frac{Et^3}{12\,(1-\nu^2)} \tag{B.2}$$

where E is the modulus of elasticity of the sheet, t is the thickness, and ν is the Poisson's ratio.

This work deals only with sheets that are initially flat and have prescribed curved folds, assuming that the initial deformation will occur as a concentrated rotation at the crease and the adjacent material will deform to accommodate the global structural motion. These assumptions are used to formulate the structural analysis framework using the FE approach. The folds are modeled on a local zero-length basis to allow a localized rotation, while the adjacent material is modeled separately with conventional three-dimensional elements.

A simple, circular sheet with a single curved crease is used as the basis for the analyses presented in this appendix. This sheet is pictured in Figure B.1 and defined in Figure B.2. The sheet

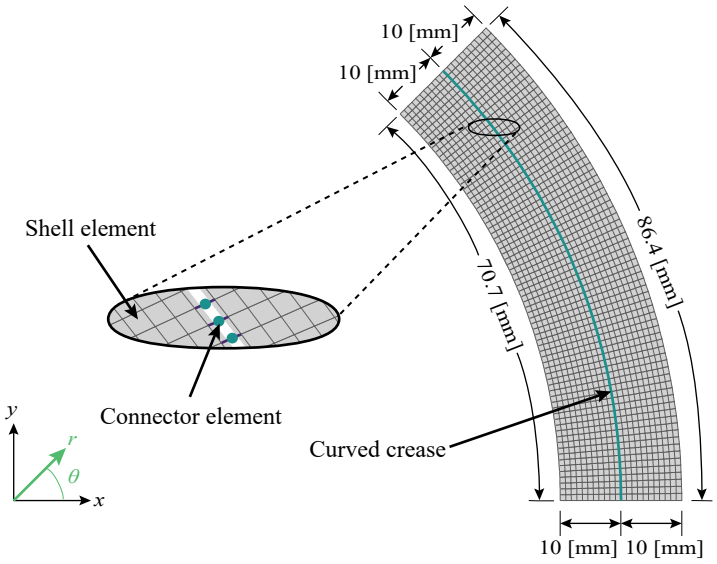

Figure B.2 – Finite element model mesh. The radius of the crease is 100 [mm], and the discretized mesh has 1628 shell elements.

is a segment of a circular annulus subtending an arc angle, $\theta_a = \pi/4$ [rad] with an inner radius, $r_i = 90$ [mm] and an outer radius, $r_o = 110$ [mm]. A fold line is imposed concentrically within the annulus section at a radius of $r_f = 100$ [mm] with an approximate length of 78.5 [mm]. The area of the inner sheet adjacent to the fold is approximately 746 [mm^2], and the area of the outer sheet is approximately 825 [mm^2].

For this simple model with constant dihedral angle between the inner and outer sheets, the curved crease remains nearly planar after folding without significant torsion. Therefore, the directors in the deformed surface should lie approximately perpendicular to the crease, following the radial direction (Dias et al., 2012).

B.3 Analytical Model

The FE model is built starting from a flat, two-dimensional state. The curved crease divides the sheet into two separate sub-regions of the entire structure. Each of these sub-regions is discretized separately, and the crease line serves to connect the two sub-regions (see Figure B.2). A conventional S4 shell element is used to model the thin sheet in the two sub-regions (Dassault Systèmes Simulia Corp, 2014). The shell elements can form a mesh that conform to the geometry of the

sub-region, and can allow large, nonlinear bending deformations as well as small membrane deformations.

Because the sub-regions are discretized separately, there are collocated nodes at the crease. Connector elements are used to link these corresponding nodes, and simulate the behavior of the fold line. The join and rotation connection behaviors available in the commercial software are used to model the crease. The join connection prevents spatial motion between the nodes on the two sub-regions, but allows free rotation in all directions. The rotation connection adds a rotational stiffness between the two nodes. The rotational stiffness is placed perpendicular to the curved crease. Figure B.2 shows the single curved crease discretized with 22 shell elements in the radial direction, r, and 74 in the rotational direction, θ. In total, 75 connectors are used to link the two sub-regions.

For these simulations, the material properties of Mylar® sheets documented in previous studies are used (Lechenault et al., 2014). The Modulus of Elasticity, E, is specified to be 4000 [MPa], the Poisson's Ratio is $\nu = 0.38$, and the thickness is $t = 0.127$ [mm]. In other studies, the model can be adapted to use other material properties as well. The rotational stiffness of the fold is defined to be substantially more flexible than the adjacent material. A local fold stiffness is defined based on Filipov et al. (2017), with the length scale factor $L^* = 200$ [mm] to simulate an unusually flexible crease. The local fold stiffness is thus found to be $k_f = 4 \times 10^{-3}$ [N-mm] per [mm] of crease.

An analysis where the single curved crease is folded using applied connector rotations (see next subsection) is used to perform a convergence study on the mesh discretization. The total elastic strain energy in the sheet versus the total number of shell elements in the mesh are presented in Figure B.3. The results converge, and a discretization with a total of 1628 shell elements was chosen (see Figure B.2) that gives a result that is within 0.23% of a mesh with approximately double the number of elements.

In this paper, four methods of actuation and restraint are employed which are capable of folding the sheet from the initial flat state to the final three-dimensional form (see Figure B.4). All four methods use an x-, y-, and z-direction restraint at one corner of the sheet and a y-, and z-direction

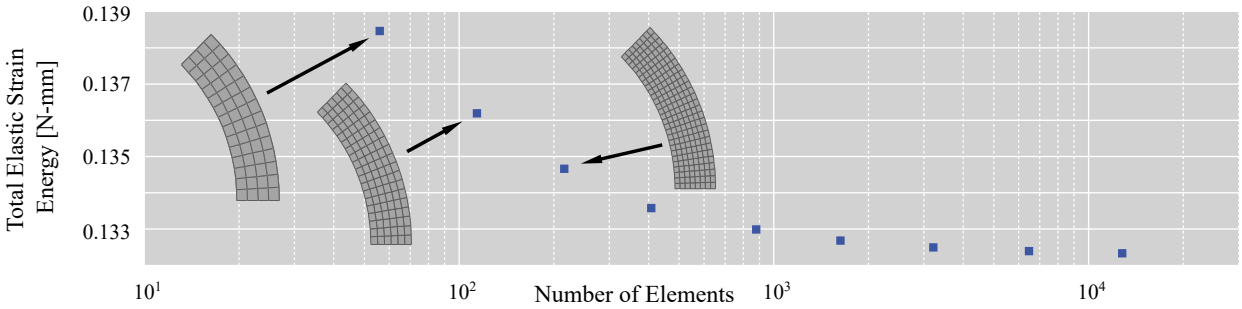

Figure B.3 – Convergence study on the shell discretization. The total energy is shown with respect to the number of shell elements in the mesh. Note: the final mesh is shown in Figure B.2.

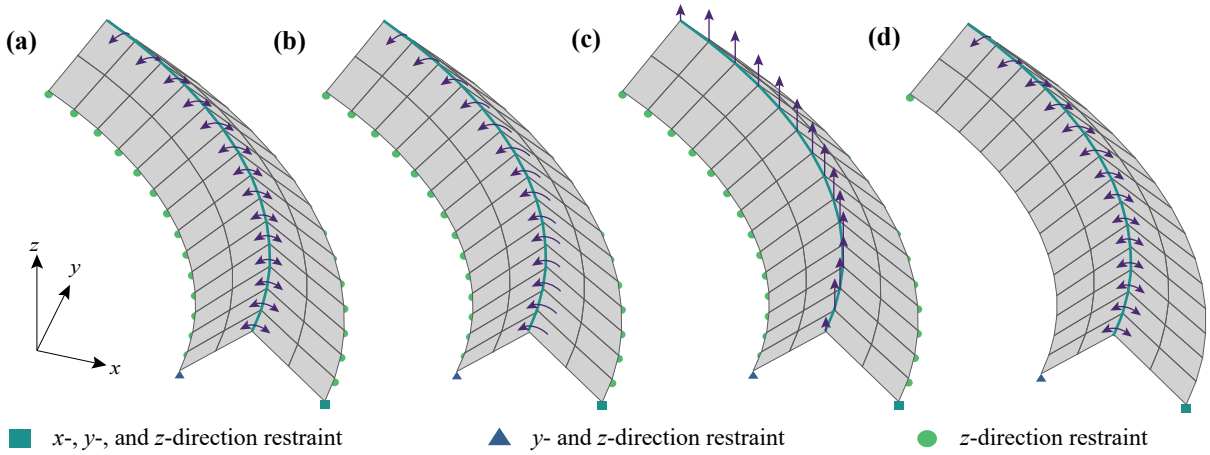

Figure B.4 – Boundary conditions imposed on the structure to induce folding. **(a)** Applied rotations, **(b)** applied moments, **(c)** applied force, and **(d)** applied rotations and reduced z-restraints. Note: these are not representative meshes used in analyses.

restraint at the corner closest to the first. The first three actuation methods additionally restrain the nodes along the inner and outer edges of the sheet in the z-direction.

The four methods presented in Figure B.4 are denoted as: (a) *Applied rotation*, where a rotation of $\pi/2$ [rad] is applied to the connectors (i.e. at the crease) to actuate the folding; (b) *Applied moments* are employed at the connectors to incrementally actuate the system until an average dihedral angle of $\pi/2$ [rad] is met at the crease; (c) an *Applied force* is placed upward at the crease nodes to incrementally move the system in the z-direction until a dihedral angle of $\pi/2$ [rad] is met at the crease; and (d) a case similar to the first where *Applied rotations* and reduced z-restraints are used. The crease connectors have an applied rotation of $\pi/2$ [rad], but the system is free to deform with vertical supports only at the corners instead of along the side edges.

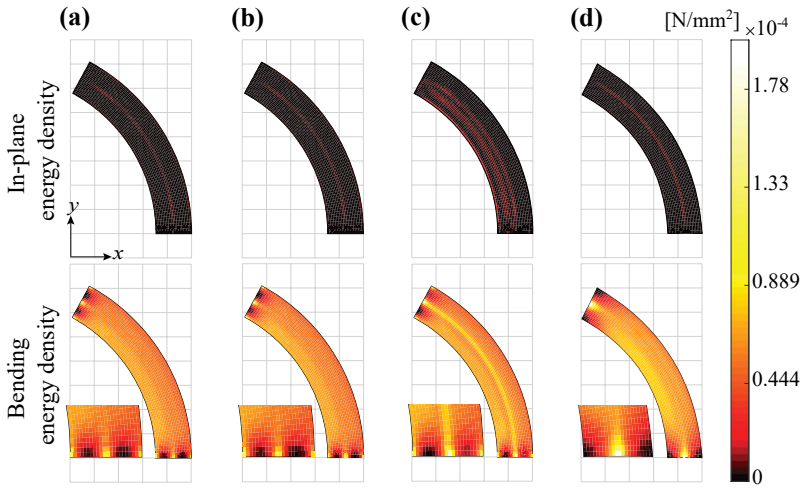

Figure B.5 – Strain energy distribution in single curved-crease origami. In-plane energy (top) and bending energy (bottom) using **(a)** applied rotations, **(b)** applied moments, **(c)** applied force, and **(d)** applied rotations and reduced z-restraints. Close-up views of bending energies are shown at lower left.

B.4 Folding of a Single Curved Crease

This section presents the results from the FE analysis for each of the four actuation methods. These results are compared to a theoretical, developable surface model of the single curved crease.

The direction and magnitude of strain energy within the shell elements indicates the modes of deformation in the thin sheet that are experienced during the folding. Figure B.5 shows the energy distribution across the deformed FE models, separated into in-plane and bending energies. In-plane energy (shear and stretching) is much smaller than the bending energy, indicating that primarily bending deformations are needed to reach the deformed shape. This finding supports the assumption that the developable surface can deform along a curved line by bending.

As expected, all four actuation methods show a large discrepancy between the bending and in-plane energies (see Table B.1). In all four cases, there is a concentration of in-plane energy at the crease. These in-plane deformations occur despite the high stiffness relative to bending because the small local deformations would reduce the total energy in the system. The in-plane deformations accommodate the change between the zero-principal curvature on the sheet and large curvature localized on the crease (as predicted by Dias et al. (2012)). The applied force case in Figure B.5(c) shows the highest amount of stretching energy of the four cases, with stretching

Table B.1 – Strain energy quantities by actuation type.

Energy type	Applied rotation	Applied moment	Applied force	Applied rotation (reduced B.C.s)	Theoretical developable surface
In-plane [N-mm]	1.67e-3	1.67e-3	3.14e-3	1.62e-3	–
Bending [N-mm]	5.30e-2	5.31e-2	5.56e-2	4.97e-2	6.29e-2
Total [N-mm]	5.47e-2	5.48e-2	5.87e-2	5.13e-2	6.29e-2
% In-plane	3.06%	3.05%	5.34%	3.15%	–

concentrated at the fold and also throughout the sheet closer to the inside radius. This stretching energy is due to the global application of force which propagates down to the z-restraints at the edge. The actuation method with reduced z-restraints in Figure B.5(d) shows a uniform distribution of in-plane energy, with stretching occurring primarily in the center of the crease. This case allows more global deformation which allows to minimize both in- and out-of-plane deformations.

For bending, a similar trend in all four actuation cases is that the ends of the system have concentrations of high and low energies. In the middle of the system, bending energy is higher at the inner radius, and reduces gradually towards the outer radius. These results correspond to the theoretical conical curvature discussed in the following subsection. The bending energy for the force actuated method (c) also has a decrease in energy from the inner radius, but with a strip of higher energy parallel to the crease. This concentration of bending energy may be due to the force acting orthogonally to the surface of the thin sheet. The force may be causing the elements to bend locally like a cantilever.

Figure B.5 also emphasizes the bending energy distributions at the ends of the model. For the three actuation methods with full z-restraints at the edges (a-c), energies are concentrated both at the crease and at the corner of the thin sheet, with little bending energy in between. The concentrations of low bending energy occur at the ends because there is no adjacent material, and locally the sheet can remain flat with minimal curvature in all directions. For the case with reduced z-restraints (d), the bending energy is concentrated only at the fold, and the entire edges remain flat thus minimizing the bending energy.

The energy divided into total in-plane and total bending energies are presented in Table B.1. The cases with applied rotations and applied moments ((a) and (b)) have nearly the same energies

and energy distributions (see Figure B.5). The case with applied forces (c) has a higher total energy than the other cases, likely because the applied forces do not correspond well with the overall deformation, and local deformations are needed to reach the $\pi/2$ [rad] rotation at the crease. This case, also has the largest percentage of in-plane energy. The case with reduced z-restraints (d) has the lowest total energy of all the cases. The boundary conditions are least restrictive, and the system can deform both globally and locally to minimize the total energy while satisfying the prescribed crease deformation.

Comparison with theoretical results. The analytical FE results are compared with a theoretical, mathematical solution for the bending energy assuming that the developable surface bends in a conical shape, with no localized stretching or shearing. The theoretical solution consists of two cone sections: one for the inside sub-region, and a second for the outside sub-region. The two cones meet at the crease. Figure B.6(a) shows a schematic of the outside sub-region folded around a conical shape. The conical shape is determined from the flat geometry of the sheet and the angle, β, between the vertical line and the cone. An angle of $\beta = \pi/4$ [rad] would result in a dihedral angle of $\pi/2$ [rad]. The cone heights, H_c and H_f, and the cone radius, r_c, can be calculated using trigonometric relations and the radii defining the flat geometry, r_f and r_o for the outside sub-region. The arc angle of the cone, θ_c, can be calculated noting that the outside arc length of the cone and the flat sub-region are the same ($\theta_a r_o = \theta_c r_c$ for the outside sub-region). The mean curvature, M, along the height of the cone can be calculated as

$$M = \frac{|u|}{2au^2\sqrt{1+a^2}}, \tag{B.3}$$

where u is the vertical distance from the apex and $a = r_c/H_c$. The principal curvature can be calculated as $k_1 = 2M$ and Equation B.1 can be used to integrate over the surface of the cone. The empirical solution for the total bending energy of the curved-crease annulus is then calculated using two cones sections, with the curvature decreasing from the inside radius towards the outside radius (see Figure B.6(b)). The theoretical solution does not have local curvature discrepancies,

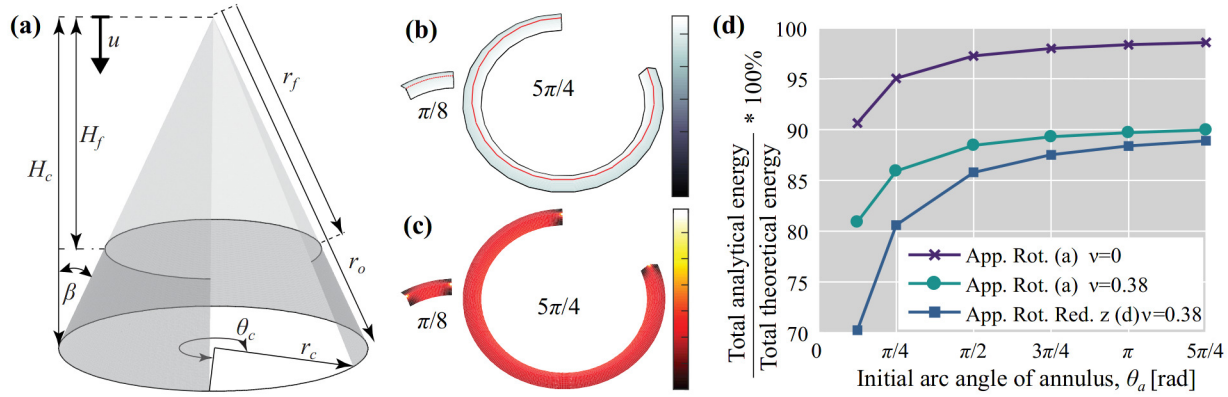

Figure B.6 – Comparing FE results to theoretical bending energy. **(a)** Conical shape for approximating theoretical bending. **(b)** Curvature based on conical shape. **(c)** Analytical bending energy with an applied rotation and $\nu = 0.38$. The results for (b) and (c) show two arc lengths. **(d)** Analytical results approach the theoretical as the annulus arc angle increases.

and thus bending energy is constant radially.

The analytical FE results approach the theoretical solution as the annulus arc length θ_c is increased, and larger systems are analyzed (see Figure B.6(d)). The longer that the arc length, the longer the section of uniform bending energy in the middle of the sheet (see Figure B.6(c)). With the increased length, the ends which allow for zero curvature have a smaller effect in the total energy. The results as shown, however, only converge to around 90% of the total theoretical energy. This discrepancy is likely due to the effect that the theoretical bending stiffness D_b of the sheet in Equation B.2 overestimates the stiffness for this case. The Poisson effect for the curved-crease analysis is likely small because the width of the sheet (with zero principal curvature) is relatively small to the length of the curve creased system (with k_1 principal curvature). The FE analyses re-run with $\nu = 0$ where the theoretical bending stiffness is $D_b = Et^3/12$ converges closer to the theoretical solution. In all cases the FE approximation has a lower energy than the theoretical solution, because the deformed shape is less prescriptive than that specified by the conical shapes with uniform bending.

Each of the four actuation methods offer similar deflected shapes and total energy, but have different functional advantages and disadvantages. For instance, the applied rotations in method (a) give a known dihedral angle over the entire crease and an overall well controlled shape (due to the z-restraints on the edges). This approach is useful for verifying the FE model with theoretical

calculations, but does not allow for unpredictable fold deformations. If a structure is folded with method (a) and is loaded afterwards, the crease angle would remain fixed which would be unrealistic. The applied moment method (b) alleviates this restriction with little difference in total bending energy and energy distribution, but the dihedral angle cannot be easily prescribed and might differ along the length of the fold. A significant difference in dihedral angle was not observed for the simple case but would likely be more significant for more complex curved-crease structures. The applied force actuation (c) is unique in that the forces used to fold the crease propagate through to the structural restraints, causing in-plane stretching. Taking this stretching into account could be important for actuation methods like form pressing for the 3D assembly of origami (Schenk et al., 2011). The method of folding (d) is the least restrained approach, which in some ways is closest to the free behavior of the system. This method for folding would be useful for further exploring the intrinsic properties of the thin sheet. Depending on the desired use and function of the curved-creased structure, different methods for folding and actuation should be considered.

B.5 Other Variations of Curved-Crease Systems

Although this paper uses a simple, single curved-crease model, the methodology used to simulate folding can be applied to any curved-crease structure made from a flat, thin sheet (e.g. Demaine et al. (2015)). Figure B.7 shows two examples of curved-crease structures that can be simulated with FE models. Each of these examples starts with thin, flat sheets divided by curved creases into separate sub-regions. For models where the crease experiences torsion, actuation methods with local connector rotations or moments can be used to fold the sheet. An unrestrained model with applied moments or rotations will allow a final shape to be generated without prior knowledge of its exact geometry (see Figure B.7(a)). For models where the crease remains planar after folding, any of the four actuation methods can be employed (see Figure B.7(b)).

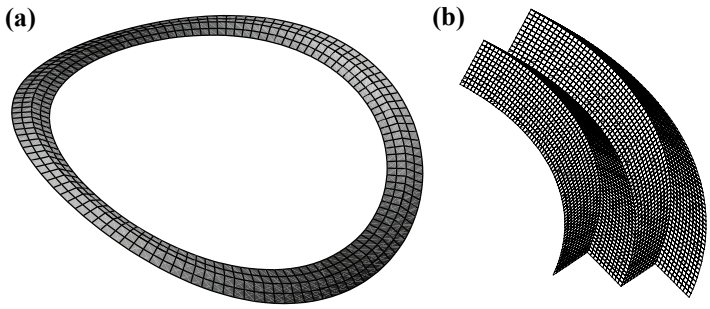

Figure B.7 – Examples of other curved-crease geometries for **(a)** full annulus inspired by Dias et al. (2012) and **(b)** annulus section with two mountain folds and one valley fold.

B.6 Conclusions

This appendix presents a finite element implementation for the modeling of curved-crease origami where a crease follows a non-linear path on the initially flat sheet. Four methods of folding the initially flat sheet into a three-dimensional form are presented and compared, showing how the final deformed shapes are similar and shell energies differ only slightly for the different folding methods. In all cases, bending energies are lower at the edges of the sheet, with distributed bending energy increasing towards the inner radius of the curved-crease system. In-plane energies were small compared to out-of-plane bending. At most, stretching and shearing accounted for five percent of the total energy when out-of-plane forces were used to fold the system. The analytical results compared well with a theoretical solution based on pure bending along developable conical surfaces.

Each of the four actuation methods come with their own functional advantages and disadvantages, which must be considered when deciding how to model a curved-crease structure. This appendix is primarily based on a simple, single curved crease, but the methodology can be applied to more complex and interesting deployable structures with potential applications in multiple scales and disciplines. The actuation methods examined in this paper can better inform analytical methods that would be used to study the intrinsic properties of curved-crease structures. Further investigation of how simple developable surfaces, like cone sections, can inform the analysis of curved-crease structures may lead to simplified analytical frameworks to inform the design of

these structures.

FE excels at modeling the local behaviors of thin sheets under folding. For instance, the end effect found earlier could not be captured with such fine resolution using a low-degree-of-freedom model, such as the bar-and-hinge method. The biggest drawbacks of FE for curved-crease origami are slow speeds and lack of reliability. For even simple structures as these creased annuli, analysis takes several minutes to complete. For origami geometries that are larger and more complex, analysis can take several hours. Additionally, folding more complex structures, especially those with multiple creases, can encounter convergence problems in Abaqus. To overcome this reliability obstacle, one would need to refine the analysis parameters and the mesh for each geometry. This is a time-intensive process that does not work well for parametric sweep tests. For analyses requiring understanding the global deformation and structural behavior of origami, the bar-and-hinge method is preferred.

References

Abdelmohsen, S., Adriaenssens, S., Gabriele, S., Olivieri, L., and El-Dabaa, R. (2019). Hygroscapes: Innovative shape shifting façades. In Bianconi, F. and Filippucci, M., editors, *Digital Wood Design: Innovative Techniques of Representation in Architectural Design*, Lecture Notes in Civil Engineering, pages 675–702. Springer International Publishing. https://doi.org/10.1007/978-3-030-03676-8_26. Cited on page 121.

Abramowicz, W. and Wierzbicki, T. (1979). A kinematic approach to crushing of shell structures. In *3rd International Conference on Vehicle Structural Mechanics*. https://doi.org/10.4271/790992. Cited on page 28.

Agarwal, T., Yun Hann, S., Chiesa, I., Cui, H., Celikkin, N., Micalizzi, S., Barbetta, A., Costantini, M., Esworthy, T., Grace Zhang, L., Maria, C. D., and Kumar Maiti, T. (2021). 4D printing in biomedical applications: emerging trends and technologies. *Journal of Materials Chemistry B*, 9(37):7608–7632. https://doi.org/10.1039/D1TB01335A. Cited on page 99.

Anumodh, R., Singh, B., and Zuber, M. (2021). Morphing applications in automobiles: A review. *International Journal of Vehicle Design*, 85(1):1–31. Cited on page 100.

Arora, R. K. (2015). *Optimization: Algorithms and applications*. CRC Press, New York. https://doi.org/10.1201/b18469. Cited on page 148.

Asfaw, A. M. and Ozbulut, O. E. (2021). Characterization of shape memory alloy energy dissipators for earthquake-resilient structures. *Structural Control and Health Monitoring*, 28(4):e2697. https://doi.org/10.1002/stc.2697. Cited on page 99.

Aysta, J. (2019). Red/yellow fabriano. *Origami Resource Center*. https://www.origami-resource-center.com/curved-creases.html. Cited on page 17.

Badger, J. C., Nelson, T. G., Lang, R. J., Halverson, D. M., and Howell, L. L. (2019). Normalized coordinate equations and an energy method for predicting natural curved-fold configurations. *Journal of Applied Mechanics*, 86(7). https://doi.org/10.1115/1.4043285. Cited on pages 28, 51, 105, 109, 132, and 179.

Beex, L. A. A. and Peerlings, R. H. J. (2009). An experimental and computational study of laminated paperboard creasing and folding. *International Journal of Solids and Structures*, 46(24):4192–4207. https://doi.org/10.1016/j.ijsolstr.2009.08.012. Cited on page 43.

Bende, N. P., Evans, A. A., Innes-Gold, S., Marin, L. A., Cohen, I., Hayward, R. C., and Santangelo, C. D. (2015). Geometrically controlled snapping transitions in shells with curved creases. *Proceedings of the National Academy of Sciences*, 112(36):11175–11180. https://doi.org/10.1073/pnas.1509228112. Cited on pages 5, 30, and 100.

Bhatia, A. (2014). How a 19th century math genius taught us the best way to hold a pizza slice. *Wired*. https://www.wired.com/2014/09/curvature-and-strength-empzeal/. Cited on page 8.

Bhooshan, S., Bhooshan, V., Shah, A., Louth, H., and Reeves, D. (2015). Curve-folded form-work for cast, compressive skeletons. In *Proceedings of the Symposium on Simulation for Architecture & Urban Design*, pages 221–228, Washington, DC. Society for Computer Simulation International. Cited on page 18.

Bouaziz, O. (2013). Geometrically induced strain hardening. *Scripta Materialia*, 68(1):28–30. https://doi.org/10.1016/j.scriptamat.2012.08.008. Cited on page 66.

Brancart, S., Vergauwen, A., Roovers, K., Van Den Bremt, D., De Laet, L., and Temmerman, N. (2015). UNDULATUS: design and fabrication of a self-interlocking modular shell structure based on curved-line folding. In *Proceedings of the IASS 2015 Symposium "Future Visions"*, Amsterdam. Cited on page 19.

Buri, H. U., Stotz, I., and Weinand, Y. (2011). Curved folded plate timber structures. In *IABSE-IASS 2011 London Symposium*, London, UK. IABSE-IASS. Cited on page 19.

Chilvers, I. (2009). Bauhaus. In *The Oxford Dictionary of Art and Artists*. Oxford University Press, 4th edition. http://www.oxfordreference.com/view/10.1093/acref/9780199532940.001.0001/acref-9780199532940-e-212. Cited on page 17.

Cimolai, G., Dayyani, I., and Qin, Q. (2022). Multi-objective shape optimization of large strain 3D helical structures for mechanical metamaterials. *Materials & Design*, 215:110444. https://doi.org/10.1016/j.matdes.2022.110444. Cited on page 148.

Concilio, A. and Ameduri, S. (2020). Morphing wings review: aims, challenges, and current open issues of a technology. *Proceedings of the Institution of Mechanical Engineers, Part C: Journal of Mechanical Engineering Science*. https://doi.org/10.1177/0954406220944423. Cited on page 99.

Cottrell, J. A., Hughes, T. J. R., and Brazilevs, Y. (2009). *Isogeometric analysis: Toward integration of CAD and FEA*. John Wiley & Sons. Cited on page 163.

Cui, W. Q., Gfeller, T., Fernando, D., Heitzmann, M. T., and Gattas, J. M. (2018). Conic crease patterns with reflecting rule lines. In Lang, R. J., Bolitho, M., You, Z., Boakes, N., Budd, C., Chen, Y., Frecker, M., Guest, S. D., Hull, T. C., Klett, Y., Mitani, J., Pardo, J., Paulino, G. H., Schenk, M., Tachi, T., Uehara, R., and Wang-Iverson, P., editors, *Origami 7: Proceedings of the 7th International Meeting on Origami in Science, Mathematics and Education*, volume 4, pages 1329–1344. Tarquin. Cited on page 19.

Dassault Systèmes Simulia Corp (2014). *ABAQUS FEA Version 6.14*. Cited on page 185.

Dayyani, I., Shaw, A. D., Saavedra Flores, E. I., and Friswell, M. I. (2015). The mechanics of composite corrugated structures: A review with applications in morphing aircraft. *Composite Structures*, 133:358–380. https://doi.org/10.1016/j.compstruct.2015.07.099. Cited on page 65.

Demaine, E. D. and Demaine, M. L. (2015). History of curved-crease sculpture. http://erikdemaine.org/curved/history/. Cited on page 17.

Demaine, E. D., Demaine, M. L., Huffman, D. A., Koschitz, D., and Tachi, T. (2014). Characterization of curved creases and rulings: design and analysis of lens tessellations. In Miura, K., Kawasaki, T., Tachi, T., Uehara, R., Lang, R., and Wang-Iverson, P., editors, *Origami 6: Proceedings of the 6th International Meeting on Origami in Science, Mathematics and Education*, volume 1, pages 209–230. American Mathematical Society, Tokyo, Japan. https://doi.org/10.1090/mbk/095.1/20. Cited on page 114.

Demaine, E. D., Demaine, M. L., Huffman, D. A., Koschitz, D., and Tachi, T. (2018). Conic crease patterns with reflecting rule lines. In Lang, R. J., Bolitho, M., You, Z., Boakes, N., Budd, C., Chen, Y., Frecker, M., Guest, S. D., Hull, T. C., Klett, Y., Mitani, J., Pardo, J., Paulino, G. H., Schenk, M., Tachi, T., Uehara, R., and Wang-Iverson, P., editors, *Origami 7: Proceedings of the 7th International Meeting on Origami in Science, Mathematics and Education*, volume 2, pages 573–590. Tarquin. Cited on pages 7, 24, and 169.

Demaine, E. D., Demaine, M. L., and Koschitz, D. (2011). Reconstructing David Huffman's legacy in curved-crease folding. In *Origami 5: Proceedings of the 5th International Conference on Origami in Science, Mathematics and Education*, pages 39–52. CRC Press, Singapore. https://doi.org/10.1201/b10971. Cited on pages 17 and 24.

Demaine, E. D., Demaine, M. L., Koschitz, D., and Tachi, T. (2015). A review on curved creases in art, design and mathematics. *Symmetry: Culture and Science*, 26(2):145–161. https://doi.org/10.26830/symmetry_2015_2. Cited on pages 17, 34, 100, and 192.

Dias, M. A. and Audoly, B. (2014). A non-linear rod model for folded elastic strips. *Journal of the Mechanics and Physics of Solids*, 62:57–80. https://doi.org/10.1016/j.jmps.2013.08.012. Cited on page 28.

Dias, M. A., Dudte, L. H., Mahadevan, L., and Santangelo, C. D. (2012). Geometric mechanics of curved crease origami. *Physical Review Letters*, 109(11). https://doi.org/10.1103/PhysRevLett.109.114301. Cited on pages 28, 30, 34, 185, 188, and 193.

Dias, M. A. and Santangelo, C. D. (2012). The shape and mechanics of curved fold origami structures. *Europhysics Letters*, 100(5):54005. https://doi.org/10.1209/0295-5075/100/54005. Cited on pages 28 and 100.

Ding, F. and Kareem, A. (2020). Tall buildings with dynamic facade under winds. *Engineering*, 6(12):1443–1453. https://doi.org/10.1016/j.eng.2020.07.020. Cited on page 99.

Dudte, L. H., Vouga, E., Tachi, T., and Mahadevan, L. (2016). Programming curvature using origami tessellations. *Nature Materials; London*, 15(5):583–588. https://doi.org/10.1038/nmat4540. Cited on pages 41, 125, and 158.

Duncan, J. P. and Duncan, J. L. (1982). Folded developables. *Proceedings of the Royal Society of London. Series A, Mathematical and Physical Sciences*, 383(1784):191–205. https://doi.org/10.1098/rspa.1982.0126. Cited on pages 3, 23, 24, 29, 34, 48, 103, 169, 175, 179, and 183.

Epps, G. and Verma, S. (2013). Curved folding: design to fabrication process of RoboFold. In *Shape Modeling International*, pages 75–83, Poole, UK. Cited on page 19.

Filipov, E. T., Liu, K., Tachi, T., Schenk, M., and Paulino, G. H. (2017). Bar and hinge models for scalable analysis of origami. *International Journal of Solids and Structures*, 124:26–45. https://doi.org/10.1016/j.ijsolstr.2017.05.028. Cited on pages 35, 43, 44, 54, 108, 109, and 186.

Filipov, E. T. and Redoutey, M. (2018). Mechanical characteristics of the bistable origami hypar. *Extreme Mechanics Letters*, 25:16–26. https://doi.org/10.1016/j.eml.2018.10.001. Cited on page 60.

Filipov, E. T., Tachi, T., and Paulino, G. H. (2015). Origami tubes assembled into stiff, yet reconfigurable structures and metamaterials. *Proceedings of the National Academy of Sciences of the United States of America*, 112(40):12321–12326. https://doi.org/10.1073/pnas.1509465112. Cited on pages 5, 12, and 66.

Filz, G. H. and Kumrić, I. (2017). Z-Snap Pavilion – advanced fabrication and assembly of self-locking, bending active modules into a semi-double-layer, shell-like structure. In *Proceedings of IASS Annual Symposia*, volume 2017, pages 1–8, Hamburg. IASS. Cited on page 19.

Fiorito, F., Sauchelli, M., Arroyo, D., Pesenti, M., Imperadori, M., Masera, G., and Ranzi, G. (2016). Shape morphing solar shadings: A review. *Renewable and Sustainable Energy Reviews*, 55:863–884. https://doi.org/10.1016/j.rser.2015.10.086. Cited on page 99.

Fraser, M., Zurob, H. S., and Wu, P. (2018). Comparing the effect of geometry on the stress-strain response of isolated corrugation structures and corrugation reinforced composite structures. *Composite Structures*, 187:308–315. https://doi.org/10.1016/j.compstruct.2017.12.076. Cited on page 66.

Fuchi, K., Buskohl, P. R., Bazzan, G., Durstock, M. F., Reich, G. W., Vaia, R. A., and Joo, J. J. (2015). Origami actuator design and networking through crease topology optimization. *Journal of Mechanical Design*, 137(9). https://doi.org/10.1115/1.4030876. Cited on page 125.

Fuchi, K. and Diaz, A. R. (2013). Origami design by topology optimization. *Journal of Mechanical Design*, 135(11). https://doi.org/10.1115/1.4025384. Cited on pages 125 and 158.

Fuchs, D. and Tabachnikov, S. (1999). More on Paperfolding. *The American Mathematical Monthly*, 106(1):27–35. https://doi.org/10.1080/00029890.1999.12005003. Cited on pages 24, 34, 48, 103, 169, and 178.

Garrett, D., You, Z., and Gattas, J. M. (2016). Curved crease tube structures as an energy absorbing crash box. In *ASME 2016 International Design Engineering Technical Conference and Computers and Information in Engineering Conference*, Charlotte, NC. ASME. https://doi.org/10.1115/DETC2016-59784. Cited on pages 5 and 30.

Gattas, J. M., Lv, W., and Chen, Y. (2017). Rigid-foldable tubular arches. *Engineering Structures*, 145:246–253. Cited on page 66.

Gattas, J. M. and You, Z. (2014). Quasi-static impact response of alternative origami-core sandwich panels. In *International Design Engineering Technical Conferences and Computers and Information in Engineering Conference*. American Society of Mechanical Engineers Digital Collection. https://doi.org/10.1115/DETC2013-12681. Cited on pages 21 and 34.

Gattas, J. M. and You, Z. (2015). The behaviour of curved-crease foldcores under low-velocity impact loads. *International Journal of Solids and Structures*, 53:80–91. https://doi.org/10.1016/j.ijsolstr.2014.10.019. Cited on page 67.

Gholamhoseini, A., Khanlou, A., MacRae, G., Hicks, S., Scott, A., and Clifton, C. (2018). Short-term behaviour of reinforced and steel fibre–reinforced concrete composite slabs with steel decking under negative bending moment. *Advances in Structural Engineering*, 21(9):1288–1301. https://doi.org/10.1177/1369433217739710. Cited on page 66.

Gilewski, W., Pełczyński, J., and Stawarz, P. (2014). A comparative study of origami inspired folded plates. *Procedia Engineering*, 91:220–225. https://doi.org/10.1016/j.proeng.2014.12.050. Cited on pages 65 and 67.

Gillman, A., Fuchi, K., and Buskohl, P. R. (2018). Truss-based nonlinear mechanical analysis for origami structures exhibiting bifurcation and limit point instabilities. *International Journal of Solids and Structures*, 147:80–93. https://doi.org/10.1016/j.ijsolstr.2018.05.011. Cited on page 35.

Gracias, D. H., Kavthekar, V., Love, J. C., Paul, K. E., and Whitesides, G. M. (2002). Fabrication of micrometer-scale, patterned polyhedra by self-assembly. *Advanced Materials*, 14(3):235–238. Cited on page 66.

Grieco, L. (2012). 13th international architecture exhibition: Arum by Zaha Hadid. designboom. https://www.designboom.com/architecture/13th-international-architecture-exhibition-arum-by-zaha-hadid. Cited on page 19.

Gu, H., Shaw, A. D., Amoozgar, M., Zhang, J., Wang, C., and Friswell, M. I. (2020). Twist morphing of a composite rotor blade using a novel metamaterial. *Composite Structures*, 254:112855. https://doi.org/10.1016/j.compstruct.2020.112855. Cited on page 99.

Holmes, D. P., Roché, M., Sinha, T., and Stone, H. A. (2011). Bending and twisting of soft materials by non-homogenous swelling. *Soft Matter*, 7(11):5188–5193. https://doi.org/10.1039/C0SM01492C. Cited on page 99.

Howell, L. L. (2013). Compliant mechanisms. In McCarthy, J. M., editor, *21st Century Kinematics*, pages 189–216, London. Springer. https://doi.org/10.1007/978-1-4471-4510-3_7. Cited on page 4.

Hu, W., Lum, G. Z., Mastrangeli, M., and Sitti, M. (2018). Small-scale soft-bodied robot with multimodal locomotion. *Nature*, 554(7690):81–85. https://doi.org/10.1038/nature25443. Cited on page 99.

Huang, H., Hagman, A., and Nygårds, M. (2014). Quasi static analysis of creasing and folding for three paperboards. *Mechanics of Materials*, 69(1):11–34. https://doi.org/10.1016/j.mechmat.2013.09.016. Cited on page 43.

Huffman, D. A. (1976). Curvature and creases: a primer on paper. *IEEE Transactions on Computers*, C-25(10):1010–1019. https://doi.org/10.1109/TC.1976.1674542. Cited on pages 23, 24, 34, 169, and 183.

Iwaki, R. (1986). Tiger mask. *Origami Art Museum, Colonia del Sacramento, Uruguay*. https://origamiartmuseumcolonia.wordpress.com/list-of-museum-items/artists/roy-iwaki-usa/. Cited on page 18.

Jha, A. and Dayyani, I. (2021). Shape optimisation and buckling analysis of large strain zero Poisson's ratio fish-cells metamaterial for morphing structures. *Composite Structures*, 268:113995. https://doi.org/10.1016/j.compstruct.2021.113995. Cited on page 148.

Jiang, C., Mundilova, K., Rist, F., Wallner, J., and Pottmann, H. (2019). Curve-pleated structures. *ACM Transactions on Graphics*, 38(6): Article 169. https://doi.org/10.1145/3355089.3356540. Cited on page 26.

Jiao, P. and Alavi, A. H. (2021). Artificial intelligence-enabled smart mechanical metamaterials: advent and future trends. *International Materials Reviews*, 66(6):365–393. https://doi.org/10.1080/09506608.2020.1815394. Cited on page 164.

Jung, J., Yoon, K., and Lee, P.-S. (2020). Deep learned finite elements. *Computer Methods in Applied Mechanics and Engineering*, 372:113401. https://doi.org/10.1016/j.cma.2020.113401. Cited on page 164.

Ketchum, M. S. (1955). Design and construction of a folded plate roof structure. *ACI Journal Proceedings*, 51(1):449–456. https://doi.org/10.14359/11688. Cited on page 66.

Kilian, M., Flöry, S., Chen, Z., Mitra, N. J., Sheffer, A., and Pottmann, H. (2008). Curved folding. *ACM Transactions on Graphics*, 27(3):1–9. https://doi.org/10.1145/1360612.1360674. Cited on page 25.

Kim, M.-H., Nam, S., Oh, M., Lee, H.-J., Jang, B., and Hyun, S. (2021). Bioinspired, shape-morphing scale battery for untethered soft robots. *Soft Robotics*. https://doi.org/10.1089/soro.2020.0175. Cited on page 99.

Kim, W., Byun, J., Kim, J.-K., Choi, W.-Y., Jakobsen, K., Jakobsen, J., Lee, D.-Y., and Cho, K.-J. (2019). Bioinspired dual-morphing stretchable origami. *Science Robotics*, 4(36):eaay3493. https://doi.org/10.1126/scirobotics.aay3493. Cited on page 100.

Kirillova, A. and Ionov, L. (2019). Shape-changing polymers for biomedical applications. *Journal of Materials Chemistry B*, 7(10):1597–1624. https://doi.org/10.1039/C8TB02579G. Cited on page 99.

Klett, Y., Middendorf, P., Sobek, W., Haase, W., and Heidingsfeld, M. (2017a). Potential of origami-based shell elements as next-generation envelope components. In *2017 IEEE International Conference on Advanced Intelligent Mechatronics*, pages 916–920, Munich, Germany. https://doi.org/10.1109/AIM.2017.8014135. Cited on pages 21 and 67.

Klett, Y., Zeger, C., and Middendorf, P. (2017b). Experimental characterization of pressure loss caused by flow through foldcore sandwich structures. In *2017 International Design Engineering Technical Conferences and Computers and Information in Engineering Conference*. American Society of Mechanical Engineers Digital Collection. https://doi.org/10.1115/DETC2017-67890. Cited on pages 21 and 67.

Koschitz, R. D. (2014). *Computational design with curved creases : David Huffman's approach to paperfolding*. Doctoral thesis, Massachusetts Institute of Technology. Cited on pages 16 and 17.

Kreyszig, E. (1991). *Differential Geometry*. Dover, New York. Cited on pages 101, 102, and 169.

Kuribayashi, K., Tsuchiya, K., You, Z., Tomus, D., Umemoto, M., Ito, T., and Sasaki, M. (2006). Self-deployable origami stent grafts as a biomedical application of Ni-rich TiNi shape memory alloy foil. *Materials Science and Engineering: A*, 419(1):131–137. https://doi.org/10.1016/j.msea.2005.12.016. Cited on page 1.

Lang, R. J. (1996). A computational algorithm for origami design. In *Proceedings of the 12th Annual ACM Symposium on Computatinoal Geometry*, pages 98–105, Philadelphia, PA, USA. https://doi.org/10.1145/237218.237249. Cited on page 125.

Lang, R. J., Nelson, T. G., Magleby, S. P., and Howell, L. L. (2017). Kinematics and discretization of curved-fold mechanisms. In *Proceedings of the ASME 2017*, Cleveland, OH. ASME. https://doi.org/10.1115/DETC2017-67439. Cited on pages 24, 55, 104, 169, 177, and 178.

Lang, R. J., Tolman, K. A., Crampton, E. B., Magleby, S. P., and Howell, L. L. (2018). A review of thickness-accommodation techniques in origami-inspired engineering. *Applied Mechanics Reviews*, 70(1). https://doi.org/10.1115/1.4039314. Cited on page 165.

Lechenault, F., Thiria, B., and Adda-Bedia, M. (2014). Mechanical response of a creased sheet. *Physical Review Letters*, 112(24):244301. https://doi.org/10.1103/PhysRevLett.112.244301. Cited on pages 43, 72, and 186.

Lee, N. and Close, S. (2013). Curved pleat folding for smooth wrapping. *Proceedings of the Royal Society A: Mathematical, Physical and Engineering Sciences*, 469:20130152. https://doi.org/10.1098/rspa.2013.0152. Cited on page 20.

Lee, T.-U., You, Z., and Gattas, J. M. (2018). Elastica surface generation of curved-crease origami. *International Journal of Solids and Structures*, 136-137:13–27. https://doi.org/10.1016/j.ijsolstr.2017.11.029. Cited on pages 28, 34, and 51.

Leong, Chit, C. (2011). Simulation of nonzero Gaussian curvature in origami by curved-crease couplets. In Wang-Iverson, P., Lang, R. J., and Yim, M., editors, *Origami 5: Fifth International*

Meeting of Origami Science, Mathematics, and Education, pages 53–67. CRC Press. https://doi.org/10.1201/b10971. Cited on page 125.

Liu, K., Hacker, F., and Daraio, C. (2021). Robotic surfaces with reversible, spatiotemporal control for shape morphing and object manipulation. *Science Robotics*, 6(53):eabf5116. https://doi.org/10.1126/scirobotics.abf5116. Cited on page 99.

Liu, K., Novelino, L. S., Gardoni, P., and Paulino, G. H. (2020). Big influence of small random imperfections in origami-based metamaterials. *Proceedings of the Royal Society A: Mathematical, Physical and Engineering Sciences*, 476(2241):20200236. https://doi.org/10.1098/rspa.2020.0236. Cited on page 100.

Liu, K. and Paulino, G. H. (2017). Nonlinear mechanics of non-rigid origami: an efficient computational approach. *Proceedings of the Royal Society A: Mathematical, Physical and Engineering Sciences*, 473(2206):20170348. https://doi.org/10.1098/rspa.2017.0348. Cited on pages 35, 36, and 108.

Luu, C. (2017, June 11). McDonald's is giving its fries the rainbow treatment for the best reason. *Refinery29*. https://www.refinery29.com/en-us/2017/06/158544/mcdonalds-rainbow-pride-fries. Cited on page 20.

Mahadevan, L. and Rica, S. (2005). Self-organized origami. *Science*, 307(5716):1740–1740. https://doi.org/10.1126/science.1105169. Cited on page 72.

Martínez-Martín, F. J. and Thrall, A. P. (2014). Honeycomb core sandwich panels for origami-inspired deployable shelters: Multi-objective optimization for minimum weight and maximum energy efficiency. *Engineering Structures*, 69:158–167. https://doi.org/10.1016/j.engstruct.2014.03.012. Cited on page 165.

MathWorks (2022). Find minimum of function using genetic algorithm - MATLAB ga. https://www.mathworks.com/help/gads/ga.html. Cited on page 149.

Melancon, D., Gorissen, B., García-Mora, C. J., Hoberman, C., and Bertoldi, K. (2021). Multistable inflatable origami structures at the metre scale. *Nature*, 592(7855):545–550. https://doi.org/10.1038/s41586-021-03407-4. Cited on page 165.

Mentrasti, L., Cannella, F., Pupilli, M., and Dai, J. S. (2013). Large bending behavior of creased paperboard. I. Experimental investigations. *International Journal of Solids and Structures*, 50(20):3089–3096. https://doi.org/10.1016/j.ijsolstr.2013.05.018. Cited on page 43.

Miller, B. and Ziemiański, L. (2020). Optimization of dynamic behavior of thin-walled laminated cylindrical shells by genetic algorithms and deep neural networks supported by modal shape identification. *Advances in Engineering Software*, 147:102830. https://doi.org/10.1016/j.advengsoft.2020.102830. Cited on page 165.

Mintchev, S., Shintake, J., and Floreano, D. (2018). Bioinspired dual-stiffness origami. *Science Robotics*, 3(20):eaau0275. https://doi.org/10.1126/scirobotics.aau0275. Cited on page 100.

Mitani, J. (2011). A design method for axisymmetric curved origami with triangular prism protrusions. In Wang-Iverson, P., Lang, R. J., and Yim, M., editors, *Origami 5: Fifth International Meeting of Origami Science, Mathematics, and Education*, pages 437–447. CRC Press. https://doi.org/10.1201/b10971. Cited on page 125.

Mitani, J. (2019). *Curved-Folding Origami Design*. CRC Press. https://doi.org/10.1201/9780429059179. Cited on page 18.

Mitani, J. and Igarashi, T. (2011). Interactive design of planar curved folding by reflection. In *Pacific Graphics*. https://doi.org/10.2312/PE/PG/PG2011short/077-081. Cited on pages 26 and 50.

Miura, K. (1985). Method of packaging and deployment of large membranes in space. Technical Report 618, The Institute of Space and Astronautical Science. Cited on page 1.

Miyashita, S., DiDio, I., Ananthabhotla, I., An, B., Sung, C., Arabagi, S., and Rus, D. (2015). Folding angle regulation by curved crease design for self-assembling origami propellers. *Journal of Mechanisms and Robotics*, 7(2):021013. https://doi.org/10.1115/1.4029548. Cited on page 21.

Nagy, L., Rhode-Barbarigos, L., Adriaenssens, S., and Kilian, A. (2015). Conceptual design of a single-crease origami-arc inspired movable footbridge structure. *International Journal of Space Structures*, 30(2):75–84. https://doi.org/10.1260/0266-3511.30.2.75. Cited on pages 21 and 35.

Nassar, H., Lebée, A., and Monasse, L. (2017). Curvature, metric and parametrization of origami tessellations: Theory and application to the eggbox pattern. *Proceedings of the Royal Society A: Mathematical, Physical and Engineering Sciences*, 473(2197):20160705. https://doi.org/10.1098/rspa.2016.0705. Cited on page 125.

Nelson, T. G., Lang, R. J., Pehrson, N. A., Magleby, S. P., and Howell, L. L. (2016). Facilitating deployable mechanisms and structures via developable lamina emergent arrays. *Journal of Mechanisms and Robotics*, 8(3):031006. https://doi.org/10.1115/1.4031901. Cited on pages 21, 30, and 166.

Nie, Z., Jiang, H., and Kara, L. B. (2020). Stress field prediction in cantilevered structures using convolutional neural networks. *Journal of Computing and Information Science in Engineering*, 20(1). https://doi.org/10.1115/1.4044097. Cited on page 164.

Norman, A. D., Seffen, K. A., and Guest, S. D. (2008). Multistable corrugated shells. *Proceedings of the Royal Society A: Mathematical, Physical and Engineering Sciences*, 464(2095):1653–1672. https://doi.org/10.1098/rspa.2007.0216. Cited on page 66.

Norman, A. D., Seffen, K. A., and Guest, S. D. (2009). Morphing of curved corrugated shells. *International Journal of Solids and Structures*, 46(7):1624–1633. https://doi.org/10.1016/j.ijsolstr.2008.12.009. Cited on page 66.

Ogawa, H. (1972). *Forms of paper*. Van Nostrand Reinhold. Cited on page 17.

O'Rourke, J. (2011). *How to fold it: the mathematics of linkages, origami, and polyhedra*. Cambridge University Press. https://doi.org/10.1017/CBO9780511975028. Cited on page 3.

Peraza-Hernandez, E. A., Hartl, D. J., Malak, R. J. J., and Lagoudas, D. C. (2014). Origami-inspired active structures: a synthesis and review. *Smart Materials and Structures*, 23(9):094001. https://doi.org/10.1088/0964-1726/23/9/094001. Cited on page 5.

Pini, V., Ruz, J. J., Kosaka, P. M., Malvar, O., Calleja, M., and Tamayo, J. (2016). How two-dimensional bending can extraordinarily stiffen thin sheets. *Scientific Reports*, 6: Article 29627. https://doi.org/10.1038/srep29627. Cited on pages 7, 8, 23, and 103.

Pokkalla, D. K., Poh, L. H., and Quek, S. T. (2021). Isogeometric shape optimization of missing rib auxetics with prescribed negative Poisson's ratio over large strains using genetic algorithm. *International Journal of Mechanical Sciences*, 193:106169. https://doi.org/10.1016/j.ijmecsci.2020.106169. Cited on page 148.

Rabinovich, M., Hoffmann, T., and Sorkine-Hornung, O. (2019). Modeling curved folding with freeform deformations. *ACM Transactions on Graphics*, 38(6): Article 170. https://doi.org/10.1145/3355089.3356531. Cited on pages 26 and 31.

Raducanu, V. A., Cojocaru, V. D., and Raducanu, D. (2016). Structural architectural elements made of curved folded sheet metal. In *Complexity & Simplicity - Proceedings of the 34th eCAADe Conference*, volume 2, pages 409–416, Oulu, Finland. Cited on page 19.

Resch, R. (1970). Yellow folded cones: Kissing. *Ron Resch Official Website*. http://www.ronresch.org. Cited on page 17.

Ricci, A., Ponzio, C., Fabbri, K., Gaspari, J., and Naboni, E. (2021). Development of a self-sufficient dynamic façade within the context of climate change. *Architectural Science Review*, 64(1-2):87–97. https://doi.org/10.1080/00038628.2020.1713042. Cited on page 121.

Rivera-Tarazona, L. K., Bhat, V. D., Kim, H., Campbell, Z. T., and Ware, T. H. (2020). Shape-morphing living composites. *Science Advances*, 6(3):eaax8582. https://doi.org/10.1126/sciadv.aax8582. Cited on page 99.

Rodrigues, G. V., Fonseca, L. M., Savi, M. A., and Paiva, A. (2017). Nonlinear dynamics of an adaptive origami-stent system. *International Journal of Mechanical Sciences*, 133:303–318. https://doi.org/10.1016/j.ijmecsci.2017.08.050. Cited on page 1.

Rodrigues, O. (1840). Des lois géométriques qui régissent les déplacements d'un système solide dans l'espace, et de la variation des coordonnées provenant de ces déplacements considérés indépendamment des causes qui peuvent les produire. *Journal de Mathématiques Pures et Appliquées*, 5:380–440. https://archive.org/details/s1journaldemat05liou/page/380/mode/2up. Cited on page 178.

Sakovsky, M. and Ermanni, P. (2020). A thin-shell shape adaptable composite metamaterial. *Composite Structures*, 246:112390. https://doi.org/10.1016/j.compstruct.2020.112390. Cited on page 99.

Schenk, M., Allwood, J. M., and Guest, S. D. (2011). Cold gas-pressured folding of miura-ori sheets. In *Proceedings of the International Conference on Technology of Plasticity*, pages 459–464. ICTP. Cited on page 192.

Schenk, M. and Guest, S. D. (2011). Origami folding: a structural engineering approach. In Wang-Iverson, P., Lang, R. J., and Yim, M., editors, *Origami 5: Fifth International Meeting of Origami Science, Mathematics, and Education*, pages 291–303. CRC Press, New York, 1st edition. https://doi.org/10.1201/b10971. Cited on pages 35 and 108.

Schenk, M., Viquerat, A. D., Seffen, K. A., and Guest, S. D. (2014). Review of inflatable booms for deployable space structures: Packing and rigidization. *Journal of Spacecraft and Rockets*, 51(3):762–778. https://doi.org/10.2514/1.A32598. Cited on page 165.

Seffen, K. A. (2012). Compliant shell mechanisms. *Philosophical Transactions: Mathematical, Physical and Engineering Sciences*, 370(1965):2010–2026. https://doi.org/10.1098/rsta.2011.0347. Cited on page 28.

Seong, D. Y., Jung, C. G., Yang, D. Y., Moon, K. J., and Ahn, D. G. (2010). Quasi-isotropic bending responses of metallic sandwich plates with bi-directionally corrugated cores. *Materials and Design*, 31(6):2804–2812. https://doi.org/10.1016/j.matdes.2010.01.009. Cited on page 66.

Shah, D., Yang, B., Kriegman, S., Levin, M., Bongard, J., and Kramer-Bottiglio, R. (2021). Shape changing robots: Bioinspiration, simulation, and physical realization. *Advanced Materials*, 33(19):2002882. https://doi/org/10.1002/adma.202002882. Cited on page 99.

Shin, D. and Kim, Y. Y. (2020). Data-driven approach for a one-dimensional thin-walled beam analysis. *Computers & Structures*, 231. https://doi.org/10.1016/j.compstruc.2020.106207. Cited on page 164.

Sivanandam, S. N. and Deepa, S. N. (2008). *Introduction to genetic algorithms*. Springer. https://doi.org/10.1007/978-3-540-73190-0. Cited on page 148.

Slabaugh, G. G. (1999). Computing Euler angles from a rotation matrix. *http://eecs.qmul.ac.uk/˜gslabaugh/publications/euler.pdf*. Cited on pages 130 and 139.

Smeijsters, M. (2014). Skull. https://www.flickr.com/photos/derodeolifant/15569755709/. Cited on page 18.

Tachi, T. (2010). Origamizing polyhedral surfaces. *IEEE Transactions on Visualization and Computer Graphics*, 16(2):298–311. https://doi.org/10.1109/TVCG.2009.67. Cited on page 125.

Tachi, T. (2011). Rigid-foldable thick origami. In Wang-Iverson, P., Lang, R. J., and Yim, M., editors, *Origami 5: Fifth International Meeting of Origami Science, Mathematics, and Education*, pages 253–264. CRC Press. https://doi.org/10.1201/b10971. Cited on page 165.

Tachi, T. and Epps, G. (2011). Designing one-DOF mechanisms for architecture by rationalizing curved folding. In *Proceedings of the International Symposium on Algorithmic Design for Architecture and Urban Design*, Tokyo, Japan. Cited on pages 19, 25, and 28.

Tang, C., Bo, P., Wallner, J., and Pottmann, H. (2016). Interactive design of developable surfaces. *ACM Transactions on Graphics*, 35(2): Article 12. https://doi.org/10.1145/2832906. Cited on page 25.

Tang, R., Huang, H., Tu, H., Liang, H., Liang, M., Song, Z., Xu, Y., Jiang, H., and Yu, H. (2014). Origami-enabled deformable silicon solar cells. *Applied Physics Letters*, 104(8):083501. https://doi.org/10.1063/1.4866145. Cited on pages 1 and 165.

Thill, C., Etches, J. A., Bond, I. P., Potter, K. D., and Weaver, P. M. (2010). Composite corrugated structures for morphing wing skin applications. *Smart Materials and Structures*, 19(12):124009. https://doi.org/10.1088/0964-1726/19/12/124009. Cited on page 66.

Timoshenko, S. and Woinowsky-Krieger, S. (1959). *Theory of Plates and Shells*. McGraw-Hill, New York, 2nd edition. Cited on page 68.

Vergauwen, A., Laet, L. D., and Temmerman, N. D. (2017). Computational modelling methods for pliable structures based on curved-line folding. *Computer-Aided Design*, 83:51–63. https://doi.org/10.1016/j.cad.2016.10.002. Cited on pages 28, 30, 35, and 183.

Vurtur Badarinath, P., Chierichetti, M., and Davoudi Kakhki, F. (2021). A machine learning approach as a surrogate for a finite element analysis: Status of research and application to one dimensional systems. *Sensors*, 21(5):1654. https://doi.org/10.3390/s21051654. Cited on page 164.

Walker, A. and Stankovic, T. (2022). Algorithmic design of origami mechanisms and tessellations. *Communications Materials*, 3(1):1–8. https://doi.org/10.1038/s43246-022-00227-5. Cited on page 125.

Wang, W., Li, C., Cho, M., and Ahn, S.-H. (2018). Soft tendril-inspired grippers: Shape morphing of programmable polymer-paper bilayer composites. *ACS Applied Materials & Interfaces*, 10(12):10419–10427. https://doi.org/10.1021/acsami.7b18079. Cited on page 99.

Watanabe, Y. and Mitani, J. (2018). Interactive modelling of curved folds with multiple creases considering folding motions. *Computer-Aided Design and Applications*, 16(3):452–465. https://doi.org/10.14733/cadaps.2019.452-465. Cited on pages 26, 114, and 180.

Weisstein, E. W. (2019). Cone. From MathWorld – A Wolfram Web Resource. https://mathworld.wolfram.com/Cone.html. Cited on page 50.

Wenz, F., Schmidt, I., Leichner, A., Lichti, T., Baumann, S., Andrae, H., and Eberl, C. (2021). Designing shape morphing behavior through local programming of mechanical metamaterials. *Advanced Materials*, 33(37):2008617. https://doi.org/10.1002/adma.202008617. Cited on page 99.

Wertheim, M. (2004). Cones, Curves, Shells, Towers: He Made Paper Jump to Life. *The New York Times*. https://www.nytimes.com/2004/06/22/science/cones-curves-shells-towers-he-made-paper-jump-to-life.html. Cited on page 24.

Woodruff, S. R. and Filipov, E. T. (2018). Structural analysis of curved folded deployables. In *16th Biennial International Conference on Engineering, Science, Construction, and Operations in Challenging Environments*, pages 793–803, Cleveland, OH. ASCE. https://doi.org/10.1061/9780784481899.075. Cited on pages 9, 30, 35, 51, and 182.

Woodruff, S. R. and Filipov, E. T. (2020a). A bar and hinge model formulation for structural analysis of curved-crease origami. *International Journal of Solids and Structures*, 204-205:114–127. https://doi.org/10.1016/j.ijsolstr.2020.08.010. Cited on pages 34, 63, 108, 109, 121, and 161.

Woodruff, S. R. and Filipov, E. T. (2020b). Curved creases redistribute global bending stiffness in corrugations: theory and experimentation. *Meccanica*. https://doi.org/10.1007/s11012-020-01200-7. Cited on pages 9, 56, 65, and 100.

Woodruff, S. R. and Filipov, E. T. (2022). Bending and twisting with a pinch: Shape morphing of creased sheets. *Extreme Mechanics Letters*. https://doi.org/10.1016/j.eml.2022.101656. Cited on pages 7, 34, and 99.

Wriggers, P. (2008). *Nonlinear finite element methods*. Springer. https://doi.org/10.1007/978-3-540-71001-1. Cited on page 108.

Wu, L., Liu, L., Wang, Y., Zhai, Z., Zhuang, H., Krishnaraju, D., Wang, Q., and Jiang, H. (2020). A machine learning-based method to design modular metamaterials. *Extreme Mechanics Letters*, 36:100657. https://doi.org/10.1016/j.eml.2020.100657. Cited on page 164.

Yang, K., Xu, S., Shen, J., Zhou, S., and Xie, Y. M. (2016). Energy absorption of thin-walled tubes with pre-folded origami patterns: numerical simulation and experimental verification. *Thin-Walled Structures*, 103:33–44. https://doi.org/10.1016/j.tws.2016.02.007. Cited on page 34.

Yang, Y., Vella, K., and Holmes, D. P. (2021). Grasping with kirigami shells. *Science Robotics*, 6(54):eabd6426. https://doi.org/10.1126/scirobotics.abd6426. Cited on page 100.

Yao, H., Gao, Y., and Liu, Y. (2020a). FEA-Net: A physics-guided data-driven model for efficient mechanical response prediction. *Computer Methods in Applied Mechanics and Engineering*, 363:112892. https://doi.org/10.1016/j.cma.2020.112892. Cited on page 164.

Yao, S., Zhu, H., Liu, M., Li, Z., and Xu, P. (2020b). Energy absorption of origami tubes with polygonal cross-sections. *Thin-Walled Structures*, 157:107013. https://doi.org/10.1016/j.tws.2020.107013. Cited on page 5.

Yasuda, H., Yamaguchi, K., Miyazawa, Y., Wiebe, R., Raney, J. R., and Yang, J. (2020). Data-driven prediction and analysis of chaotic origami dynamics. *Communications Physics*, 3(1):1–8. https://doi.org/10.1038/s42005-020-00431-0. Cited on page 164.

Yasuda, H., Yein, T., Tachi, T., Miura, K., and Taya, M. (2013). Folding behaviour of Tachi–Miura polyhedron bellows. *Proceedings of the Royal Society A: Mathematical, Physical and Engineering Sciences*, 469(2159):20130351. https://doi.org/10.1098/rspa.2013.0351. Cited on page 43.

Zhai, Z., Wang, Y., Lin, K., Wu, L., and Jiang, H. (2020). In situ stiffness manipulation using elegant curved origami. *Science Advances*, 6(47):eabe2000. https://doi.org/10.1126/sciadv.abe2000. Cited on page 100.

Zhang, Z., Qiu, T., Song, R., and Sun, Y. (2014). Nonlinear finite element analysis of the fluted corrugated sheet in the corrugated cardboard. *Advances in Materials Science and Engineering*, 2014:654012. https://doi.org/10.1155/2014/654012. Cited on page 66.

Zirbel, S. A., Trease, B. P., Magleby, S. P., and Howell, L. L. (2014). Deployment methods for an origami-inspired rigid-foldable array. In *Proceedings of the 40th Aerospace Mechanisms Symposium*, pages 189–194. Mechanisms Education Association. Cited on page 165.

Zirbel, S. A., Trease, B. P., Thomson, M. W., Lang, R. J., Magleby, S. P., and Howell, L. H. (2015). HanaFlex: a large solar array for space applications. In *Micro- and Nanotechnology Sensors, Systems, and Applications VII*, volume 9467, pages 179–187. SPIE. https://doi.org/10.1117/12.2177730. Cited on page 165.